# Synaptic and cellular mechanisms underlying functional responses in mouse primary visual cortex

Marta Gajowa

**Université Paris Descartes**

**École Doctorale Interdisciplinaire Européenne Frontières du Vivant**
**Neurophotonics Laboratory, CNRS UMR8250 (dir. V. Emiliani)**

# *Synaptic and cellular mechanisms underlying functional responses in mouse primary visual cortex*

*Marta Gajowa*

Presented at 23.11.2018

Supervised by Lyle Graham

Jury composition :
Brice Bathellier – reviewer
Alain Destexhe – reviewer
Laurence Cathala – jury member
Federico Trigo – jury member

# Abstract

This thesis describes two projects which examine functional neuronal processing in the primary visual cortex of the mouse, from both a population and a single cell perspective.

The first part focuses on the development of an all optical stimulation and readout biological preparation, for the eventual application of constructing a functional synaptic map of primary visual cortex. More specifically, my findings are for the characterization of opsins for this protocol using in vitro recordings from slices of mouse primary visual cortex and CHO cells. I show examples of well working opsin constructs that provide photocurrents enabling induction of an action potential, and how the various features of opsin viral constructs can influence their usability in the context of a functional connectivity project, judged based on whether the evoked photocurrent can lead to reliable induction of an action potential. I describe the biophysical parameters of the studied opsins and their influence on desired temporal patterns of action potentials. Under 2 photon holographic illumination, ReaChR opsin enables sub-milisecond control of single action potential, but the long kinetics of this opsin influences the temporal control for inducibility of the train of action potentials. Results with CoChR - mCardinal stress the influence of opsin expression variability in the preparation, which impacts effective optogenetically induced spiking. I also show how modeling studies facilitate understanding of the influence of biophysical parameters on the evoked current, and can provide a tool to predict the output of different stimulation protocols that take into account conditions influencing the evoked photocurrent.

In the second part I examine visually-evoked synaptic excitatory and inhibitory responses and dissect their influence on the spiking cell output, thus the functional I/O transfer function, based on a large (~60 cell) dataset of in vivo whole-cell patch recordings in mouse primary visual cortex. This part is based on the development of a novel, closed-loop in-vivo protocol that uses the dynamic-clamp method to re-inject parameterized versions of visual-evoked responses back into the same neuron. I find a diverse set of dynamical relationships between visually-evoked excitation and inhibition, with in general weak cross-correlations across the entire response, and occasional highly synchronized transient responses. Inhibitory inputs are consistently larger and show stronger fluctuations than excitatory inputs, with overall higher frequency content. These results suggest that the dynamics of the neuronal code differ between excitatory and inhibitory pathways, and provide constraints on theoretical descriptions based on balanced states between the two. I find that the spiking response to both visually-evoked and steps of simulated synaptic excitation is significantly modulated both linearly and non-linearly by, respectively, visually-evoked and steps of inhibition, including increasing excitation threshold, and reducing both gain and the saturation response. Comparison of the original visual spiking responses to those from the dynamic-clamp protocols suggest quantitative constraints on the relevant time-scale for the underlying neuronal code, in particular when considering rate-based versus spike time - based descriptions.

KEYWORDS: Visual cortex, optogenetics, in-vivo electrophysiology, synaptic interactions, dynamic-clamp

**Acknowledgements:**

I would like to say thank you to all good-hearted people I met during this journey.

First of all, I would like to thank my supervisor Lyle Graham for being a true supervisor during last four years. Thank you for all the support I got on many occasions during the thesis and before, during my master studies. Especially, thank you for the team work and trust, which help me to grow scientifically and as a researcher, for reasonable and thoughtful advices and for challenging me on the daily basis.

Secondly, I would like to thank the members of the thesis advisory committee: Alain Destexhe, Uwe Maskos and Alberto Bacci, for useful insights, advice and guidance in taking hard decisions.

Thirdly, I would like to thank to the whole 'FdV family' (officially known as the FdV doctoral program) – for organizing such an amazing doctoral school. Special thank you to student scientific coordinators - Sofie Leon and Maria Molina Calavita - for their help in navigation during thesis, possibly straight to the goal; Elodie Kaslikowski, for taking care about all formal side of the program and saving me a lot of stress; David Tareste and Francois Taddei, for creating a friendly and open atmosphere and scientific courses program, which was truly useful and put us out of the comfort zone encouraging to think wider.
A special thank you needs to be said to the FdV scientific board members for their support and useful discussions about scientific life and all career advices -Melissa McCartney, Andrew Murray, Suzannah Rutherford and Saskia van der Vies.
Thank you to the whole CRI family for fostering creativity and sharing their vision of education.

To my family. Thank you to my partner for being a companion in all this journey. For his support expressed in the coffee in the morning and taking over much of the duties of our everyday life, so I could focus on thesis only, especially in the final part of the thesis.
Thank you to my parents for supporting all my crazy ideas and not putting a pause to my excessive additional activities schedule when I was younger. For teaching me that 'the knowledge is the only thing no one can take back from you' and extrapolating this rule to all life domains.
To my brothers and sisters – who expressed their support in many unexpected ways which touch my heart and give a lot of strength.
To my closest friends on whom I could count:
Ida, Anna and Kuba the trio with whom I could share both good and worse moments.
I would also like to acknowledge the support of the Neurophotonics Laboratory, in particular the PhD students and lab members for all the common work, the
afterwork and in the meantime of the work. Special thank you to Alexis, Oscar, Marco and Florance who closely shared with me not only the office but also the PhD experience. A big thank you to all the members of Neurophotonic Laboratory, for all the lessons and shared knowledge, good advices

and sincere good-heartedness. Special thank you to Dimitrii, Eirini, Valeria, Rosella, Emmanuelle, Fabio, Nicolo and Abeer.

And to many others to whom I could talk during moments of weakness and get an advice and with whom I was sharing the good moments.
Thank you! ♥♥♥

# Table of Contents:

# 1. Introduction

Feature selectivity of cortical neurons, one example of functional properties in the brain, is the ability of neurons to respond to particular stimulus attributes - e.g. the receptive field of a neuron in primary visual cortex (V1) with respect to object movement direction. This thesis contributes to understand how feature selectivity arises in mouse V1. It is divided into two parts, each based on distinct approaches to elucidate visual processing mechanisms, the first at a population level and the second at the single neuron level.

First, on a population level, I have developed tools towards an eventual project that combines 2-photon optogenetics, 2-photon imaging and traditional whole cell electrophysiology to map functional connectivity in V1. This map will provide a link between cell tuning (i.e. cell function) and network architecture, enabling quantitative and qualitative distinction between two extreme scenarios in which cells in mouse V1 are either randomly connected, or are associated in specialized subnetworks. Here I describe technical validation of the method, with the main focus on finding the appropriate biological preparation and reagents.

Second, based on whole-cell patch recordings of single mouse V1 neurons in vivo, I characterize visually-evoked synaptic conductances and the associated neuronal input-output (I/O) transfer function. I employ a novel closed-loop in vivo protocol based on a combination of current, voltage and dynamic clamp recording modes. I first measure the basic I/O transfer function of a given neuron with current steps under current clamp, and with excitatory and inhibitory conductance steps under dynamic clamp. I then measure the visually evoked spiking output of the neuron, under current clamp, and its synaptic conductance input, under voltage clamp. Finally, I reintroduce variations of the visually evoked conductance input to the same cell, under dynamic clamp, to construct the functional I/O transfer function. I find that visually evoked synaptic excitation and inhibition are dynamically unbalanced in visual cortex, which I describe in the context of theories based on balanced excitatory inhibitory states. I describe and compare the different I/O transfer functions, which allows a characterization of the mathematical operations performed by the neuron. I find that synaptic inhibition based on visual responses has both a linear and divisive impact on the spiking response to synaptic excitation based on the same visual response. Furthermore, modifications of the relative scaling and the temporal characteristics of the reintroduced synaptic excitation and inhibition enables dissection of each component's role in shaping the spiking output, as well as to infer overall differences between various physiological cell types (e.g. regular-adapting, presumably excitatory, versus fast-spiking, presumably inhibitory, neurons). Finally, examination of the transfer functions, in particular their dependence on temporal modifications, provides insights on the relationship between the neuronal code and the biophysical properties of neurons and their network.

## 1.1. Thesis outline

The first part of my thesis is focused on the efforts undertaken towards the validation of an 'all-optical stimulation and readout' protocol. Combined with the in vivo patch clamp technique, this approach has been developed in order to map functional connectivity of V1. In this context neuronal function is defined as feature selectivity, and connectivity by the pattern and strength of the synapses providing input to a given neuron, characterized by their individual receptive field properties. Such a population map is a necessary step to link network architecture and circuit function, and thus to understand visual processing mechanisms on a population level.

To more fully understand the neuronal processing that underlies circuit function, the functional mapping, characteristic to systems neuroscience, needs to be supported by a biophysical study elucidating neuronal computation at the single cell level. This comprises the second part of my thesis, where I have described the transformation of synaptic input evoked during visual stimulation to the neuronal spiking output. This was accomplished by the application of a closed loop approach, combining traditional patch clamp protocols with the use of the dynamic clamp recording mode in vivo, enabling the systematic probing of a cell with modifications of its original "natural" synaptic input. This probing protocol helps to describe the different roles of excitatory and inhibitory synaptic components in shaping the neuronal output, and thus the mathematical operations underlying neuronal processing,
Thus, contributing towards understanding the neuronal code and neuronal biophysics of computation.

In chapter 2 I describe briefly the logic behind the technical aspects of each part of the project, the specific biological questions, and finally a common scientific context for both projects. Next, I will focus on my contributions to the functional connectivity mapping project (Chapter 3), explaining various aspects towards validation of the optogenetic methods. Since the thesis duration allowed only for contributing to technical aspects of the all optical stimulation and readout I present the results of my work and contribution to other lab projects in that context.

In the second part of my thesis I will present my results on studying functional processing in mouse visual cortex, focusing on two aspects:
-Characterization of visually evoked synaptic conductances, thus contributing to understanding visual circuit functioning (Chapter 4)
-Description of the input-output transfer function of single neurons, thus contributing to general understanding of neuronal processing rules (Chapter 5)

Although many of the techniques used in the second part were well established in the laboratory, which enabled more focus on the scientific problem, they are not widely used. More importantly, the development and in vivo application of the dynamic clamp method based on conductance measurements of functional responses is novel. Therefore, some sections of this thesis are dedicated

to explaining the method in detail, and to elaborate on important technical aspects influencing the interpretation of the measurements. Some part of the discussion (chapter 6) refers to the technical aspects, as well as compare the findings with the literature.

All the tools used in both parts of this thesis project shaped my understanding of the problems and scientific perspective with a mutual benefit. I am closing this thesis with a small comparison of the two technological approaches used, stressing the limitations and possibilities they give (Chapter 6, section 6.6).

In summary, this thesis is an interdisciplinary work, integrating different approaches to a problem, using different technical combinations and applying elements of theoretical investigations to the experimental work.

# 2. Deciphering brain function in terms of network architecture and neuronal biophysics

The early visual system, including V1 decomposes the visual scene into single, simple attributes. The cells in V1, the first major cortical area that receives visual input from the lateral geniculate body in the thalamus, respond selectively to these decomposed attributes - for example, to the orientation and direction of a visual feature. Orientation and direction selectivity (tuning) was first discovered by Hubel and Wiesel in the cat and was a seminal result towards understanding how visual processing occurs(Hubel and Wiesel 1962). Since then, an enormous body of work has been aimed towards understanding how the neurons in V1 are wired together and what is the role of each cell in the circuit.

In this section I am presenting a short synthesis of the knowledge regarding both the V1 circuit architecture and feature selectivity. This synthesis provides the reader with the background knowledge about V1 circuit – the model of this thesis.
In this first part I am only focusing on findings describing neuronal architecture or tuning in V1 separately. In the following sections, I am describing both projects of this thesis with addition of more project-specific scientific context.

## 2.1.1 Primary Visual Cortex of a mouse

**Neuronal circuit architecture in V1**

Visual cortex, as a part of the neocortex, follows the universal structure of six distinguishable layers of neurons, as well as the less well-defined concept of cortical columns. In rodents the cortical column is considered to have a diameter of 0.3 mm and contain around 7 500 neurons (Markram et al. 2004)L2/3, which is the main focus of the thesis, lies 125-135µm below the brain surface(Xu et al. 2016). As in other parts of the neocortex, it contains around 20-30% of interneurons and 70-80% of excitatory cells. This ratio varies a bit in between layers, with exception of L1, which contains almost only interneurons (Markram et al. 2004).
Neocortical circuit architecture seems to follow a universal structure among different modalities, repeating a similar motif (Mountcastle 1997) with subtle but essential modifications are found between different cortical areas. In general, excitatory connections of various modalities obey a certain laminar organization of structure and connections. Thalamic input arrives in L4, whose neuronal afferents mainly contact L2/3. Descending projections from L2/3 terminate in L5 and L6 (Gilbert and Wiesel 1979). In L2/3, excitatory pyramidal cells tend to connect with each other sparsely, with only a 19% probability (Hofer et al. 2011).

**Functional properties of cells in V1 (focus on the L2/3)**

Description of receptive fields in cat primary visual cortex (Hubel and Wiesel 1962) initiated characterization of cell functional properties and tries to find the link between cell function and circuit architecture. Receptive fields are parts of the space within a stimulus is influencing response of a particular neuron. As such, receptive fields presence and shape is a consequence of a circuit architecture at all the previous stages. In this context, the first, very simplistic definition of neuronal function is to react when the stimuli will appear in the receptive field of a given neuron. This definition is further developed, as neurons differ between each other in the response they provide, depending on various stimuli characteristic. The functional properties of neurons such as orientation and direction selectivity, investigated in this thesis, and others, like spatial and temporal frequency, speed or contrast, together creates the necessary primitives for the eventual perception of a visual scene in higher visual areas.

There is no complete agreement between authors about the exact numbers and proportions of cells selective to various functional parameters. These differences are usually due to different methods, which can favor one or another type of cells (Gao, DeAngelis, and Burkhalter 2010). The work of Niel and Stryker on mouse V1 receptive field properties, using silicon electrode arrays, has provided useful data concerning functional properties of cells in mouse V1. Indeed, the mouse model has only been extensively investigated in recent years, motivated by the possibility of genetic modifications that are impractical with the cat. Generally, the selectivity of V1 neurons in the mouse to various attributes of visual stimuli increases in more upper layers (Cristopher M Niell and Stryker 2008) (Figure 1), suggesting that these layers are fulfilling a key role in the perception of the image. These authors determined that 74% of cells are selective to the orientation of a drifting grating, with a predominance of narrowly tuned cells, especially in the upper L2/3. Analysis of direction selectivity (by comparison of responses to opposite directions that correspond to the same orientation) revealed that about 23% of orientation selective cells are also tuned for a preferred direction, with a bit higher selectivity for cells in L2/3 and 4. This finding corresponds to other findings in the mouse, rat, rabbit and macaque, with the number varying between 24-28% between different species (reviewed in Gao et al., 2010).

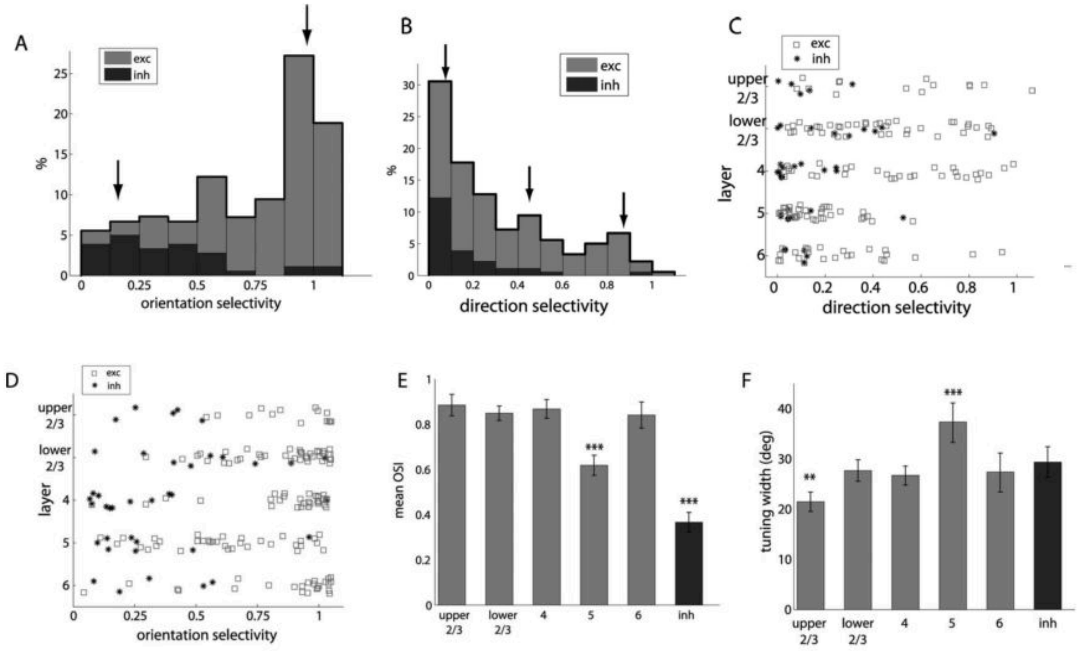


*Figure 1 . Orientation and direction selectivity in mouse V1 (modified after C. M. Niell & Stryker, 2008). (A) Histogram presenting all orientation selective cells distribution of orientation selectivity index. Excitatory and inhibitory cells are marked in grey and black respectively. (B) Same as A, for direction selectivity index. (C) and (D) Layer distribution of direction and orientation selectivity index. (E) Mean OSI values for layer and inhibitory cells. (F) Tuning width change across layers. In more superficial layers, both the orientation and direction selectivity indices are higher and more sharply tuned.*

The same authors also report spatial frequency tuning (in cycles of a presented grating pattern per degree of visual field), which defines the width of the bar in the grating, in the range of 0.02 – 0.09 c/deg, with the preferred median being equal 0.03c/deg. Similar values were recorded in L2/3, equal to 0.04 c/deg for excitatory neurons. The selectivity of inhibitory neurons and neurons in layer 6, is characterized by a significantly lower preferred spatial frequency of 0.02 c/deg. The median preferred spatial frequency of the mouse was found to be significantly different than in a cat (0.9 c/deg) and macaques (1.5-4.2 c/deg), corresponding to the much lower spatial resolution of mice vision (reviewed in (C. Niell 2015). Additionally, in 90% of neurons, a specific cut off value was found that is always lower than ~0.43c/deg, above which the activity of cells decreases to 10% (Gao et al., 2010).

Temporal frequency tuning indicates the timing acuity of neurons, with more than 90% of V1 cells showing temporal frequency tuning (Gao et al., 2010) (median response frequency of ~2Hz, and ~4Hz for layer 4 cells).

Interestingly, the spontaneous firing rate of neurons vary between layers and types; excitatory neurons in L2/3 discharging on average 1 spike in 10s (0.01 Hz), whereas for layer 5 the average is close to 2Hz for excitatory cells and 1 Hz for inhibitory cells. The presentation of a visual stimuli typically elicits response rates of around 4.7 and 14 Hz, for excitatory neurons in L2/3 and L5, and

inhibitory cells, respectively (C. M. Niell & Stryker, 2008). It is noteworthy to point out that the increase of the spiking frequency during the visual response above baseline is most dramatic for excitatory cells in L2/3. Moreover, inhibitory cells, and cells in L5, which have the highest spontaneous spiking frequency, are at the same time characterized as being least selective cells for various stimulation properties. This might suggest the different role of L2/3, L5 and interneurons in the information processing (and possibly different code).

A change in stimulus contrast has a weak influence on tuning properties, rather acting as a scale factor for the response amplitude, with the strongest response at 100% contrast. Although it is worthy to mention that we can distinguish cells which respond quickly to even small changes in contrast tend to be characterized by steep contrast saturation curve (sigmoidal), whereas other neurons have a lower sensitivity to contrast change (Gao et al., 2010). Cells in L2/3 are especially sensitive to contrast change (C. M. Niell & Stryker, 2008).

## 2.2. Functional network architecture of primary visual cortex

### 2.2.1. Optical interrogation of network architecture

Understanding of any system requires understanding two components: the circuit architecture and its individual unit functions. In the context of the primary visual cortex circuit the connections between the cells constitute the circuit structure. The neuronal function is the ability of a neuron to respond selectively to a repertoire of a stimuli. Historically, researchers had access only to one elements of the circuit - the structure or the function (as reviewed in previous subsection), sometimes supplemented with indirect measurement of the other component. Usually, also the description in hand was limited to only a snippet of the real, physiological situation, because of technological limitations. This situation limited strongly the success in linking the two essential circuit components.

In this project we had the goal to develop a protocol to perform a large scale functional connectivity mapping of V1, filling the gap between pure structural or functional maps by providing the link between the two. To achieve that a validation technique with a functional biological preparation is needed. The designed combination of techniques includes:

- calcium imaging: use of a fluorescent probe, which reports the level of neuronal activity (firing) during visual stimulation. This step would provide information about the function of a neuron, for instance, its tuning.
- “whole-cell” patch clamp technique: a traditional electrophysiology technique to monitor the membrane potential of a neuron or its currents fluctuations. This technique serves in this protocol for detection of synaptic connections between cells.
- optogenetics technique: enables genetic modification of neurons to make them light sensitive. This technique combined with 2 - photon photostimulation gives the possibility to excite single or groups of neurons by light and thus, map the connections between pre- (stimulated by light) and post-synaptic (patched) neuron.
- 2 - photon Computer Generated Holography - technique enabling light shaping into a desired spatial pattern, allowing to illuminate and photoactivate only specific neuron of interest.

In the context of the combination of these techniques, my contribution to the project falls into developing a biological preparation which could be used effectively to apply this electro-optical investigation of the functional connectivity map.
Practically, in this project my focus has been the searching of the right optically sensitive channel (opsin), which could be paired with calcium sensor for in-vivo recording in mouse V1.

## 2.2.2. Background based perspectives of the structure-function mapping approach

The functional mapping protocol described in previous section, enables to screen an unprecedented high number of pre-synaptic candidates during experimental session than other existing technique, such as, for instance, patch-clamp pair recording. Additionally, due to whole-cell patch clamp, the strength of the connection and or input conductance could be assessed. Added to that anatomical context information about the function of the total, or at least the majority, of the cells screened for connection would enable us to strive today neuroscience questions by providing more accurate large-scale description of the circuit performance. Such a description would enable us to understand how the function of cell emerges from the circuit architecture, how important is the wiring pattern, if it exists, towards creating tuning properties and finally, what are the strategies of information processing and how are they different between rodents and other mammals?

Below, I will elaborate on some of the hypotheses existing in literature providing the experimental background and pointing out how the proposed combination of techniques would help to investigate particular aspects of functional connectivity.

### *2.2.2.1. Functional subnetworks or random connections*

What is the connectivity pattern between similarly oriented cells in mouse V1? How important is the wiring pattern, if it exists, towards creating tuning properties?

The work of (Ko et al. 2011) suggests the existence of functional subnetworks of pyramidal cells. The double step protocol, using first OGB calcium imaging in vivo and second multi - electrode patch clamp connectivity studies in vitro was applied to investigate in detail the connectivity between pyramidal cells in relation to their tuning. Results revealed that cells sharing the same orientation or direction sensitivity tend to be more frequently connected. The big caveat of interpreting of this work is the fact that the second part was done in vitro and thus some of the connections were cut. On the other hand, the number of cells examined was also low (one could investigate group of 3 - 4 cells at a time).

Similar functional subnetwork perspective is emerging form studies of Wertz et all. GCaMP6s calcium imaging in the mouse shows that in about one third of pyramidal cells in L2/3, all presynaptic cells share the same selectivity as the target neuron (creating tuned networks) (Wertz et al. 2015). This study took advantage of retrograde trans-synaptic trafficking of rabies virus inducing GCaMP6s expression, injected to single pyramidal cell in L2/3, allowing the expression of calcium indicator that was restricted to a target pyramidal cell and all its pre-synaptic neurons. The remaining two thirds of the identified networks were untuned. The spatial distribution of the connections showed that majority of presynaptic cells lie in an approximately 200µm wide lateral area arising from L2/3 or L4, suggesting the existence of functional layer modules (at least two type, tuned and not tuned) within the presynaptic network (Wertz et al., 2015). On the other hand, theoretical work of (Hansel and van

Vreeswijk 2012) shows that in mouse V1 a totally random connectivity between the cells is enough to obtain orientation selectivity observed.

This contrasting examples stress the need of a systematic, big-scale study investigating connectivity and function at the same time to learn the rules about how such subnetwork would be created and the tuning differences within such an ensemble of cells is still not well explained.

#### *2.2.2.2. Connectivity description and its influence for signal processing:*

a) Assessment of the main information flow paths

An exemplary mapping study, with the use of glutamate uncaging, showed that excitatory neurons in L2/3 of V1 receive the strongest excitatory input from L4 and L5a, weaker from L2/3 and minimal from L6. On the other hand, excitatory L2/3 neurons were reported to receive a majority of inhibitory inputs from L2/3, L4, L5a and L1 Inhibitory connections in L2/3 were also much easier to detect, taking into account their high IPSC amplitude (~50 pA) and the probability of inhibitory input to excitatory cell was assessed to be around 50% within L2/3, and 30% if the input was from L4. Additionally, this study found that cells in L2/3 do not receive significant inhibitory transmission from deep infragranular layers (L5 and L6, low probability of connection and small amplitudes) and are the only excitatory population that obtain connections from interneurons in L1 (Xu et al. 2016)

This work done in slices in vitro provides useful information about possible paths of information flow at the level of local circuit. Additionally, drafted before Connectivity in V1 can be complemented with the findings of other researchers focusing more in detail on particular connections examining more in detail their specific properties and the cell type they relate. For example, studies on rat V1 showed that fast – spiking interneurons preferentially connect to neighboring PCs, which in turn provided them with reciprocal excitation (Yoshimura and Callaway 2005). Furthermore, a fine scale circuit rule was noticed. Fast spiking interneurons were usually connected with two other PCs, which were also reciprocally connected. Such fine-scale circuits were not found in the case of adapting, inhibitory neurons (Yoshimura & Callaway, 2005).

It is hard to integrate together precise information about the connectivity of specific cell types within layers because studies are done with the use of different techniques that can potentially influence the results (e.g. the amplitude and latency of inputs, and the percentage of connections between different cell types) and the consequent interpretation. Once again, this is why descriptive, mapping studies on a large scale are highly valuable.

b) The number and role of the weakly and strongly connected subnetworks

Apart from distinction to functional subnetworks, researchers described weakly and strongly connected subnetworks in V1. OGB imaging studies coupled with patch clamp recordings showed

that pyramidal cells (PCs) with correlated calcium imaging responses shared strong reciprocal connections in L2/3, even if there were far more weak connections, and weak connections linked neurons with uncorrelated responses (Cossell et al. 2015).

Thanks to population and layer specific ChR2 expression, the studies demonstrated that somatostatin interneurons (SOM) connect to pyramidal neurons with a 43% probability, typically at a target location 200µm from the soma (Adesnik et al. 2012) This connection was characterized by a post-synaptic signal amplitude (31,3±11,5 pA) that was twice as large, and a latency (1,29±0,2 ms) that was shorter, in comparison to PC to PC input (amplitude: 15,7±2,36 pA, latency: 3,33±0,42 ms)(Fino and Yuste 2011). On the other hand, fast-spiking, weakly tuned interneurons (considered to be PV expressing interneurons, comprising up to 10% of neuronal population) receive input from neighboring PCs with a high 88% probability (EPSP amplitude ~1 mV) (Hofer et al., 2011).

Presented studies present a snippet of circuit architecture with insights into subpopulations building the circuit. Again, integration of the knowledge inferred from studies using different techniques pose obstacles for results interpretation and this suggest again the need a more versatile and high throughput investigation approach. In the context of these findings it would be especially interesting to ask what the proportion of suggested previously tuned vs untuned networks is and what would be the role of weak connections towards shaping the post-synaptic cell's response.

c) The role of the inhibitory/ excitatory populations

Investigation of the inhibitory network has benefited from the use of calcium imaging. One of the earliest studies of GABAergic neurons with calcium imaging (using Fura-2 sensor) confirmed a broader tuning of interneurons in comparison to PCs (Sohya et al. 2007). This result was confirmed via a combination of OGB imaging and immunohistology, where broad tuning was shown to be a characteristic feature of all inhibitory neurons, regardless of type (PV, SOM, VIP - positive) (Kerlin et al. 2010). Additionally, combining OGB loading and electron microscopy has allowed for the retracing of connections between cells of known function, showing that inhibitory cells in L2/3 receive excitatory input from differently tuned cells in the neighborhood, which could explain the broad tuning of interneurons (Bock et al. 2011).

These findings raised the question about the function of different cell types, especially in the context of different connection schemas between each inhibitory cell subtype and PCs. Subsequently, inhibitory networks started to be investigated with optogenetic tools. The combination of conditional expression of ChR2 in particular cell types and layers, with patch clamp recordings, allowed more insight on that question. PV interneurons (supposedly fast –spiking cells), which target perisomatic regions of PCs, were found to sharpen neuronal feature selectivity. This was an effect specific to PV interneurons, since expression of ChR2 in SOM or VIP interneurons did not influence the tuning properties of a target cell (S.-H. Lee et al. 2012). A similar hypothesis was posed earlier in an investigation of feature selectivity of simple cells (the majority located in L2/3(Gao et al., 2010; C. M.

Niell & Stryker, 2008) with the use of the dynamic clamp method. The study showed that an increase of inhibition delivered by the dynamic clamp sharpened tuning. In addition, a decrease of inhibition caused a reduction of cell selectivity (B.-H. Liu et al. 2011).

In these findings the 1-Photon optogenetic combined with single patch clamp recording allowed only to assess the influence direction of a whole population excitation on a single cell pyramidal cell function and thus, provides us only a snippet of a real situation.

#### *2.2.2.3. Integration of synaptic input by the cell*

a) Population perspective

The balance between excitatory and inhibitory inputs shapes the spiking output of the neuron. Such balance includes both the ratio and strength of excitatory and inhibitory synapses to the output cells, as well as their temporal interplay.

The study comparing the selectivity of excitatory and inhibitory input conductance in cats with selectivity of the cell for either orientation or direction selectivity showed three possible input schemes, which contribute in different ways to the output response of a cell. The majority of cells (60% for orientation selectivity and 70% of those for direction selectivity) had both excitatory and inhibitory inputs tuned to the same orientation/ direction as the cell's output, with some differences in input selectivity, in particular the relative width of the input tuning curves. Importantly, in general the temporal overlap of the excitatory and inhibitory input conductances were out of phase for the preferred stimulus and in phase for the non- preferred stimulus. The other two groups, less frequently detected but still significant, were either characterized by a complete mismatch in the preferred orientation / direction for both inputs and the cell output, or partial mismatch, where only the excitatory conductance was tuned similarly as the cell output (Cyril Monier et al. 2003).

Similar measurements of the excitatory and inhibitory inputs in mouse did not show the change in phase observed in cats, but found that both excitatory and inhibitory inputs were similarly tuned as the spike output with a high correlation ($r = 0.83$) ( a. Y. Y. Tan et al. 2011; B.-H. Liu et al. 2011) (Figure 2). In both of these studies, cell type was not assessed, but it is likely that taking into account the number of cells recorded both excitatory and inhibitory cells were represented.

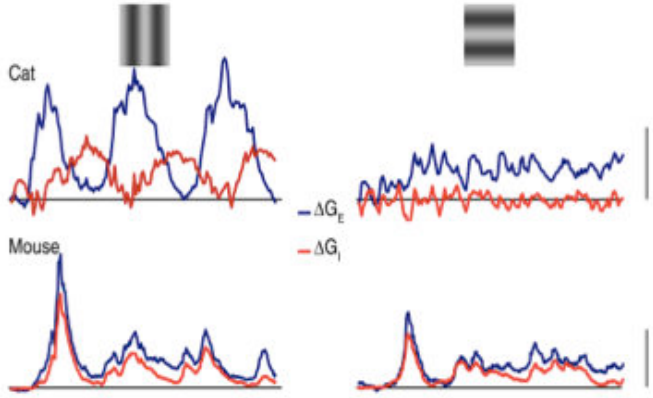


*Figure 2 Visually - evoked conductances for cat and mouse in response to preferred(left) and orthogonal orientation(right). Scale bar for mouse: 5nS, for cat 2 nS. After Tan et al.2011*

Both of these measurements, try to relate synaptic input measured in the cell by conductance measurements with the cell output and function. Conductance measurements provide the information about summed synaptic input from all the circuit before the recorded cell but the information about the function of the particular presynaptic cells and the weight of their contribution to the postsynaptic cell is unknown. The mapping protocol could provide this context.

b) Single cell perspective

A study combining targeted patch-clamp in vivo and fast 2- photon calcium imaging (GCaMP6s) showed that neurons in mouse visual cortex have several differently tuned 'hot spots' in their dendrites, which seems to be spaced randomly. Such 'hot spots' could be described as areas on the dendrite responding selectively for visual stimulation. 72% of these 'hot spots' were sharply tuned, and were found in all recorded cells regardless of the degree of spike tuning (or lack of tuning) (Jia et al. 2010). Another, study utilizing GAaMP6s presented similar hot spots. Additionally, an analysis of spine tuning in relation to cell selectivity showed that summed synaptic input to individual neurons allow for reliable prediction of neuron orientation preference (Wilson et al. 2016) (study conducted on ferret).

These studies focused on analysis of the functional profile of both the whole cell and its sub-compartments could largely benefit by adding the information about influence of specific pre-synaptic cell of known type and function. It would enable to ask about connections distributions and strength shading light into the mechanism of creation of described hot spots. In other words, one could verify if the hot spots are created by single cell vs. several cells input and what would be their origin and input strength.

#### *2.2.2.4. Current background knowledge synthesis*

Altogether, these results suggest a sparse network of pyramidal cells in V1 with some degree of specificity among their connections and synaptic strength (strongly connected networks of PCs, whose selectivity properties would be strongly correlated), contrasted with a dense but weak connectivity of inhibitory neurons that provide a representation of local activity that counterbalances the more specific excitation. Excitatory and inhibitory synaptic connectivity is spatially balanced across the excitatory neuronal network in V1. Statistical comparison of the location of synaptic inputs across cortical layers did not show a significant difference, showing that pyramidal neurons obtain a similar distribution of inhibition and excitation across V1 layers (Xu et al., 2016). The balanced distribution of excitation and inhibition is contrasted with unbalanced tuning properties across cortical layers, which suggest an increase in information filtering across layers (stronger selectivity in more upper layers), especially in the L2/3, which receives input from all other layers. Nevertheless, the exact mechanism and rules of information flow, especially in the L2/3, is still not well understood.

The specific application of the methods developed in this project will fill several gaps in current knowledge, in particular because of our all in-vivo approach, in contrast to previous studies. For example, we will be able to derive functional connectivity data based on a larger population that previous work (Cossell et al. 2015; Ko et al. 2011). Comparison of synaptic conductance measurements between visually-evoked responses and optogenetic stimulation of candidate afferent neurons will allow us to gain insight in the balance description between inhibition and excitation on the recorded cell, in particular to decipher quantitative and qualitative differences between intra and interlayer connections. Indeed, it is important to perform such studies in vivo, among other reasons given the physiological high synaptic background activity present in the context of studies reporting how global brain state can significantly modify the synaptic properties of an investigated (Kwan and Dan 2012).

## 2.3. Synaptic-spike transduction of cortical neurons

### 2.3.1. Electrophysiological interrogation of function - neuronal biophysics and experimental approach

Feature selectivity differs among the neurons in V1. Although the majority of V1 neurons respond to differently oriented stimuli, tuning might change on cell to cell basis within the same population of cells (e.g. Pyramidal neurons) (Cristopher M Niell and Stryker 2008). Understanding of the link between the synaptic input to a cell, which might differ depending on cell function, and spiking output, which constitutes the signature of cell feature selectivity is crucial to understand neuronal processing. To characterize this link, we are asking about both the nature of synaptic input and about the biophysical computations performed by the neuron. The biophysical approach adopted in this project searches for the mechanisms that enable cells equipped with the same cellular machinery to vary their output depending on the input. Furthermore, it will dissect the role of different components important for the process and help to describe biologically relevant information for a given neuron. In the end, this biophysical description frames neuronal processing as mathematical operation/s, which can then be translated into theoretical studies.

Therefore, in the second part of the thesis I am focusing on characterization of two aspects:

1. The visually evoked synaptic input: In this part I am measuring variations in the amplitude and dynamics of synaptic inputs. Observation, of synaptic input changes as a signature of circuit wiring might provide insights into feature selectivity.

2. The input – output transfer function of a neuron: In this part I describe how the synaptic input to a cell shapes the neuronal spiking output. I am searching for a universal description of a neuron as an integration unit. Such description should be true for neurons not only in V1 but also provide general insights into the nature of neuronal computation. Further, I am taking into account the electrophysiological firing type of the cell (FS, RA vs. bursting) eventually for describing how the general I/O function changes depending on the neuronal population under consideration.

Experimental approach:

We validate a closed-loop protocol for single cell probing in vivo in the low anesthesia regime (0,25% isoflurane). The protocol combines traditional whole cell protocols under current and voltage clamp mode with the application of dynamic clamp. Dynamic clamp performed under *in vivo* conditions constitutes the main novelty and heart of the closed loop approach enabling us to mimic synaptic input coming to a cell from the circuit and to provide iterative modification of that input dynamics *in vivo.*

As first steps, we characterize the cellular properties of a neuron and the spiking response of a cell to a given stimulus direction. Next, in voltage clamp mode, we measure visually evoked conductances associated with the same visual stimuli. This initial part of the protocol serves to describe the variability of synaptic inputs occurring in visual cortex and provides the reference synaptic input waveforms for the next part of the closed loop. In the second part, the synaptic input waveform based on visually-evoked conductance measurements is iteratively modified and reintroduced back to the same neuron, while recording spiking output. Comparison of spiking outputs and artificially introduced synaptic waveforms provide the input-output transfer function of a single neuron.

The subsequent modifications of the synaptic input applied during the protocol scales the amplitude of excitatory and inhibitory components and thus, changes the E/I ratio. This step enables the dissection of the different roles of excitation and inhibition in neuronal computation. Additionally, changes in the temporal dynamic of both components, thus changes in the integration time window, enables a description of the relevant resolution for the neuronal code.
Some of the cells were also probed by the application of stereotypical conductance steps. This synaptic input constitutes the simplified temporal dynamics and a constant E/I ratio. As such, this project contributes to the question of the importance of spike timing for the neuronal code and how the balance between excitation and inhibition (E/I balance) determines functional responses.

In summary, we are able to characterize the neuronal input-output transfer function that describes the mathematical operations underlying neuronal processing depending on electrophysiological type of the cell.

Application of such a closed-loop protocol have a few important advantages. First, we are able to perform measurements in vivo under close to physiological conditions taking advantage of intact circuit architecture and the low anesthesia brain state.
Second, we are performing all the recordings on the same cell, taking advantage of extracting function, synaptic input and cellular parameters at the same time. In contrast, to other studies, we are able to interact with the cell using a repertoire of various physiologically relevant scenarios. For example, we could apply synaptic input with an increased excitatory component. In the same manner, we could apply different input characteristics of the input in particular bandwidth. The impact of these manipulations on the cell enables us to infer rules of neuronal processing at biophysiological level.

### 2.3.2 Perspectives based on current background

One of the mysteries of neuroscience is understanding the neuronal code.
Previous attempts towards describing the neuronal code have been restricted by the range of information measured, thus allowing only for eavesdropping of a particular group of cells in a particular situation. In contrast, the Chinese whispers (telephone) game we play with the neuron enables us to observe signal processing within the context of the same cell in a unique place in the

circuit. Providing quantitative insights into brain computation serves both basic physiological studies as well as identification of pathophysiological mechanisms. Additionally, this study provides important constraints that are applicable to theoretical studies and industrial applications, e.g. processor architectures based on neuronal networks.

First, presented in this work characteristic of neuron allows to gain more insight into the neuronal code. More precisely, we were able to describe the functional I/O properties of neurons and eventual differences between different electrophysiological types or recording cortical layers.
Secondly, as this work is embedded in the context of visual circuit, the results deliver insight into the mechanisms of visual processing in primary visual cortex of the mouse. Information about visually evoked conductance, has been reported in a few papers (Haider, Häusser, and Carandini 2013; B.-H. Liu et al. 2011; A. Y. Y. Tan et al. 2011), and to date there is no complete agreement in the reported results. Our analysis of conductance measurements further contributes to the topic about synaptic dynamics in V1 in the context of cell selectivity at the level of its inhibitory and excitatory inputs and its functional spiking output.
Presented project allows for revision of some previous findings and push the understanding of neuronal computation forward.

#### *2.3.2.1. Excitatory/Inhibitory balance in V1*

There is a common agreement in the field about balanced E/I ratio at the level of the whole circuit. However, the reported in various studies ratios differ depending on the definition of balance and conditions of study. Study of (Xue, Atallah, and Scanziani 2014) investigated E-I balance in pyramidal cells of V1. They establish presence of E-I balance ratio at the level of unitary postsynaptic currents in all pyramidal cells, even if the cell to cell amplitude of synaptic excitation and inhibition was varying. Similar finding providing definition of E-I balance might be find in other papers (M. S. Wehr and Zador 2003; Haider et al. 2006; Haider, Häusser, and Carandini 2013). On the other hand, In the (Haider, Häusser, and Carandini 2013; B.-H. Liu et al. 2011) the predominance of inhibition was clearly presented. Predominance of inhibitory conductance over excitatory was also found previously in anaesthetized cat intracellular recordings (M. Rudolph et al. 2007).
In our project, we have measured the evoked conductance in almost awake animal condition. Therefore, we are able to discuss presented findings and provide a detailed description of excitatory-inhibitory balance in mouse primary visual cortex. Further, we are scaling the excitatory and inhibitory components and probe neuron using different E/I ratios. This step, enables us to change the E-I ratio and see the neuronal response for eventual change.

Additionally, by probing neuron with different E-I ratios we regularly probe neurons with inhibitory part lower than this originally recorded. Results from such ratios can be discussed in the context of studies applying optogenetic silencing to a distinguish role of particular population of inhibitory neurons in the circuit (Adesnik et al. 2012; Xue, Atallah, and Scanziani 2014).

#### *2.3.2.2. Temporal dynamics of Excitatory and Inhibitory part*

Temporal relation of excitation and inhibition can provide insights into circuit processing mechanisms. Conductance measurements in cat area 17 reveled close to 180 degrees temporal shift between excitatory and inhibitory components, which was confirming 'push-pull' theories constituting visual processing (A. Y. Y. Tan et al. 2011). In contrast, in mice such relation was not found, and only small temporal shifts was measured (majority cells smaller than 30 degrees) ( A. Y. Y. Tan et al. 2011)(Fig.2, previous section). Additionally, the short delay of inhibition in reference to excitation found in rat primary auditory cortex was found to sharpen temporary precise neuronal response for the sound frequency (M. S. Wehr and Zador 2003).
Results of our project will be discussed in the context of various temporal dynamics recorded in low anesthesia regime. Additionally, the modifications of the temporal dynamics (conductance steps injections) elucidate importance of fluctuations for synaptic components.

#### *2.3.2.3. Influence on the integrative neuron properties*

Several theoretical and experimental studies tried to respond the question about the neuronal code. On one end we have the rate-based code hypothesis, according to which the information is encoded in the averaged spiking rate. It says that neuron act as temporal integrator. On the other end we have spike time-based code according to which the neuron act like coincidence detector. However, nowadays it is postulated that the neuron (pyramidal) operates in between these two modes (Rudolph and Destexhe 2003; Ratté et al. 2013). Conductance change during visually- evoked response varies strongly in time and amplitude fulfilling description of high conductance state (Destexhe, Rudolph, and Paré 2003). One of the biggest consequences of conductance change is the change of the neuronal time constant and resulting from it temporal window for input integration. Therefore, this change influences the operating mode of the neuron. On the other hand, it is also postulated that the input characteristic – it's synchrony influences neuronal processing (Ratté et al. 2013).

In this study, we are measuring visually - evoked conductance and therefore will provide description of the synaptic input dynamics to the cell. We will investigate the amplitude of excitatory and inhibitory part and their 'sharpness' changing in time providing description of the input synchrony coming from the circuit (averaged over repetitions). Further, the probing applied in this study delivers experimental evidence about neuron output in various E/I balance conditions as well as with various fluctuating inputs. Thus, we are delivering direct experimental evidence of neuronal computation, which in turn provides further understanding of the relation between synaptic input influence on the neuron processing.

#### *2.3.2.4. I/O transfer function*

Conductances shapes the spiking output of a neuron. However, there is no common agreement about how this phenomenon occurs. More precisely, how excitatory and inhibitory parts influence the output. Some of the experimental studies point to the presence of synaptic noise as to the modulator of neuronal gain (Destexhe, Rudolph, and Paré 2003). Other studies point out possible mechanisms influencing neuronal gain like the activation of particular channels was experimentally shown (Vervaeke et al. 2006; Graham and Schramm 2018).

Here, we are asking about the role of shunting inhibition and excitation in shaping of the neuronal output. According to our knowledge our probing protocol investigating influence of various E/I ratios and fluctuation levels constitute a first experimental demonstration of this kind *in vivo*. We will show how I/O transfer function is changing upon inputs as simple as conductance steps or physiological, visually evoked synaptic input and its smoothed version. This description will provide a rich base of qualitative and quantitative parameters.

#### *2.3.2.5. Common ground of both projects*

The ultimate goal of all kinds of functional connectivity projects (referring to the physical connections, their synaptic strength, spatial arrangement or systematic description of the local architecture) is to understand link between the function of a cell and circuit architecture. The understanding of the process ultimately should deliver a description of precise neuronal computation process. Systems neuroscience endeavors to describe local and global architecture in order to predict the synaptic input and link it with various architecture arrangements.

In a project where cells' connectivity would be mapped while knowing the cell function, the goal would be to infer how much each projection could contribute to the cell functional response. For that, a characterization of connections and the statistics on their number and strength is needed (Figure 3, left). Reversing this question to a single cell perspective means that the connections characteristics can be approximated by conductance measurements (Figure 3, right) which is done in the I/O transfer function project of this thesis.

Focusing on how the cell processes inputs from the circuit, delivers understanding on the biophysical operations performed by the cell, independently from the architecture of the circuit. It is characterizing the whole synaptic input to the cell. The functional connectivity project on the other hand, describes how the subparts of synaptic input contributes for cell response and from where physically they come from. In this context, the transfer function project complements the mapping project described in previous sections. Ultimately both projects results should be in agreement.

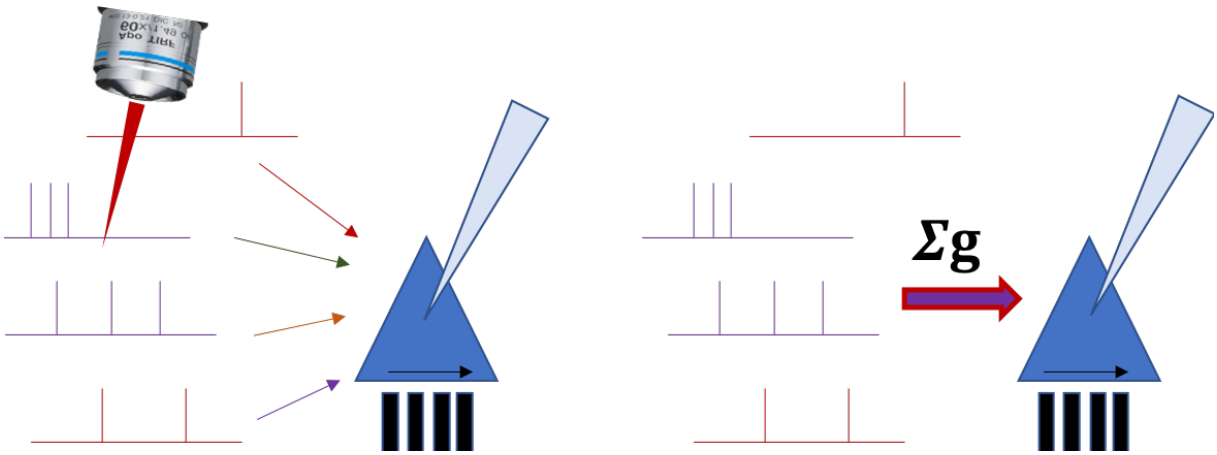


*Figure 3 conceptual project comparison. Left – functional connectivity project. Right – I/O transfer function project. Functional connectivity is inferred by sequential holographic stimulation of opsin expressing presynaptic candidate and assessment of the post synaptic candidate current/voltage changes. The function of a cell is characterized based on calcium imaging step. On the other hand, the transfer function project does not recognize single cell inputs but the sum of the whole visually evoked synaptic input to a cell (split to a inhibitory and excitatory component). The cell function is inferred by assessment of spiking evoked in response to various direction/orientation of drifting grating.*

# 3. An all-optical approach towards circuit interrogation

## 3.1. Experimental Challenges: optical and molecular tools

The achievements of an all-optical optogenetic control and monitoring of cell activity is a main challenge in the field of optogenetics. To tackle this problem one requires a proper combination of optical and molecular tools.

More specifically, concerning the photoactivation of neurons, one would like first, to be capable to induce activity on specifically selected neurons, with **single cell resolution.**
Additionally, the timing of the photoinduced should be controlled will **millisecond temporal resolution**.

Here in this work we will use an optical technique, better described in the next section - Computer Generated Holography, that will allow to shape light over specific cell body of interests. This approach, developed and widely characterized by the Emiliani's laboratory, when applied under 2-photon excitation, allows to photoinduce activity of arbitrary sub-ensemble of neurons deep in tissue with high spatial and temporal resolution (more details in the following section 3.1.1) (review from Oron et al. 2012).

The right biological preparation, which requires the combination of a calcium sensor and an opsin that provides the desired precision, is under development and my first part of the thesis was devoted to this optimization. During the project duration I have contributed to test various opsin candidates for the desired performances. Additionally, my work contributed to draw the clear limitations of the constructs available at that time and to understand better the importance of the fundamental biophysical properties of light-gated channels to achieve a reliable all-optical method for circuits mapping.

In the next sections I will introduce the reader with technical part of the protocol used for opsins validation as well as with basic informations about light-gated channels and calcium sensors. I will finish this part with the description of the desired biological preparation, and I will present the results of the subprojects I was working on. I finish this chapter with a short discussion of these results and perspectives for an all-optical circuits manipulation.

### 3.1.1. Optical tools for optical-channels activation

Together with the development of genetic tools, optical technologies are improving. In fact, the choice of the activation method is as important as the choice of the optogenetic tool, and there is a strong co-dependence between the two, as some activation methods will show better performance in combination with different opsins. Today, a broad range of optical designs is available to

researchers. 1-photon microscopy allows efficient and relatively easy activation of optical channels in cell populations (Boyden et al. 2005; Judkewitz et al. 2009; S. Lee et al. 2012; Tye et al. 2011). Together with the development of genetic tools, optical technologies are improving. In fact, the choice of the activation method is as important as the choice of the optogenetic tool, and there is a strong co-dependence between the two, as some activation methods will show better performance in combination with different opsins. Today, a broad range of optical designs is available to researchers. 1-photon microscopy allows efficient and relatively easy activation of optical channels in cell populations (Guo, Hart, and Ramanathan 2009; Szabo et al. 2014). However, there is still a wide range of applications in which single cell resolution deep in tissue is required.

2- photon illumination-based techniques provide much better penetration and spatial resolution allowing the illumination to remain localized on the volume of the target -the opsin expressing cell (Packer et al. 2012; Eirini Papagiakoumou et al. 2010). However, the low 2-photon cross section of opsin and the small single channel conductance, made difficult to achieve the reliable triggering of action potential in neurons with a single static 2-photon diffraction-limited spot. To address this problem, enlarging the excited surface in order to target as many light-gated channels as possible in opsin expressing cells, has been an important goal for the development of 2-photon techniques for optogenetics.

We can distinguish two main groups of methods aimed at improving the light delivery to the tissue: scanning and parallel approaches. Scanning approaches are based on quick movement of a tiny diffraction limited laser spot across several points in the sample. To induce sufficient current to bring the cell to action potential threshold, the excitation spot must “visit” several places across the cell membrane, stopping at each long enough to open the channels. To improve scanning approaches, the scanned diffraction-limited spot can be slightly enlarged by underfilling the back aperture of the objective, to be able to activate bigger population of channels per scanned location. Together, these factors have allowed for successful photostimulation of ChR2-expressing single neurons under 2-photon illumination (Rickgauer and Tank 2009) while, more recently, simultaneous scanning of multiple points allowed multicell in vivo excitation expressing the slow opsin C1V1 (Packer et al. 2015)(Yang 2016). Nevertheless, this intrinsically sequential approach, exciting point and by point and not simultaneously each location, can affect efficiency in current integration or can impose some limitation in the achievable temporal performances (Ronzitti et al. 2017). This is true particularly with fast opsin (with short off kinetics).

On the contrary, parallel approaches are based on exciting the entire targeted area at once, typically the whole cell body. This can be achieved by using optical approaches based on the modulation of the phase of the laser beam, which allows the creation of an arbitrary shape of illumination. Two techniques has been developed and applied in Emiliani’s lab for this purpose: Computer Generated holography (CGH (Lutz et al. 2008)) or generalized phase contrast (GPC) (Eirini Papagiakoumou et al. 2010) (Figure 4). Computer generated holography is based on the calculation of a phase hologram that, once projected at the rear aperture of the objective, using liquid crystal spatial light modulator

(LC-SLM), it reshapes the laser beam in arbitrarily defined patterns. Generalized phase contrast instead, is a technique based on interferences between two differently dephased parts of the laser beam, that can reproduce arbitrary intensity pattern on the sample plane.

These two approaches, although presenting some differences, they can both reproduce pattern of illumination tailored over specific region of interest with micrometric lateral precision. Additionally, when applied under 2-photon excitation and coupled with an approach named temporal focusing (Oron, Tal, and Silberberg 2005), illumination can be well confined also on the axial direction, resulting in an excitation volume that can match the size of a typical neuronal cell body.

Both the GPC and CGH techniques have been used successfully in optogenetics over past years (Bègue et al., 2013; Hernandez et al., 2016; Papagiakoumou et al., 2010; Szabo et al., 2014). The simultaneous illumination of all the light-gated channels over the cell surface allows to maximize current integration, exploiting at the maximum the characteristic of each opsin optimizing the temporal performances in the photoactivation. As a consequence, these techniques can work very efficiently with both slow and fast kinetics opsins. Indeed, the performance of parallel approach was shown in combination with ChR2 (Papagiakoumou et al., 2010), C1V1 (Bègue et al., 2013), ReaChR (Chaigneau et al. 2016), Chronos (Ronzitti et al. 2016) and CoChR (Shemesh et al. 2017).As will better discussed in the Results section, in all these preparations single cell photoactivation was achieved, and high temporal precision was obtained, characterized by a short AP latency (<10 ms) and jitter (<1 ms) , and spiking frequencies up to 100 Hz was achieved for fast Chronos opsin (Ronzitti et al. 2016).

However, the limitation of parallel approach could be the total laser power needed for targeting all of a desired group of cells, that could be either not achievable or could induce thermic damage (Picot et al. 2018). The use of amplified pulse lasers can overcome this limitation and significantly reduce the required laser power.

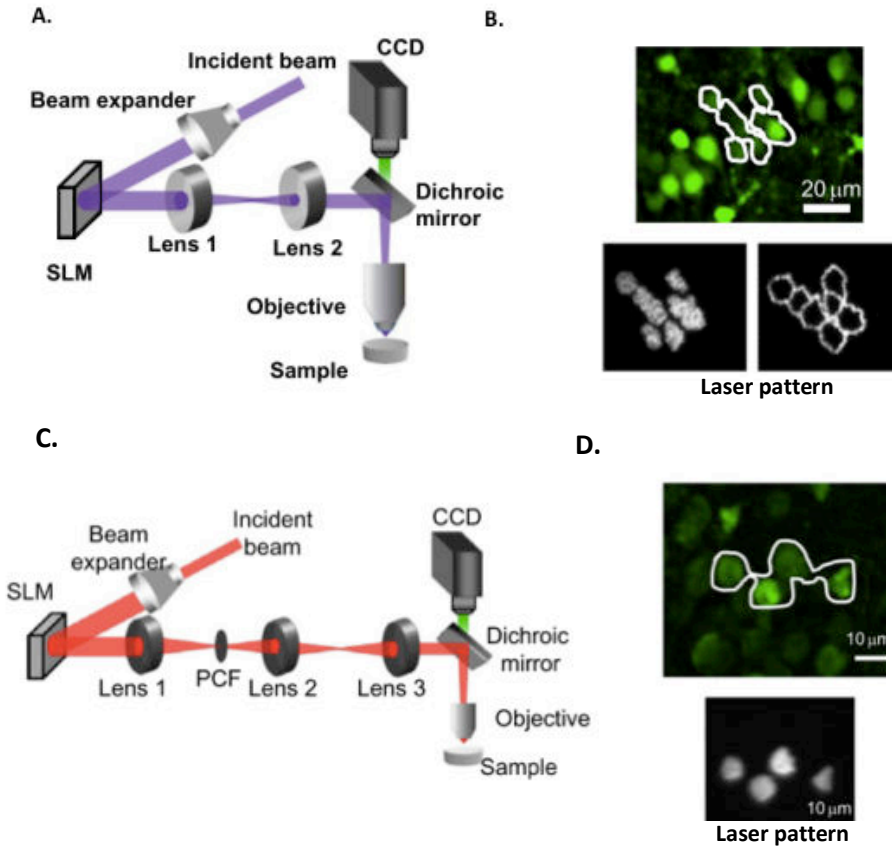


*Figure 4 Parallel optical techniques for two-photon optogenetics. A: Schema of an optical holographic set up, and (B) few example of excitation pattern of a group of cells and its contour C: Schema of an optical GPC set up and (D) example of excitation shape, drawn based on a fluorescent image of the cells. (Modified after (Oron et al 2012)).*

## 3.1.2. Light activated channels (opsins)

### *3.1.2.1. Historical background*

The origin of the idea of introducing Channelrhodopsin (ChR) – an algal protein enabling phototaxy – into neuronal cells appears for the first time in two papers – first by Boyden and Deisseroth, who expressed ChR2 in hippocampal neuronal culture (Boyden et al. 2005) and second by Zhuo-Hua Pan and colleagues who expressed it in retina (Bi et al. 2006). An interesting anecdote is that both papers were first rejected by high-profiles journals, and their findings were treated with skepticism and no appreciation of the potential for the new technique.

Although the symbolic beginning of optogenetics in neuroscience is typically considered to be in 2005, at that moment there were already a few groups working on techniques which would enable the stimulation of neuronal tissue by light. Inspirations were taken from photoreceptors, whose signal pathways were known. This approach enabled the expression in neuronal tissue constructs,

allowing light modulation of activity, but the preparations were hard to control and use. In 2002, Drosophila genes encoding photoreceptor composed of arrestin-2, rhodopsin and a α-subunit of G protein (so called "chARGe") were expressed in neurons, but this solution had the disadvantage that all three components needed to be present in a cell to make it photosensitive (Zemelman et al. 2002). One year later the same group proposed a different system – a combination of a ligand-gated ion channel and its agonist in caged form which could be released by light, causing a neuronal depolarization. This solution was easier to control temporally in comparison to the previous one, and required expression of only one ion channel in the membrane (Zemelman et al. 2003). Another team presented a slightly different approach. Instead of trying to express receptors that already existed in various organisms, the group of Kramer and Trauner applied an engineering approach. They developed a new chemical gate (named SPARK) that conferred light sensitivity to an ion channel. The drawback of this method was the requirement of using two different wavelengths to switch the channel on and off (Banghart et al. 2004). Then, in 2005 Nagel and Bamberg introduced Channelrhodopsin-2 (a wild type ChR2), a "perfect" light sensor that they expressed in Xenopus oocytes and HEK cells and that addressed the previous disadvantages (Nagel et al. 2005). From there, only one more step was needed to construct a genetic sequence to express ChR2 in cultured hippocampal neurons. This construct was able to stably express with no supplementation requirements, giving depolarization upon 1-photon stimulation that elicited action potentials with millisecond temporal precision, the best performance at that time (E S Boyden et al., 2005). Among all the previously proposed solutions, ChR2 was the easiest and most precise tool. The application of the new tool spread quickly, with the first in vivo application, in C. elegans, published just three months later, showing behavioral change of an animal under 1-photon illumination, and by this result showing clearly the power of optogenetics (Nagel et al., 2005). Since then, optogenetics has been applied to study different brain regions and other neuronal tissues in a variety of species, as well as other than neuronal tissues (Deisseroth 2015; Han 2012; Szabo et al. 2014; Tye et al. 2011).

In 2007 the second important for optogenetic field step has occurred. It became possible to inhibit (hyperpolarize) cells by the use of a light-driven chloride pump named Halo or NpHr (Han and Boyden 2007; Zhang et al. 2007). Both names come from the name of archaebacterium – *Natronomas pharaonis* – in which this pump naturally occurs.

Several new opsins have been discovered or engineered during the last years, with a variety of biophysical properties, activation wavelength and fluorescent reporter color. This diversity allows for different combinations of opsins in order to address specific scientific needs of stimulating neuronal tissue (Gunaydin et al. 2010; Klapoetke 2014; Kleinlogel et al. 2011; Mattis et al. 2012).

### *3.1.2.2. Opsin characteristic based on ChR2*

Channelrhodopsin-2 (ChR2) was the first light-activated channel used to depolarize neurons by light (E S Boyden et al., 2005). It is the best described opsin and is frequently used as a reference protein in the field. ChR2 is a naturally occurring protein in the green alga *Chlamydomonas reinhardtii* whereby it mediates phototaxis. ChR2 is composed of 7 trans-membrane helices, which create a pore for ion flow. Blue light illumination causes photoisomerization of the chromophore retinal attached to the 7th trans-membrane helix, which leads to a conformational change of the channel (Kato et al. 2012; Han 2012)( Figure 5). ChR2 is permeable mainly to monovalent cations and calcium ions. Although ChR2 has a low selectivity, it is not unspecific, because it doesn't conduct anions (Nagel et al. 2006). The magnitude and direction of photocurrents change with the membrane potential according to the changes in the ion concentration gradient, thus a passive (ohmic) ion movement (Nagel et al. 2006)., with a single channel conductance around 40 fS (Feldbauer et al. 2009). In neuronal tissue, ChR2 expresses well enough to depolarize neurons above the action potential threshold and elicit reliable spiking up to 30 Hz in hippocampal culture neurons under 1-photon illumination (Boyden et al. 2005).

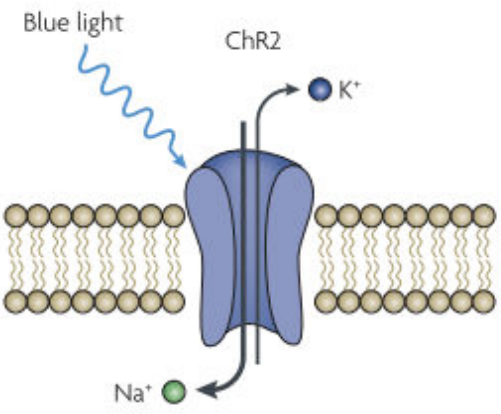


*Figure 5 Cartoon of single ChR2 channel (Zhang et al). Channel opens under blue light illumination enabling passive ionic flow.*

The ChR2 channel opens rapidly upon blue light illumination (~460nm), responding with a fast, inward current (Figure 6). Upon sustained illumination, the photocurrent decays to a steady- state current (desensitization phase), with the current returning to baseline after switching the light off. These phases have characteristic durations for a given opsin, thus $\tau_{on}$, $\tau_{desensitization}$ (inactivation) and $\tau_{off}$ respectively. For ChR2, this kinetics are: $\tau_{on}$ ~10 ms, $\tau_{desensitization}$ ~25ms and $\tau_{off}$ ~12 ms (Mattis et al. 2011).

A four-state model was proposed to describe the biophysical properties of ChR2, including two closed states: dark and light adapted (DA and LA respectively), together with two open states: O1 and O2. The first open state, O1, corresponds to the fast, outward current just after photostimulation. The second open state, O2, dominates after application of an extended light pulse. Thus, the steady- state current represents the balance between the O1 and O2 states, being smaller than the fast peak current at stimuli onset because of a lower sodium permeability of the O2 state (Berndt et al. 2010; Hegemann and Möglich 2011). Although the four-state model is broadly accepted in the field, simpler 2- and 3- state models have also been proposed to describe the kinetics of ChR2 and other opsins.

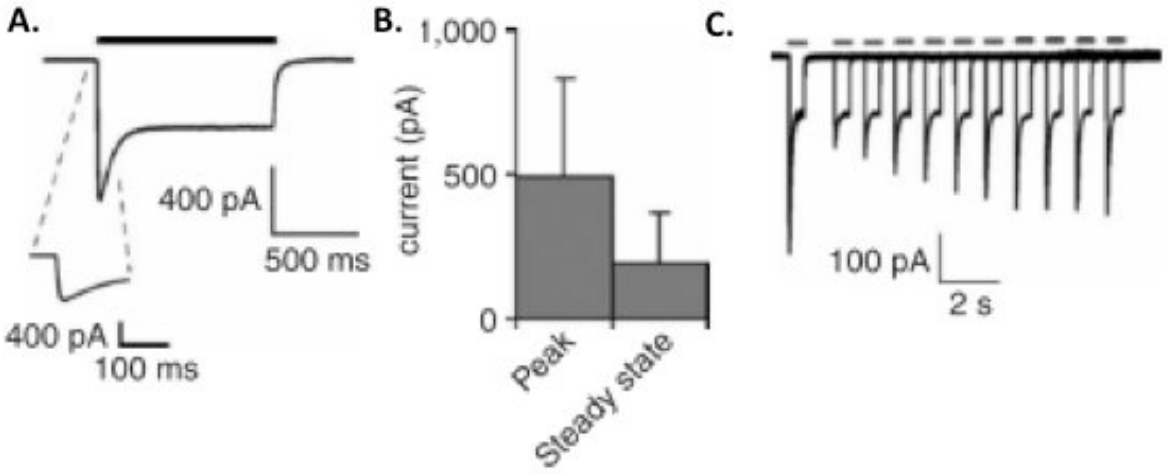


*Figure 6 Photocurrent obtained by photostimulation of ChR2-expressing neurons in hippocampal neuronal culture. (A) Inward current in response for 1 second photostimulation, showing this opsin's characteristic kinetics. Inset – expanded initial phase of current transient. (B) Average and SD of current amplitude comparing peak transient and steady state phases. (C) Ten overlaid current traces recorded from a hippocampal neuron illuminated with pairs of 0.5-second light pulses (indicated by grey bars), separated by intervals varying from 1 to 10 seconds, illustrating the recovery time from desensitized state. (E S Boyden et al., 2005)*

ChR2 has been thoroughly studied and as such has become a reference opsin, with which new opsins are frequently compared (Gunaydin et al. 2010; Kleinlogel et al. 2011; Mattis et al. 2011). The engineering of new opsins was a natural next step to broaden the possibilities of optogenetic studies. For example, although ChR2 is able to reliably elicit spiking in neurons, when stimulated with repetitive light pulses it fails to elicit spikes at relatively high frequencies, because of slow off kinetics that gives a prolonged depolarization, and sometimes extra spikes in response to a given pulse. This limitation motivated efforts to modify the channel in order to obtain different biophysical properties, for example ChETA, a red shifted variant of ChR2 (Gunaydin et al. 2010). The kinetics of ChETA is two times faster than ChR2, allowing for reliable spiking of photostimulated cells up to 200 Hz using 2-ms pulses.

Another interesting ChR2 mutant is the calcium-translocation channel rhodopsin CatCh, which exploits the activation of native membrane channels to obtain faster kinetics of the voltage response (Kleinlogel et al. 2011). By increasing the permeability of calcium ions, the inner membrane surface potential was depolarized, allowing for activation of sodium voltage-gated sodium channels. This indirect pathway increased the obtained photocurrent. Furthermore, the repolarization phase of the photocurrent induced depolarization was accelerated by calcium-activated potassium BK channels.

New opsins are continuously under development, including candidates with different vectors and promoters for expressing the construct, different expression times, and different photosensitivities giving the ability to fit the opsin to a specific area or scientific question. On the other numerous characteristic parameters were described and the need to range and compare various constructs

appeared. To address this challenge recent papers have compared several opsins derived from various organisms and their modifications, under both 1-photon (Mattis et al. 2012) and 2- photon (Papagiakoumou et al., 2010) illumination and in vivo (I.-W. Chen et al. 2018).

### 3.1.3. The "Holy Grail" opsin – characteristic

Opsins make neurons light sensitive. Behind this one simple statement, there is a lot of hidden details and tedious work necessary in order to obtain a working biological preparation with the help of which neurons will indeed be sensitive to a light stimulation in the desired manner. The second part of this statement – the desired opsin performance – is the reason why new opsins keep emerging. The first characterized and used opsin, ChR2, is not universal enough to respond to all the scientific questions we would like to answer. As the literature portrays, the usage of the 'right' opsin can open new possibilities for a researcher, giving access to new areas of investigation (Inagaki et al., 2014; Lee et al., 2012; Schild&Glauser, 2015).

What defines the right opsin is not an easy question to answer, and mainly depends on the scientific goal of the project. In some cases, the answer is additionally limited by technological development or the available equipment. This question needs also to be answered in the context of our project. Below I will review the most important features of opsins and their importance for the functional connectivity all - optical study. Thus, I will describe how the Holy Grail opsin for the project should look like, taking into account the scientific goals of the project. I will also describe particular experiments based on which the opsin feature would be assessed.

Temporal resolution

The mapping project aim to mimic the physiological neuronal communication by the use of opsin photostimulation. This is the main reason why the desired opsin should have fast kinetics. Short times of opening and closing of the channel, as well as the ability to quickly move from one state to another, is essential for obtaining good temporal resolution. To check the kinetics parameters, each investigated opsin is expressed in cells (in slices and/or CHO cells). Single, patch clamped cells are photo-stimulated with increasing laser power and time to find tau on, tau off, tau desensitization parameters and laser saturation power (power at which the photocurrent evoked is saturated). All of these features – opening time, closing time and desensitization time, are usually correlated with each other among all known opsins (Mattis, Tye, Ferenczi, Ramakrishnan, O'Shea, Prakash, Gunaydin, Hyun, Fenno, Gradinaru, Yizhar, et al., 2011; Prakash et al., 2012b). Therefore, some opsins are described as fast (e.g. Chronos), some as slow (e.g. ReaChR, C1V1) and it refers to described biophysical parameters of channel behavior.

Ideally, we would like to reach a spike rate, which would mimic the evoked activity to a visual stimulus. This activity will be different between layers and among cell types. In L2/3 of V1 of a mouse,

overall reported spike rates are in the range of 0-20 Hz for an excitatory cell and 0- 40 Hz for interneurons (C. M. Niell& Stryker, 2008). Thus, the first feature of an ideal opsin would be ability to reliably elicit spikes up to 20 – 40 Hz (with known or predictable spike times). Additionally, opsin expressing cell performance should not be strongly influenced by sustained or repeated photo-stimulations. The recovery time of the population of channels in the membrane will also influence the opsin performance. Evoked spiking of the neuron is checked by applying various and repeated photo-stimulation protocols during whole cell patch of the opsin expressing cell. From this step we can learn if the opsin evokes enough photocurrent to reach the spike threshold, what is the amplitude of evoked photocurrents, what is the probability of spike initiation, what frequency of spiking is possible to achieve and how precise the spiking would be in time (measuring of spiking jitter and latency).

Opsin efficacy

"Effectiveness" of the optical preparation is another commonly used term to describe the performance of various channels. This term encompasses a combination of features, including single channel conductance (which is low for optical-channels, ~40fS), opsin light sensitivity and expression level. This last factor is also related with the targeting of the opsin protein to the membrane. It is common to exclude some constructs of the opsin during engineering or the characterization phase of a new opsin because of poor membrane trafficking (Inagaki et al., 2014). It is an important feature, because end users of a given channel, cannot influence targeting to the membrane by modifying expressing protocols. On the other hand, functional expression level, defined as the number of channels per membrane area, can be slightly modified, for instance by changing the volume or the concentration of the injected virus that contains the opsin sequence or the expression time. We can also influence the expression level by using strong promoters Cre – dependent conditional expression, to target a specific cell subpopulation (Packer, Roska, &Häusser, 2013). Overall, effectiveness of opsin and performance stability would be assessed based on comparing all the results from opsin excitation. We would look for how big are the differences in between particular cells and in between animals. The smaller the differences the more reliable the opsin, ensuring that upon a designed light stimulation parameters the opsin will induce a particular number of action potentials with known, possible low jitter and latency.

Light sensitivity

A general term light sensitivity includes a combination of effectiveness of optical preparation and laser source interaction with the brain tissue. First, lasers have a limited power, which needs to be evenly distributed among the targeted cells (in case of stimulating several cells at a time). Second, laser illumination produces heat when it is absorbed by the tissue. Therefore, an excessively high power could perturb cell homeostasis, leading to changes in responsiveness or even to death. This is why the ideal opsin should be highly light sensitive (operating at low laser powers). Although

nowadays the available lasers allow to minimize those obstacles, these factors should be taken into account during design of the set up and experimental protocol.
Assessment of the exact number of cells which we need to target in the mapping project is not straightforward. It is possible to image hundreds of cells in single plane nowadays (Ch'ng& Reid, 2010; Ohki et al., 2005), but photo-stimulating such a large group of cells simultaneously might not be physiological or easy to interpret. A recent study on mouse V1 investigating functional ensembles (defined as group of cells that are co-active during functional responses) point out that the average number of cells in a single imaging plane coactivated, is about 20 neurons in a 250x250 µm FOV) (Carrillo-Reid et al., 2016). In this context it is important to use an opsin, which is sufficiently light sensitive to work reliably in the range of low laser powers (e.g. below 1 mW/µm$^2$ per cell or lower). This would enable us to target several cells in the investigated area. Tissue heating induced by near-infrared laser during multiphoton microscopy is a serious obstacle for technology development. It was estimated that the use of 100 mW of power at the depth of 250 µm to illuminate 1 mm$^2$ leads to an increase in the tissue temperature on average 1.86 ± 0.25 °C for 950 nm wavelength (Podgorski& Ranganathan, 2016), whereas even a 1°C rise in temperature can influence neuronal firing rates in vivo (Stujenske, Spellman, & Gordon, 2015). A smaller scan area will result in larger temperature changes at a given power. It is also important to take into account not only the single peak of power, but also the total exposure time for various illuminations, as there is no single threshold of power tolerable for the tissue (Podgorski& Ranganathan, 2016). The light sensitivity is usually assessed experimentally by providing the laser threshold power that elicits a single action potential in repeatable way. This information tell researcher how much laser power will be needed to elicit spiking and assess how much cells could be target at a single time.

Single cell precision

Ideally, the opsin expression should be restricted to the soma or its proximity. This would improve the chances of recording an unbiased signal from connected pairs during circuit connection mapping. The opsin in the post-synaptic cell processes in the proximity of the pre-synaptic cell could be activated during photo-stimulation of the latter. In real experiments this kind of artefact hinders the interpretation, especially if we take into account large number of connections between the cells. Single cell confinement would be tested by photo stimulating over the neuron body and its sub-compartments to assess evoked photocurrent and change in membrane potential. This step is especially important for appearing constructs which expression is restricted to the soma (and proximal parts of processes).

All-optical approach

Up to now the various opsin features mentioned, aim to mimic neuronal activity. Here, I focus on describing features of opsin enabling pairing with calcium indicator. In the mapping project, we aim to combine the opsin with a calcium sensor in one functional preparation. In this context it is desirable to have reporters of two different colors for both optical tools. Since the majority of well-

established in the field calcium indicators are tagged with GFP (see also below in the Calcium indicators section), it would be convenient to have an opsin with a red fluorescent protein attached. This would allow a clear distinction between cells, which express both opsin and calcium sensor, or only one of them. Preferably, the opsin sequence should also use a p2A linker (or other cleavage sequence) in between opsin gene and reporter. The advantage of p2A sequence is that it generates a proportional expression of both genes (Kim et al., 2011), which would then allow estimation of the opsin expression in the cell based on reporter brightness. Moreover, a p2A linker causes a separation of the adjacent parts of the sequence during transcription and translation. This results in the opsin targeting to the cell membrane, with the reporter staying in the cytosol, enabling easier identification of expressing neurons (Figure 7).

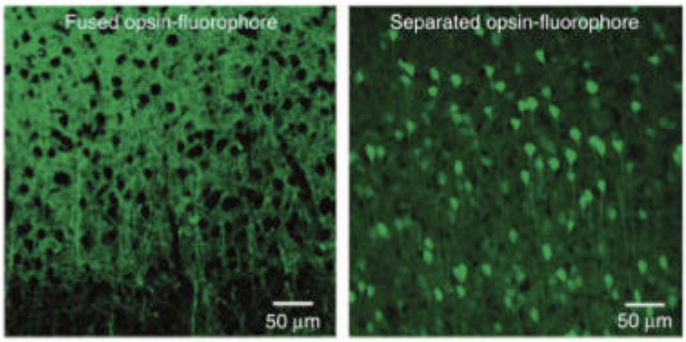


*Figure 7 . Difference between 2P image of a tissue expressing an opsin fused with a fluorophore sequence (right) and an opsin linked with fluorophore by p2A sequence (left). (Prakash et al., 2012a).*

Additionally, the desired opsin would have an excitation spectrum, which doesn't overlap with the calcium sensor spectrum. An opsin excitation spectrum is describing evoked photocurrent as a relation of stimulation wavelength. Usually, finding the spectrum is an initial step of characterizing an opsin expressed in CHO cell culture.

Analysis of 2-photon spectra (Figure 8) reveals the spectral overlap of some opsins with calcium sensors. A practical consequence of the substantial cross-talk is opsin channel activation during calcium imaging step. Thus, the desired opsin should be characterized by an excitation spectrum peak shifted towards red and/or characterized by narrower absorption spectrum, than usual opsins.

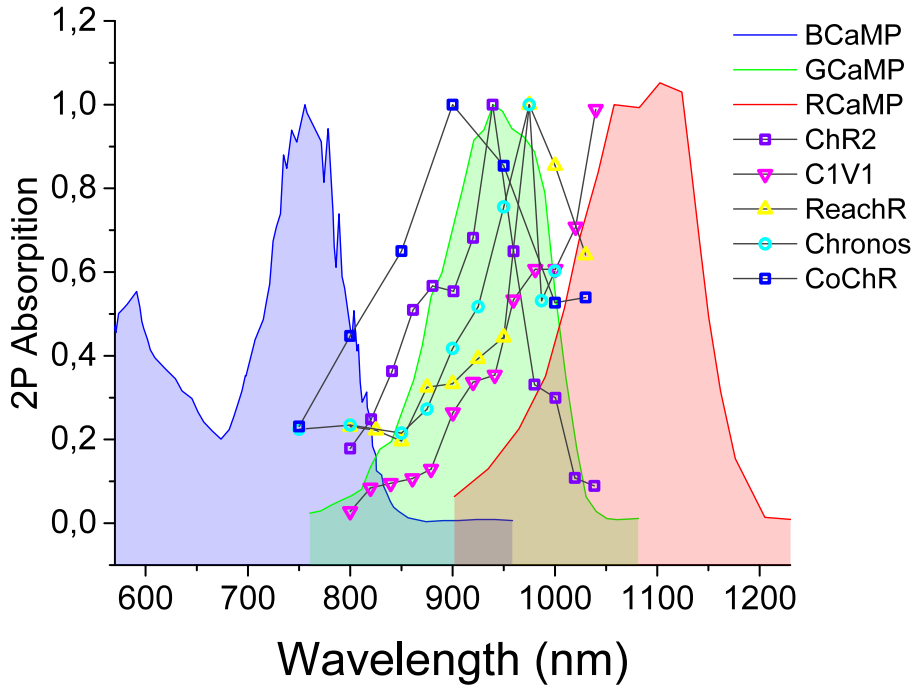


*Figure 8 Spectral overlap between opsins and three genetically encoded calcium indicators. The 2P opsin spectra were measured in Emiliani lab. The green spectrum indicates GCaMP protein family spectrum. Substantial overlap od all the opsins pose a challenge towards combination of calcium imaging and optogenetics.*

In summary, the ideal opsin would be characterized by fast kinetics and high light sensitivity. As reported these two features are usually inversely correlated (Mattis, Tye, Ferenczi, Ramakrishnan, O'Shea, Prakash, Gunaydin, Hyun, Fenno, Gradinaru, Yizhar, et al., 2011). Additionally, the ideal opsin would be reported in the tissue by a red fluorophore, to distinguish it from the calcium indicator, or alternatively would be expressed together with genetically encoded calcium indicator, which makes it sure that the two proteins are expressed in the same cell. The 2-photon excitation spectrum of the opsin should be also separated from that of the calcium indicator. There would be a great advantage to use a construct whose expression is restricted to a soma part of the cell only.
However, the ideal opsin didn't exist at the starting point of the project, thus forcing us to seek a balance between all the desired features.

Very recently, the opsin which seem to fulfill some of the drafted requirements has appeared – ChroME (Mardinly 2018). It is a soma-targeted red variant of Chronos opsin, characterized by fast kinetics. Under 2-photon holography it is possible to obtain currents up to 2 nA and reliably induce various spiking patterns in a population of cells with single cell precision. The next years will show if that construct will be the "Holy Grail" of optogenetics.

## 3.1.4. Calcium indicators

In recent years, calcium imaging has provided vital insight into brain physiology and circuit connectivity. Calcium imaging has been used to record the population activity of particular circuits and of circuit subpopulations, during spontaneous or evoked activity (Andermann et al. 2013; Ch'ng and Reid 2010; Kwan and Dan 2012; Bathellier, Ushakova, and Rumpel 2012), as well as for single cell recordings. The most commonly used indicators for such studies are from the OGB and GCaMP families especially GCaMP6, since it is characterized by much higher signal- to-noise ratio and faster kinetics (T.-W. Chen et al. 2013). Table 1 shows an overview of calcium imaging studies performed on L2/3 of rodents V1 (with one exception from barrel cortex), comparing technical aspects, which are relevant for choosing an indicator for the current project.

### *3.1.4.1. Mechanisms of work*

Calcium indicators provide an indirect measurement of the neuronal activity. Typical resting calcium concentration in neurons is 50-100 nM, rapidly rising to levels 10 – 100 times higher during electrical activity, primarily due to the opening of voltage- dependent calcium channels and release from intracellular stores. Together with the increase of calcium the emitted by indicator fluorescence increases. For this reason, calcium imaging is a reliable method to measure a neuron's spiking activity.

OGB-1 AM is a chemical indicator based on the calcium chelator BAPTA, a calcium- specific aminopolycarboxylic acid. BAPTA is highly selective for Ca2+ ions (Kd ~100nM at pH 7.0) and is characterized by fast on-off rates for metal ions binding (Tsien 1980). For population imaging purposes OGB calcium sensor is introduced to the tissue by glass electrode filled with the dye. Application of positive pressure allows to deliver the dye in the extracellular space. The molecule of dye is binned with acetoxymethyl (AM) ester – a hydrophobic, charged molecule which passively diffuse across membranes and release calcium indicator after the cleavage of AM ester by intracellular esterase (which is present in the cell).

GCaMP6 protein family is based on single EGFP protein, which changes the level of fluorescence due to change of conformation after calcium binding to the molecule. As it is a protein, it can be genetically expressed in the tissue. This gives possibility to benefit from wide range of genetic tools used for protein expression to drive selective presence of the indicator in some type of cells only.

### *3.1.4.2. OGB vs GCaMP6 comparison*

Both indicators have advantages and disadvantages, which need to be considered in the context of a specific scientific question. GCaMP6s has fast kinetics (rise time peak – 0.2 s / 1AP (half decay time 0.6 s) and gives a wider range of fluorescence changes, thus providing a good signal-to-noise ratio. The GCaMP6 fluorescence change is much larger compared to other indicators. This is an undeniable advantage of the GCaMP6 protein family, which were designed and mutated in order to increase

brightness while binding calcium, as well as to enhance its sensitivity (T.-W. Chen et al. 2013), giving the possibility of recording the change in fluorescence level in response to single action potential. The fluorescence grows almost linearly with the number of spikes (Figure 9) resulting in high fluorescence levels (dF/F of 500-600%) for responses to preferred stimuli (Dana et al. 2014; T.-W. Chen et al. 2013). On the other hand, the percentage of cells responsive to the optimal visual stimulation is lower for GCaMP6s than for OGB-1 AM (look Table 1 at the end of the section). This difference could be explained by sparser expression of GCaMP, which is even more evident for transgenic lines. Additionally, OGB-1AM has a much smaller range of fluorescence changes (5 – 60% for optimal visual stimuli) in comparison to GCaMP6s, with a fluorescence change to a single spike of ~20%. In the context of Visual Cortex activity, these different characteristics make the direct comparison between OGB and GCaMP6s difficult, especially if the criterion for classifying a cell as responsive is set to 6% of fluorescence change threshold (T.-W. Chen et al. 2013). This criterium could lead to an underestimation of the OGB – 1AM responding population, in particular excluding broadly tuned inhibitory cells.

On the other hand, a possible weak point of GCaMP6 is sparseness of expression and a low basal level of fluorescence, especially for some transgenic lines. In particular, lower expression levels means, that higher laser powers must be used for recording responses (which will also activate opsin expressed in the cells). It has been reported that expression in transgenic lines is biased in favor of the pyramidal cell population, although indeed this line was constructed under Thy-1 promoter, which drives expression mostly in projecting neurons (Dana et al. 2014). In contrast, OGB-1 AM penetrates all cell types equally, with no bias within the loading area including glial cells (Stosiek et al. 2003). Slower kinetics than the GCaMP protein family (half decay time ~1,5s) (Akerboom et al. 2012) might be the weak point of OGB, as well as a much narrower range of fluorescence change.

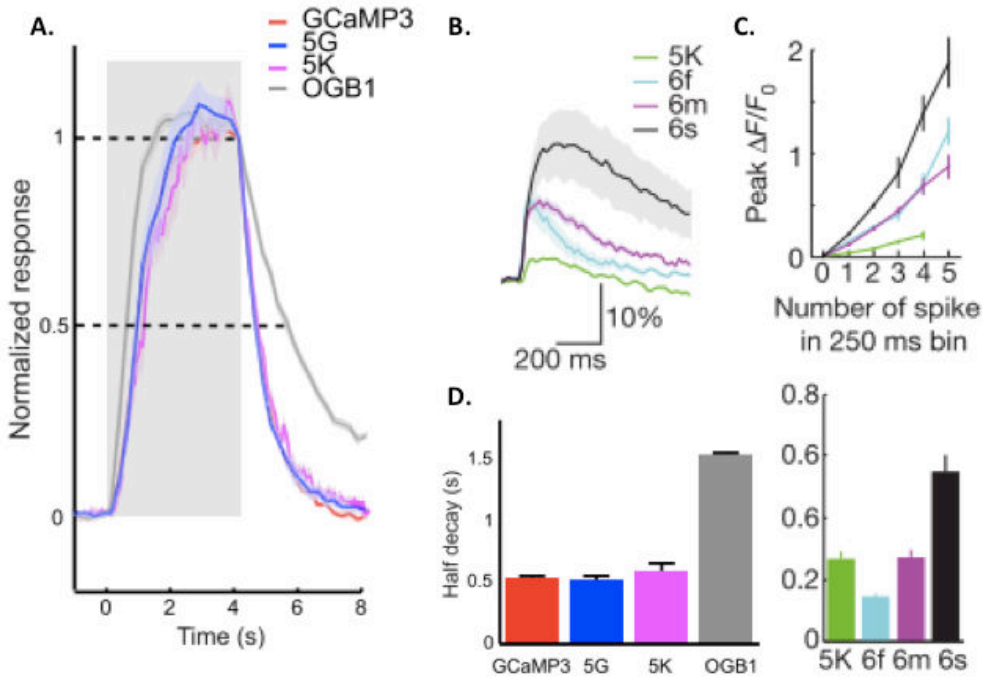


*Figure 9 Kinetics of OGB-1 compared with GCaMP protein family. Normalized fluorescence response in time (A). There are no big differences between the old generation of GCaMP and OGB – 1 calcium indicators. Single AP fluorescence rise of GCaMP6 compared to GCaMP5 (B). GCaMP6s presents a much larger fluorescence change than the rest of the GCaMP family. Increase of fluorescence signal in response to multiple spikes, showing linear dependence. Color code as in B. Half decay time of different calcium indicators (D) left – color code as in A, right – color code as in B. (Modified after (Akerboom et al. 2012; T.-W. Chen et al. 2013)).*

| % of tuned cells detected (orientation) | dF/F for optimal stimuli | dF/F for single spike | dF/F spontaneus activity | imaging power under objective | imaging frequency | calcium indicator | anaesthesia type | anaesthesia dose | animal | comments | reference |
|---|---|---|---|---|---|---|---|---|---|---|---|
| not reported | ~60% | not reported | 20% | <70 mW | 5 ms line- 200 Hz | AM - ester indicators | ketamine/xylasine or urethane | 0,1/0,01 or 1,9 mg/kg | mouse | in vivo and in vitro (till 10th week); 6h of imaging reported with ni big fluorescence loss, barel cortex | Stosiek et al., 2003 |
| 61% | up to 30 % | not reported | not reportes | < 45 mW | 0,81-1,63 s/frame (1,2-0,6 Hz) | OGB-1 AM | urethane and ketamine | 1,5 g/kg and 20 mg/kg | rat | | Ohki et al., 2005 |
| 34% for PC, 40% for GABAergic interneurons | ~5% for GABAergic interneurons, ~10% for PC | not reported | not reported | not reported | ~3Hz | Fura-2 | urethane | 1,9 mg/kg | mouse | low n in the study | Sohya et al..,2007 |
| 79% | | 5%-after Kerr et al..,2005 | up to 70-80% | <50 mW | 1.6s/rame (0,6 Hz) | OGB-1 AM | isoflurane | 0,5-1 % | rat | | Yeang H.Ch'ng and R. Clay Reid, 2010 |
| 70% | 20% on the dendrite | 20% for 2 AP | not reported | not reported | 30 or 6- Hz | OGB-1 AM | isoflurane | 0,80% | mouse | dendritic calcium imahgin | Jia et al.., 2010 |
| 18% for PV cells, majority of PC | 5-10% for PV cells,20% for PC | not reported | not reported | not reported | 7,6 or 15,2 Hz | OGB-1 AM | Fenantyl,Midazolam, Medetomidin, mantained with isoflurane | 0,05,5 and 0,5 mg/kg, 0,3-0,5% | mouse | | Hofer et al.,2011 |
| 68% | up to 20% for higly tuned cells | not reported | not reported | <50 mW | 7,6 Hz | OGB-1 AM | Fenantyl,Midazolam, Medetomidin, mantained with isoflurane | 0,05,5 and 0,5 mg/kg, 0,3-0,5% | mouse | | Ko et al.., 2011 |
| 70% | 20% | up to 70% | 10-20% | < 320 mW | different for each conditions | OGB-1 AM | isoflurane with chlorprothixene and urethane | 0,05mg/kg and 0,75 mh/kg | mouse | paper presents fast imaging techniques | Rózsa et al., 2012 |
| 56% in chronic recordinngs | 250% | 20%-30% | not reported | 35-50mW | 15 or 60 Hz | Gcamp6s (AAV expressed) | isoflurane with chlorprothixene | 0,5 %,20uL at 0,33mg/mL i.m | mouse | | Chen et al..,2013 |
| 10% or 45% for GP4.3 orGP4.12 strain respectively | 500-600% | 100% | not reported | 145 mW | 15 Hz | Gcamp6s (transgenic line) | isoflurane | 0,50% | mouse - transgenic | | Dana et al.., 2014 |
| 43% | 100-up to even ~500% | not reported | not reported | not reported | 30 Hz | Gcamp6s rebies virus retrograde trasing | isoflurane with chlorprothixene | 0,25%, 2,5 mg/kg | mouse | | Werts et al..,2015 |
| 71% | 150% for soma and ~50% for single spine | not reported | not reported | 16-40 mW | 30 Hz | Gcamp6s (AAV expressed) | isoflurane | 1-2% | ferret | | Wilson et al., 2016 |

*Table 1. Calcium imaging studies in primary visual cortex of a mouse – literature overview*

## 3.2. Strategies to obtain an all-optical preparation

The biological preparation enabling the mapping project would be characterized by the presence of both calcium indicator and opsin channels in the highest possible percentage of neuronal population in V1. To achieve this goal a few strategies could be applied. We have taken into consideration a calcium probe (OGB or GCAMP6s) paired with a red actuator. The GCaMP6s and opsin combination could be achieved in two alternative ways: by using GCaMP6s transgenic mice, in which opsin construct is expressed after viral AAV injection in V1, or by inducing expression of both GCaMP6s and opsin using viral AAV injection. During the thesis duration I was working in all presented strategies in parallel testing various opsin constructs.

### 3.2.1. Characterization of CoChR - mCardinal viral construct

#### *3.2.1.1. CoChR opsin - background information*

CoChR is an opsin naturally occurring in *Chloromonas oogama* algae. The characterization of CoChR is similar in many aspects to ChR2, which is probably the reason of the relatively small interest of this opsin among the community (only one paper on *C.elegans* model published). CoChR is an opsin with quite similar kinetics and excitation peak wavelength to ChR2. However, in 1 - Photon conditions, the turn-off kinetics of the channel (τoff) is much longer (~100ms) and the 90% time to peak is a bit shorter (~4.5ms) than ChR2. Additionally, CoChR recovers more from desensitization during the dark period (~80% during the 1st second). Furthermore, CoChR elicits a much larger current when compared to other opsins (3.5 nA; assuming optimal wavelength of stimulation) (Klapoetke 2014).

The soma-targeted version of CoChR - GFP construct was characterized in 2-photon conditions by Emiliani group (in parallel to mCardinal construct testing presented in this section below), confirming the good efficiency of the opsin and favorable kinetics (Shemesh et al. 2017). The opening time of the CoChR channel (τon) was equal to 5.7±2.6ms, whereas the τoff 37±13ms. The power at the threshold, allowing reliable triggering of action potentials, was equal to 0.03±0.01 mW/$\mu m^2$ (amplified pulse laser), although increasing the power to 0.07mW/$\mu m^2$ allowed obtaining a 15ms latency and spike jitter below 1ms. Therefore, the characteristic of the opsin was promising for the mapping project and all - optical approach.

The interest in testing this opsin was mainly driven by its high photocurrents and its fast recovery from desensitization. In light of promising results coming from characterization of CoChR-GFP version we decided to characterize the 2- photon properties and expression of the opsin version fused to the red reporter mCardinal. This version would enable easy distinction of opsin bearing neurons in tissue co- expressing GCaMP6s. However, from the onset of testing it was expected that the kinetics of the opsin won't be changed by combination with different actuator. However, the exact expressed

genetic sequence could influence the ratio of opsin expression and thus, the amplitude of photocurrent obtained.

#### *3.2.1.2. CoChR-mCardinal initial screening*

A group of 4-5 weeks c57BL mice (n=15) were injected with AAV8 hSyn-ChR86-mCardinal construct (titer: 1.9x10e12) in L2/3 of V1 (animals injected with the help of Nidal Bouzekri - master student at internship in the group). After 7-11 weeks, the brains were extracted, and tissue prepared for electrophysiological recordings (details in methods section). The initial screening aimed at characterizing opsin expression reliability between animals, amplitude of evoked photocurrents, and spike inducibility in the context of the mapping project.

Results:

Expression of CoChR-mCardinal varied across animals and cells, and a 2P-photstimulation powers, needed to trigger one action potential, ranged from 0,5 to 1,4 mW/µm$^2$. Expression spread, ranged between 1 to 8 consecutives 300-µm slices of tissue. Targeting opsin-positive cells was not possible directly. The viral construct resulted in opsin and reporter expression in all neuronal compartments and some clusters of fluorescence was visible only. In this situation, cells were patched randomly within the area of high expression, judged based on the level of mCardinal fluorescence during 1-photon imaging (Figure 10).

The characterization of opsin's kinetics was obtained under 2-photon holographic illumination at 920 nm in voltage-clamp configuration. Spots of 15 µm were used to photoactivate the channels, photocurrents were recorded, and current rise and decay were fitted with a mono-exponential function. The results obtained are consistent with the kinetics published in (Papagiakoumou et al., 2018): $\tau_{on}$ (currents rise time fit) = 5.7±2.6ms; $\tau_{off}$ = 37±13ms. The dependence of currents from photostimulation power is shown in Figure 11. CoChR photocurrents saturated at laser powers between 0.55 and 0.8 mW/µm².

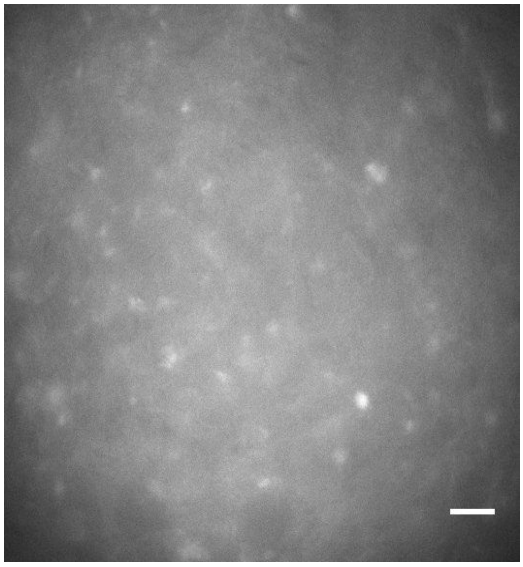

*Figure 10 Expression of CoChR – mCardinal in brain slices. Wide field fluorescence image of opsin expressing area. Lack o cleavage sequence resulted in dimmed fluorescent signal in the expressing area. Scale bar indicates 15 µm.*

Despite the fact that the cells were chosen randomly, the level of opsin expression was quite uniform and high enough to elicit single action potential in about the 70% of cells under 2-photon illumination in current-clamp configuration (Figure 11 inset, 8 cells out of 11). The rest of cells (about 30%) included situations when AP was induced once or twice but failed in the rest of 3 repetitions at the maximum power, or the induced depolarization was too low to reach spiking threshold at all. When increasing the stimulation power action potential latency decreased and spike jittering was reduced (Figure 12), resulting in a more reliable control of light-induced spikes timing. The photostimulation of neurons in current –clamp configuration was done with a threshold power (enough to allow reliable triggering of one action potential in 15 ms photostimulation) ranging from 0.5 to 1.5 $mW/\mu m^2$ at 920 nm (Figure 11). Additionally, in those cases where the opsin expression allowed for eliciting a single spike reliably with low light power, it was possible to induce trains of spiking up to 100 Hz, although typically some spikes were missing during the train of stimulations (Figure 13). During stimulation with high frequency pulses, indeed, the influence of opsin $\tau_{off}$ was visible, as well as the level of opsin expression together with the neuronal cell subtype: between two consecutive photostimulations at high frequencies a sustained depolarization, caused by the slow decay time, could generate extra spikes. A second behavior observed was the increase in latency and jitter values during trains due to the CoChR current desensitization, leading to a decrease in spike timing reliability and to the loss of some spikes.

In some cells with a lower level of expression it was not possible to induce spiking in response to low powers and short (i.e. 5ms) light pulses. However, it was often possible to reliably trigger action potentials for longer 15 ms pulses or for higher laser powers increased at values close to saturation (Figure 14). Note, that examples of cells displayed at the Figure 13 and Figure 14 differs substantially in the power at the threshold (indicated in grey color) and evoked photocurrent averaged amplitude for each cell.

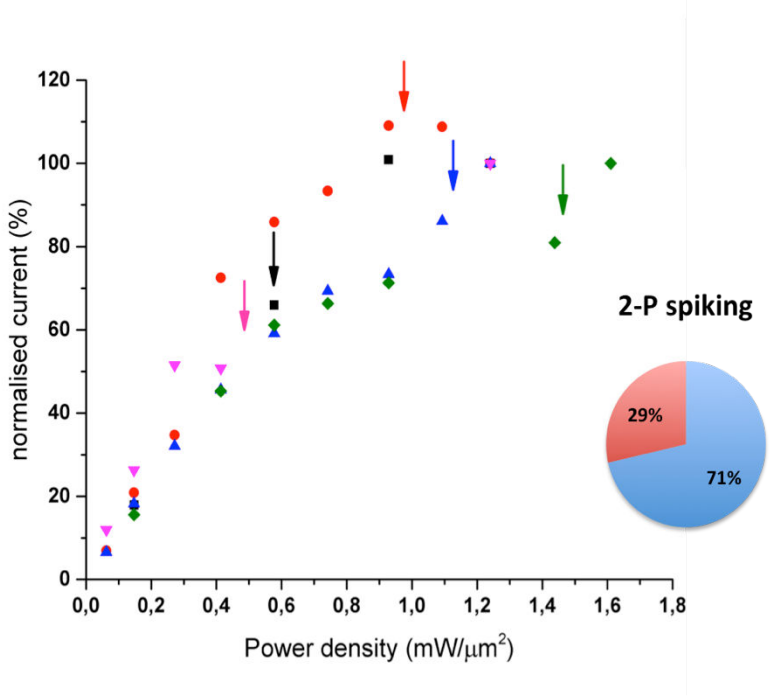


*Figure 11 Photocurrent elicited by holographic photostimulation of the neurons expressing CoChR – mCardinal. Normalized current is plotted as a function of increasing power density (n=5). Arrows indicates the power which allowed for triggering an action potential for a given cell under current clamp, showing that there was a large variability in the level of opsin expression. Inset- overall, reliable spiking rate (blue) versus non-reliable spiking (red) under 2-photon stimulation (n=11).*

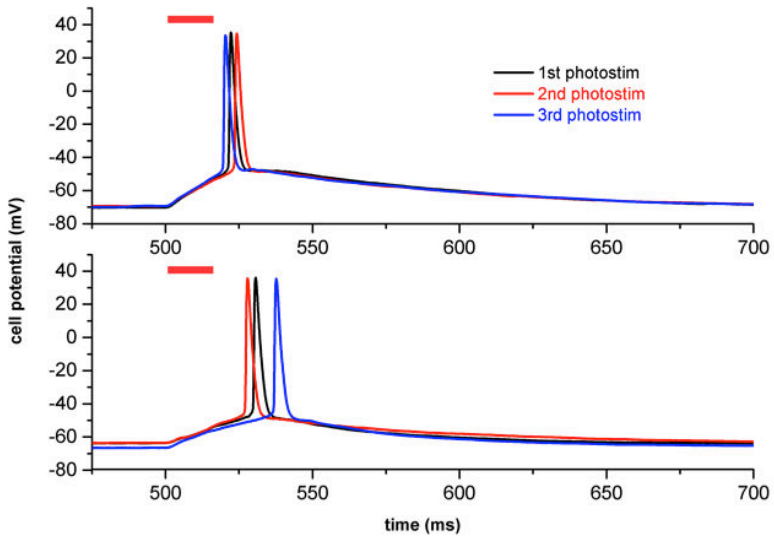


*Figure 12 Example spiking of a CoChR-mCardinal cell with three subsequent photostimulations separated by 40 seconds. Two different power were used: at threshold, for this cell 0,58 mW/µm² (bottom), and a higher power, here 0,93 mW/µm² (top). Decrease of spiking latency and jitter is evident for increased stimulation power. Red square indicates the stimulation duration (15 ms).*

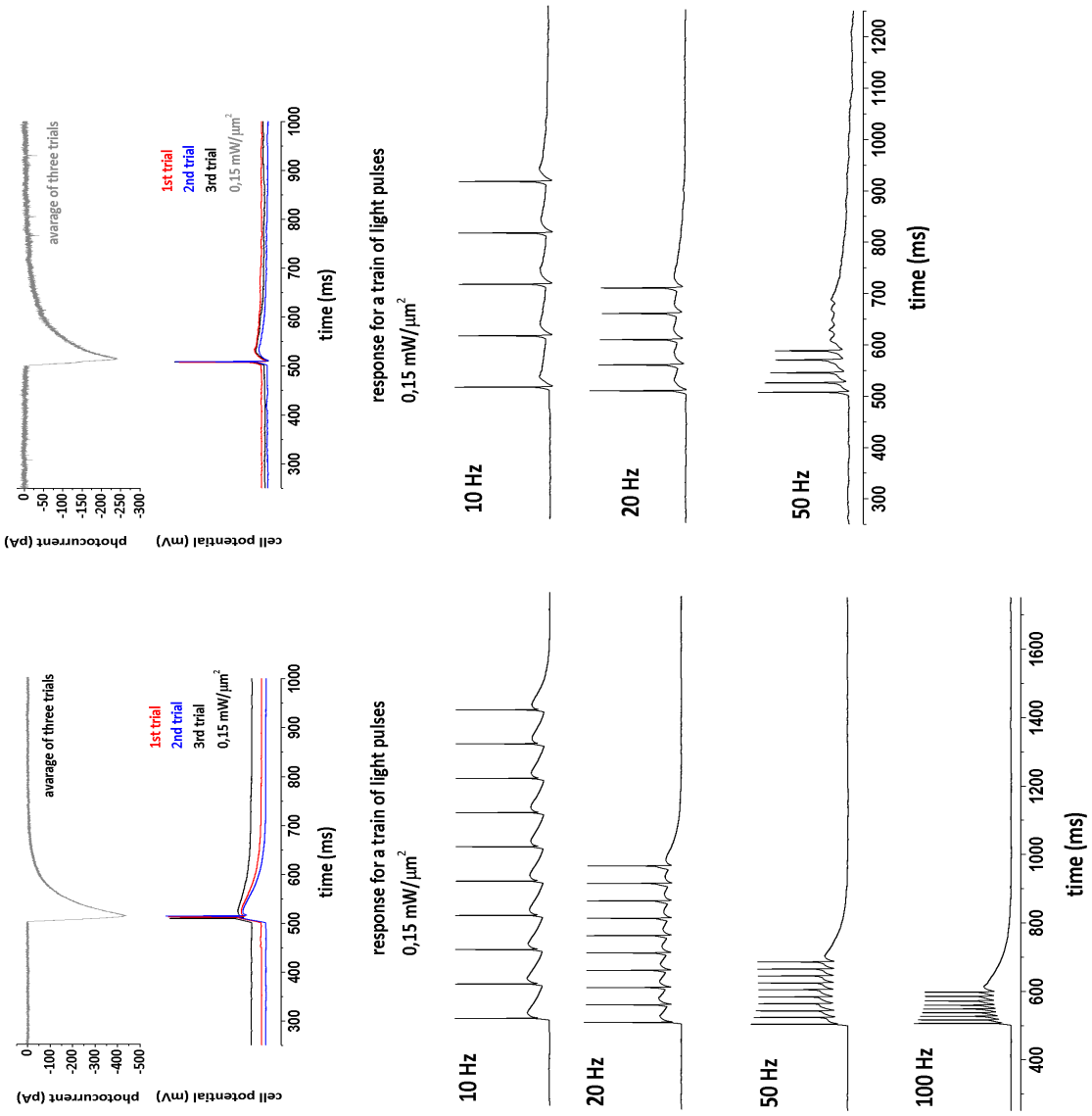


*Figure 13 CoChR-mCardinal opsin expression allowed for triggering trains of action potentials up to 100 Hz in highly expressing cells. Example from 2 interneurons (left and right part of the picture). Upper panel shows photocurrent amplitude and reliable spiking of cells under illumination conditions applied for train pulses. Bottom panels present the response of cells to a train of light pulses with increasing frequency. Some spikes were lost while high frequencies trains were applied.*

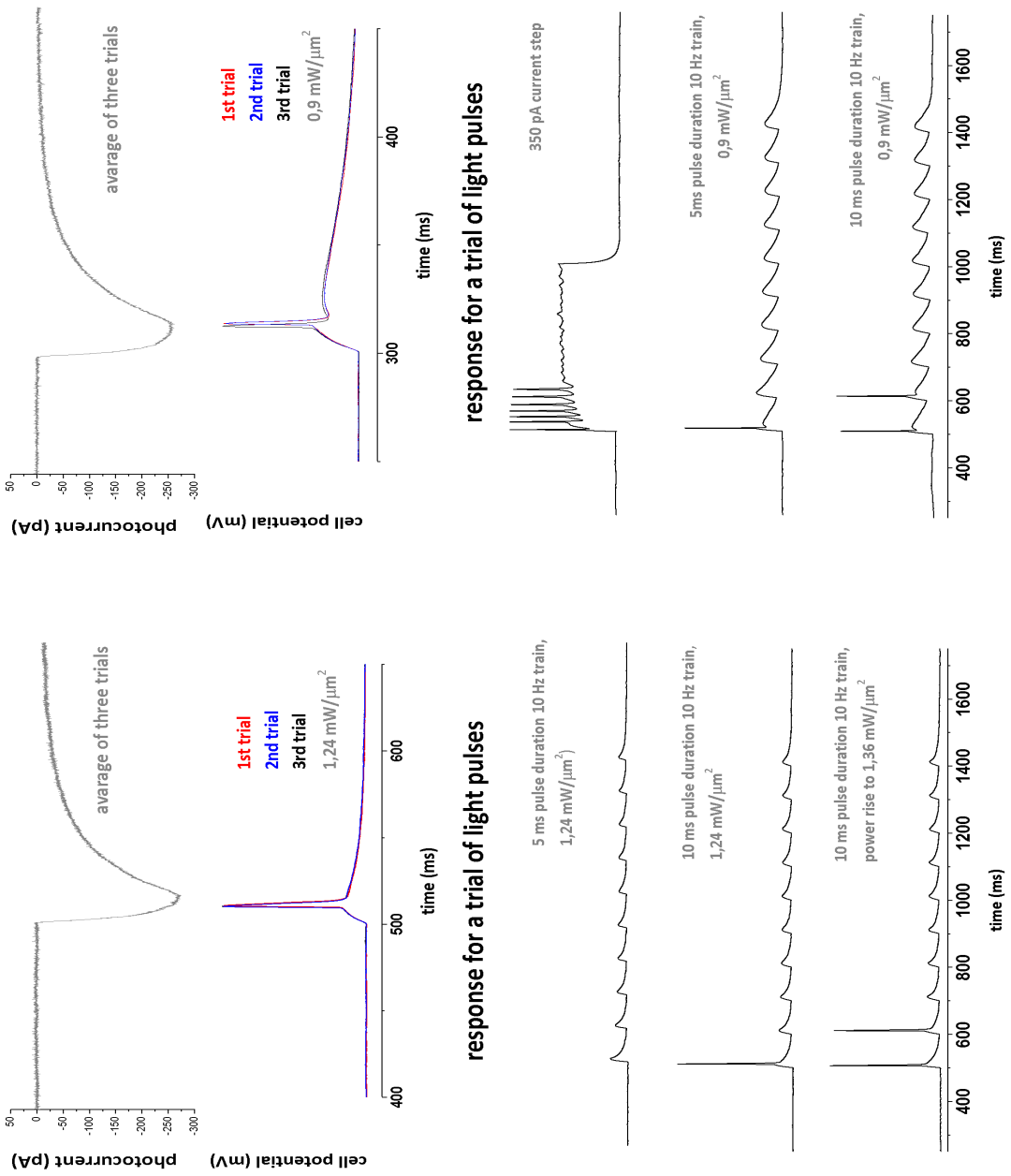


*Figure 14 . Repetitive light pulse stimulation of CoChR-mCardinal opsin failed to trigger spike trains in low expressing cells. Example from 2 cells (left and right part of the picture). Upper panel shows photocurrent amplitude and reliable spiking of cells under the illumination conditions applied for train pulses. Bottom panels present the response of cells for a 10 Hz train of light pulses. For the cell on the left, the low level of opsin expression prevented spikes for 5 ms pulse photostimulation train., and only sub-threshold depolarizations are visible. Increasing the pulse duration to 10 ms triggered only one action potential for the first pulse. A subsequent increase in the light power triggered only two spikes. For the cell on the right, fast repetitive firing was achieved in response to a 350pA current step, but in contrast a 5 or 10 ms photostimulation pulse train resulted in only one or two action potentials at the maximum laser power density.*

In summary, the CoChR-mCardinal construct appears to work well in L2/3 of V1. It is possible to elicit reliable spiking and in some cases trains of spikes up to 100 Hz, depending on the cell type and opsin expression level. In addition, we did not observe any negative effect of the red reporter on the health of the tissue. However, the small testing group shown variability in the obtained parameters. Probably a higher dose of injected viral construct could provide less variable results and parameters more similar to those obtained by other group members coming from CoChR-GFP (classical construct, not soma targeted).

Finally, a soma-targeted version of CoChR-GFP construct was under testing in the team and it has been characterized under 2-photon holographic stimulation by Emiliani's group, confirming the good efficiency and favorable kinetics of the CoChR opsin (Shemesh, et al. 2017). Therefore, the characteristic of the opsin under two-photon illumination were promising for the mapping project and applicable for an all-optical approach.

In conclusion, mCardinal-CoChR opsin construct, especially a somatic version, could be further investigated as a candidate for investigation of functional connections. In addition, further work would be needed to pair this construct with GCaMP6s.

### 3.2.2. Characterization of ReaChR-tdTomato viral construct

Among the several actuators characterized during my PhD, a special focus has been dedicated to the investigation of performances of ReachR-TdTomato. I have been implicated in this project that involved recording on acute brain slices and with multiple illumination sources for photostimulation. In 2016, these results have been subject of a publication in 'Frontiers in Cellular Neuroscience' that I co-sign and ReachR construct is currently used in the laboratory for *in-vivo* project enabling 2-photon stimulation of neurons in mouse V1.

#### *3.2.2.1. State of the art: ReaChR characteristic in 1P*

ReaChR (Red-activatable Channel Rhodopsin) is a variant of channelrhodopsin engineered to increase membrane trafficking and expression level compared to other opsins. It was designed on the basis of the VChR1 genome – a red shifted excitation spectrum opsin with a few changes in its genomic sequence. First, the replacement of the N-terminus from the first transmembrane domain with the corresponding sequence from the ChIEF opsin resulted in an increase in the membrane trafficking. Second, transmembrane domain F was replaced by the corresponding sequence of VChR2 in order to increase the expression level. A similar substitution was used to enhance ChR2 expression level in between ChR1 and ChR2 chimeras. Third, another mutation, L171I, lead to a correction of kinetic properties, which had suffered from a very long and poorly recovering desensitization. This engineering process was completed with success delivering the ReaChR opsin (Lin et al. 2013).

ReaChR is characterized by excellent trafficking to the cell membrane and a high sensitivity to light, making it an excellent candidate to perform 2-photon stimulation. Additionally, in comparison to the majority of opsins, it's excitation is red-shifted with the 1-photon peak around 600nm, favorable for a better penetration of stimulation light in the tissue and for a potential coupling with GCaMP sensors. The high sensitivity and large photocurrents come at the price of slow kinetics of the channels, as these two features seem to be inversely correlated (Mattis et al., 2011). Specifically, the characteristic current decay was estimated around 140 ms this value though significantly higher in comparison to ChR2, it is still shorter than another red-shifted opsin, C1V1(E122T) (Figure 15), and

ReaChR allowed to elicit reliable spiking in 1-photon excitation with a rate up to 30 Hz (Lin et al. 2013).

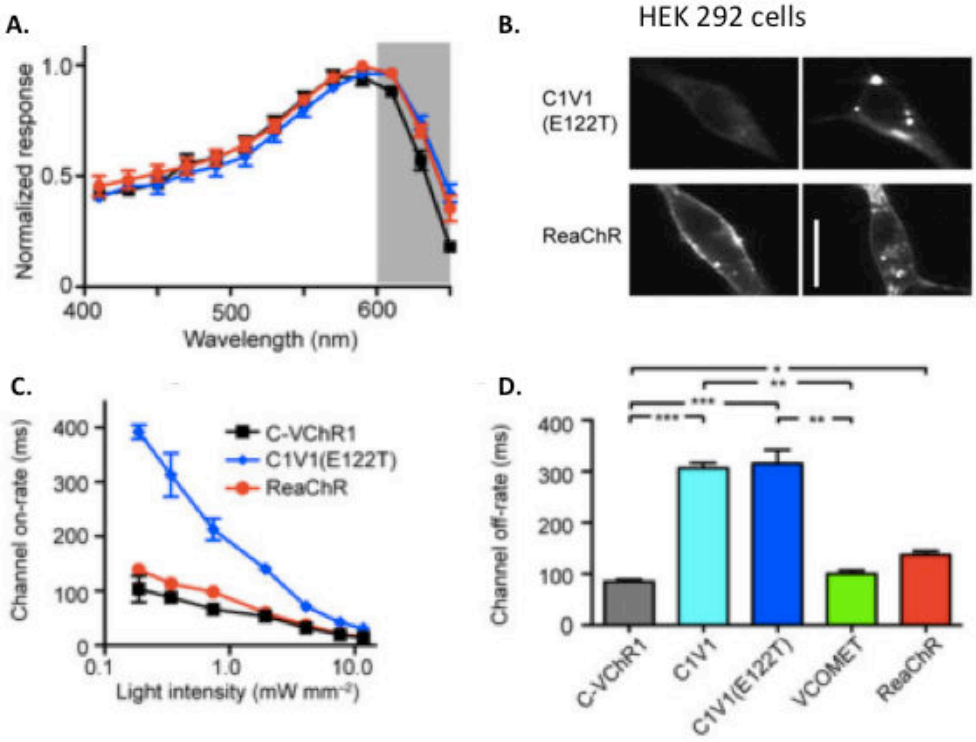


*Figure 15 . 1-photon ReaChR characteristics. Absorption spectrum (A), color code as in C. Opsin expression in HEK 292 cell line (B). ReaChR traffics well to the membrane in contrast to C1V1, which tends to aggregate in the soma cytosol. Opening (C) and closing (D) times of ReaChR in comparison to other red-shifted constructs (Modified after Lin et al., 2013).*

### *3.2.2.2. ReaChR characteristic in 2P*

2-photon characterization of ReaChR in CHO cells and acute brain slices in our laboratory have confirmed previous findings and explored ReaChR potential under 2 – photon conditions (Chaigneau et al., 2016). Photostimulation with 2-photon holography showed ReaChR light sensitivity and good channel trafficking, allowing to achieve reliable spiking at unprecedentedly low laser powers (saturation at 0.10 ± 0.03 mW/µm$^2$).

Kinetics and spectrum:

The rise time (TR) of ReaChR (extracted as the time constant of an exponential fit of the rising part of the current) measured in CHO cells depended on laser power and varied from 8 ± 2ms (0.3 ± 0.1mW/µm2) to 145 ± 39ms (0.008 ± 0.002mW/µm2). Decay time (TD, defined as the exponential decay constant of the current after photostimulation) was independent from the power density, and equal to 212 ± 24ms. These values are consistent with the slow kinetics of ReaChR found under 1P illumination (at current saturation: TR = 20 ± 0.6ms; TD =137 ± 7.1ms (Lin et al. 2013)).

The obtained spectrum shows the 2-photon peak between 975 and 1000 nm, that confirmed the ReachR opsin as more red-shifted with respect to ChR2 (Figure 8). Even if the spectrum of ReaChR was assessed by tunable Ti:Sapphire laser, it was possible to effectively used ReaChR by exciting it with pulse amplified laser at 1040 nm. At this wavelength 75% of ReaChR current at saturation is evoked but because of the opsin characteristic and the design of the viral construct we used it was possible to excite reliably spiking.

The conditions to evoke an AP in cortical layer 2/3 cells were characterized. ReaChR was expressed in the visual cortex of mice using AAV1 CamKII-ReaChR-p2a-YFP or AAV1 Ef1-ReaChR-p2a-dTomato. Constructs with the p2a sequence between ReaChR and the fluorescent reporter facilitate the identification of opsin-expressing cells and allow easy identification of expressing cells under 1 or 2-photon illumination. Expressing cells in the layer 2/3 were patched and successively target with holographic photostimulation spot.

The AP threshold was reached for a power range of 0.02 - 0.03 mW/$\mu m^2$ depending on a cell type (0.025 ± 0.022 mW/$\mu m^2$, n=43 cells). This is about half the power needed to reach current saturation (resulting in on average 740 ± 210 pA of photocurrent) and corresponds to extremely low total power of less than 6 mW sent to the cells. This is a result of both good expression and sensitivity of the opsin together with the efficient amplified laser source used.

Additionally, investigation of temporal performance of ReaChR opsin for single spike induction was done, by varying stimulation parameters such as pulse length and intensity. The amplified laser source together with the opsin good expression ratio resulted in fast and repeatable current integration. As expected, decreasing pulse length, increased light power density threshold (from 0.025 mW/$\mu m^2$ for 10 ms up to 0.09 mW/$\mu m^2$ for 1 ms pulses) needed for spike induction. Taking into account the low powers needed for ReaChR activation allows for shortening or elongating the pulse within a range of parameters which will provide reliable spiking. In this context ReaChR is a 'flexible' opsin, which could be applied to stimulate cells by using different photostimulation protocols, but also different laser sources conjoined with holographic stimulation. Similarly, increasing the power of stimulation shortened spike jitter and latency (Figure 16).

However, similarly to the ReaChR engineers reported (Lin et al. 2013), we observed additional spikes or lost spikes in a train. Although this is an undeniable drawback, it was possible to find photostimulation parameters to accommodate the opsin performance to specific needs. In particular, by increasing the power it was possible to minimize the influence of long kinetics. As a result, more channels were open at the same time reaching the threshold for eliciting an action potential with shorter latency and smaller jitter (Figure 16). On average, trains of 5 APs could be elicited up to ~15 Hz for pyramidal cells, ~35 Hz for fast spiking cells (Figure 17).

In summary, ReaChR is a very efficient opsin, working similarly well with green and red fluorophore, but its slow kinetics allow only for a moderate control of time - resolved cell activity. Although, good

temporal control is possible to achieve by using two laser sources for single spike generation, for train spike induction the influence of long kinetics is visible, and it is hard to control spiking occurrence.

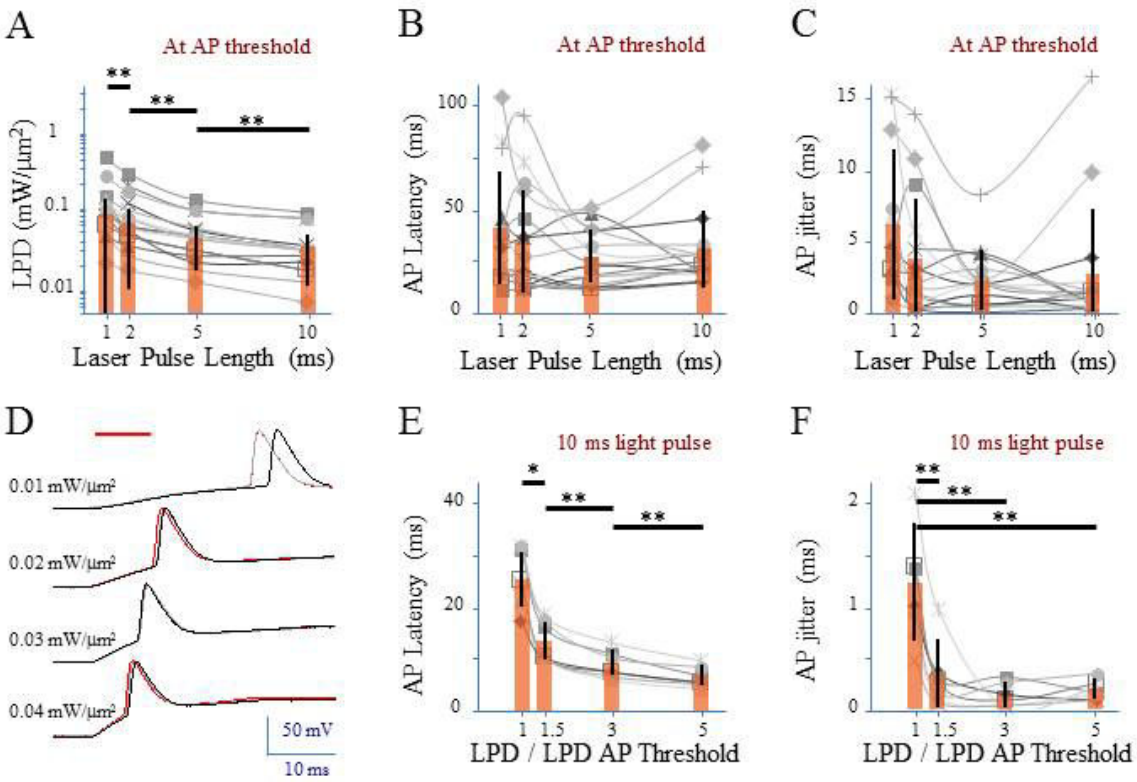


*Figure 16 Conditions to elicit reliable spiking and influence of the power for latency and jitter. Laser power (LPD) necessary to evoke an AP with 1 to 10 ms long 2P holographic spots (A) (15 µm diameter over the cell soma). Individual cells (gray), average (orange bars) and s.d. (error bars). Latency (B) and jitter (C) between the AP evoked by 1 to 10 ms long 2P holographic spots at the LPD for AP threshold and the onset of the 2P stimulation. Voltage response of a L2/3 pyramidal cell expressing ReaChR (D). Latency (E) and jitter (F) between the AP evoked by 10 ms long 2P stimulation and the onset of 2P stimulation at various ratios of power (LPD). (Modified after (Chaigneau et al. 2016).*

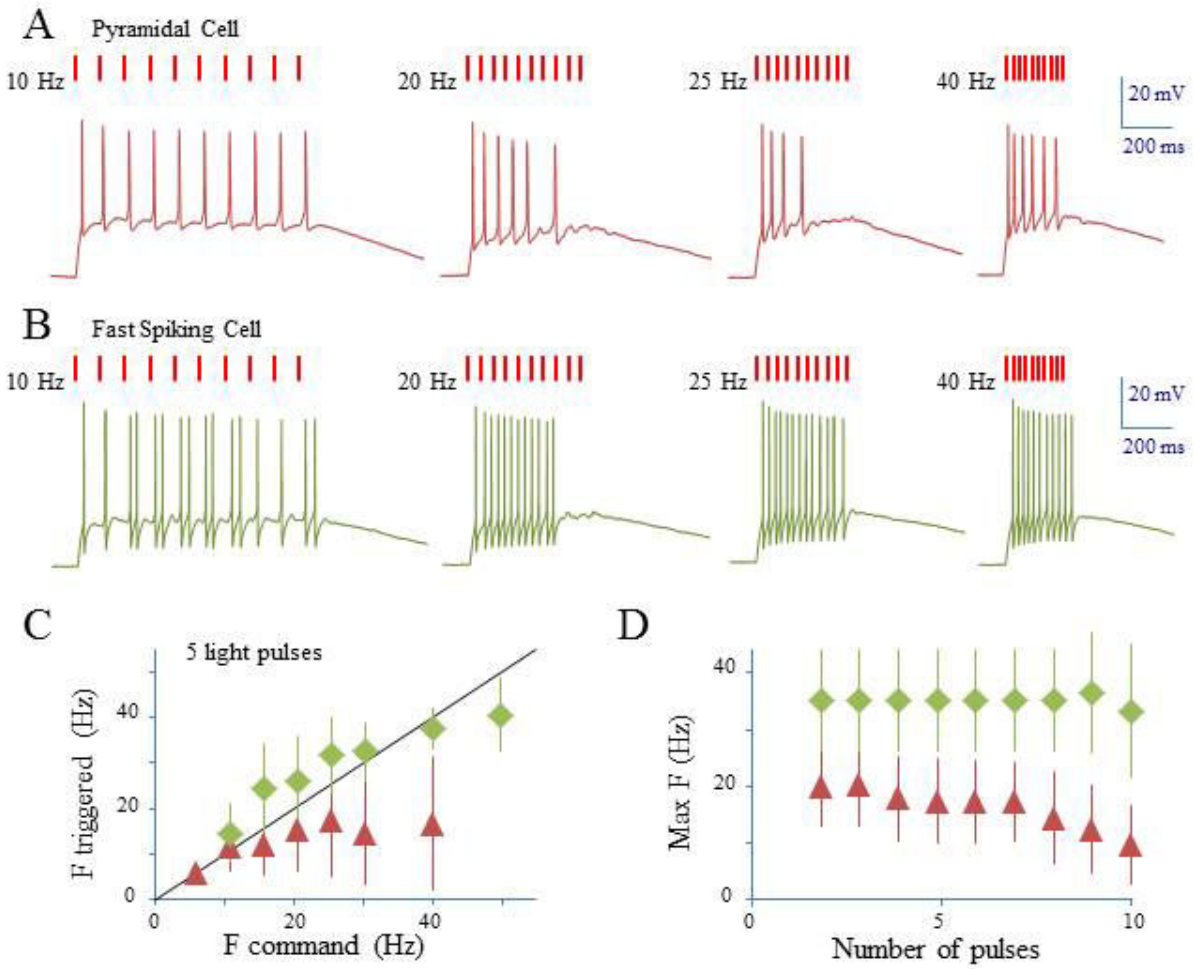


*Figure 17 Photostimulation of ReaChR expressing cells with trains of 10 ms pulses. Evoked trains of APs in single L2/3 cells: example of a pyramidal cell (A) and fast spiking cell (B). Plot of the maximum AP elicited frequency for pyramidal cells, low threshold spiking (LTS) cells (red triangles) and fast spiking (FS) cells (green diamonds) (C). Maximum AP frequency reached for trains of a given number of light pulses for pyramidal cells and LTS cells (red triangles) and FS cells (green diamonds) (D). (Modified after Chaigneau et al., 2016).*

### *3.2.2.3 ReaChR opsin fitting for all-optical recording*

The high light sensitivity and good membrane targeting of ReaChR-tdTomato opsin motivated us to consider ReaChR a good candidate to investigate functional connectivity.
In this context, we performed further characterization concerning its capability to provide single cell resolved photoactivation. This part was my main contribution to the published paper.

Characterizing spatial confinement of ReaChR within the neuron:

2 - photon holography provides high spatial resolution enabling to shape the area of stimulation to the specific needs and take advantage of the full potential of the opsin expressed in the neuron. However, to apply it in connectivity experiments one need to characterize how much opsin present

in the distal and proximal processes will contribute to the potential change in the soma to avoid false positive connection detection in the real connectivity experiment.
Stimulation of the opsin expressing pre-synaptic cells will result with EPSP in case of connection presence at the post-synaptic neuron. A similar in amplitude change in membrane potential might be also elicited by stimulation over the investigated cell processes. To distinguish the true connection from an artifact originating from opsin expressed in the processes it is needed to characterize what is the ReaChR opsin confinement within the cell and how big changes would be induced by stimulating outside the soma.

To characterize this effect, I have performed experiments on the ReaChR-p2A-tdTomato expressing tissue, assessing the opsin triggered depolarization and eventual spiking. Cells were patched with the presence of Alexa dye in the internal solution and synaptic blockers in the external solution. First, the soma of the cell would be photo-stimulated (15µm spot, at 950nm) to find the power at which action potential can be reliably induced (spiking threshold power). Second, the stimulation area would be moved in various positions over processes and stimulated with the same power as in the first step. The stimulation in the same sequence of positions was repeated three times.

The sequence stimulation induced depolarization up to 10,5mV, but usually the amplitude was between 1 – 4 mV (average change for all cells: 3,72 ±2,29mV, n=5 different sequences measured at 3 different cells, 25 spots in total) (Figure 18). Depolarization was not dependent on the distance from the soma (varying between 20-100um), and never resulted in triggering an action potential.

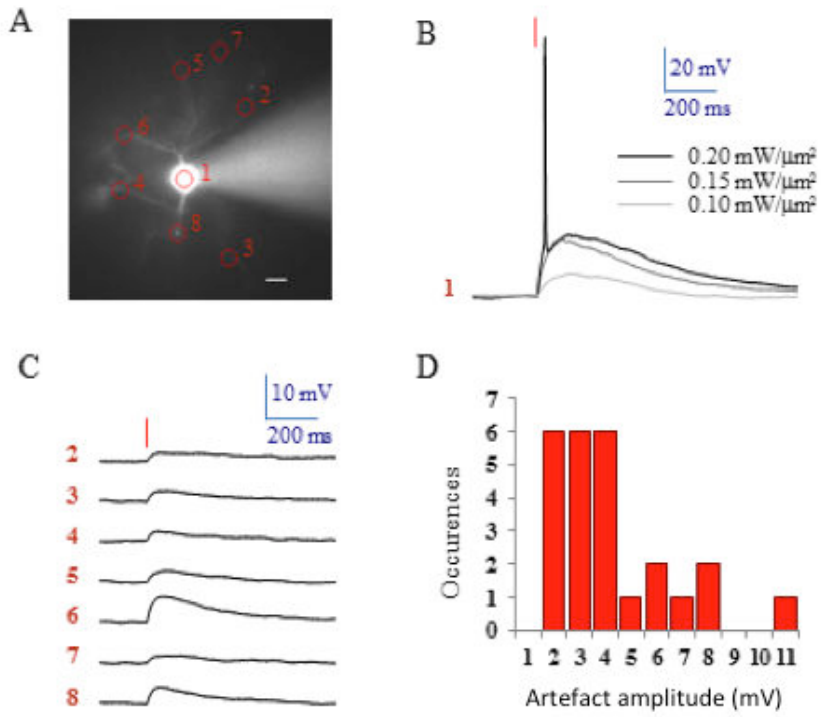


*Figure 18 AP threshold with standard femtosecond Ti:Sapphire laser and spatial specificity of 2P holographic stimulation of ReaChR. Widefield fluorescence image of L2/3 ReaChR-expressing neuron filled with 20 µM*

*Alexa 594 (A). Scale bar: 15 µm. Voltage response (single recording) to a 10 ms long (red line) 2P holographic stimulation with a Ti:Sapphire laser at 950 nm using a circular spot on the cell soma (1 in panel A, 15 µm diameter) for increasing stimulation powers (B). Average voltage response (artifact) (n = 3 repetitions) to a 10 ms long (red line) 2P holographic stimulation on numbered circular spots (15 µm diameter) in panel A (C). Stimulation power: 0.2 mW/µm$^2$. Distribution of the averaged artifact amplitude (n = 3 repetitions, 25 spots, 3 cells) (D). Distance from the soma from 15 to 100 µm, as shown in panel A. Stimulation powers were corresponding to the one used to reach the AP threshold for 2P stimulation on the cell soma for each cell (0.15 to 0.25 mW/µm$^2$).*

These results put in evidence some limitation in reaching single cell resolution photoactivation required to detect synaptic connections, which is necessary for connection assessment in functional connectivity project. Although the depolarizations elicited *in vitro* were not high enough to induce action potential, they would still generate artifactual depolarization during connection testing protocol for mapping of connections, that could be misleadingly interpreted as effective connections. Application of the soma restricted optical channel would undoubtedly allow for performing connectivity experiments in easier to interpret manner and with less artifact.
Alternatively, designing an experimental algorithm to distinguish the artefactual potential changes from the true connection would be needed. Application of long light pulses could possibly be helpful to differentiate opsin induced potential changes by using the kinetics of the opsin (which is slow for ReaChR opsin, especially in contrast to synaptic activity).

### 3.2.3. Co-expressing of multiple viruses in the V1 using AAV injection

Motivations:

Adeno-Associated Viruses (AAV) injection ensures harmless and long-time gene expression of desired protein (Betley and Sternson 2011). It is also a widely used method to deliver to the brain tissue DNA of optical channels and GCaMP calcium indicators. AAV induced expression involves injecting a portion of solution containing viral capsids in the brain tissue. The capsid contains the DNA, which we would like to be delivered to the neuronal nucleus where it would be integrated. The integration of genomic material delivered would result in protein expression.
Each capsid type is morphologically different, and this results in a different capability to invade the cells. This difference is expressed by the virus serotype (Aschauer, Kreuz, and Rumpel 2013). On the other hand, the expression strength and the specificity of the expression in a given cell population depends on the promoter at the beginning of the DNA sequence.
Thus, for obtaining co-expression of GCaMP6s and opsin we decided to test if injection of two mixed viruses (one for opsin, second for GCaMP6s) of the same serotype and promoter will allow to obtain a functional biological preparation suitable for an optical interrogation of circuit connectivity.

In order to reach this goal, we worked together with the team of Deniz Dalkara from the Institute de la Vision, who designed and produced the opsin and GCaMP6s constructs that we describe and characterize in this section.

Action:

This project was split into three tasks:

1) Checking the co-expression of the opsin and fluorescent reporter (no GCaMP expression in this step), by in vitro (cortical brain slice) patch-clamp recordings of photo-stimulated reporter-positive cells. Besides establishing the population overlap of reporter and opsin expression, I aimed for functionally responsive opsin expression, allowing reliable inducement of action potentials.
During the whole project duration, I have tried two serotypes of virus – AAV2.7m8 and AAV 9.2YF, and three opsins subsequently – CatCh, Chronos and CoChR (precise sequences and their titers are described in the methods section).

First, opsin and actuator viruses were freshly mixed before the surgery (2:1 proportion), and total volume of 3 µl was injected into cortex targeting L2/3 of V1. Patch-clamp recordings of tdTomato – positive cells in cortical brain slices 5-9 weeks after injection were made to evaluate opsin and reporter co - expression.
Second, the opsin efficiency of some of the viral constructs were first assessed in CHO cells culture transfected with the constructs before testing in animal tissue.

2) Checking the co-expression ratio of GCaMP6s together with fluorescent reporter

3) Combination of all three viral sequences to obtain a high co-expression preparation of light responsive cells overlapped with GCaMP6s expression, and assessment if the presence of fluorescent reporter is crucial for obtaining functional protocol

Results:

High co-expression was present for both CatCh and Chronos opsin (89% for CatCh, 25 cells of 28 reporter expressing cells; 84% for Chronos, 16 cells of 19 reporter expressing cells) when the AAV2.7m8 serotype was used. This serotype showed a dense and spatially confined expression restricted to small area around the injection site (Figure 19). Nevertheless, while there was satisfactory co-expression, the amount of opsin expression was too low to induce reliable spiking (Figure 20). Data obtained under 1 – photon illumination showed that only half of the CatCh expressing cells were able to trigger an action potential. Under 2 – photon illumination, elicited photocurrents were insufficient to induce action potential in all cells. Chronos-expressing cells gave slightly better results. Under 1 – photon illumination, spikes could be elicited in 71% of cells, although the experimental group was small (n=7). Under 2-photon illumination, reliable spiking was observed

in only 22% of cells (consistent action potential response over three trials). Additionally, only a single action potential could be elicited in 22% of cells despite increasing stimulation power. In the case of remaining 56% of reporter expressing neurons it was not possible to trigger an action potential in response to 2- photon stimulation, with only low amplitude currents observed under voltage clamp (Figure 21).

In parallel to this work, a pilot cohort of injections with GCaMP6s together with CatCh opsin and reporter were performed. This showed promising results, with a co-expression of around 80% based on confocal image analysis. However, we decided to first work on the proper level of opsin expression before further development of a more complicated injection protocol using three sequences.

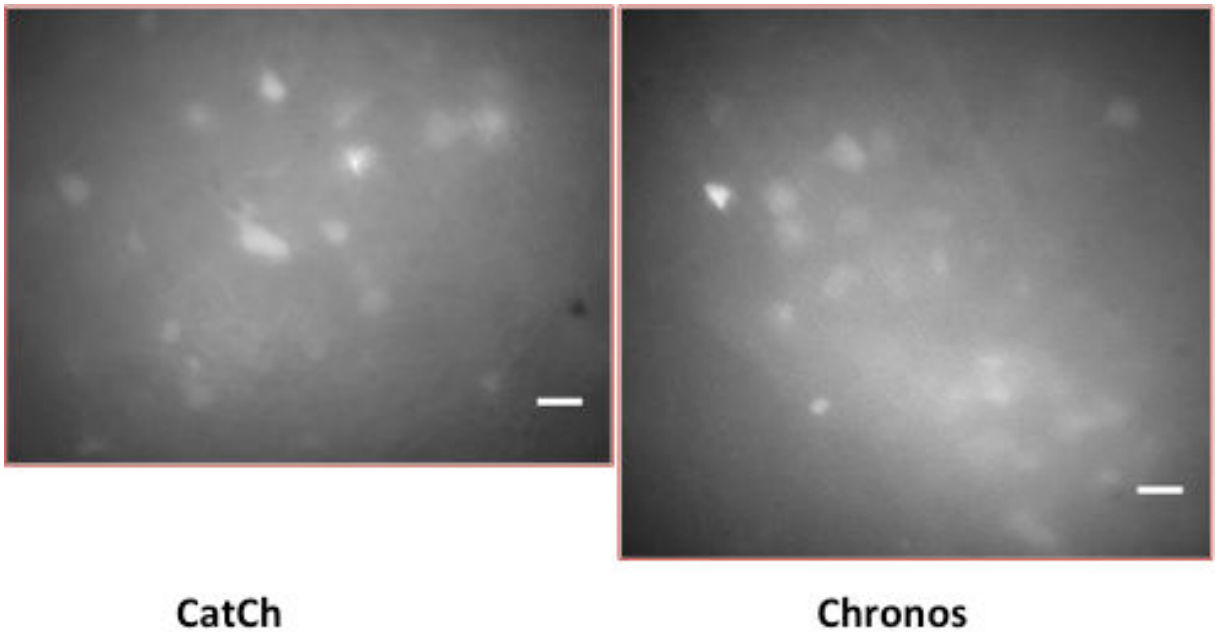


*Figure 19 Wide field fluorescence images presenting CatCh and Chronos expression in L2/3 of mouse V1 brain slices. Scale bars – 15 µm.*

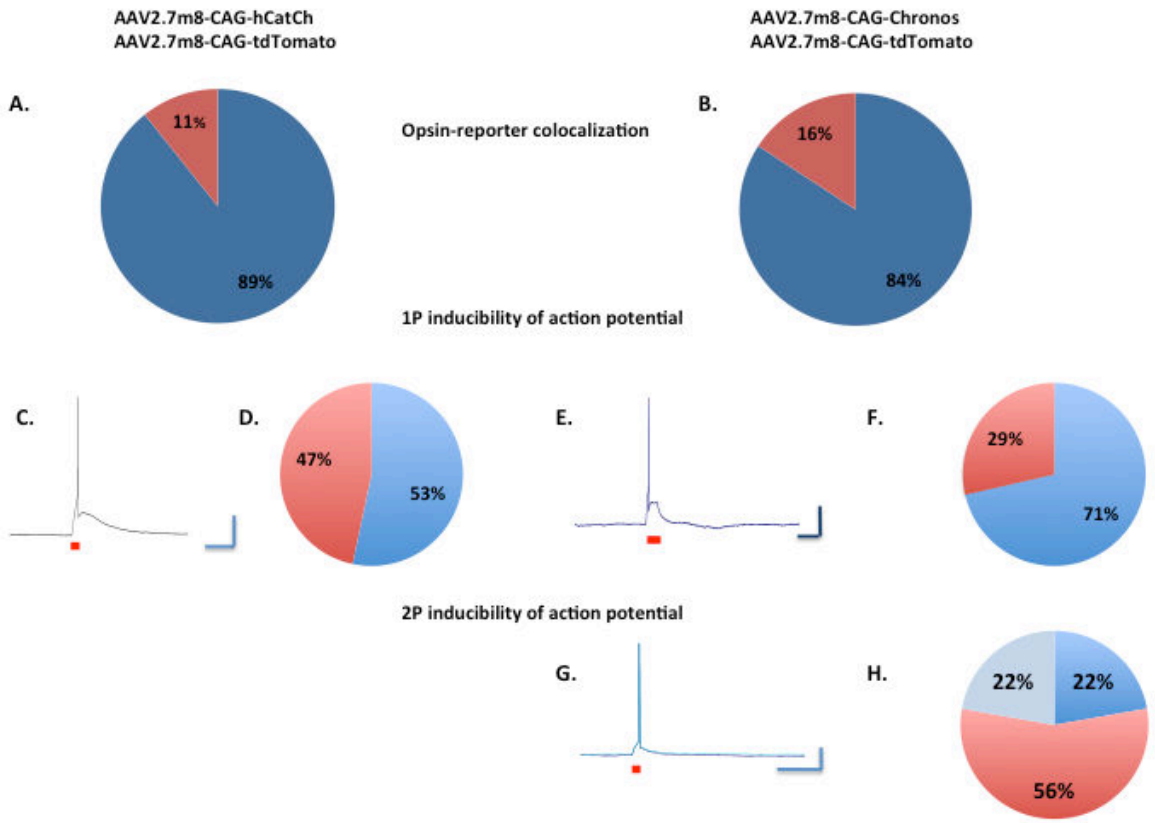


*Figure 20 Summary of co-expression obtained by opsin and reporter (tdTomato) sequence injection into mouse primary visual cortex, using AAV2.7m8 serotype. Picture shows two opsins - CatCh (left part of the cartoon) and Chronos (right part of cartoon).*

*Top: Opsin – reporter colocalization assessed by targeted patch of reporter-positive cells and photostimulation pulses for CatCh (A, n=28) and Chronos (B, n=19). Blue color indicates cells expressing both – opsin and reporter, red color indicates cells expressing only the reporter.*

*Middle: Inducibility of action potentials under 1-photon conditions. Example spikes induced by short 1–p holographic illumination of CatCh (C) and Chronos (E) expressing cells. Scale bars 100 ms and 20 mV. Summary plots presenting the ratio among of all opsin expressing cells of reliable spiking cells (blue) and those with subthreshold photocurrents (red) - CatCh opsin (D) (n=15), Chronos opsin (F) (n=7).*

*Bottom: Inducibility of action potentials under 2-photon holographic illumination. Example spikes induced in Chronos expressing cell (G) and the ratio of successfully spiking Chronos expressing cells (H, light blue – one spike, dark blue – reliable multiple spiking, red – failure, n=9). The photocurrents of CatCh expressing cells were too low to induce action potentials.*

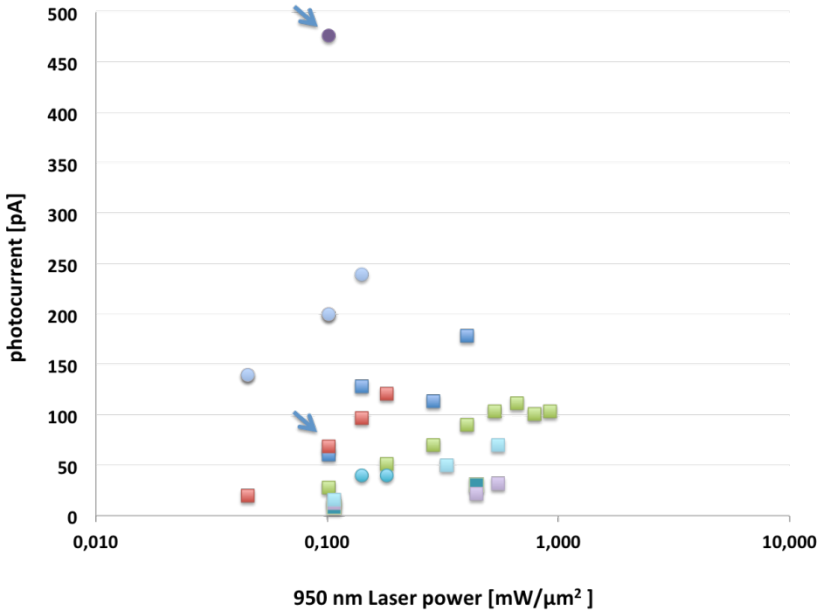


*Figure 21 Current elicited under 2-photon illumination on Chronos expressing neurons (n=9). Circles – cells photostimulated with amplified pulse laser; squares – cells photostimulated with Ti:Sapphire laser. Arrows points to elicited photocurrents, which triggered reliable spiking. Different colors indicate data from different cells.*

Our next step was to test the AAV9.2YF capsid serotype, as this step should provide a larger spread of expression. We first compared the expression of tdTomato following injections in mouse V1 of the same tdTomato containing sequence encapsulated with either the AAV2.7m8 and AAV9.2YF serotype viral capsids. Expression was assessed by analysis of fluorescent images taken on both experimental set ups used for the study (1 – photon 3i set up, and 1-photon imaging, 2-photon stimulation set up (described in the methods section)). Special care was taken to ensure the same illumination conditions for the images obtained from the two set ups. We found that the tdTomato reporter expression with the new serotype AAV9.2YF was spread in a larger tissue volume compared to the AAV2.7m8 serotype (~700µm and ~400µm from beginning to the end of expression area length in anterior-posterior direction measured in L2/3 respectively) and sparser, but still with sufficient expression to easily identify labeled cells in both set ups. Expression of the AAV9.2YF serotype was also faster (after 4 weeks reached maximal brightness), although after 4 weeks we observed fast bleaching of the reporter (after exposure for around 1-minute period of epifluorescent illumination the difference in tissue brightness was visible). Finally, AAV2.7m8 serotype showed increased cell expression after 5 weeks after injection (in comparison to the level of fluorescence measured after 4th week) (Figure 22).

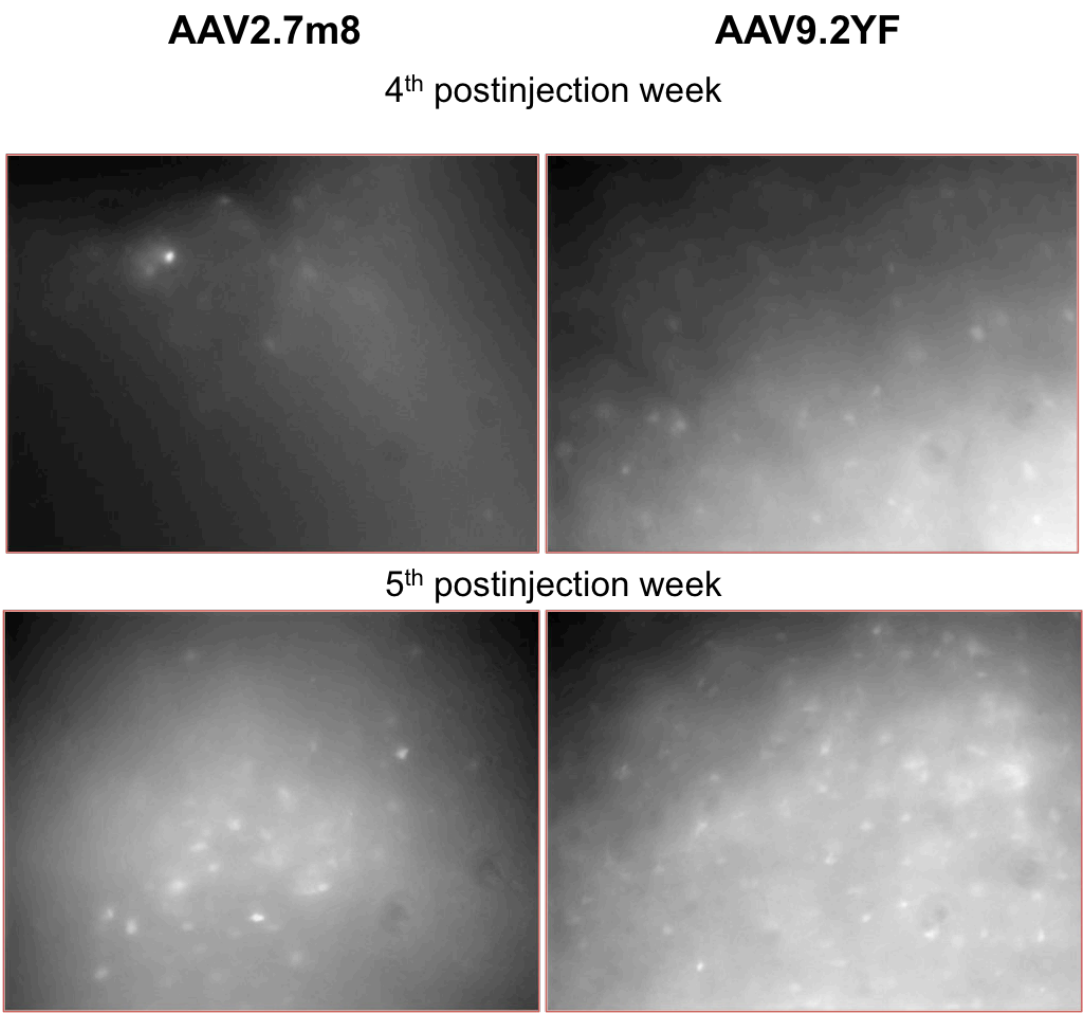


*Figure 22 Comparison of tdTomato expression induced by two serotypes of the virus – AAV2.7m8 (left column) and AAV9.2YF (right column) at 4 (top) or 5 (bottom) weeks after injection. Expression linear spread using the AAV9.2YF serotype was twice as large, as well as expressing with a shorter incubation time. AAV2.7m8 expression was more confined and less sparse. The level of expression increased between 4th and 5th week resulting in higher fluorescence levels measured on the somas, whereas AAV9.2YF fluorescence level did not change noticeably between the 4th and 5th week.*

Taking into account these results, we decided to continue with the AAV9.2YF serotype. 3 groups of animals were injected with the AAV9.2YF –tdTomato sequence mixed with AAV9.2YF – Chronos (either 1,5; 2,25 or 3 µl total injected volume, 1:2 proportion). Animals were injected with three different volumes of the mixed virus taking into account the higher titer of the new viruses. Additionally, the new injection set up was installed in the meantime, which forced the changes in injection speed (thus duration of the injection). In such new conditions injecting of 3 µl were hard to perform and some injections were finished before injecting full volume to prevent the animal death. Tests were started on animals injected with 2,25 and 3 µl of injection mixture, as the level of expression should be the highest in these groups. Surprisingly, a small group of reporter-positive cells showed either no or only small (~20 pA) photocurrents, even when high power density of light was used. Examination after a longer post-injection time (8th week) did not give better results. In

addition, a non-tdTomato expressing cell patched as a control, also responded to photo-stimulation with similarly low current (Figure 23). Thus, the opsin expression level was too low with this serotype to continue. Additionally, the co-expression ratio could also decrease, but the data set is too small to conclude on this point definitely.

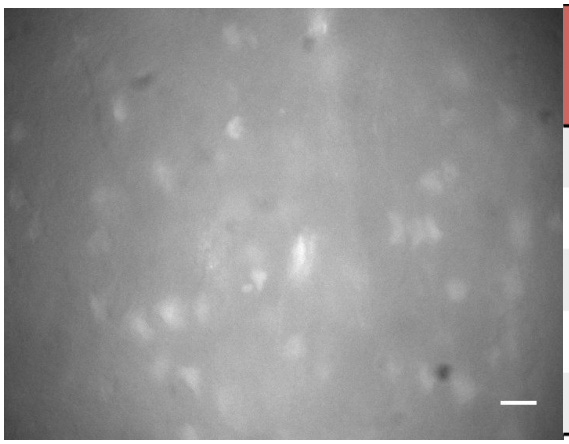

| cell number | group | Maximal photocurrent elicited (pA) | Maximal laser power density used mW/µm² |
|---|---|---|---|
| cell1 | tdTomato-positive | 64,3 | 0,9 |
| cell3 | tdTomato-positive | 27 | 0,62 |
| cell4 | tdTomato-positive | 0 | 0,62 |
| cell5 | tdTomato-positive | 23,7 | 0,62 |
| cell6 | tdTomato-negative | 10 | 0,62 |

*Figure 23 Expression of AAV9.2YF-Chronos virus in the neuronal tissue. Left: tdTomato expression labels the neurons enabling targeting. Scale bar 15 um. Right: Photocurrent elicited by holographic stimulation with maximal power density. tdTomato-positive neurons photocurrents were negligible taking into account the high-power density used and post injection period. Additionally, a tdTomato-negative neuron (cell6) also responded to photostimulation with a small photocurrent of 10pA, which may indicate that population expressing reporter and population expressing opsin are no longer overlapping so highly as before.*

As a third step, we decided to check the performance of the sequences in a more efficient manner using CHO-K1 cell culture, as this preparation was familiar for the laboratory members. CHO (Chinese Hamster Ovary) cells are a line of epithelial cells that is a widely used system for evaluating the mammalian expression of plasmids, in particular with patch clamp electrophysiology to study the biophysical properties of trans-membrane channels. Specifically, the lack of tight junctions between cells, and a low expression of endogenous ion channels, thus a high intrinsic input impedance, allows for good separation of expressed channel currents (Gamper, Stockand, and Shapiro 2005; Vacher and Dufy 1994), which is very important for the investigation of light sensitive channels. The native cells present very little current at typical voltage clamp command potentials, usually within 50 -100pA. The resting membrane potential was measured to be in the -10 - 0 mV range (supported also by my measurements). This preparation allowed us to assess the level of opsin expression by measuring photostimulation elicited currents, as well as to assess if the opsin is well trafficked to the membrane by the presence of fluorescent clusters in the cells. We have tried two constructs that were prepared for us, both of which contained a p2A linker: tdTomato-p2A- CoChR and tdTomato-p2A-Chronos. Cells containing plasmid were detected by observing expressed tdTomato reporter in the cytosol (Figure 24).

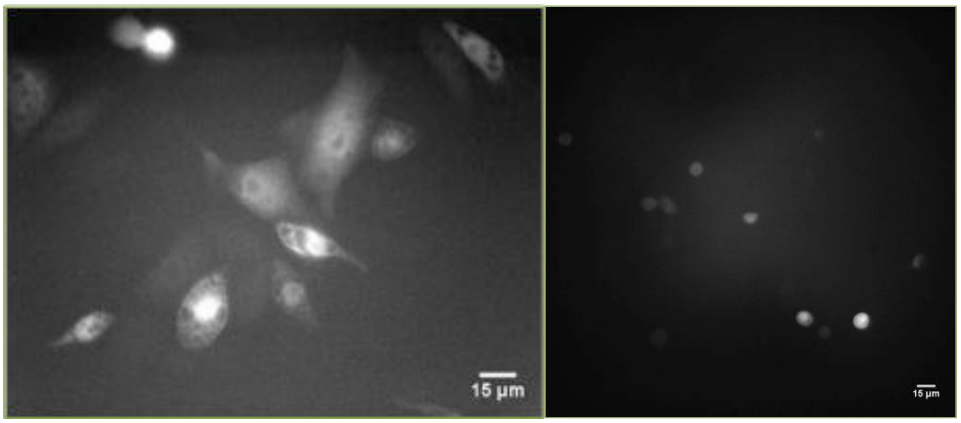


*Figure 24 Wide field fluorescence images of expression of tdTomato –p2A-CoChR(left) and tdTomato-p2A-Chronos(right) plasmid expression in CHO cell culture.*

In my experiments, CoChR expressing CHO cells responded to photostimulation with small currents, especially in comparison to another green version of the CoChR plasmid (CoChR-YFP, Ed Boyden lab) (Figure 25). Some of the data from the two opsins was collected on the same day in order to ensure the same experimental conditions for comparison of tdTomato-p2A-CoChR and CoChR-YFP. Cells expressing the green version of the opsin responded with high photocurrents, whereas the current amplitude from cells expressing the red version were very small, with a maximum about 100pA using high power and an illuminating shape that covered the entire cell.

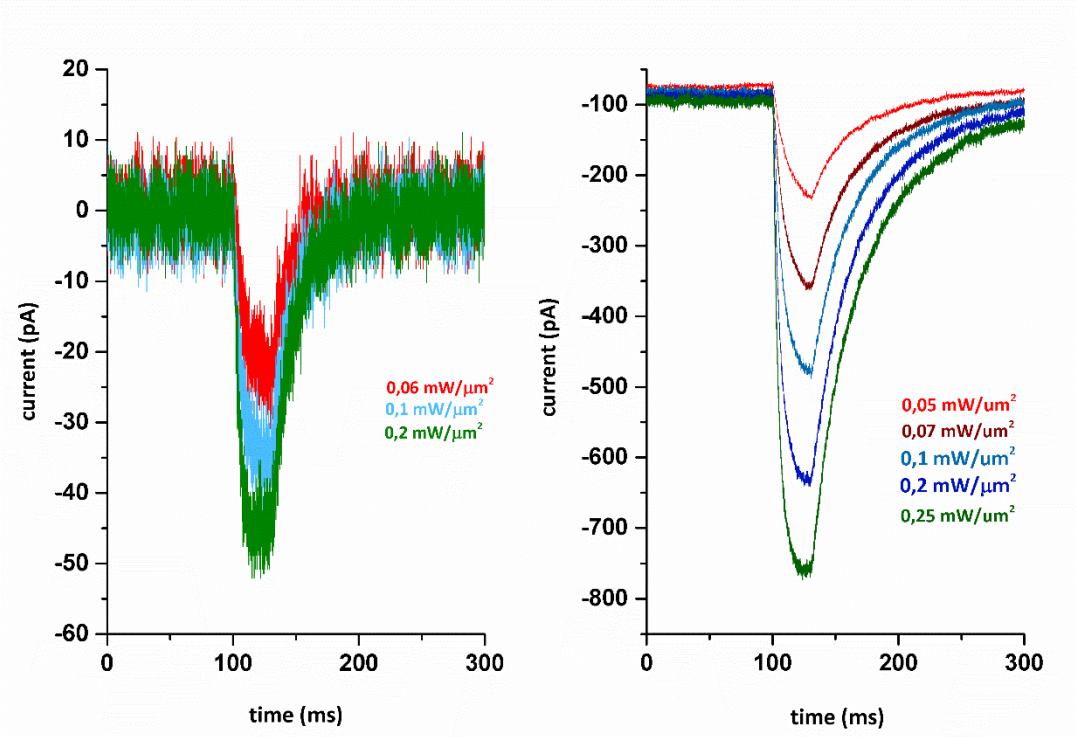


*Figure 25 Comparison of results obtained from CHO cells culture transfected with either tdTomato –p2A-CoChR or CoChR-YFP. Example current traces with different light power densities obtained by holographic stimulation with a 10 µm diameter spot on cells expressing tdTomato –p2A-CoChR (Left) and CoChR-YFP (Right). Note the large difference in photocurrent amplitude between the cells.*

Chronos expressing CHO cells also nicely expressed the tdTomato reporter. The fluorescence level was strong, allowing for fast identification of cells for patching (Figure 24). However, while the tdTomato expression was good, without any visible abnormalities, the elicited photocurrents were negligible and often absent (Figure 26). This could be caused by a low level or total lack of expression of the opsin part of a sequence, or by problems with membrane trafficking.

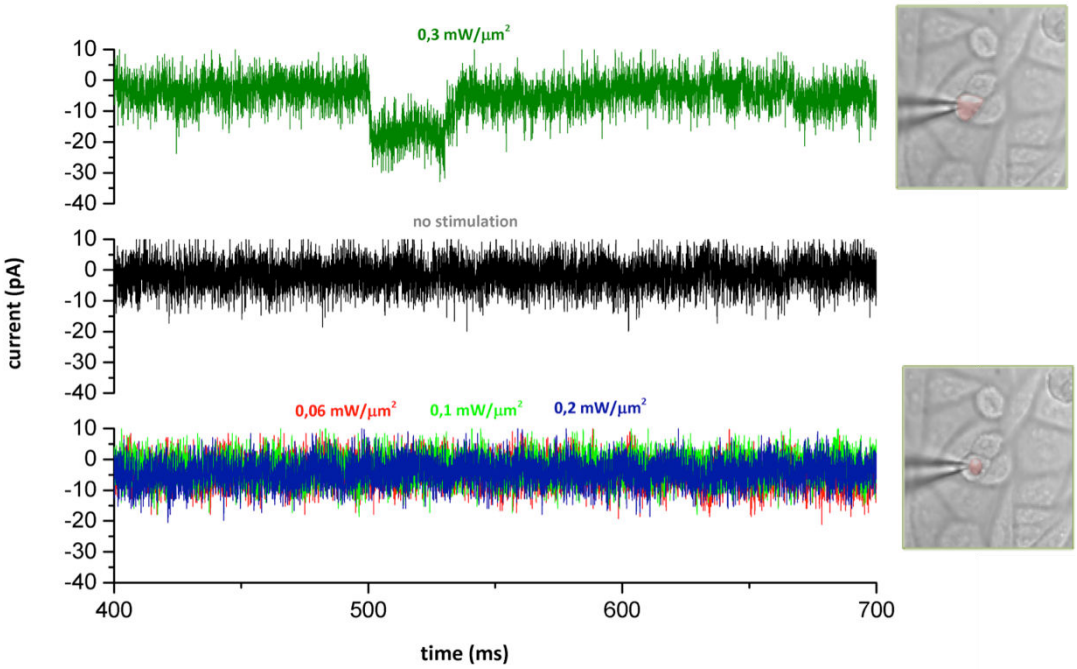


*Figure 26 Summary of results of tdTomato-p2A-Chronos expressing CHO cells. Example traces recorded from CHO cells: Upper – photostimulation shape covering whole cell area, Ti:Sapphire laser. Middle – no photostimulation. Bottom –photostimulation with 10µm diameter spot, amplified pulse laser. Different colors indicate increasing power of stimulation as indicated by the legend.*

### 3.2.4. Discussion on boosting expression

There are various factors influencing the expression level. Some of them could be controlled by changes introduced by experimenter; some require changes in the design of the construct sequence and should be precisely planned before starting the optimization of expression.

The AAV serotype is the first important choice to be made, as different serotypes of AAV present various tropisms, expression levels and spread in the tissue. For gene expression in the mouse brain tissue a few existing serotypes were compared in terms of transfection efficiency and spread (Aschauer, Kreuz, and Rumpel 2013). The emerging consensus from the literature points to AAV1 (in other notations: AAV2/1), AAV8 (AAV2/8) and AAV9 (AAV2/9) as the strongest expressing serotypes in the neocortex of a mouse, characterized by a spread in between all cortical layers. The AAV2

serotype was characterized by a quite low efficacy of expression, and as well as a confined area. In my work I was using viruses provided by collaborators – AAV2.7m8, AAV9.2YF (Co-expressing of multiple viruses), AAV8 (CoChR-mCardinal opsin) and AAV1 (ReaChR opsin). The AAV2.7m8 serotype, is based on the AAV2, but the changes introduced in the capsid structure (addition of 7m8 protein) improves the transduction in the retina and striatum of a factor of 2 (Khabou et al. 2016). Both versions of the AAV2 serotype – the classical one and modified, are characterized by small spread in the tissue. This is in agreement with our results, as both AAV2.7m8-CatCh co-injected with AAV2.7m8-tdTomato, and AAv2.7m8-Chronos co-injected with AAV2.7m8-tdTomato constructs showed confinement expression. I cannot judge the increase in terms of expression level in AAV2.7m8 in visual cortex, as I have not worked with the classical version of this serotype. Nevertheless, the expression level provided by the construct based on AAV2.7m8 serotype was low. AAV2.7m8-CatCh expressing cells were triggering spikes only in 50% of the cases (1-photon holographic stimulation), whereas AAV2.7m8-Chronos elicited low photocurrents in comparison to other Chronos version tested in our lab (AAV8-Chronos-YFP). This was not a satisfying result, but I decided to continue the Chronos test on another set up under both 1 – and 2-photon illumination. This was motivated by the fact that the 1-photon peak on the Chronos absorption spectrum is at 500nm, and that the 1-photon set-up that I used previously was providing only illumination with 405nm, which according to the spectrum elicits only 25% of the photocurrent. After the change of the set up and stimulation of the opsin expressing cells with a closer to the peak wavelength, I obtained spiking under 1-photon illumination in 71% of neurons (at 470-500 nm) and 22% using 2-photon illumination (at 950nm) (Figure 20).

The second serotype I worked with was AAV9-2YF, which is based on the AAV9 serotype, which strongly expresses in the neocortex. The improvement of serotype transduction efficacy was due to the introduction of additional point mutations on two of the seven surface-exposed capsid tyrosine residues (Dalkara et al. 2012). The expression induced by tail vain injections of AAV9 and AAV9-2YF showed that the modified capsid resulted in 4 times larger expression assessed by mRNA extraction from the retina. In the same paper, the cortical level of expression was assessed by image comparison, and as in previous case there was a visible significant increase in expression. The comparison of the serotypes AAV2.7m8 and AAV9-2YF in the V1 of a mouse showed that the latter serotype results in a larger area of expression, and the fluorescence level was visibly higher after 4th week after injection. After the 5th post-injection week the fluorescence level was similar. On the other hand, testing of co-expression of the AAV9-2YF-Chronos and –tdTomato co-injected viruses was terminated quickly, due to the extremely low photocurrent induced by 2-photon holographic stimulation and the observation that expression of tdTomato was sparse and wide, especially in the case of animals examined 8 weeks after injection.

AAV1 and AAV8 serotypes are characterized by a similar level of expression in neurons (Murlidharan, Samulski, and Asokan 2014). Indeed, in the results obtained in our lab, the level of expression of the constructs based on these serotypes was similar. However, the data from the tissue expressing AAV8-CoChR-mCardinal presented variability in terms of cellular level of expression, which was not

observed to the same extent in the expression of other constructs. It is worth mentioning that the injection protocol and set up was changed during the time of this opsin screening, which could possibly influence our results and make the reported comparisons less precise. Specifically, for the red CoChR construct, we injected 1µL of virus, as compared to 1,5 µL for the AAV8-CoChR-GFP (ChR86) and AAV1 Ef1α-ReaChR-p2A- tdTomato. We could possibly obtain better results by higher volume injections, as the injected volume and titer could boost the expression level. This could be explained by an increase in the probability of uptake by the cell due to introducing a higher quantity of viral particles in the intracellular space.

The injected volume and titer is the next important aspect to take into account during the optimization of opsin expression. Indeed, according to the literature, to obtain an expression of AAV mediated gene one needs to inject a volume of virus containing at minimum concentration of $10^{10}$ viral particles/ml, and usually a concentration of $10^{12\text{-}13}$ is advised (Watakabe et al. 2015; Aschauer, Kreuz, and Rumpel 2013; Tye et al. 2011). This is in agreement with our observations. The second trial of AAV2.7m8-Chronos and –tdTomato mixture characterized by lower number of particles/ml than desired, resulted in negligible expression which was not visible in the tissue.

The choice of promoter is another aspect, which should be taken into account because it can drive the expression of the gene specifically to a cell type (Betley and Sternson 2011). A comparative study investigating various AAV serotypes and three widely used promoters, CMV, SynI and CaMKII, provided useful insight in effects of various combinations of the serotype and promoter for the expression in brain tissue of marmoset, mouse and macaque (Watakabe et al. 2015). All the promoters show tropism towards neuronal expression. However, the CMV promoter was expressing in both glial cells and neurons, with low cellular level of expression in neurons. SynI and CaMKII provided expression only for neuronal cell types with predominance of interneurons (SynI) and pyramidal cells (CaMKII). This is in agreement with our results. Data collected on AAV8-hSyn-CoChR-mCardinal show higher expression rate allowing for spike triggering for interneurons (7/9) than in pyramidal cells (2/4). Although this confirms the tendency, the number of patched cells was too low, (especially in the pyramidal cells) to draw firm conclusions. During work on this serotype I was mainly focusing on interneurons, as these data could provide help for other projects in our group. The CMV promoter, which was attached for CatCh (n=26) and Chronos (n=17) opsin constructs tested, showed however unequal proportions between tdTomato expressing patched pyramidal cells (~30% in both variants) and interneurons (~ 70% in both variants). Although tdTomato expression in those cells was clearly visible, it is hard to judge the general level of expression between the subpopulations, because the opsin expression was too low to induce spiking. Additionally, the level of tdTomato expression was not assessed and as it is a very bright fluorescent protein, the cells with various level of expression were visible and targeted for patch recordings.

The fluorescent reporter enables recognition of cells expressing the target protein. In my study I was using constructs comprising tdTomato or mCardinal, which are red fluorescent proteins. The red actuator in tested constructs was desired to enable easy distinction between calcium indicator in the

cell and expressed opsin. Theoretically different fluorescent markers do not influence performance of the protein to which they are attached. However, depending on sequence design, a reporter can impair the expressed protein function and trafficking to the final destination (Jensen 2012; Snapp 2005). This influence could have an indirect character, as it might be caused by different steric interactions in the folded protein in the situation when the fluorescent reporter is bigger than the expressed protein. If we consider size of the opsin (25-30kDa for type I opsin protein form algae) and most common fluorescent reporters (GFP-26.9 kDa, mCherry-28.8 kDa, tdTomato – 54.2 kDa), we see that this could take place in the case of the tdTomato reporter. Another harmful influence of the reporter for expressed protein may be an effect of attaching the reporter directly to the N instead of C terminus, or the usage of linkers, which are too long (therefore there would be not enough space in a plasmid for following protein) or too short (therefore the actuator might provide a physical obstacle for anchored in the membrane opsin channel). However, a detailed knowledge about the structure of the sequence and potential influence of each part is beyond the topic of my thesis. I will then summarize my observations in a descriptive manner.

In agreement with the paper introducing mCardinal reporter (Burg et al. 2014) I have not observed any negative influence of mCardinal or tdTomato reporter on my data in cases when the opsin was effectively working. Additionally, the fact that mCardinal and GFP reporters are characterized by similar size together with lack of reported harmful influence of widely used for protein tagging GFP can support my observations.

The size of tdTomato might, on the other hand, explain negative results obtained during the plasmid testing (multi virus co-expression). Despite equipping the sequence with a p2A linker, which splits the reporter part from the channel before they fold therefore any steric influence of the two components is excluded, the large tdTomato dimer occupies a significant place in the AAV vector limited capacity. To big construct inserted into the plasmid might affect in low expression and problems during plasmid amplification. We examined plasmid sequences containing first the tdTomato sequence with the opsin as a second gene after p2A linker. Test of these plasmids showed a good expression of tdTomato but presented very small photocurrent. Additionally, the plasmid concentration was smaller than the plasmids obtained from different sources, which could explain some problems with the production efficacy of consecutive construct portions. As additional support of this hypothesis is delivered by the good results provided by the ReaChR opsin. This construct was first containing the opsin and after p2A linker tdTomato was working efficiently. On the other hand, both CoChR and Chronos sequences delivered by other collaborator were fused to the fluorescent tag. These plasmids expressed in CHO cells provided high photocurrents. From an informal communication, we have learned that this opsin could be targeted to the membrane more efficiently when fused directly with reporter than without one, which would also explain our results, as well as the poor photocurrent obtained by AAV2.7m8/AAV9-2YF –Chronos virus co-injected with -tdTomato virus.

Application of p2A or IRES cleavage sequences between the fluorescent reporter and an opsin could improve cell recognition during experiments. These sequences are recognized by ribosomes during translation, enabling editing of the same RNA chain from two starting points and thus splitting the two (Goedhart et al. 2011; Kim et al. 2011). They are commonly used to express more than one gene under the same promoter. The useful difference between the p2A and IRES sequences is the ratio of expressed gene before and after the sequence. P2A sequence efficiency is close to 90% and both genes are expressed at very close to equal level. It is also small (18-22 aa = 60 nucleotides) in comparison to IRES (~500 nucleotides), which helps save limited space in the AAV capacity. In comparison, IRES provides non-equal expression in favor of the upstream gene. Potentially this could be useful for designing a construct containing opsin- IRES-GCaMP6s, as GCaMP6s expression would be around three times smaller than the opsin and still provide a fluorescent tag. In such scenario higher opsin expression would allow to use lower laser powers for optogenetic stimulation. Alternatively, a flipped construct combining GCaMP6s-IRES-opsin, could possibly provide higher expression of GCaMP6s allowing for application of lower imaging laser powers and at the same time lower opsin expression could enable less opsin activation during imaging. The AAV capacity could be however a problem in both scenarios and other DNA vectors would need to be taken into account.

The main goal of multi virus co-expression project was obtaining co-expression of both GCaMP6s and opsin. We first tried to induce expression of 'naked' opsin together with tdTomato marker (by co-injection of two viruses sharing the same AAV serotype and promoter). A similar test of the expression of two fluorescent reporters under the same CMV promoter was presented in (Goedhart et al. 2011) on HELA cells transfected with strong transfecting reagent (Lipofectamine). They obtained a 0.6 correlation coefficient but various level of expression for both expressed reporters. In comparison, insertion of the IRES or p2A linker (correlation coefficient 0.8 and 0.9, respectively) resulted in a much smaller variability in the expression level obtained in different cells. Usage of such linkers would provide higher stability of our preparation and increased control of expression level. We obtained 80-90% co-expression level. This could be explained by a small spread of the AAV2.7m8 serotype, which undoubtedly influenced the probability of virion uptake by cells. As the serotype of virus and promoter was the same for the tdTomato and opsin sequence, we could assume that by random uptake cells will contain a mixture of sequences close in proportion to the injected value (2 parts of opsin to 1 part of tdTomato). This hypothesis could be supported by the data obtained from the test of AAV9- 2YF, whose bigger spread seems to influence the emerging co-expression ratio between tdTomato and opsin.

## 3.3. Characterization of opsin kinetics in CHO cells: towards the modeling of photocurrents

In this section I describe performed two photon holographic excitation and patch clamp recording on CHO cells expressing different opsin to investigate their kinetics parameters. These data have been recently published in a book (Two-photon optogenetics by computer-generated holography. In: Stroh A (ed) Optogenetics: a roadmap. Springer, New York.) and, integrated with the theoretical work of another PhD student of lab, are currently the basis in the ongoing implementation of a model capable of simulating 2P-induced currents under different illumination conditions.

Motivations:

The broad repertoire of opsins enables us to take advantage of their different properties and combine them with the best light delivery technique.
Nevertheless, as I discussed in the previous sections of this thesis the low cross section of opsins and small volume of excitation under confined 2-photon illumination, requires careful optimization to achieve photoinduced spiking in a reliable way and with high temporal precision. Optimization that needs to take into account several aspects, from opsin properties and expression level to the proper light delivery technique.

In this context, it's particularly important to understand the biophysics underlying elicited photocurrent dynamics and a fine characterization of the kinetics of the photoinduced current observed for different opsins.
In the literature, the main focus has been dedicated to characterization and modulization of ChR2 induced currents (Schneider, Grimm, and Hegemann 2015; Schneider, Gradmann, and Hegemann 2013) and, expect few cases (Rickgauer, Deisseroth, and Tank 2014) mainly under 1- photon condition.

A fine characterization, and eventually, the capability to model and simulate photoinduced curves from multiple opsins under 2-photon excitation is still missing and will be particularly useful to interpret and design optogenetic experiments.

For instance, as described in section 3.1.1, 2P excitation is typically performed either under holographic or spiral scanning excitation. The knowledge and prediction of the response of different opsin could allow to optimally choose the most convenient technique and the respective illumination parameters.

In the following section I briefly present my contribution in the characterization of the kinetic of 3 different opsins, (ReachR, CoChR, Chronos) and I show how these data, analyzed and coupled with

the theoretical work of another PhD student in the group, allowed the calibration of simplified model to simulate photocurrents.

Experimental strategy:

The investigation of photocurrents' kinetics has been performed with electrophysiological recording on opsin transfected CHO- K1 cellular culture. This preparation, lacking endogenous channels, limit influence of other intrinsic conductances during recordings.
Performance of three opsins - ReaChR(n=13), CoChR (n=22) and Chronos (n=20) was examined in this study. The opsins were chosen based on their kinetic parameters, to represent slow, intermediate and fast channel respectively.

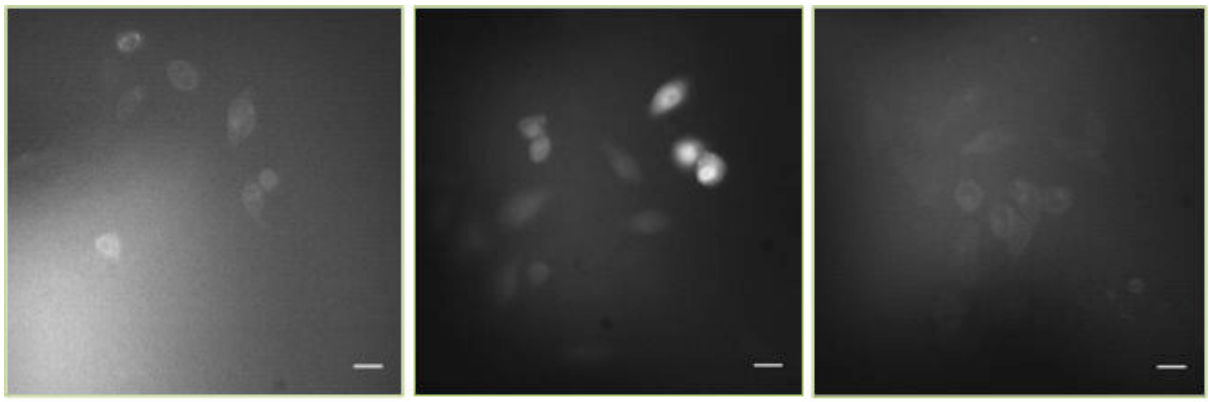


*Figure 27 Expression of three different opsins in cellular culture. Scale bar indicates 15 µm, each photo size: 200x200 µm. A clear difference between the constructs is seen. ReaChR opsin contains a p2A linker and the reporter is filling the cytosol of the cells. Chronos and CoChR do not contain p2A linker – the opsin expressed in membrane is visible as the fluorescent shape of the cell.*

Under epifluorescent illumination the opsin expressing cells were identified and patched (Figure 27). During recording the access resistance was checked frequently, often between each stimulation. Only cells patched with no leak current and in which the change of access resistance was lower than 20% were taken into account (Figure 28). The same conditions were maintained for recordings from different opsins as well as between each recorded cell. We also screened our data set to identify the cells providing similar current amplitudes in response to the same laser power density stimulation between sets of photo-stimulations, to make sure that we incorporated a similar number of channels. Additionally, an interval of at least 1-2 minute between stimulations was kept allowing for full opsin recovery from desensitized state.

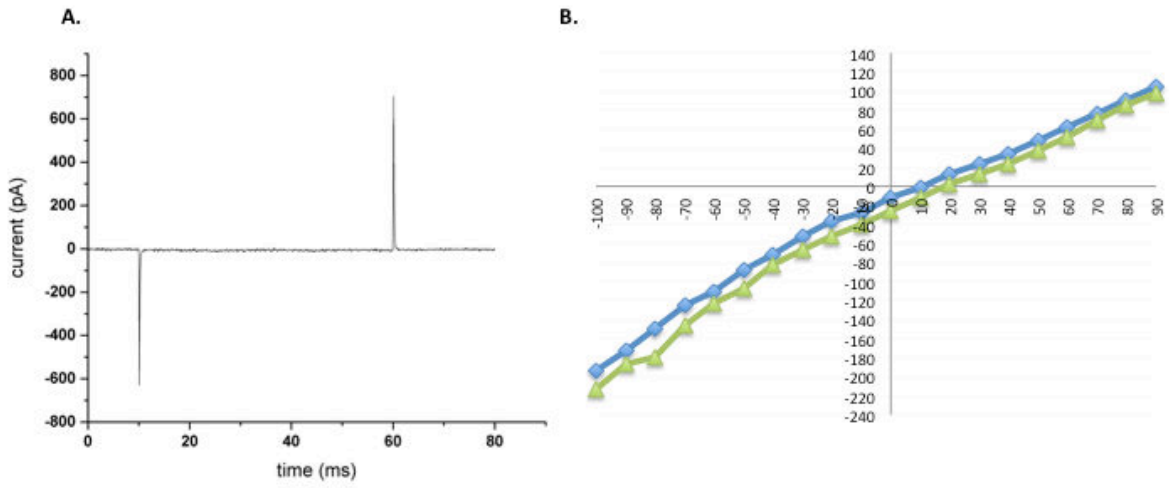


*Figure 28 Native CHO cells electrophysiological parameters. Exemplary trace of patched cell in whole cell configuration under 10 mV potential steps application (averaged over 100 repetitions) (A). Large transient current and fast tau value is characteristic for CHO cells. I-V curves of two CHO cells (B) obtained by applying different potential values. Resting membrane potential is equal – 12mV and -26mV for cell 1(blue) and 2 (green) respectively. The average access resistance and membrane capacitance values for native cells are: 12, 43±3,11 MΩ and 16,91±5 pF.*

The photostimulation protocol used consisted on performing long stimulation (typically from 1 to 4 s) under various excitation power. The use of long illumination time allowed to explore the complete dynamic of the photocurrent. As observed in the exemplary traces in Figure 29, during photostimulation we can identify 3 different regimes. An initial rise of the current, a first decrease until the reach of an intermediate steady state, and a final decrease toward zero current value due to the closing of the channels after the photostimulation. A monoexponential fit of the current in these three regimes will allows us to characterize and quantify the differences in the kinetics among different opsins. Such time constant will be defined as respectively, $\tau_{on}$, $\tau_{inact}$, and $\tau_{off}$.

Additionally, we also applied some stimulation protocols consisting on train of short (<100 ms) illumination pulses at different frequencies to better investigate the effect of both slow off kinetics and channel inactivation.

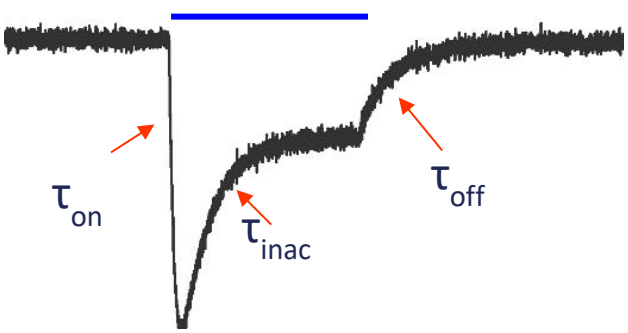


*Figure 29 Example of the shape of a typical photocurrent induced by a long (2s) photostimulation light pulse. Transients between different regimes can be identified by characteristic times: $\tau_{on}$ for the rising time of the current, $\tau_{inac}$, for the decay from peak to the intermediate steady state, τoff for the final decay of the current.*

Results and general remark

Photocurrents for multiple cells were recorded, corresponding to various illumination intensity. This allowed at first to extract the dependence of the peak current as a function of power and identify the saturation power density for the 3 different opsins, obtaining:
0,28 mW/µm$^2$ for ReachR, 0,54 for mW/µm$^2$ for CochR and 0,86 mW/µm$^2$ for Chronos.

Saturation powers allowed to define an absolute power scale between the 3 opsins and then compare their kinetics accordingly.
Consequently, the criterium we followed was to analyze and compare currents kinetics of different opsin when excited at its own saturation power density.

Example of photocurrents corresponding excitation at or close to saturation power density are reported in Figure 30.

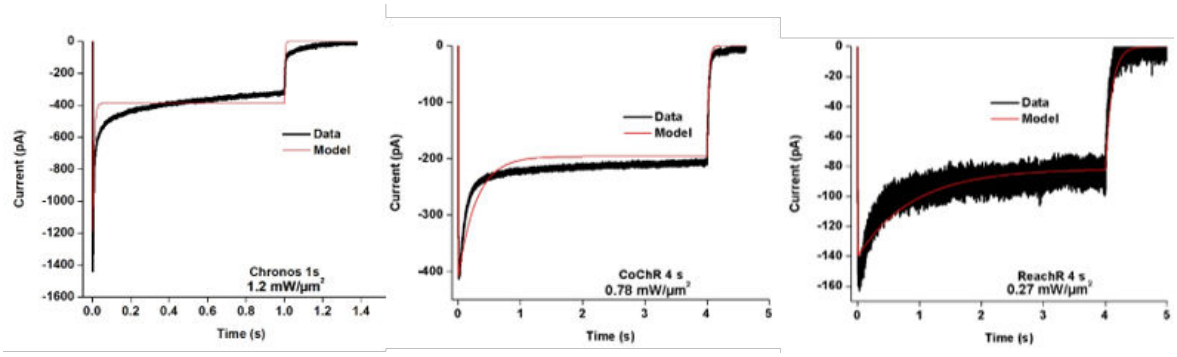


*Figure 30 Example of photocurrents recorded under holographic photostimulation at a power density corresponding (or close to) the saturation one. (Excitation performed at 950 m with a Ti:Sapphire laser, rep. rate 80 MHz, pulse width 1000 fs). The red curves are simulated curves based on a three states model (described in the next section).*

As described before, exponential fit of the different region of such curves allows me to define some key parameters that characterize the kinetics of the opsin. The obtained results are reported in the Table 2.

*Table 2 Kinetics parameters measured for Chronos, CoChR and ReaChR opsins.*

**Kinetics parameters for different opsins**

| | Chronos | CoChR | ReaChR |
|---|---|---|---|
| $\tau_{on}$ (ms) | 0.73 | 2.4 | 8 |
| $\tau_{inact}$ (ms) | 9.3 | 200 | 443 |
| $\tau_{off}$ (ms) | 4.2 | 31 | 94 |

These parameters put in evidence very clearly the differences between the different opsins and confirmed previous 1-photon based investigation underlining, for instance the fast responses of Chronos and the slow kinetics of the ReachR. More generally, these kinetic parameters can provide some practical boundaries on the spiking pattern possible to obtain with a given opsin. For instance, the $\tau_{on}$ parameter, characteristic time for the opening of the channels, will influence the light pulse duration necessary to evoke an action potential. On the contrary, the $\tau_{off}$ characteristic time for closing of the channels, will determine the minimal delay between two different light stimulation and therefore will influence the maximal frequency of photoinduced spiking.

But in order to better understand the meaning of these parameters, the behavior of the channels and to achieve the possibility to model and predict photoinduced current, the data were used to develop and validate a simplified model of the channel dynamic, parallelly implemented during the PhD of Alexis Picot, another student of our laboratory.

Modeling of photocurrent dynamics:

The results described in this section comes from the work of A.Picot. Therefore, I am only briefly describing the results to which I have collected the data.

Based on electrophysiological recordings a population model was built to investigate the dynamics of the photocurrent in time.
The model predicts the current according to the well-known (Koch 1999) equation:

$$I = g(Vm - Erev)$$

Where, the reversal potential, $E_{rev}$ for majority of opsins is around 0. Prediction of the current evoked is however more complicated than it would be seen from this equation as the conductance of the channel depends on several interacting nonlinearly parameters like e.g. stimulation wavelength and conditions like temperature or pH (Evans et al. 2016). The conductance we measured comes from population of channels expressed and activated during photo-stimulation and thus varies from cell to cell. At the same time, our recordings were performed with stable temp, pH, wavelength and power conditions. Therefore, the final equation used in our model is defined:

$$I(t) = g'f(\varphi, t)Vm$$

where g' constitute not the conductance of the channel *sensu stricto* but the conductance evoked by the activated channels population in a given conditions and $\varphi$ describes the stimulation power in mW. $V_m$ parameter was kept constant during Voltage clamp experiments at -40 mV. Therefore, the evoked current depends on $\varphi$ and time and the function *f* essentially represent the total number of activated channels during time.

In literature, few models have been developed to reproduce the precise photocycle of opsins, in which the molecules evolve across different conformation, some of them representing conducting states. Although the more accepted models are based on photocycle made of 4 or 6 possible states (Nikolic, Degenaar, and Toumazou 2006), here, for the sake of simplicity and practicality, we will consider a simplified 3 state model: two non -conducting state, the ground closed state (C) and the Desensitized on (D), on open conducting state (O). Only the channels in the open state contribute to current. The possible transition between states are represented in **Błąd! Nie można odnaleźć źródła odwołania.**. Importantly the transition from closed to open state is driven by light absorption.

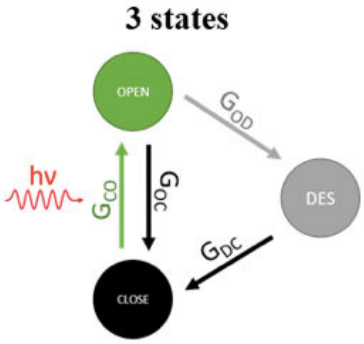


*Figure 31 Schema of 3 state model under investigation (description in the text)*

A set of differential equations describes the interactions between the population of channels in a given state in time:

$$\dot{C} = G_{CO}O + G_{DCD} - G_{CO(\varphi)}C$$
$$\dot{O} = G_{CO(\varphi)}C + G_{OC}O - G_{OD}O$$
$$\dot{D} = G_{OD}O + G_{DC}D$$
$$O + C + D = 1$$

Transitions between the states are described by transition probabilities ('G' coefficients in the equation). To find these probabilities we applied a fitting procedure of the experimental photocurrents. The experimental data were filtered and properly normalized, and then, iteratively, various transition rates values were explored, and the model data output was compared with experimental data to minimize the difference and variation between experimental set and the model output.

*Table 3 Table showing the transition parameters obtained for the 3 opsins based on the 3-state model. The "Short" column gives the parameters that are better suited for millisecond illuminations, the "Long" column for seconds-long illuminations. (courtesy of Alexis Picot).*

| | Chronos | | CoChR | | ReachR | |
|---|---|---|---|---|---|---|
| | Set of transition parameters [$s^{-1}$] | | | | | |
| | Short | Long | Short | Long | Short | Long |
| $G_{CO}$ | 0.08 | 0.08 | 0.08 | 0.03 | 0.02 | 0.01 |
| $G_{OC}$ | 215 | 170 | 35 | 35 | 12.5 | 9 |
| $G_{OD}$ | 90 | 90 | 1.85 | 3.5 | 0.7 | 1.2 |
| $G_{DC}$ | 20 | 30 | 2 | 3.7 | 0.24 | 1.5 |

An example of result of simulated curve by the model are reported as red curves in the Figure 32.

Besides some discrepancies, the model works quite well for capturing the main behavior of the photocurrent curves. The set of transition probabilities obtained from fitting of several set of experimental data are reported, for completeness, Table 3. Importantly, all these transitions are considered light independent, except for $G_{CO}$ transition from close to opens state, that is power dependent. Reported value corresponds to a stimulation at saturation power density. Notably, the model is not dependent on opsin expression level as that factor only influences the amplitude of the elicited current but not its dynamics.

This set of parameters can therefore be applied to reproduce different excitation condition. For instance, we tested its capability to reproduce currents induced by train of excitation pulses. As visible in Figure 32, the model was capable to reproduce the main features of the photocurrent traces for both CoChR and ReachR opsin, stimulated at different frequencies.
Interestingly, the model was capable to reproduce the decrease in the peak current along the train stimulation of CochR, due to the transition of some of the channels from open to desensitized state (panel a). On the contrary, in the case of ReachR, with a long $\tau_{off}$, the summation of sequential excitation results in an increase of the peak current along the train.

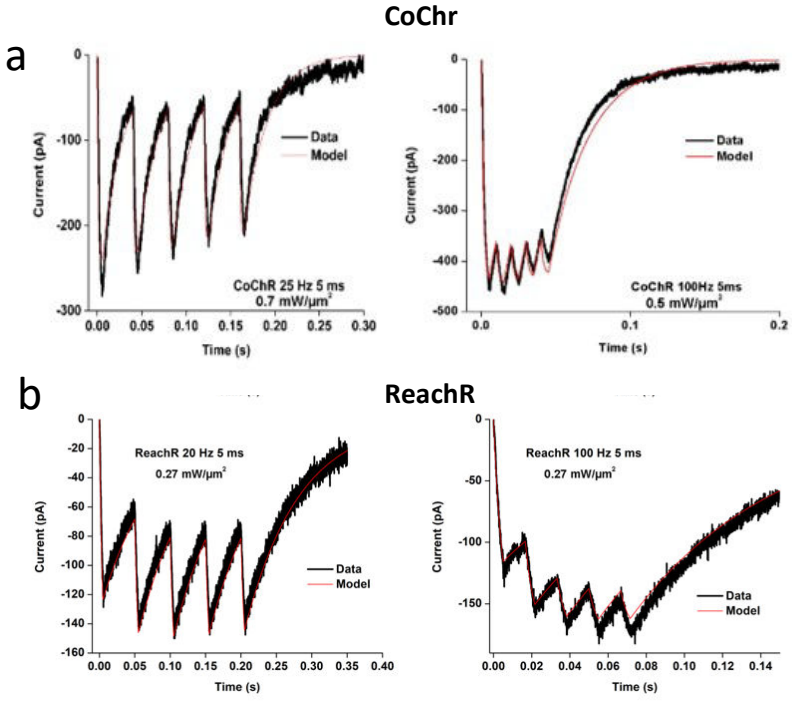


*Figure 32 Photocurrents elicited by train of light pulses (5 ms) of holographic illumination: a) Photocurrents induced on CHO cell expressing CoChR by 5 pulses at 25 Hz (left ) and 100 Hz (right).b) Photocurrents induced on CHO cell expressing ReaChR by 5 pulses at 20 Hz (left ) and 100 Hz (right). Red curves represent the result of the simulation. They have been provided by Alexis Picot*

In conclusion, in this subproject of my PhD thesis I have characterized the opsin kinetics of multiple optogenetic actuator under 2-photon excitation. The resulting data has been used to validate photocurrent model that could enable us to predict current dynamics for multiple actuators. This tool will be further developed and will become a tool for efficient design and interpretation of optogenetic experiments.

For instance, the model can and is currently used in the group to investigate and compare holographic illumination and spiral scanning performances. Modeling of the two protocols can allow to properly choose the opsin to use in each condition, to optimize the illumination parameters, and better adapt them to the specific experimental needs.

## 3.4. Discussion

Two photon patterned illumination, as already discussed, is a powerful approach to efficiently confine illumination on specific targets of interest, for instance around the cell body of a neuron deep inside a scattering tissue (Papagiakoumou et al. 2010, Papagiakoumou et al. 2013).
Nevertheless, it remains important to assure that the confinement of illumination is enough to guarantee true single cell resolved photoactivation.

Negative results importance

Negative results are equally important for scientific discoveries as the positive ones. They enable strategy verification and are integral part of each project. Reporting negative results has its own value for scientific community, especially in fast developing fields and techniques development. It is also a part of each person education. For these reasons I have decided to include in this thesis some of the work which did not resulted in expected effect, even if quite often the final conclusion about what exactly did not worked is missing. All these results contributed to verification of the team strategy.

The validation of a 2-photon all-optical method was the goal of our team, as well as the first milestone of my PhD project. The efforts of all the team with contribution of my work resulted in drawing the challenges to overcome in a more precise way and was driving the work not only of our group but also entire community.

### 3.4.1 Reaching threshold for spiking

A high level of opsin expression is crucial for 2-photon investigations. In comparison to 1- photon wide field stimulation, in 2-photon conditions the effective membrane area targeted by light is smaller. This results in a substantial difference of the obtained photocurrent in both conditions (even up to 5 times lower amplitude under 2P stimulation according to our team observations). Two-photon holography enables to obtain more precise recordings at the level of single cell or cell compartment. On the other hand, the small conductivity of optical channels motivated the interest in opsin variants which provide a high photocurrent in response for 2-photon holographic stimulation (CoChR, ReaChR) or whose kinetics is fast (Chronos), ensuring reliable spiking. ReaChR opsin was designed to improve membrane trafficking and expression (see section 1.4.1 “Introduction of ReaChR”), which resulted in an average current of 740±210 pA (at saturation power) under 2-photon holographic stimulation. CoChR opsin naturally was eliciting high photocurrents up to 3,5 nA in 1-photon conditions. High photocurrents (500-600 pA) were also observed in some of CoChR-mCardinal and in CoChR-GFP expressing cells. In the case of both variants, these large elicited photocurrents allow for triggering trains of action potentials, even at frequencies at which the interval between stimulation is shorter than the closing time of the channel. The CoChR-mCardinal screening experiments provided additional data on train inducibility at high frequencies, stressing the importance of the high level of opsin expression (Figure 13 vs. Figure 14). It was usually possible

to trigger a single spike if the cell photocurrent amplitude was around 200pA. Even higher photocurrent was needed to elicit reliably trains of action potentials. The influence of closing time kinetics on photocurrent during stimulation with train of light pulses is shown in Figure 33, presenting the CoChR photocurrent elicited in CHO cellular culture during light pulse stimulation.

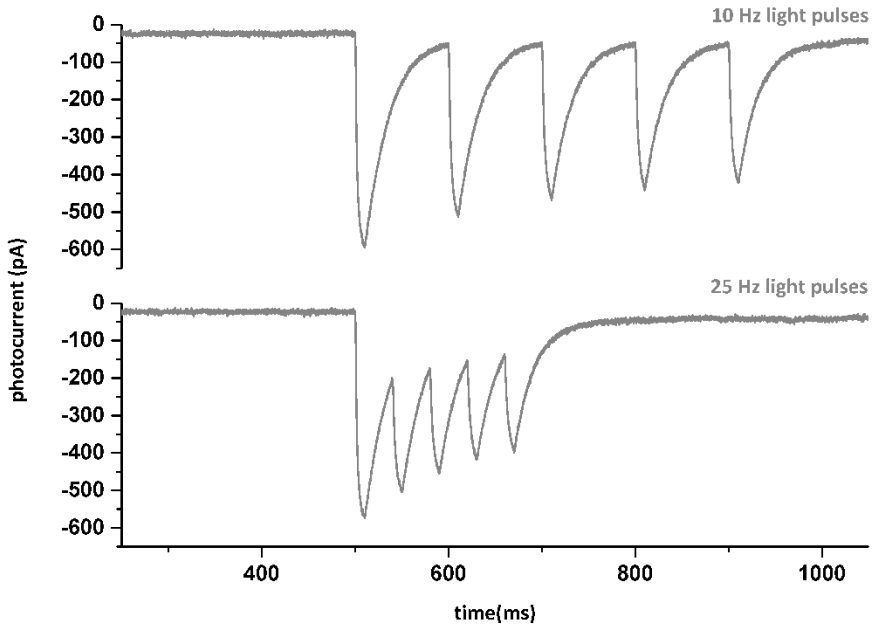


*Figure 33 Influence of $\tau_{off}$ kinetics during stimulation with light pulses. First peaks in the train are characterized by higher amplitude. The amplitude of each next peak is influenced by both open states of the optical channel and is striving to the steady-state phase.*

Chronos expressing cells were eliciting on average 415±213pA in interneurons and 368±172pA in pyramidal cells, which is sufficient to trigger a single spike (Ronzitti et al. 2017). Additionally, the extremely fast kinetics of this variant allows for reliable train photostimulation.

Modeling studies constitute a great help to the experimenter in understanding the opsin performance, influenced by opsin kinetics combined with the level of expression. By participation in the modeling study in our group based on CHO cells recordings I have gained experience and understanding of various aspects of opsin properties. Such a tool substantially shorter the initial experimental part dedicated to find opsin properties and the possible limitations.

### 3.4.2. Dealing with artifacts – limitations of the technique and possible improvements

The second axis of my work was focused around artifacts associated with unwanted opsin activation. These artifacts could be observed in two contexts: 1) due to opsin activation outside the soma, 2) due to opsin activation during imaging. Both artifacts undermine our effort to obtain an all-optical approach for investigation of connectivity.

The first type of artifact is visible when a holographic pattern is moved outside the soma onto the neuronal processes of recorded cell. The results I presented on Figure 18, together with recent investigation performed in our group (Shemesh et al. 2017) put in evidence some limitations arising from the fact that the opsin is typically not only expressed on cell body but also on dendrites. Therefore, by focusing light of a neuronal cell body, one could accidentally induce artefactual illumination of neuropils of a neighboring cell, inducing undesired activity on that cell.

The magnitude of the artifact varies between opsin variants and can result even in the induction of an action potential. The CoChR-GFP construct that examined in the lab elicits action potentials with ~30% probability when stimulated with a grid of spots targeting other cells in the proximity (Shemesh et al. 2017). Test I performed on ReaChR expressing cells was different as the photostimulation pattern was moved along the processes only. Analysis of the ReaChR elicited artifacts showed that artifact amplitude is not dependent on the distance to the soma. Additionally, this stimulation *in vitro* never resulted in triggering an action potential when the power was at the threshold or slightly above. The amplitudes of artifact were varied between 0,5-11 mV, with most frequently 3-4 mV amplitude (Fig. 34). Taking into account the input resistance of a neuron (100-200 MΩ), the obtained photocurrent artifact would be in the range of 20-50 pA given a 4 mV artifact under current clamp.

However, the two tests of the CoChR-GFP and ReaChR-dTomato opsin variants described above differ in the power applied during the photostimulation of processes/ neighboring cells as well as the laser source used. This might be the reason for the big differences in the spiking statistics. In the test of CoChR-GFP a smaller spot was used (thus, higher power density) to examine the artifact elicited on the processes and at the soma, whereas the shape and size of the holographic pattern was preserved during the testing of ReaChR. Some single example of recordings in which a slightly higher power density than the power at the spiking threshold was applied did not change the 0% incidence of spike triggering outside the soma (data not presented). Both tests were done with the presence of synaptic blockers, which allow us to claim that the artifact comes from opsin activation expressed in the processes of recorded cell as opposed to synaptic events. Even if this artifact did not trigger a spike, it remains an obstacle for a clean connectivity experiment, as the arborization of cell is quite dense in the cell's proximity. It is easy to imagine a scenario when a pre-synaptic candidate targeted by light stimulation provides a false-positive response because of unintentional photostimulation of a process of the postsynaptic, recorded cell passing through the area of stimulation. Additionally, analogic ReaChR tests *in vivo* shown that action potentials are occasionally induced while stimulating processes (E. Papagiakoumou et al. 2018).

Indeed, the initial connectivity experiments with ReaChR gave hard to interpret results. To exclude the situation where the response contains an artifact, I attempted to patch an opsin-negative cell while photo-stimulating neighboring opsin-positive cells (Fig. 34). A few experimental days provided interesting results, though they are difficult to explain. The majority of theoretically negative cells responded to soma stimulation with a depolarization or even a triggered spike when the usual power

at the threshold was applied. One possible explanation could be that even if the p2A linker ensures an equimolar expression of the actuator and reporter, in the case of an extremely low expression level, in some cells it was sufficient to obtain opsin activation, causing the observed artifact. However, the numbers of cells patched (n=10) minimize the probability of a mistake influencing the collected data it would be interesting to investigate this topic further, using routine 2-photon scanning for cell targeting, as it provides a much better resolution and signal-to-noise ratio compared to LED illumination, which was used in majority of the recordings that I made. It would also be interesting to define the meaning of opsin negative expression, since the results put in question the assumption of judging opsin expression level based only on reporter fluorescence.

Indeed, the two examples described above point to the unreported in the literature perspective and stress the need of careful characterization of opsin in the context of a particular technique.

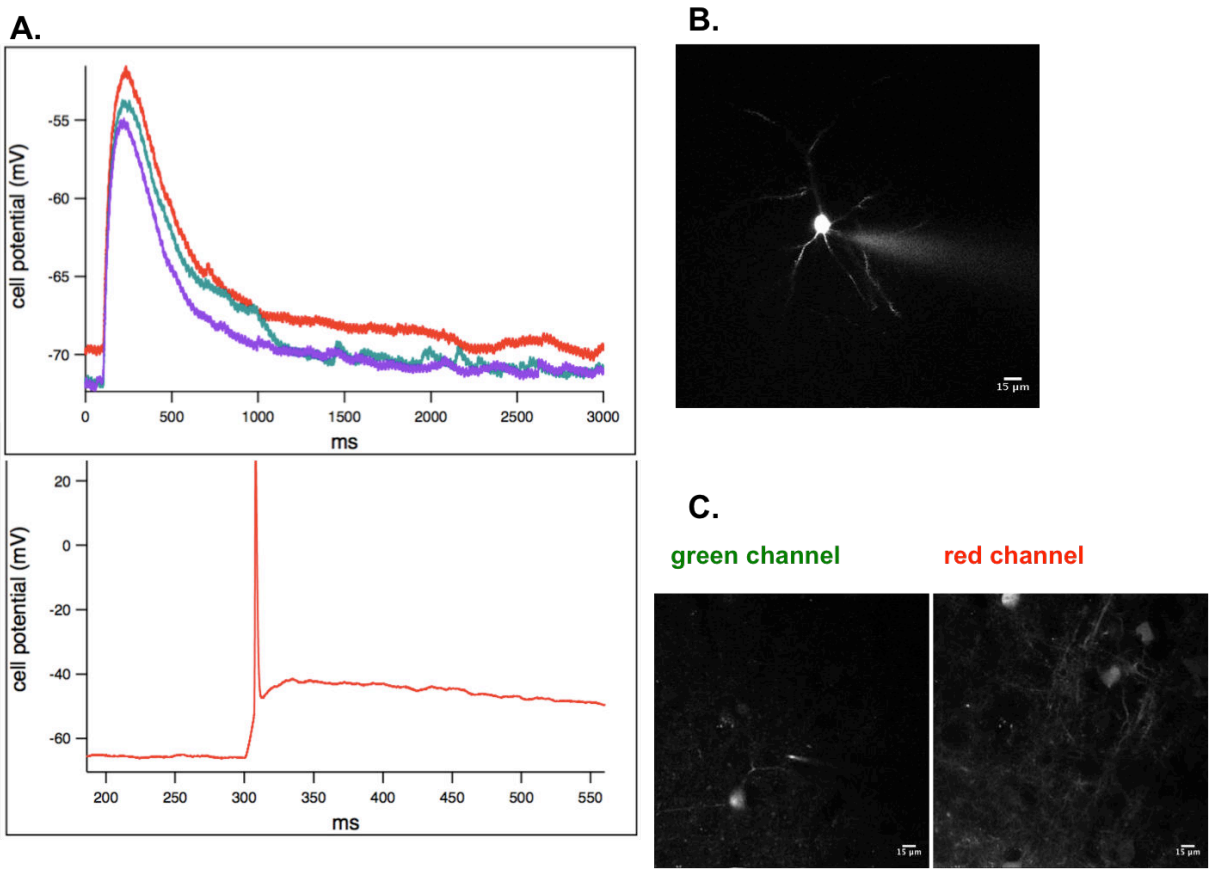


*Figure 34 Connectivity experiment demonstration. Two examples of photocurrent elicited by photostimulation on patched opsin - negative cell(top) and associated with it potential change (bottom) (A). Note the long kinetics of voltage deflections in each trace presented (coming from the same cell), which would suggest ReaChR opsin activation. Variation in the level of expression of the opsin in between cells is a serious obstacle in performing clean connectivity experiment. Negative-opsin cell perfused with Alexa 488 (B). Exemplary photos over the same field of view taken with green (Alexa 488) and red channel (tdTomato) showing lack of the red fluorescence sign in the area of patched cell (shown by pipette in the green channel photo) (C).*

Returning to the question of an artifact originating from opsin activation present in the cell processes, there are two possible ways to minimize it. The first would be to adjust the holographic shape to find modified one that would minimize the artifact elicited outside the soma, but still provided sufficient activation of the opsin in the pre-synaptic candidate that would allow spike triggering. Second, the opsin constructs restricted to the soma expression could improve our efforts in validating a clean connectivity experiment. Indeed, application of soma restricted opsin might provide more effective solution.

During the first part of my PhD I took part in the characterization of a version of soma targeted CoChR opsin based on the protein sequence NAV1.2 targeting sodium channels. I observed a significant improvement in the localization of the channels in the soma, with respect to the conventional CoChR. Nevertheless, provided photocurrent was too low to reliably induce spiking. Additionally, previous studies suggested that this sequence could induce alteration of neurons excitability (Grubb and Burrone 2010). This construct was then abandoned but based on this first characterization and by using the same experimental protocols I applied, the project continued, and new constructs have been investigated. In 2017 our group published a somatic version of CoChR, called also soCochR (Shemesh et al. 2017).

In the literature there are additional reported cases of soma-targeted opsin variants. Authors of one such study used a Kv2.1 potassium channel construct to guide the expression of ChR2 to the membrane, thus narrowing the expression to the soma and proximal dendrites (Baker et al. 2016). Usage of the ChR2 soma restricted construct lead to efficient photostimulation and reliable spiking of the targeted cell, although the results were collected at very high powers, which makes direct comparison more difficult. It should be noted that the results of Baker et al. show a large decrease of elicited photocurrent as the photostimulation area moved along the processes (~90% within a proximity of ~50 µm), taking into consideration the average photocurrent elicited at spiking threshold of a cell (222,7 ± 27,21 pA) this would lead to an artifact of about 22 pA (Fig. 35). Thus, this is a similar photocurrent magnitude with that elicited in our study with ReaChR photostimulation outside the soma.

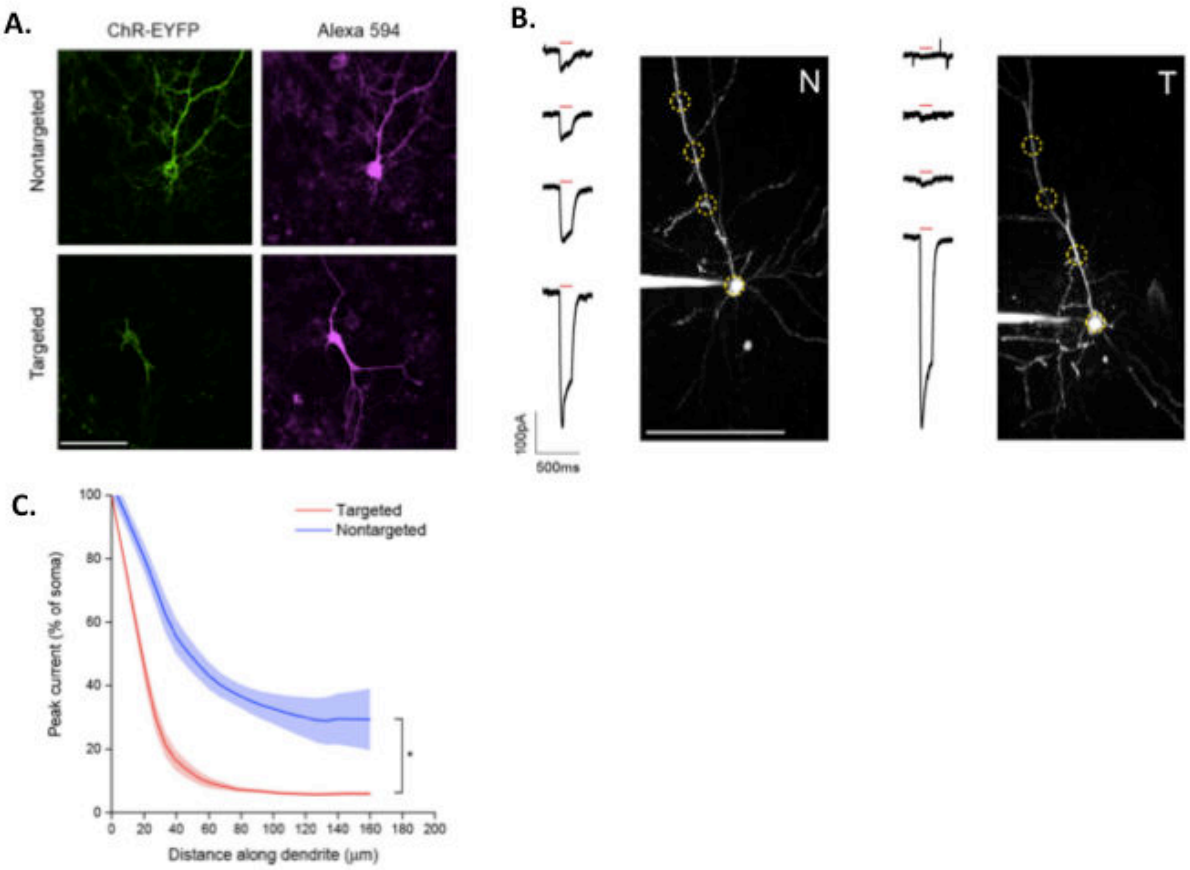


*Figure 35 . Soma targeted ChR2 performance. Fluorescence photos of ChR2-EYFP (green) and filled with Alexa 594 dye (magenta) cortical neurons (A). Scale bar – 100 µm. Representative recordings from two pyramidal neurons expressing non-targeted classical (left) and targeted (right) ChR2 construct (B). Scale bar – 100µm. Mean (lines) and s.e.m. (shaded area) photocurrents elicited by temporally – focused stimulation along the single dendrite (C).*

The somatic CoChR construct investigated in our laboratory also would evoke similar artefact at the soma proximity. Although, as presented in the paper there is a difference between the current evoked by the somatic and basic CoChR construct, the opsin expression is still present in the distal parts but at substantially lower level (Shemesh et al. 2017). At the end is it important to mention, that all the compared opsin studies were done in *in vitro* conditions and one could expect that the artefact amplitude will change in *in vivo* conditions.

The characterization of soma targeted constructs put in evidence clear advantages of soma targeted opsins for neuronal connectivity mapping (Shemesh et al. 2017; Baker et al. 2016; Mardinly, Oldenburg, and Pégard 2018). However, still a small current (depending on cell Rin) will be evoked by activation of the opsin in the soma proximity, which pose a challenge to distinguish and characterize connectivity in the circuit. In this context a third, intermediate solution for performing connectivity experiments could be proposed. The artifact obtained in the processes within ~50 µm of the soma could still contribute to the response, but as it decreases with distance (in the case of

somatic constructs), we could obtain a much lower artifact at around 100 µm from the soma. Second, this artifact will present the same dynamics and shape at each photo-stimulation trial (given the same photostimulation position). It might be possible, then, to distinguish it from a synaptic response. (Xu et al., 2016) mapped the connections visual cortex with the help of glutamate uncaging. This work provides useful information regarding the post-synaptic response amplitude recorded from pyramidal cells in L2/3. According to the authors, the mean IPSC of inhibitory cells form L2/3 and 4 was in the range of 50 pA. It could be then worthwhile to start our connectivity experiments by mapping connections for which the expected post-synaptic response would be larger than obtained artifact. The paper presenting all-optical approach to study visual ensembles formation also stresses the presence of artifact due to photostimulation (Carrillo-Reid et al., 2016). In this work, the authors characterized the artifact, showing that one can distinguish the physiological response from the artifact. Considering both, the magnitude of the artifact due to opsin activation outside the soma, and the current progress in soma restricted opsin design, it would be worthwhile to perform a connectivity study using both somatic CoChR and ReaChR variants, as we could use these results for method validation.

The second type of artifact is connected with spectral overlap between a particular opsin and a calcium indicator. Unwanted opsin activation during scanning the field of view with the wavelength for calcium imaging (800nm for OGB, 920nm for GCaMP) is a serious obstacle in combining optogenetic stimulation and 2-photon calcium imaging. This artifact was expected as it was shown in previous studies combining 2-photon GCaMP3 imaging and ReaChR induced activity to investigate the impact of two cellular subpopulations of Drosophila melanogaster on courtship behavior (Inagaki et al. 2014). We have also recorded this artifact in our team during investigations on Chronos and ReaChR opsins (data not shown). Although the existence of the artifact can be expected after analyzing the 2-photon spectra of various opsin in comparison to the 2-photon spectrum of GCaMP6 or OGB-1, the actual influence of overlapped spectra during recordings is difficult to predict, taking into account the variable properties of opsins. Although the characteristics of Chronos suggest that combinations with this opsin would have the highest probability of success, specifically because of its fast kinetics and higher optimal power at spiking threshold than the other two opsins, all the pairs could probably provide successful results depending on the goal. It is also interesting to consider the possible advantages of application of soma restricted CoChR, as the activation coming from the dendritic arborization would be avoided.

The choice between calcium sensors constitutes important variable. As reviewed in OGB vs GCaMP and Tab.1 both calcium indicators have their advantages and disadvantages. OGB -1 and GCaMP6s varies in their kinetics and range of dF/F. Additionally, GCaMP6s imaging in V1 presents a lower percentage of detected orientation/direction selective cells than it would be expected from the literature based on electrophysiological protocols. This difference could be explained by the fact that GCaMP6s needs to be genetically expressed in the cells, and the population of cells targeted with expression would depend on the exact tool chosen (rabies virus retrograde expression, AAV mediated expression under particular promoter, transgenic animals lines). In contrast OGB-1

delivered to the cell by bulk loading marks all neurons and astrocytes in the area. Additionally, the spectral separation between opsin and OGB is larger than in case of GCaMP6s.

It is important to mention that for the functional connectivity of V1 project, which was the motivation for biological preparation search, that the artefact originating from opsin activation during scanning is less important than the first type of artefact described above originating from opsin activation in the distant from the soma parts. In our experimental design we are going to use calcium imaging for establishing the orientation/direction selectivity at the beginning of the experiment. In this scenario a scanning artefact, which is incapable to trigger a spike would be tolerable. Application of imaging powers lower than the spiking threshold power for opsin would indeed depolarize the whole population of cells containing opsin, but visually evoked characteristic changes probably could be still visible. Especially, that the visually evoked response would need to be repeated a few times for each direction. Shuffling with the visual stimulus direction order and the time of visual stimulation would probably enable one to obtain information about feature selectivity independently from artefact coming from opsin activation during imaging (even assuming that it will be spiking). First, such artefact would be visible only on the cells which express both – calcium indicator and opsin (and one can expect that the overlap ratio in these populations won't be 100%). Second, the subthreshold opsin activation would depolarize the whole network and by this the background spiking activity of cells but preferred orientation probably would be still clearly visible (analogically to the current or conductance steps injection to the cell). Therefore, the goal would be to minimize the imaging artefact instead of eliminating it, which might be easier to achieve.

During the second part of our protocol, which establishes the pair-wise mapping, we would use 2-photon holography for pre- synaptic stimulation and electrophysiology (whole cell recordings and conductance measurements) for post-synaptic detection, instead of calcium imaging. The artefact originating from opsin activation of the processes could be minimized by the use of soma restricted opsin and/or exploiting knowledge about the V1 circuit architecture together with precise characterization of the artefact.

In summary, the functional connectivity project was not possible to perform in the time of thesis duration. Instead, the time was used to describe limitations of available tools – the artifacts of the ReaChR, CoChR and Chronos opsins which were available in the lab and exploring their full potential. On the other hand, I have tried different strategies to provide working biological preparation suited for V1 studies.

Taking into account characteristics of calcium indicators taken into consideration (GCaMP6 vs OGB1) the GCaMP6 would probably be easier to implement and would provide higher resolution of the recorded signal. The imaging artefact would be present surely in each of the opsin we have considered in the lab (which is visible in the power spectrum overlap summed up in the table 3). However, the artifact would probably have the smaller impact for characterizing each cell visually-evoked response in short kinetics opsin (like Chronos). Another solution which could enable

interpretation of the data containing imaging artefact that could applied is an algorithm which saves the position of scanning spot in time. This would further provide information about which calcium increases for a given cell should be considered as physiological and which as artefactual. In regard to the second artefact – being consequence of opsin expression in the entire cell – application of soma restricted opsin which are starting to appear could be the easiest solution. On the other hand, knowledge about both the circuit architecture and the artifact shape (based on opsin kinetics parameters) could be used to identify connections between the cell in the presence of artefact. Further, the modeling of current evoked by opsin photoactivation could be used not only to detect the artifact but also to subtract it.

# 4. Functional synaptic dynamics of receptive fields in primary visual cortex

As drafted in previous sections, in this study feature selectivity defines neuronal function. The function of a cell, here based on example of direction tuning, is judged based of the spiking response. What defines this response and how the synaptic input dynamics underlying the observed response looks like is the topic of this chapter. Specifically, we will look closely how visually evoked synaptic conductances change in time following a stimulus.
We will start by defining the relevant conductances, how one can measure them, and the current state of knowledge about these measurements. Further, I will present the results collected during this project, to be presented in the following manuscript (in preparation).

> Synaptic Excitation and Inhibition are Dynamically Unbalanced in Visual Cortex
>
> Marta Gajowa, Lyle Graham
>
> We describe the dynamics of visually-evoked excitatory and inhibitory synaptic conductances recorded in mouse primary visual cortex in vivo. We find a diverse set of dynamical relationships between excitation and inhibition, with in general weak cross-correlations across the entire response, and occasional highly synchronized transient responses. Inhibitory inputs are consistently larger and show stronger fluctuations than excitatory inputs, with overall higher frequency content. These results suggest that the dynamics of the neuronal code differ between excitatory and inhibitory pathways, and that while total excitation and inhibition are often balanced as a function of stimulus for selective neurons, spike output for a specific stimulus response follows a characteristic dynamic imbalance between these inputs, as opposed to fluctuations around a balanced mean input.

## 4.1. Background information

### 4.1.1. Conductance: meaning in neurophysiology

The general definition of electrical conductance, with units of siemens (S), is a feature of a material that describes current flow across the material depends on the voltage. By definition conductance is the inverse of resistance, measured in ohms. In neurophysiology we can talk about conductance in different contexts.

Channel conductance

Each channel in the neuronal membrane has its own conductance, typically on the order of tens of picosiemens (pS). While the channel is open, ions flow according to the driving force across the

membrane as a function of the relevant ionic concentrations and the size of the channel conductance. The dynamics of channel opening, and closing may be a function of time, the trans - membrane voltage, and or external and internal gating factors (e.g. neurotransmitters, [Ca]++).

Input conductance $G_{in}$

We consider a simple approximation of the neuron as a single compartment RC circuit thus, ignoring the spatially-distributed dendrites. The neuron membrane's phospholipid bilayer acts like a capacitor, whereas various membrane channels account for the resistance, with it's reciprocal defined as the cell input conductance, Gin. Note that in this thesis, we refer to $G_{rest}$ as the input conductance of the cell at rest, thus without stimulus-evoked synaptic activity. It is one of basic neuron parameters and can be measured while injecting current steps of increasing amplitude.

$$G_{in} = \frac{dI}{dV} = \frac{I_1 - I_0}{V_1 - V_0}$$

Synaptic conductance $G_{syn}$

The activation of a particular synapse will result in opening of several ion channels, and typically during evoked activity of the circuit more than one type of synapse is activated. The change of all the channels' conductance will cause current flow to the neuron:

$$I_{syn} = g_{syn}(V_m - E_{syn})$$

Currents from inhibitory and excitatory synapses (IPSC and EPSC, respectively) can be measured directly in the voltage clamp configuration at the appropriate holding potentials. Indeed, IPSC and EPSC are often investigated to obtain insight into the function of a given input local circuit or connection E/I balance (Adesnik and Scanziani 2010; Adesnik 2017; Adesnik et al. 2012; Xue, Atallah, and Scanziani 2014).
These measurements typically require blockers of intrinsic Na channels to avoid spiking for measuring IPSCs, which requires holding potentials of 0 mV.

In this thesis we applied a different approach to characterize synaptic input, because fundamentally we were interested in studying synaptic input in a functional context, and thus the quantity of interest is the synaptic conductance. Indeed, excitatory and inhibitory conductances may be derived from the standard measures of EPSCs and IPSCs. However, the functional context here is grounded in the spiking output of the neuron (both visually-evoked and from dynamic clamp protocols), and therefore Na channel blockers could not be used. Specifically, we are looking directly at conductance changes of the neuron in time during the presentation of visual stimuli. This approach allows the measured conductance to be split into its excitatory and inhibitory synaptic components, under the

assumption that these components are simply added to each other according to the parallel (and linear) RC circuit model.

$$g_{syn} = g_{exc} + g_{inh}$$

Following the RC circuit approximation, the effect of an ion channel is approximated by addition of the battery in series with the resistor. In this manner ionic channels are added to the circuit as additional resistors in series with a voltage source parallel to the other channels (Figure 36).
In neurons the voltage source accounts for the difference in ionic concentrations between the inside and outside of the cell, according to the specific ionic permeabilities of the channel in question. To understand the analogy between the electrical circuit and the cell, one can think about the energy stored in the trans - membrane ionic concentration difference as the energy stored in the battery, with the driving potential for each channel/synapse/conductance depending on the time-varying difference between the neuronal membrane potential and the reversal potential of the channel.

When a cell at rest is exposed to an excitatory synaptic conductance input, it will experience a larger inward current than when the same conductance input is activated when the cell is at a more depolarized potential. On the contrary, the same value of an inhibitory conductance will induce a larger outward current at more depolarized resting potential, than when the cell at rest. An interesting example of the influence of synaptic conductance on the evoked currents, and consequently the cell membrane potential, is for so-called shunting inhibition, caused by the activation on GABAa channels. The fact that its reversal potential is around – 70 mV, thus close to the cell resting potential, gives a nontrivial influence on cell response. Depending on the cell momentary membrane potential, this input can evoke either inward or outward currents, but the proximity of the resting potential and reversal potential for GABAa channels will yield relatively low amplitude currents, which by themselves often do not strongly influence the membrane potential. Rather, the functional signature of these input arises from the increase in the cell conductance. In particular, the influence of shunting inhibition on the cell input-output processing is investigated in this thesis.

In summary, the cell potential is the result of an ensemble of batteries of different values, and their associated channel conductances (dependent on the type and number of activated channels) present in the cell, switched on and off in time, as expressed in equation below:

$$V_m(t) = \frac{E_{exc} g_{exc}(t) + E_{inh} g_{inh}(t) + E_{rest} g_{leak}(t)}{g_{exc}(t) + g_{inh}(t) + g_{leak}(t)}$$

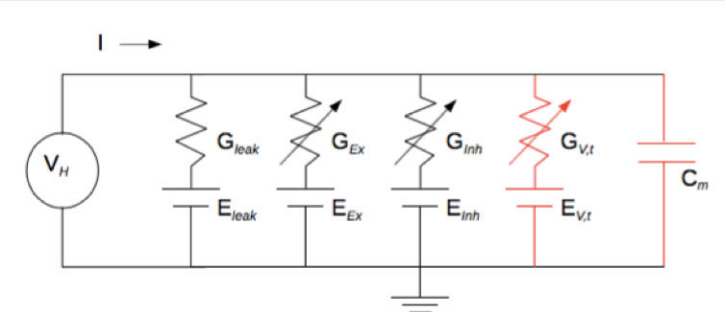


*Figure 36 Electrical circuit scheme of a neuron during VC measurement. All conductive elements are in parallel to each other ($G_{leak}$, $G_{Ex}$, $GI_{nh}$,$G_{V,t}$) with each  in a series with their corresponding reversal potentials. $G_{Vl}$ symbolize voltage dependent channels whose conductances are assumed to be constant over a range of holding potentials during the voltage clamp measurements.*

It follows that by measuring the cell conductance we can infer the dynamics of the synaptic input to a cell over time. Importantly, while the evoked current depends on both the conductance and the membrane potential at a given time, we make the assumption that the conductance of activated channels does not depend on cell state (e.g. they are neither voltage-dependent nor regulated on the time scales of interest by intracellular factors), but only on channel activation by neurotransmitters. This is why investigation of conductance (in contrast to evoked current) is better suited for measuring and reasoning about synaptic input to a cell. Additionally, the essentially “non-invasive” method approach for measuring the conductance instead of current (e.g. using channel blockers) gives us the possibility to interact with the cell in subsequent steps using simulated conductance inputs, and thus compare its spiking output during the entire duration of recording.

### 4.1.2. Synaptic conductance measurements- technical comments

For the estimation of the synaptic input, we are interested in measuring both the time-varying conductance of the cell as well as the time-varying reversal potential of that conductance. In this manner we are able to extract the excitatory and inhibitory components of the input. We measure these indirectly by evoking the same change in the system, for example the response to the same visual input, under different conditions, e.g. by applying the same stimulation while changing the holding potential under voltage clamp (VC) mode, or the holding current under current clamp (CC) mode.

In VC mode, the influence of driving force (depending on momentary reversal potential) scaled by conductance (depending on activated channels) during a given response will evoke synaptic current waveforms of different amplitudes and time-course depending on the holding potential. In CC mode, the evoked responses will be recorded as different membrane potential waveforms while applying different holding currents. In either case, the most important assumption is that application of the same stimuli will evoke “the same” response.

Performing a linear regression (Figure 37c) on the voltage and current values coming from different holding potentials/currents at each time point, provides a time-varying current-voltage relationship (IV characteristic), and thus provides the following important parameters:

1. The slope of the IV characteristic gives the conductance value of the total synaptic input and the resting conductance at a given time point
2. The intersection on the voltage axis of the IV characteristic during stimulation and the IV curve obtained at rest provides the driving force of the total synaptic input, or the effective reversal potential.
3. The intercept of IV characteristic with voltage axis (thus I=0) provides the membrane potential value of the actual response (assuming no activation of non-linear channels), e.g. what would be observed in CC mode with no applied current (important if recording is done in VC mode)

By repeating the calculation for all the time points during the response we thereby obtain waveforms of the input conductance and the momentary reversal potential values (Figure 37e), as well as the estimated membrane potential which would be measured during CC recording (I=0).

By subtracting the input conductance $G_{rest}$ from the measured conductance change (e.g. the difference between the measured slope and the slope at rest), we then obtain the total synaptic conductance at each time point:

$$G_{syn} = G_{measured} - G_{rest}$$

The estimated synaptic conductance can be described in absolute [nS] values or as the %ΔG, referring to the percent of change in comparison to baseline (rest).

The phase plot of the %G and the effective reversal potential provides information about the ratio of the excitatory/inhibitory inputs, and as well shows at which effective reversal potential the conductance change was the highest.

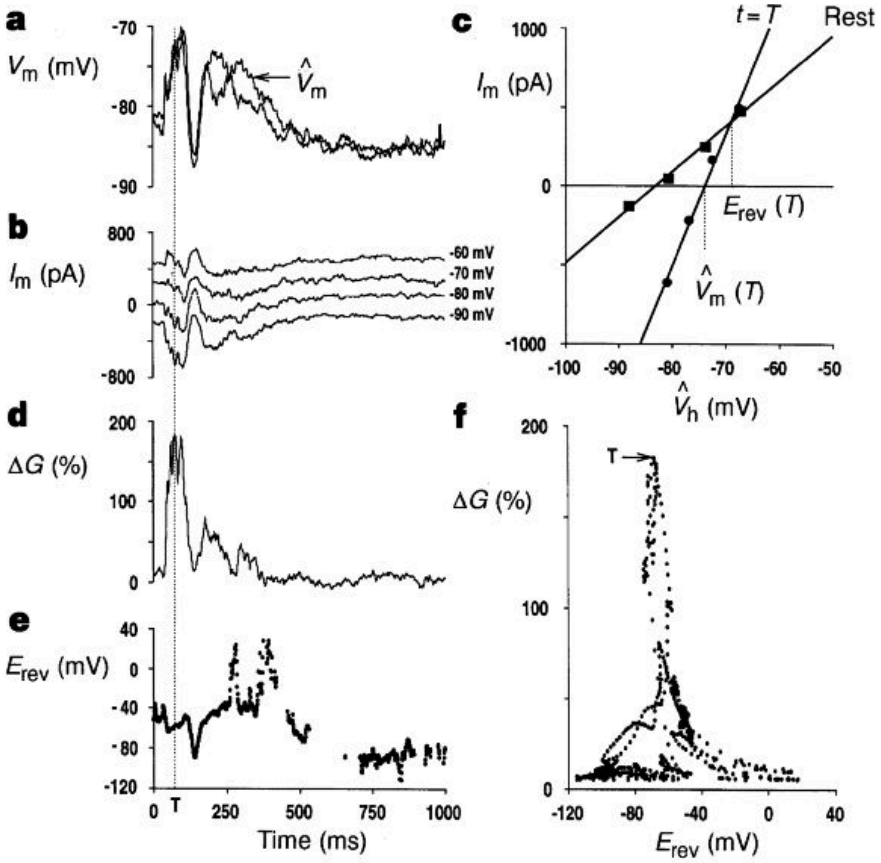


*Figure 37 Conductance estimation step by step. a. Voltage clamp responses in CC mode overlapped with predicted membrane potential (Vm) from VC currents (the intersection of I/V line with x axis in each time step) b. Visually evoked currents measured in VC mode in four different holding potentials c. output of linear regression in two exemplary time points during recording: during evoked response (circles) and at rest (squares). The slope of each I/V line gives respectively Gin at time T marked by dotted line in (a-e) and $G_{rest}$. d. Relative to Grest $dG_{in}(t)$, derived continuously during visual stimulation (repeated linear regression at each time point). e. Momentary cell reversal potential $E_{rev}$ provided by the voltage value at crossing point of the $G_{rest}$. and $Gi_n(t)$ I/V profiles. f. Phase plot of relative delta $G_{in}(t)$ vs $E_{rev}(t)$, where each point represents 1ms average. All the analysis comes from ten repetitions in each condition. After* (Borg-Graham, Monier, and Frégnac 1998).

Conductance estimation is usually performed on averaged current/voltage waveforms of several trials to reduce the influence of random events and to extract the repeatable circuit response to a stimulus. This fact indicates that the resulting conductance represents an estimation of the "true" conductance with some standard deviation. Additionally, if the conductance change at a given moment is only slightly larger than the conductance at rest, their lines on the IV plane will be close to parallel. Both of these factors cause difficulties with precise estimation of the crossing point of the two IV curves (Figure 38). To avoid the problem a threshold is often applied (5% threshold in this thesis) on the conductance change (Borg-Graham, Monier, and Frégnac 1998) as a condition to make a valid estimate of the momentary reversal potential,. to avoid uncertainty of the momentary reversal potential and therefore the value of the excitatory and inhibitory components.

For example, a cell with resting input resistance of 60 MΩ will have a Grest of approximately 16.6 nS. The 5% threshold implies a minimum conductance increase for synaptic estimation of 0.83nS (Gin >= 16.6+0.83nS). The experimental results show that the 5% threshold is not always reached during the response, which leads to discontinuities of the estimated synaptic conductance waveform.

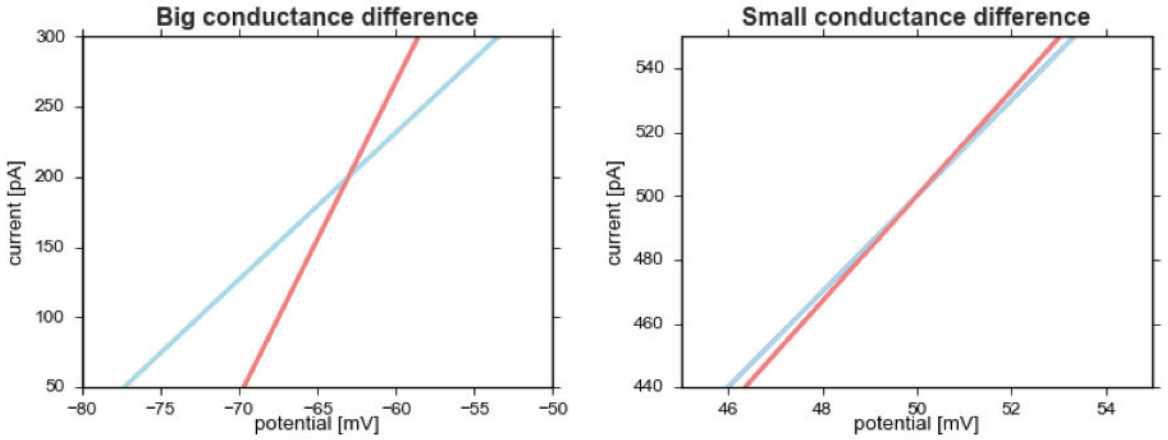


*Figure 38 need of 5% threshold. Cartoon shows example of big(left) and small(right) conductance change in a single time point. In is hard to assess where the two lines on the IV plane for small conductance change cross. Note that the lines are based on the averaged signal and therefore, it is not single point which could provide equally probable solution.*

As a first check of the conductance measurement, we use the estimated conductances to estimate the membrane potential that would be observed under current clamp.
We then compare the estimated membrane potential with the actual stimuli evoked membrane potential response. The overlap between the two potentials justifies the assumption about "the same" circuit response to the same stimulus (Figure 37 a).

### 4.1.3. The art of conductance estimation

Although the study of conductance changes has been accomplished by relatively few investigators, the results to date have provided important insights into circuit behavior. At the same time, the interpretation of the quantitative results needs to be carefully done, in particular after checking on the details of the experimental technique and data analysis. For example, what magnitude of conductance changes are actually functionally relevant? How can details of the exact method influence the result? What are the physiologically relevant parameters? In the following section I will try to shed some light into how biased one can be depending on some technological details.

Table 4 (in the end of this section) provides an overview of the literature, focusing on the technical details of conductance estimation in in vivo preparations. Different methods of conductance estimations were used, including both voltage clamp and current clamp approaches. For both protocols, cesium blockers in the patch solution (blocking outward rectifying potassium currents and improving access resistance, as well as reducing imperfect space clamp (Brown and Johnston 1983)

are frequently added. Overall, most papers provide results from a rather low number of cells, which can be explained by the length of the protocol and character of in vivo recording. In some cases, the number of both the recorded cells and the cells included in the final analysis is provided.

**Currents average or estimated conductance average**

During collecting results to the project, it was noted that number of repetitions might influence the quality of conductance estimation. This observation can be partially explained by the trial to trial variability of the evoked response to the presented several times stimuli. The data set characterized by low variability was usually providing good conductance estimation within 10 repetitions of the stimuli at each holding potential. In contrast, data set characterized by higher trial to trial variability were not providing satisfactory estimation within 10 trials and usually 12- 20 repetitions were applied. Intuitively, it can be explained by the conductance estimation method. Once the evoked currents were recorded, all trials were averaged (for each probed direction) and based on these averaged responses the conductance estimation was performed. The averaging procedure on variable data set might lead to underestimation of conductance amplitude and change of the signal dynamics. Therefore, it is valid to ask what number of repetitions will provide reliable and physiologically probable conductance estimation (which defines good estimation). Further, what would be the possible error of the estimation depending numbers of trials integrated?

The answer is important for few reasons. First, in case of low variable data set, the known minimal number of trials providing good conductance estimation allows recordings time shortening (so useful during in vivo patch!). Second, in case of variable data set (which usually was associated to not the best bridge/Rin ratio), collection of higher number of repetitions could potentially improve estimations and allow for cell inclusion in a data base. Third, gaining understanding of the link between data variability and applied number of stimuli repetition can be one of a criteria taken into account during data analysis to include or exclude given recording from analysis. Another question, connected to the conductance estimation procedure is the order applied to the averaging and linear regression procedure. In other words, if there is a difference between conductance estimated based on the current average or based on the averaging of pairwise conductance estimations.

Below, I present a comparison of conductance estimations for the same cell data set. This cell is characterized by a relatively low trial to trial variability with respect to the evoked currents (Figure 39). For both methods the individual trials (10 trials) were first low pass filtered at 200Hz with a $2^{nd}$ order Butterworth filter. Next, the analysis was split in two parts. For the first case, the evoked currents and the associated voltage traces (compensated by the uncompensated bridge during voltage clamp, or bridge error) were averaged, and the conductance estimation was performed on these averaged traces. In the second case, the conductance estimation was performed on each of the 10 trials of the evoked currents and associated voltage traces (again compensated by bridge error), and then averaging the 10 conductance waveforms.

Figure 40 presents estimation results for $G_{rest}$ and the excitatory and inhibitory conductances, depending on the order of the conductance estimation and the trial averaging. For estimation of $G_{rest}$ both methods provide the same output. In contrast, for the excitatory and inhibitory synaptic components there is a difference in between estimations. For estimations based on averaged currents the waveform is less continuous and there are more periods when conductance was not assessed due to the 5% threshold, which is imposed during splitting the conductance into its excitatory and inhibitory parts. In contrast, the waveforms coming from averaging various pairwise possible conductance traces provides slightly more continuous waveforms. This is probably due to the fact that the 5% threshold on each conductance estimation eliminates different time periods for the different pairs. In some cases, then, the conductance at a given time point will be taken into account and in the others not, resulting in a slightly higher mean final waveform.

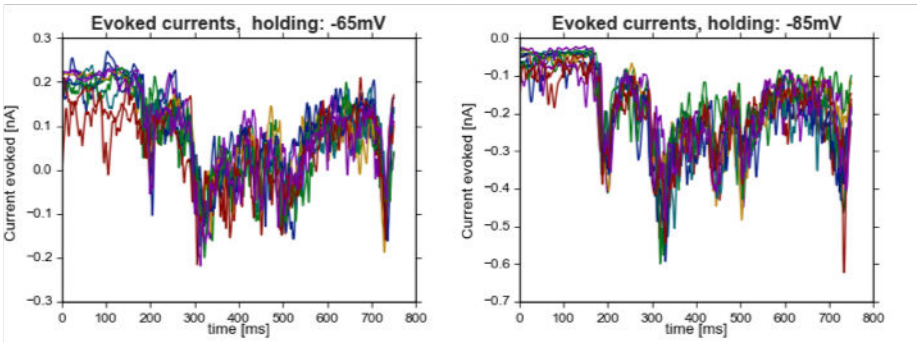


*Figure 39. Exemplary Visually evoked currents measured during VC protocol for 1 direction. 10 trials overlapped characterized by low trial to trial variability. The mean of SD in each time point was equal 0.043 nA and 0.089 nA for Currents evoked at -65 and -85 mV holding potential respectively.*

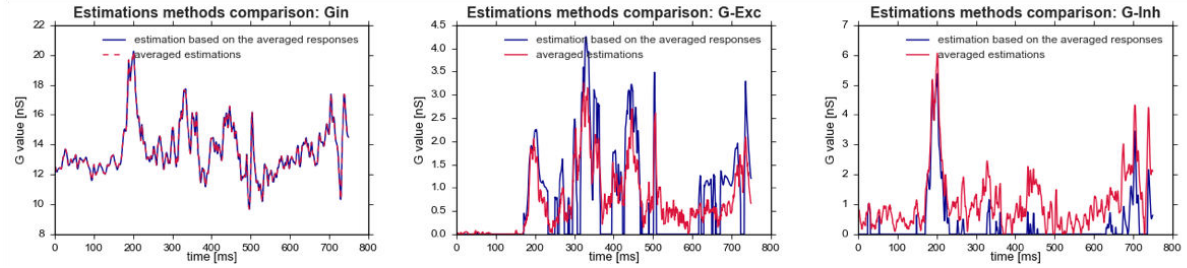


*Figure 40. Different methods of estimation. Gin (G rest), g exc and g-inh waveforms changes in time depending on the order of averaging and conductance estimation. Conductance estimation based on averaged current traces (blue) are less continuous than estimation coming from averaging conductance estimations based on single pairs of currents traces (red).*

The bootstrap analysis in Anderson et al., 2000, 2001 and other works citing this method (Table 4 Literature overview of studies using conductance measurements. In bold references of studies performed on mouse V1. at the end of the section) is based on several conductance estimations which are averaged in the second step. In comparison the analysis of Borg-Graham et al., 1998 and other works citing this method first average over at least 10 repetitions of the same stimuli and then estimate conductance from the averaged trace.

**How many trials should be taken into account**

To tackle this question, data from an example cell, characterized by low trial to trial variability were used. An iteratively increasing number of trials (from 1-10) was integrated in the analysis, exploring all possible combinations between trials. Next, the conductance estimation was performed on the averaged mean trace resulting from each possible combination. Various conductance estimations were compared between each other in each group based on number of averaged trials. First, the standard deviation was calculated at each time point between all the estimations. Second, the mean of the standard deviations was plotted against the number of trials averaged (Figure 41). Similarly, the standard error of the mean (SEM) was calculated and divided by the grand mean to provide SEM/mean ratio for each group.

This analysis shows how much each trail added at each averaging step minimized the standard deviation and SEM/mean ratio. The 5% threshold for that the example cell was equal to 0.65nS (assuming a bridge error of 0). The standard deviation equal to this value (SD=0.65nS) was achieved for the 7th trial group and was more almost twice as small for the 9th trial group (SD=0.35 nS). The SEM/mean ratio is lower than 5% was already on the group with 5 repetitions, whereas for the group of 9 repetitions the SEM/mean ratio is less than 2%. These results suggest that for recordings with relatively low variability, 10 trials provide a good quality of estimation.
To visualize differences in conductance estimation across different groups. Figure 42 presents exemplary period of evoked response superimposed on each other.

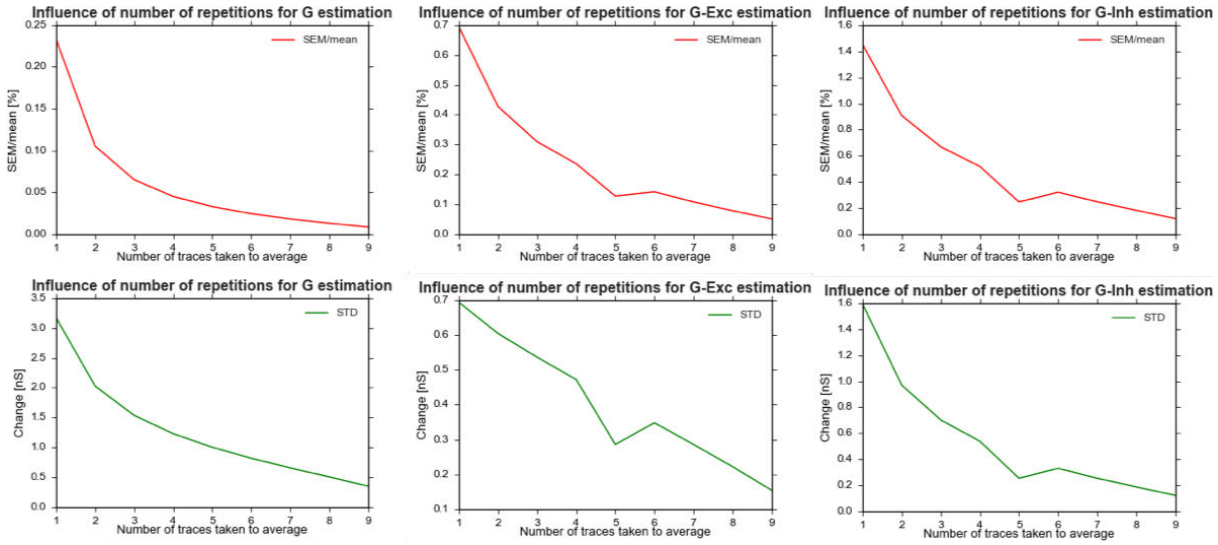


*Figure 41. Influence of number of trails integrated in conductance estimation. All three plots present the mean standard deviation (in green) and sem/mean ratio (in red) of changes between all possible conductance estimations in each group based on number of averaged trials. Data used to these plots comes from cell 2 recorded 18.11.2017 from one direction (0 degrees).*

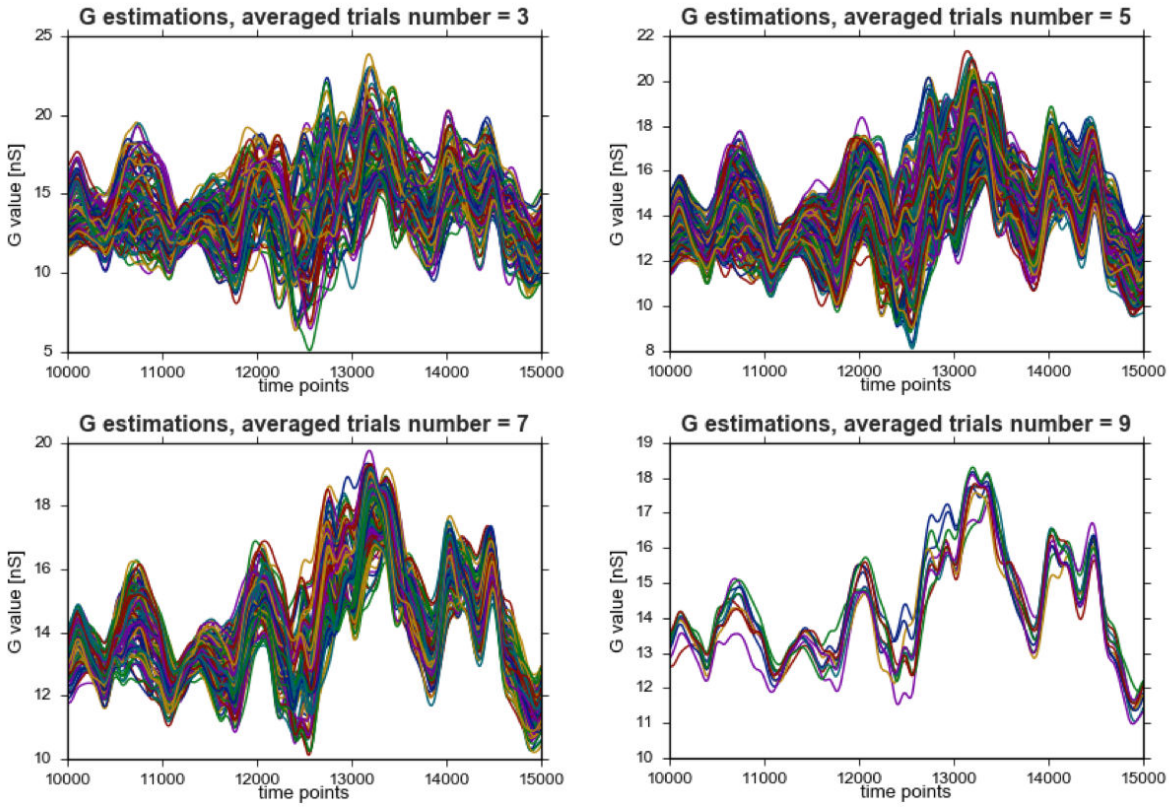


*Figure 42 Exemplary plots presenting Gin conductance estimation based on 3,5,7 and 9 trials averaged. The same period of time is plotted. Total number of combinations for each group is respectively: 120,252,120 and 10 combinations.*

**Bridge error and Input Resistance estimation**

We are estimating the conductance based on evoked currents measured in voltage clamp (VC) mode. In VC the bridge error cannot be fully compensated (Barbour 2014), which results in an underestimation of the actual conductance. We refer to the difference between the bridge compensation applied during CC and during VC mode recordings as the 'bridge error'. This error was estimated between VC and CC recordings and applied during the conductance estimation to compensate the voltage traces (according to the equation $V_{compenated}(t)=V_{holding}- (I(t) * \text{bridge error})$). The scaling effect of the bridge correction to the estimated conductance is not obvious. Additionally, the precise bridge error estimation was a challenging operation during experiment. Over the time course of the project, we applied various methods to estimate the correct bridge value. At first, we simply compared the bridge compensation applied during VC and CC protocols. The difference in the amplifier bridge compensation circuit applied to the first CC protocol after VC measurements would then be applied during the conductance estimation. However, this value was not perfect, as both the cellular parameters and cell access resistance often changed during the recordings, and a more precise value than the one adjusted on the amplifier was needed. We therefore started measuring the bridge error much more frequently, in between each CC protocol. Additionally, we measured the difference between the bridge value on the amplifier and the one estimated by an exponential fit to the voltage response to a current step protocol. Knowledge about these parameters just before and

just after the VC recordings was used to calculate the bridge error applied for the conductance estimation. The Rin value would be set as the one measured before (and/or after) in CC mode. This value was a more precise estimation because it took into account both the bridge differences caused by a not fully compensated bridge applied during VC recordings, and any eventual changes in the access resistance during recording. These steps undertaken provided an improved estimation of the bridge error, thereby improving the plausibility of the conductance estimation. Finally, monitoring cellular parameters over the entire recording period enabled us to correct some of the estimations *a posteriori* during subsequent off-line analysis, and therefore draw a more plausible interpretation of the results.

Below I present examples of the influence of the bridge error on the evoked conductance estimation for three exemplary bridge values (Figure 43) and across several bridge values (Figure 44). A clear scaling effect of the bridge error is visible, stressing the importance of a precise assessment of both the input resistance and the bridge error during recordings. The correct estimation of the bridge error is crucial for data interpretation, with too high and too low bridge errors resulting in an overestimation or an underestimation of the conductance, respectively.

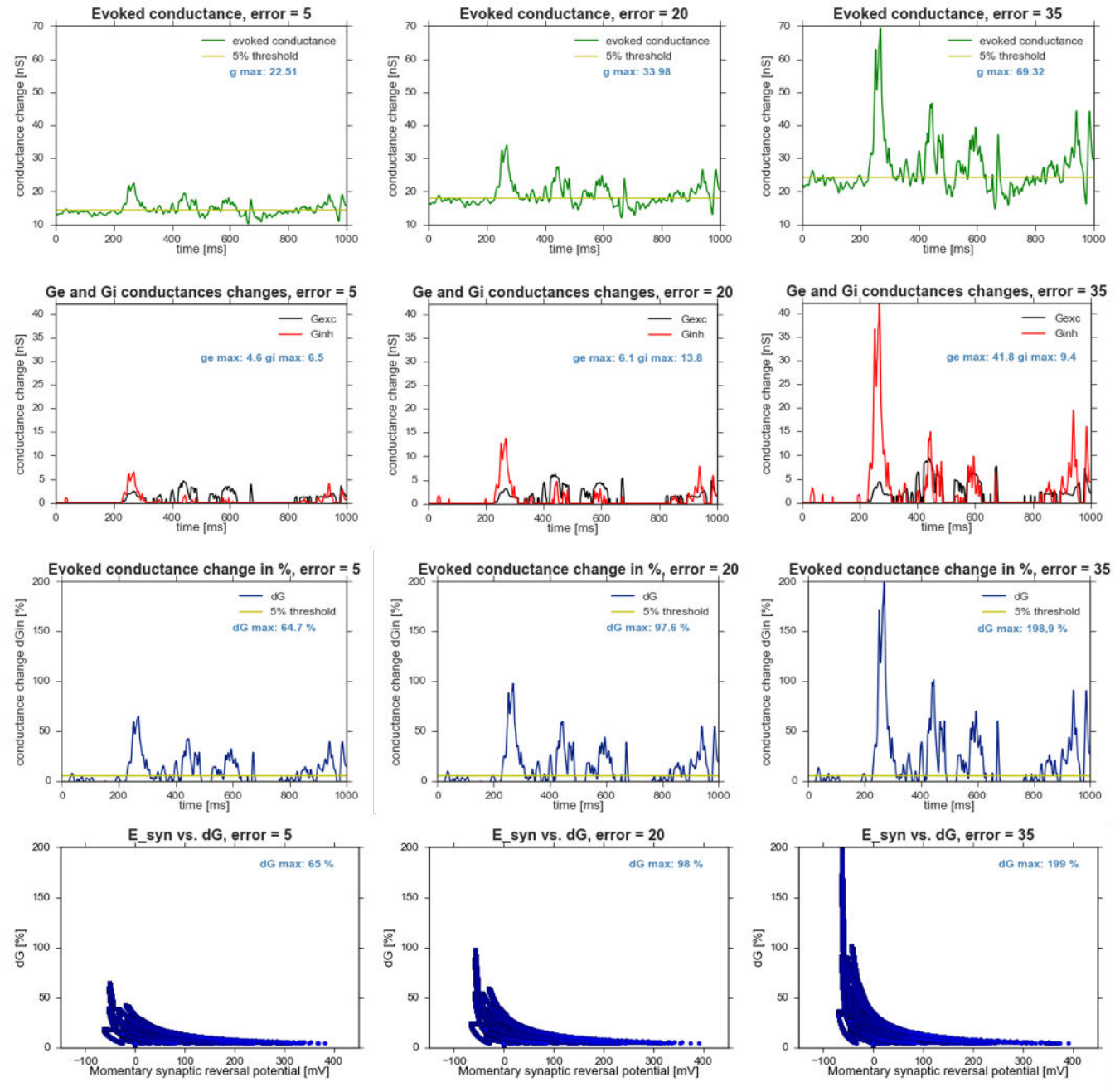


*Figure 43 Scaling effect of bridge error for various parameters of estimated conductance. All data comes from cell 2 recorded 18.11.2017. The VC protocols were done with no bridge compensation and the total bridge was 30 MOhms. Three different bridges values were used to create this cartoon: 5, 20 and 35 MOhm respectively to stress the influence of bridge error and $R_{in}$ estimation to the estimated conductance output.*

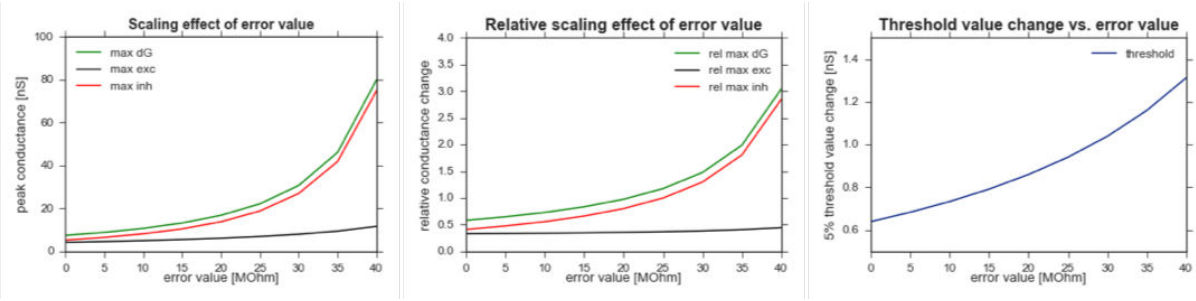


*Figure 44 Scaling effect of bridge error. Peak values of conductance estimated and its excitatory and inhibitory components (left), their relative to input resistance value (middle), influence on the 5% threshold value (right).*

*Table 4 Literature overview of studies using conductance measurements. In bold references of studies performed on mouse V1.*

| Reference | animal model | anaesthesia type | patch clamp mode for G estimation | Details on the patch solution and electrode parameters | holding and reversal potentials | conductance estimation based on | targeted area/cells | stimulation applied | how big n? | details on the method/comments |
|---|---|---|---|---|---|---|---|---|---|---|
| Brown T. and Johnston D, 1983 | giunea pig; slices | - | CC and VC | cesium ions in patch solution | 5 Vh in between -25 and -65 mV | | piramidal cell in CA3 region | electrical stimulation of mossy fibers | 12 cells from 298 recordings | one of the first conductance estimation paper |
| Borg-Graham, L., et al., 1998 | cat , in vivo | althesin | CC and VC | 0.5 mM EGTA | 5 Vh in between -50 and -90 | based on evoked currents | cat primary visual cortex | mouving grating and flashed bars | 7 from 109 CC characterised cells | first paper showing big conductance changes relevant for cell processing |
| Anderson, J., et al., 2000 | cat | thiopental sodium | CC | electrodes 4-15 MOhm, K-gluconate based internal with calcium buffers | 3-11 Ih in between -350-+200 pA; Ee=0, Ei=-85 | based on membrane potential values | cat primary visual cortex | 4s of optimised stimuli grating | 25 from 49 recordings on various holding currents; conductance estimation in 14 cells was paired with visual stimulation and 11 cells with LGN electrical stimulation;( 12 simple and 13 complex cells in total), additionally in 5 cells contrast dependence was investigated | Bootstrap analysiswas used for conductance estimation, first conductance estimation was done and after the fit over all possible estimations provided G waveform in time |
| Anderson J., et al., 2001 | cat | thiopental sodium | CC | 7-12 MOhm electrodes,0.5 EGTA in internal solution | 4-5 Ih in between -200-+100pA,Ee=0; Ei=-80 | based on membrane potential values | cat primary visual cortex | 2Hz grating optimised for spatial frequency, changing contrast and lenght of the bar | 33 cells from 52 recorded;19complex and 14 simple;22-end-inhibited; 26 cells for conductance estimation 10 for contrast influence | Bootstrap analysiswas used for conductance estimation, first conductance estimation was done and after the fit over all possible estimations provided G waveform in time |
| Borg-Graham L., 2001 | turtle, retina ex vivo | - | CC and VC | 5MOhms, 11mM EGTA in internal solution | two Vh= -60 or -90 or Ih=0 or in between -30 and 50pA | based on evoked currents and membrane potentials | patched ganglion cells | grating spaced at 22 deg | 19 cells from 34 recorded in VC cells | mixed estimation coming from CC and VC recordings method based on Graham et all 1998 |
| Taylor, R. and Vaney, D., 2002 | rabit, retina ex vivo | - | CC and VC | 4-8 MOhm, 1mM Cs-EGTA in the internal solution | Ee=0, Ei=-65 | based on evoked currents | patched ganglion cells | 12 directions spaced at 30 degrees | 28 cells | as in Graham et al 1998 |
| Monier, C. et al., 2003 | cat, in vivo | althesin | CC and VC | electrode resistance 3-5 Mohm, 0.5mM EGTA in patch solution,Rs<40 Mohm | G decomposied on 3 conductances: Ee=0; Ei=-80; Ei2=-95 mV | based on evoked current and voltages | blind patch in V1 | Full field moving gratings | 51 simple cells, 32 complex, 5 unclasified | mixed method based on Graham et all 1998 and Anderson et all 2000 |
| Wehr, M. and Zador ,A., 2003 | rat auditory cortex | ketamne, medetomidine | VC | in half of recorded cels QX-314 was added to internal solution, | 3-5 Vh values, Ee=0, Ei=-85 | based on evoked synaptic currents | primary auditory cortex | varying in frequency and intensity sounds | n=62, 32 with sodium channel blocker | modified method based on Graham et all 1998 |
| Tan, A. et al., 2004 | rat in vivo | pentobarbital | VC | 7 MIhm electrodes, EGTA in patch solution; 25-60 Rs compensated and resulting in the error 15-30MOhms | Ee=0, Ei=-70 (or -60 or -80 mV) | based on evoked currents | primary auditory cortex | varying in frequency and intensity sounds | n=39 | |
| Priebe, N., Ferster, D., 2005 | cat area 17 | ketamine, acepromazine, halotane | CC | 8-12MOhms electrodes,calcium buffers present in patch solution, for part of recordings sodium channlels blockers used | 3 Ih=0, -100,-200 pA; Ee=0, Ei=-85 or if blockers used -70 | based of membrane potential values | blind , area 17 | RF mapped, stimulus intensity recorded | n=11 for conductance measurememnts | metod similar to Anderson et all 2000 |
| Wilent, B., and Contreras, D., 2005 | rat in vivo | pentobarbital, buprenorphine | CC | Qx-314 in internal solution | Ee=0, Ei=-75mV | based on membrane potential values | somatosensory cortex, L3 and 4 | whisker stimulation at different directions | n=14 | only partial description of exact method provided |
| **Liu, B-H., et al.2011** | mouse in vivo | urethane (1.2g/kg), chlorprothixene | VC | 10mM EGTA, MK-801, 25-50Mohms Rs, 4-6Mohms resistance electrodes, cesium in electrodes for VC | two Vh at 0 and -70mV | based on evoked currents | L2/3 simple cells, V1 | drifting grating | n=12 | method as in Wehr & Zador 2003 |
| **Tan, A., et al. 2011** | mouse c57 5-12 weeks, female cats in vivo | pentobarbital, chlorprothixene for mouse; ketamice, acepromazine, sodium thopental for cats | VC and CC | 5-10 Mohm electrodes, o,5 EGTA in patch solution, for synaptic exc and inh Cs was added in the solution; Rs was in between 30-100 Mohm in CC and 30-60 MOhm in VC | Vh - 80 for Epsc and +10 for Ipsc | based on both evoked currents and membrane potential | blind patch, 250-650 um below surface, in V1 | 2 Hz 90% contrast grating, 12 directions | 7 from 11 cells in VC in mouse, additional 10 cells recorded in CC mode for mouse (17 in total), 21 for cat | method as in Wehr & Zador 2003 |
| **Heider, B., et al. 2013** | c57 bl 4-6 weeks in vivo | chlorprothixene and urethane or isoflurane(0.25-1%), awake | LFP, whole cell patch and conductance measuremen ts | electrode resistance 4-7mOhm, 0.1 EGTA in patch solution, Rs<50 Mohm | Vh=-80 and +10mV | based on evoked currents | L 2/3 of V1 | 4 directions for preferred and orthogonal orientation | n=14 for both awake and anaesthetized group, n=5 for anaestetised and n=8 for awake | method as in Wehr & Zador 2003 |

## 4.2. Conductance changes underlying visual processing

### 4.2.1. Early findings on cat primary visual cortex

Observation of conductance changes during a given activity provides knowledge about the synaptic input to a cell from the network. Describing the amplitude and the dynamics of the evoked excitatory and inhibitory synaptic components enables reasoning about neuronal processing mechanisms (Higley and Contreras 2006; Wilent and Contreras 2005; M. S. Wehr and Zador 2003). On the other hand, the ability to observe the cell output dynamics - e.g. spikes, the sub - threshold membrane potential and spikes during the same activity while knowing the underlying conductances enables a description of functional cellular properties and thus a reasoning about the biological mechanisms of neuronal processing.

Theoretical models have predicted that balanced excitation and inhibition might play role in cellular processing (Michael N. Shadlen and Newsome 1994; M. N. Shadlen and Newsome 1998). Large visually evoked conductances (113 $\pm$58% relative to $G_{rest}$) were shown to contribute substantially to cellular processing in cat visual cortex (Borg-Graham, Monier, and Frégnac 1998). The high visually evoked conductance was shown to contribute to the cell spiking output and demonstrated that inhibition might not only have suppressing character but also and more precisely a divisive effect. Subsequently, conductance measurements were made in several cortical areas in order to investigate possible mechanisms of cellular and circuit processing.

In cat visual cortex (Jeffrey S. Anderson, Carandini, and Ferster 2000) investigated the conductance changes while changing the orientation and contrast of drifting gratings. This work demonstrated an increase of conductance up to 300% together with contrast increase. However, the evoked conductance increase was highly variable between the cells. Additionally, authors claimed that the biggest conductance changes occurred for the preferred orientation in a majority of cells (tuning based on spiking output). In a group of 11 cells, 4 showed a different preferred orientation between conductance and the spike output, but the difference was smaller than 30°.
These authors concluded that the magnitude of the increase for inhibitory conductances was higher than excitation, and that the tuning for both components is similar to the tuning of the membrane potential and spike output.

The same team investigated conductance changes underlying length tuning in cat visual cortex (Anderson et al.2001). Length tuning was shown in 50% of simple cells and 75% of complex cells. The peak tuning of spikes and membrane potential response was always below 5° stimuli size. This work demonstrated that in cells tuned to stimulus length, long stimuli evoked both an increase in inhibition and a decrease in excitation, when compared with optimal stimuli.
Another feature of cells in cat visual cortex that has been investigated in the context of underlying synaptic changes is direction selectivity. Similarly to the case of orientation tuning, excitation and

inhibition were shown to be tuned for the same direction, evoking the highest amplitude changes for the preferred direction of movement (Priebe and Ferster 2005). However, it is important to add that the difference between preferred and null directions were not statistically significant for both the excitatory and inhibitory components. Moreover, the temporal interplay between excitation and inhibition was confirmed to be nearly at opposite phases (164° difference).
Visually evoked conductance changes in the context of direction and orientation tuning was also presented in (Monier et al. 2003).

These authors compared excitatory and inhibitory synaptic conductance tuning to spike-based tuning for both direction and orientation. Their overall conclusion was that these tuning relationships were diverse, describing three patterns:

1.Excitatory and inhibitory tuning the same as spiking one

2. Excitatory synaptic input co-tuned with spiking, while inhibitory synaptic input tuned with non-preferred stimulus orientation/direction

3. Excitatory and inhibitory parts tuned to non-preferred stimulus orientation/direction.

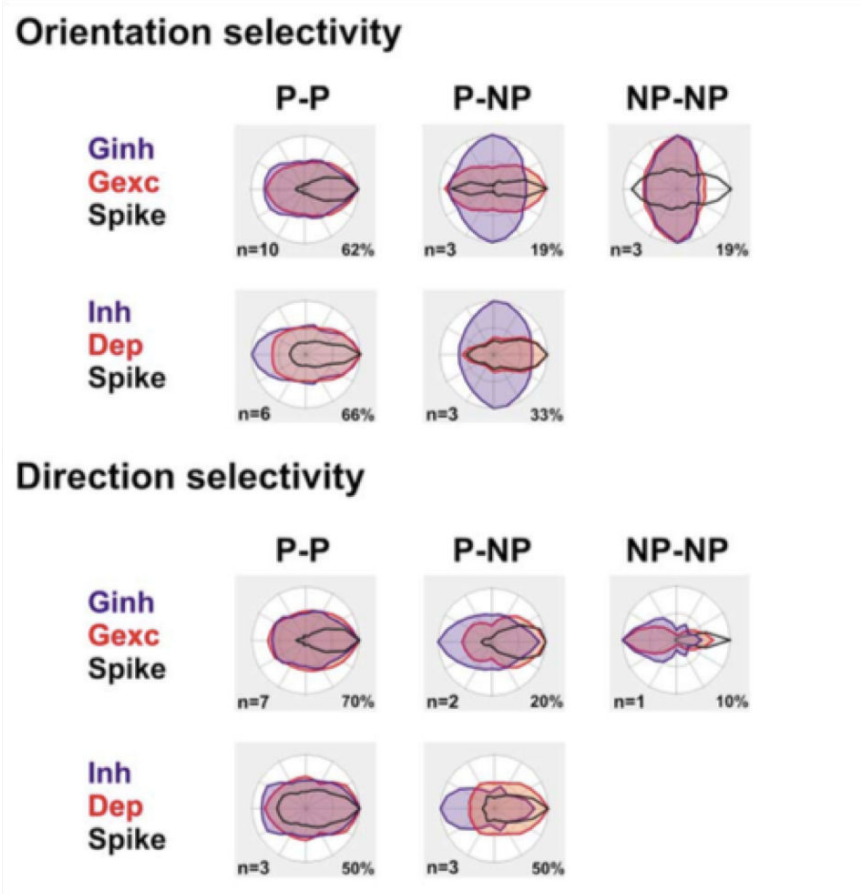


*Figure 45 Three patterns of co tuning present in cat visual cortex for orientation (top) and direction (bottom) selectivity. Top row in each panel contains results based on conductance measurements, showing three*

*possible patterns of tuning in comparison to spiking response. PP, P-NP and NP-NP corresponds respectively to group 1, 2 and 3 (main text). Lower row of each panel contains results from current clamp estimations.*

Both for orientation and direction tuning, the most frequent tuning behavior (70% of cases) was the one when the synaptic input is in agreement with the spiking tuning. However, the synaptic input tuning was always less sharp than the spiking one. The second group constituting around 20% of cases, with the inhibitory synaptic input less sharply tuned than excitation.

The least common was the third group (around 10%), where the inhibitory input was slightly more tuned to the null direction as compared to the excitatory input, even if both were less tuned to the preferred direction as compared to the null direction. The cells from the first group was characterized by the highest direction selectivity index (measured on spiking output - $0.76 \pm 0.25$) compared to the two other groups, which showed a direction selectivity index around 0.2. These authors also analyzed the temporal overlap between excitatory and inhibitory components, defining a temporal overlap index based on cross-correlation between the inputs (TO, where a TO index of 0 was interpreted as an anti-phase shift, or 180 degrees, between the components, and a TO equal 100 would mean that both components are in phase).

For the 1st group of cells, characterized by excitatory and inhibitory tuning in agreement to the spike tuning, the excitatory and inhibitory parts were out of phase for the preferred direction/orientation, and in phase for the non-preferred stimulus. For the other two cell groups a high overlap between synaptic inputs components was demonstrated.

Presented synthesis of synaptic input underlying tuning in cat visual cortex is only partially related to our work on mouse but provides a context of observed synaptic inputs, their dynamics as well as methodology used. Presented in the thesis data from mouse V1 were collected on the preferred direction.

### 4.2.2. Conductance changes in mouse primary visual cortex

Results from cat visual cortex provide an important context to our studies on the mouse, even if these species are known to have a different spatial functional architecture of cells in the cortex (Kaschube 2014). Specifically, the visual cortices of cats, ferrets and higher mammals' cells show a so called 'pinwheel' cortical organization, where similarly tuned cells are close to each other, creating areas tuned for a given direction/orientation of stimuli. In contrast, lower mammals including rodents show a 'salt and pepper' organization of the cortex, where cells seem to be randomly distributed across the cortical space. Taking into account that in general the connectivity of cells is high between neighboring cells, decreasing with the distance, it is valid to compare the synaptic inputs in these two different scenarios to find out how tuning arises in each architecture. Intuitively, the different architectures presumably could lead to different synaptic connectivity arrangements, which for

mouse could be less random than in cat (where the spatial arrangement of cells is not random). This difference in the randomness should be apparent at the level of synaptic input to the cell, for example possibly as the tuned synaptic input.

Two papers investigated orientation selectivity in mouse visual cortex based on conductance measurements (A. Y. Y. Tan et al. 2011; B. Liu et al. 2010)under anesthesia. The comparative study of Tan et al 2011 presented results from both cat and mouse neurons. In general, mice orientation selectivity was much weaker than cats, with the orientation selectivity index (OSI) based on evoked spiking rate between 0.4 and 1 for cats, as compared to 0 to 0.8 for mice (0 means that the cell responses are equal for all orientations, and 1 indicates sharp tuning for one orientation). Additionally, the distribution of cells with different OSIs was flat for mice, whereas for cats cells with high OSI were dominate (Figure 46 A). The OSI based on membrane potential changes showed a lower selectivity as compared to spikes for both cat and mice, but still the difference in the tuning was clear between species (Figure 46 B). The majority of mice cells had an OSI for the membrane potential between 0 and 0.2, whereas for cats the OSI was between 0.2 and 0.4. With respect to conductance changes, both excitation and inhibition were tuned the same as the membrane potential for mice, with the OSI index for excitatory and inhibitory components similar to each other and to the OSI of the membrane potential.

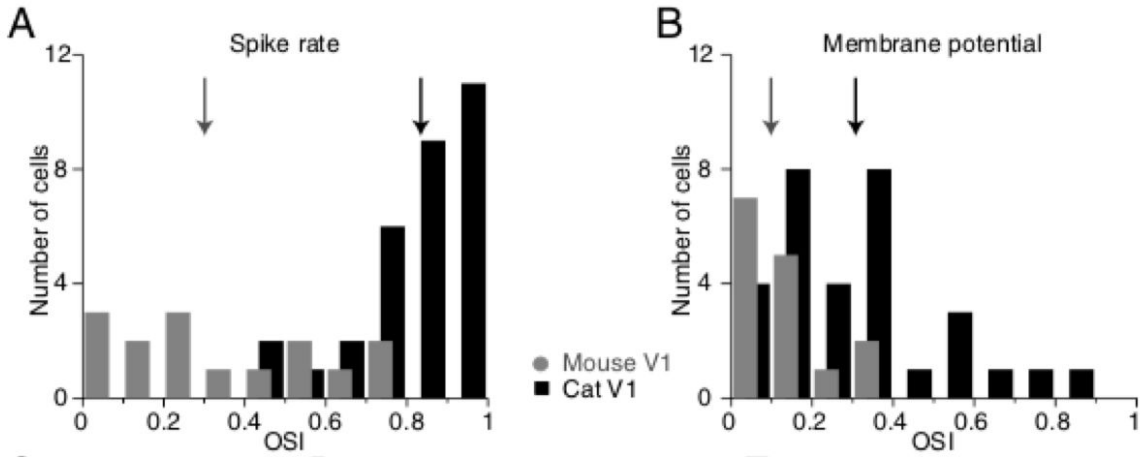


*Figure 46 Orientation selectivity index distribution in cat(black) and mouse(grey) visual cortex. A. OSI distribution based on the spiking rate response B. OSI distribution based on the membrane potential changes. (modified after Tan et al. 2011).*

An analysis of the selectivity of the response over its time course showed that the OSI index is fairly stable from the very beginning of the response in the mouse. The excitatory and inhibitory evoked conductance and the membrane potential was compared for different orientations in 25 ms periods between the onset and offset of stimuli, showing that overall synaptic input components shared the orientation selectivity of the spike output. Moreover, these authors noticed an adaptation component in the synaptic input. Comparison of the maximal peaks occurring during the first 0.5 s of the response and the last 0.5 s (total stimulation time 1.5 s at 2Hz) of the excitatory and inhibitory waveforms (assigned to the orientation evoking maximal conductance change) showed adaptation in

both components. In 30% of cells the adaptation was similar, with larger adaptation for inhibition in the remaining 70% of cells. In contrast, neurons in cat visual cortex did not show statistically significant adaptation.

The visually evoked changes of excitatory and inhibitory synaptic components differ between the two species. The response of the components for the preferred orientation stimuli for simple cells was temporally shifted for cats. In agreement with previous papers investigating synaptic dynamics underlying orientation tuning in cat, the phase shift was close to 180 ° (on average 157±7°). In contrast, these components were overall in phase in mice, with a majority of cells showing a phase shift less than 30°(average shift was 39±12°) (Figure 47).

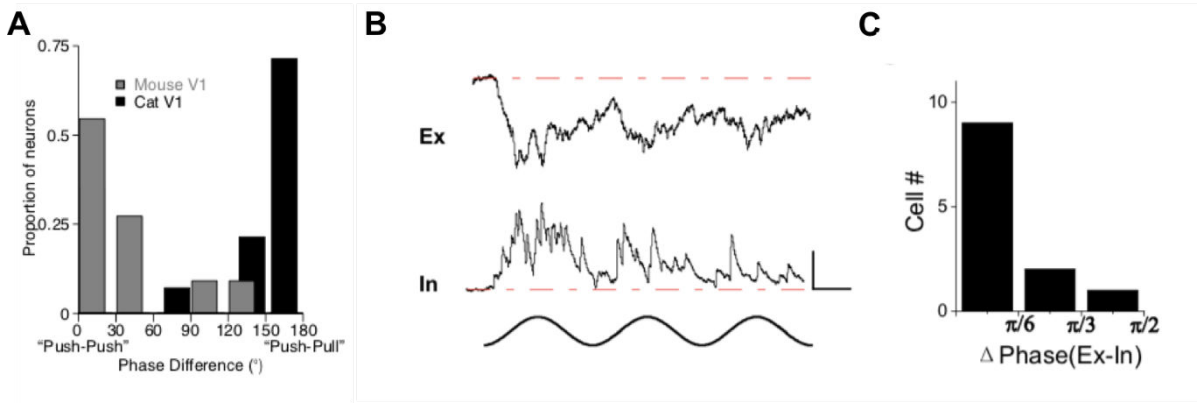


*Figure 47 Temporal interplay of excitatory vs inhibitory synaptic components in cat and mice. A. Distribution of phase shifts in cat and mice neurons (estimated as the difference between phase angles measured at 2Hz) (modified after Tan et al. 2011). B. Exemplary excitatory (Ex) and inhibitory (In) currents evoked in response to sinusoidal grating (bottom). Scale bar: 0.11(Ex)/0.3(in) nA, 200 ms. C. Distribution of difference in temporal phase in mouse neurons Temporal shift assessed by performing Fourier transform (modified after Liu et al. 2011))*

The work of Liu at al 2011 also investigated synaptic input underlying orientation selectivity in mouse primary visual cortex. The group focused on simple cells, which are present mainly in L2/3 of mouse V1 (B. Liu et al. 2009). Similarly to the findings of Tan et al. 2011, this work reported OSI values between 0 and 0.4 based on membrane potential changes. On the other hand, they reported higher and therefore more tuned OSI values based on the spiking rate response, ranging between 0.3 and 1. All simple cells in the study were considered by the authors as selective (as their OSI based on spikes was higher than 1/3)(B.-H. Liu et al. 2011).

The conductance change in simple cells was measured and the peak amplitude of synaptic components compared to construct tuning curves. The orientation dependence of the peak excitation was weak (OSI ~0.25), with a lower index for the inhibitory component. These authors also reported a general balance between excitation and inhibition, expressed as the I/E ratio, on average 2.1±0.88 defined by comparing peaks of inhibitory and excitatory conductance evoked by the same stimuli averaged per cell.

The temporal interplay between the synaptic components was established to be in phase – with a phase shift below 30° in a majority of simple cells (based on the peak response)

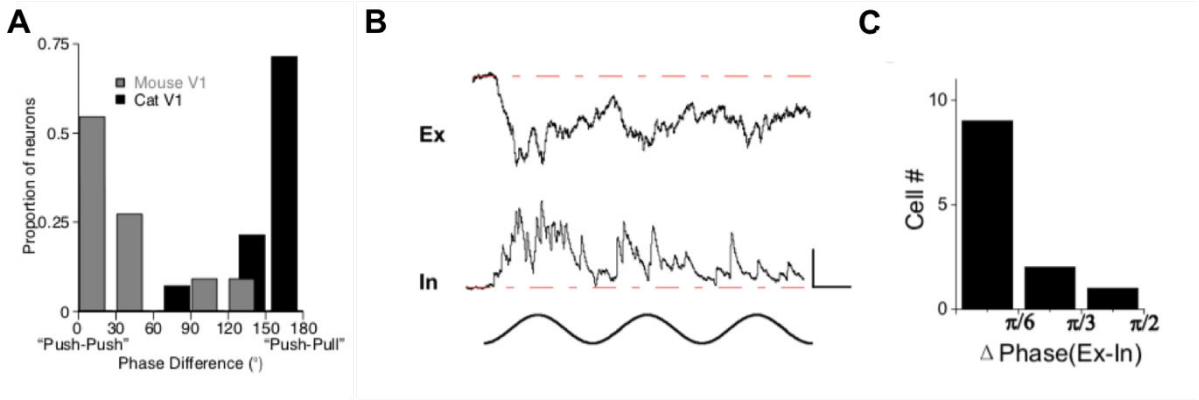


(B-H.Liu et al.2011)).

In summary, both studies in the mouse describe excitatory and inhibitory conductances as synchronous waveforms with a low OSI, in contrast to results from the cat. These studies do not provide any direct information about the amplitude of evoked conductance change, though an examination of the figures suggests rather low amplitudes of the peak conductances, with estimated ranges of 0-3nS for Ge and 0-8 nS for Gi (B.-H. Liu et al. 2011), and 0-10 nS for both Ge and Gi (A. Y. Y. Tan et al. 2011). Interestingly, the inhibitory component was frequently lower in amplitude than the excitatory part (A. Y. Y. Tan et al. 2011), suggesting an I/E ratio below 1. In contrast, as mentioned (B.-H. Liu et al. 2011) estimated an I/E ratio of around 2 based on the peak inputs. It is possible that some of these differences between the findings might be due to the technical details as well as different anesthesia protocols (look Table 4).

A bit different point of view is presented in (Haider, Häusser, and Carandini 2013). This work compares spatial selectivity and conductance changes in mouse V1 in both anesthetized and awake animals, reporting that spatial selectivity is much stronger and characterized by a faster onset in the awake state. Visually evoked conductances were dominated by inhibition in the awake condition, whereas a similar amplitude of the excitatory and inhibitory components was seen in anesthetized animals. Interestingly, these authors comment that the overall input conductance Gin did not differ between awake and anesthetized condition, both at rest and during the visual response. This suggests that, the ratio between excitation and inhibition needed to be changed between the two conditions. Indeed, the authors demonstrated that in the anesthetized group, after stimulus onset excitation and inhibition showed similar amplitudes of conductance change (ratio ~1). In contrast, during wakefulness, inhibition change was 1.4 to 2.9 times larger than excitation change. Moreover, both response onset and offset were much more rapid in the awake state, with a total response duration of less than 200ms (whereas it was prolonged up to 500 ms for anesthetized conditions). In awake conditions, the evoked excitatory component was characterized by a lower amplitude and inhibition dominated for all stimulus directions. Interestingly, in response to the brief 100ms visual stimuli used in the study, the evoked conductances were similar between all the recorded cells (n=14), evoking conductance changes relative to Gin of around 20% (with low standard deviation for awake

conditions). In both conditions, the measured amplitude for excitatory and inhibitory evoked conductance was between 0-5 nS. This work provided convincing data about changed brain dynamics influencing synaptic conductance changes seen at the level of changes E/I balance and response dynamics.

Another study in awake mice reports differences in evoked conductance between quiet wakefulness and locomotion (Bennett, Arroyo, and Hestrin 2013). The study found that that visual response during locomotion is enhanced in comparison to quiet state. During locomotion the response was characterized by higher amplitude, with lower trial to trial variability. The authors reported E/I ratio that favored inhibition. Conductance changes were averaged across stimuli windows, with reported values of 0.5 nS for Ge and 0.9 nS for Gi during quiet wakefulness, and 1.2 nS and 1.5 nS for Ge and Gi respectively for the moving state (n=8 cells examined in both states). Additionally, the effective reversal potential was more depolarized during the moving state as compared to quiet wakefulness.

Although, the results of (Haider, Häusser, and Carandini 2013) and (Bennett, Arroyo, and Hestrin 2013) might seem contradictory, it should be noted that the visual stimulation and the recording conditions were different. Haider at al used short 100 ms visual stimulation, whereas Bennet used much longer stimulation of 1.2 s. Additionally, Haider was comparing two different states – awake and anaesthetized whereas Bennett was comparing between two awake states. Both studies reported estimated conductances that were lower to those obtained in the anesthetized cat. Additionally, in agreement to (Haider, Häusser, and Carandini 2013), the work of (Bennett, Arroyo, and Hestrin 2013) reported a prevalence of the inhibitory component in both awake states. However, the difference between the excitatory and inhibitory components during locomotion was smaller than in quiet wakefulness, and the difference of each component between states is higher for excitation. Thus, during locomotion, the excitatory component relative to the quiet wakefulness changes increases more than the inhibitory component, as reflected in a more depolarized effective reversal potential. These studies stress the presence of different E/I ratio associated with different brain state.

Studies investigating conductance changes underlying feature selectivity in other modalities have been done by other groups (M. Wehr and Zador 2005; Higley and Contreras 2006; Wilent and Contreras 2005; M. S. Wehr and Zador 2003). In summary, several different patterns of conductance change have been described. For example, in auditory cortex inhibitory inputs were tuned similarly to excitation (showing a bit wider tuning) (M. S. Wehr and Zador 2003; Wu et al. 2008). In contrast, to the evident temporal interplay demonstrated in the cat visual cortex, the excitatory and inhibitory components were shown to be strongly synchronized in rodent somatosensory (Higley and Contreras 2006) and auditory (M. S. Wehr and Zador 2003) cortex, with only a short (but possibly important with respect to circuit function) latency of inhibition. Interestingly, response lag in auditory cortex was not dependent on the sound frequency(M. S. Wehr and Zador 2003), whereas in somatosensory cortex the lag between excitatory and inhibitory part seems to be stimulus dependent (Wilent and Contreras 2005).

In summary, visually evoked conductance changes in the cat are characterized by a substantial temporal interplay between excitation and inhibition, overall supporting a push pull model, at least for simple cells. Substantial evoked conductance changes, on average around 150%, are present, with a clear tuning.

In contrast, in mouse visual cortex the neuronal response is less selective (at least in case of orientation tuning) and there is no clear phase shift between the synaptic components. Additionally, inhibition was shown to be even less selective (more broadly tuned) than excitation. Although, there is prevalence of inhibition in the awake state, overall the amplitudes of changes are smaller than those measured in cat. Although the previous studies investigated the conductance orientation tuning and some aspects of dynamics of excitatory and inhibitory components, it is worth to stress that exhaustive description of visually -evoked synaptic input description was missing. The qualitative and quantitative description of visually-evoked synaptic input is one of the goal of this work and it is planned as a separate publication.

## 4.3. Investigation of synaptic input changes in light anesthesia conditions: experimental results

While the literature provides a basis for understanding the biophysics of synaptic conductances with respect to visual processing, the results to date do not present a totally consistent perspective. Reported values of conductance changes in the mouse (A. Y. Y. Tan et al. 2011; B.-H. Liu et al. 2011; Haider, Häusser, and Carandini 2013; Bennett, Arroyo, and Hestrin 2013) are relatively low in comparison to values presented in cat (Jeffrey S Anderson et al. 2014; Frégnac et al. 2003; Borg-Graham, Monier, and Frégnac 1998). Some of these changes in amplitude might be due to different visual stimulation used in different studies. Additionally, brain state seems to influence the findings (Haider, Häusser, and Carandini 2013; Bennett, Arroyo, and Hestrin 2013). In that regard, in this thesis I will present the experimental results of conductance measurements performed in mouse visual cortex, in low anesthesia condition.

In our studies 0.25% isoflurane was used, in conjunction with the sedative chlorprothixene hydrochloride. This combination enables recording of brain activity that closely resembles the quiet awake state (Bennett, Arroyo, and Hestrin 2013). Our responses were characterized by low trial to trial variability between stimuli repetitions and rapid latencies for both onset and offset of the stimuli of below 200 ms, similarly to those reported in the awake state (Haider, Häusser, and Carandini 2013).

### 4.3.1. Conductance change in mouse V1 – experimental results.

#### *4.3.1.1. Criteria for including/excluding cell for analysis*

The results presented in the following two chapters come from cells characterized by both reliable conductance estimation and dynamic clamp (DC) mode protocols. Conductance estimation in each cell was based on at least 10 repetitions of visual stimuli was recorded during collection of evoked currents during the VC part of protocol. Another condition considered estimated conductance contribution to the membrane potential changes. If at least partial overlap between the traces of averaged visually evoked potential and estimated membrane potential (based on measured conductances) was present, the cell was included in the data. Additionally, in all the cells DC protocols were performed (results in chapter 5). The averaged membrane potential dynamics induced by introducing measured conductance waveforms (with no prior modification) was compared with visually evoked one. The data set is characterized by 67 $\pm$ 20% overlap of voltages and spiking observed approximately at similar spike times (detailed results in chapter 5). Minimal number of 8 points (8 different recording condition) was set to construct basic I/O transfer function. Figure 48 show the distribution of cells according to the number of GER protocols (DC probed conditions) performed per cell. On average 35 conditions were probed which provided a dense data grid for I/O transfer function construction.

In total, 62 cells were included in the data set presented in the thesis, which allowed for the construction of 95 different I/O transfer function, and come from 47 animals (220 animals were used during total duration of the project). In some cells with sufficiently stable recordings, transfer functions were derived from different stimulus sizes and /or conductance filtering.

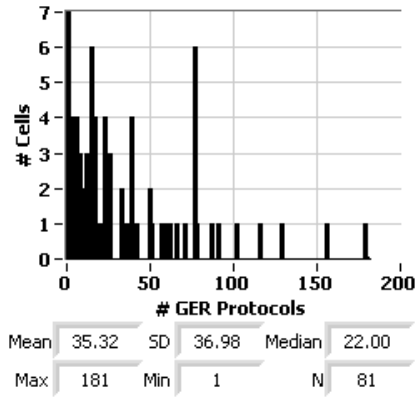


*Figure 48 distribution of all the cells containing DC recordings depending on number of GER files, which provide the number of tested E/I ratio conditions tested per cell. From 81 cells on which the attempt to perform DC recordings was done 62 fulfilled the inclusion criteria.*

One indicator of the recording quality is a low VC bridge error/Rin ratio (fig VC relative bridge error statistics). The ratio describes the relative to input resistance difference between access resistance compensation present on amplifier during VC measurements and the fully compensated during CC recordings (bridge error). On average the ratio was equal to 0.54 $\pm$ 0.31 (mean and SD)(Figure 49).

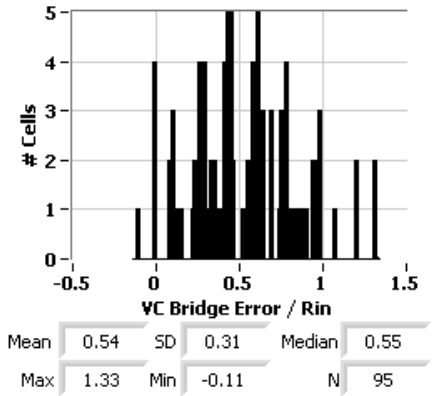


*Figure 49 VC Relative Bridge Error Statistic assessed for each I/O transfer function*

Recordings come from superficial cortical layers- mainly layer 2/3 and 1. The mean depth of recording was assessed to 146 $\pm$ 109,4 μm (mean and SD) based on the position of the tip of the electrode in the tissue. The depth of recording was estimated based on the manipulator position. Ranges of cortical depths are adopted from in vitro work of (Xu et al. 2016) and are color coded according to the layer (grey – unspecified, green-L1, blue-L2/3, purple-L4, red-L5a). Figure 50 presents the

distribution of the cell across cortical layers and the plot describing type of the cell assessed during data analysis.

Cell type was assessed based on the spike shape characteristics as Fast Spiking (FS) or Regular Spiking (RS). If the bursts were present during current step protocol (steps of increasing amplitude), the cell is described as bursting and is included in RS group.
Together, the data set contains: 48 regular spiking (including 7 bursting cells), 7 fast spiking and 7 unspecified cells (no recording allowing type assessment).

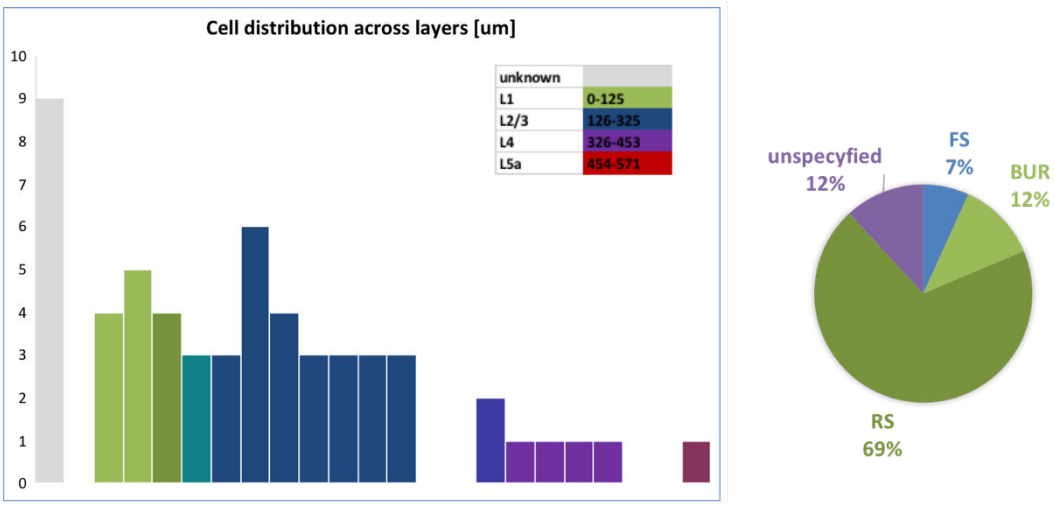


*Figure 50 Cell distribution across cortical layers and cell type. Bars of the histogram are color coded according to the layer (legend with depth ranges used written). Bars in between layers are marked by intermediate color to stress the approximated character of the measurement. Each bar indicates 20 μm intervals. The first bar shows the cells for which the depth of recording was not measured.*

Depth of recording did not influence cell parameters or quality of measurement (Figure 51). No relationship or clusters are visible on the plot relating cell parameters vs. recording depth. The means and SD for cell parameters and bridge error presents Table 5. Figure 52 shows distribution of cell input resting resistance, conductance and membrane potential. These parameters were measured several times during the recording. Center of the linear regression to all the points is shown in the distribution to provide average parameter value with no influence of the number and time of taken measurement.

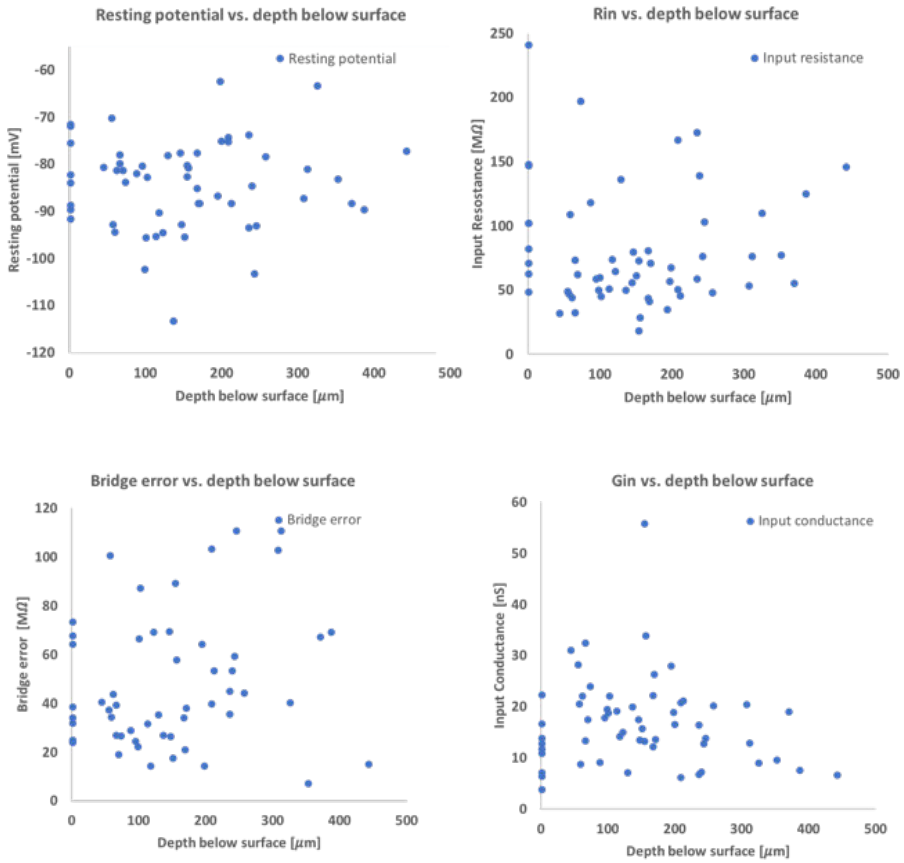


*Figure 51 Lack of depth influence to the recording and cell properties. Recordings for which depth was not provided are also included in the plots (at 0)*

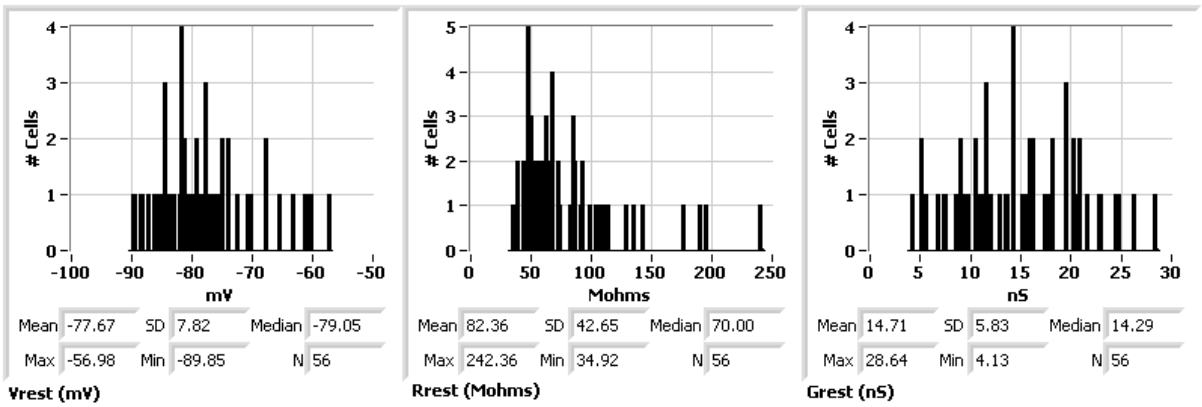


*Figure 52 Statistics of resting potential and resting input resistance and conductance (based on several measurements collected over entire recording duration).*

*Table 5 Mean and SD of cellular and recording properties for a data set measured at the beginning of recording.*

| | Resting potential [mV] | Input resistance [mΩ] | Membrane capasitance [pF] | Membrane time constant [ms] | Input resistance [nS] | bridge correction applied on amplifier [mΩ] | total bridge | depth below surface [um] |
|---|---|---|---|---|---|---|---|---|
| Mean | -83,60 | 81,21 | 0,22 | 15,02 | 17,28 | 41,81 | 46,54 | 146,34 |
| SD | 10,18 | 44,98 | 0,09 | 8,11 | 8,75 | 25,06 | 27,44 | 109,45 |

### *4.3.1.2. Stimuli -evoked conductance changes*

$G_{in}$ evoked changes:

Evoked conductance changes in response to 0.5 s grating visual stimulation were analyzed in both absolute [nS] terms and relative to resting conductance ($G_{rest}$) (Figure 53 ). Absolute values for conductance changes were in the range of 6-72 nS measured at the maximum peak for each cell after low – pass filtering the traces at 20 Hz. The mean and SD was respectively: 26.19 $\pm$ 15.17 nS respectively and the median: 20.92 nS. The relative amplitude of Gin peak was 1.12-4.58 times larger than conductance before stimuli onset (12-458%). The mean ΔG was equal 83% $\pm$ 65% (median: 66%). The distribution of ΔG shows variability of evoked changes. ΔG values looks different if instead of the maximal peaks the whole conductance change would be averaged over the time of stimuli (Figure 54). The relative conductance change varied between 0.2 and 9.83 with mean of 2.09 $\pm$1.79. The difference between the peak of evoked conductance and the average evoked conductance for each cell suggest that the evoked conductance waveforms contained many peaks.

Additionally, the average change of conductance relative to the resting state increase was 0.02-0.89 (mean and SD:0.16$\pm$0.13).

Next, evoked conductance was split in excitatory and inhibitory component based on the value of momentary reversal potential for all time points when the ΔG was bigger than 5%. The absolute range of excitatory peaks was in between 0.53-12.49 nS with the mean and SD of 3.14 $\pm$ 2.09 nS (Figure 53). The relative excitatory conductance change was in the range of 0.06-0.86 with mean of 0.23 $\pm$ 0.14. The excitatory conductance averaged over entire stimuli duration value was on average 0.65 $\pm$ 0.46 nS and 0.05 $\pm$0.03 (absolute and relative to $G_{rest}$ value respectively) (Figure 54). Thus, the average value of evoked excitation at the peak was almost 5 times higher than on average (both for absolute and relative values).

Inhibitory component changes were characterized by higher amplitudes. The absolute values (Figure 53) of measured inhibitory conductance were between 0.78 and 41.94 nS with the mean and SD of 9.74 $\pm$9.74 nS. Relative inhibitory conductance evoked was between 0.09-3.58 with the mean and SD of 0.69 $\pm$0.62. Quite big standard deviation value in comparison to the mean points to the wide distribution of all conductance changes. The inhibitory conductance averaged over entire evoked response (Figure 54) was on average 1.44 $\pm$1.57 nS which was on average 0.11 $\pm$0.12 of $G_{rest}$. The peaks for inhibition were approximately 6.5 times higher than the average inhibitory value.

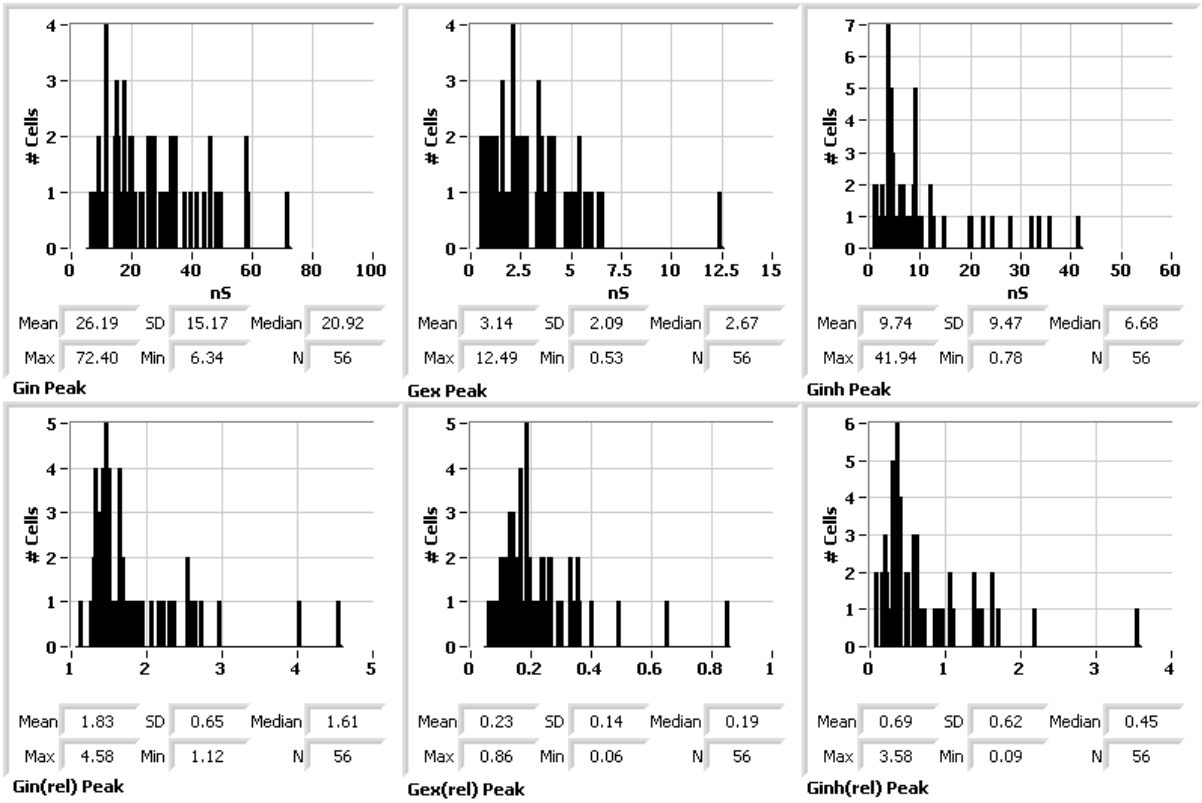


*Figure 53 Statistics of peaks of evoked $G_{in}$, $G_{inh}$ and $G_{exc}$. Relative conductance measures are taken with respect to the resting conductance $G_{rest}$. The difference between the peak values of the evoked $G_{inh}$ and $G_{exc}$ are statistically significant ($p <= 0.001$).*

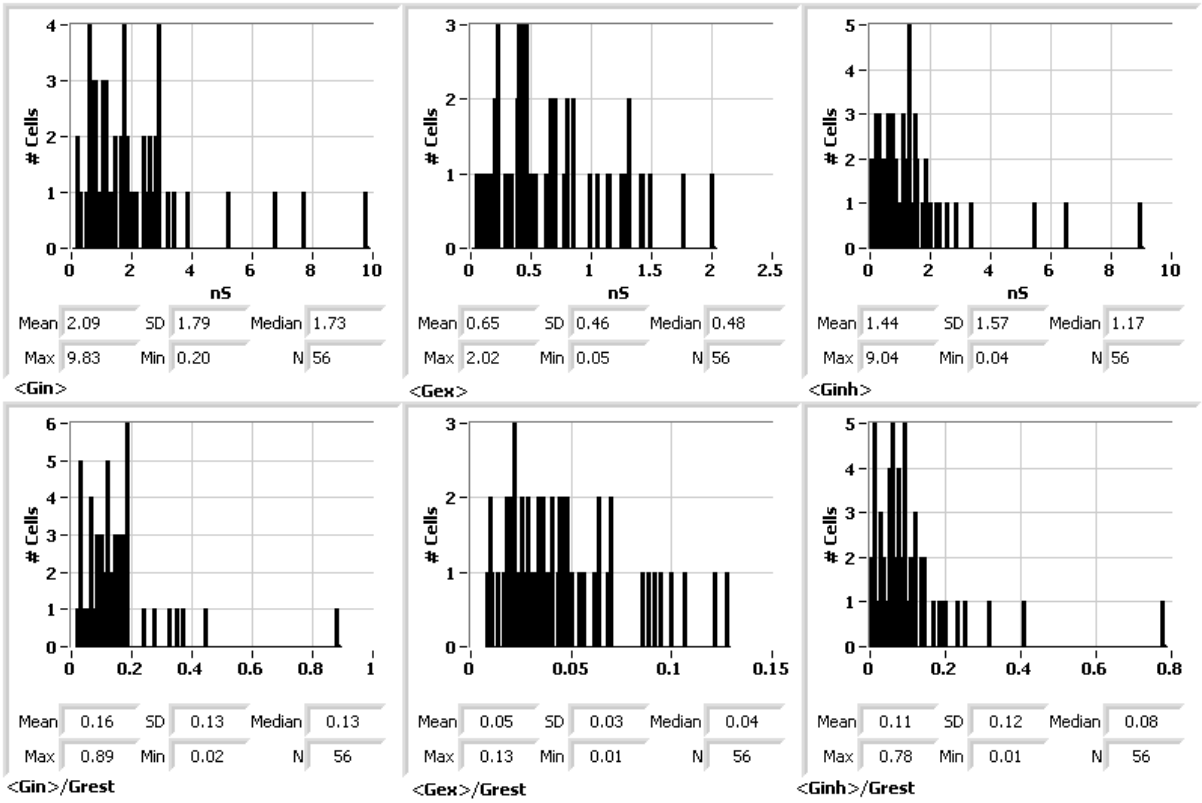


*Figure 54 Statistics of averages of evoked $G_{in}$, $G_{inh}$ and $G_{exc}$. Relative conductance measures are taken with respect to the resting conductance Grest. The difference between the average values of the evoked $G_{inh}$ and $G_{exc}$ are statistically significant (p<= 0.001).*

The distribution of momentary reversal potential Figure 55 at the maximal ΔG values shows that the maximal change occurred usually in the proximity of cell resting potential suggesting the prevalence of shunting inhibition in the evoked visual response. Although comparison of the means of resting potential and $E_{rev}$ at maximal value of ΔG (-55 ± 13.28 mV) shows that the $E_{rev}$ was almost always more depolarized than the cell resting potential (by mean of 22.16 ±14.48 mV).

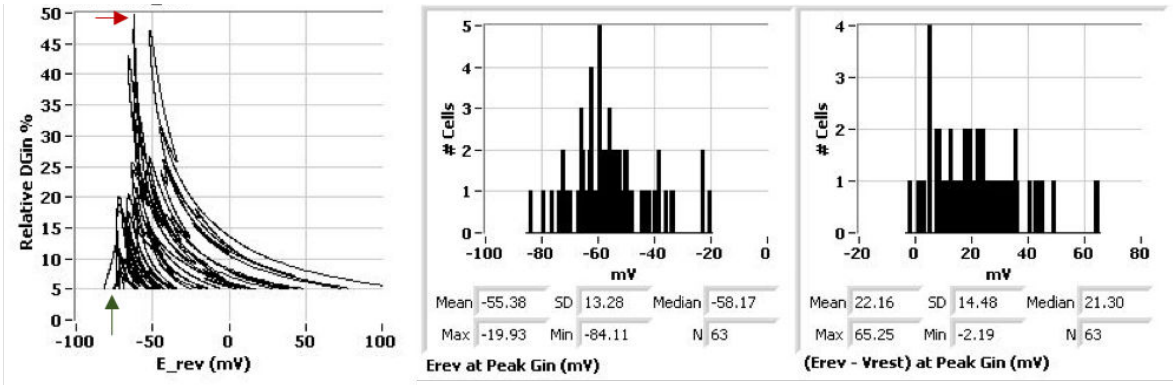


*Figure 55 Statistics of the effective synaptic reversal potential ($E_{rev}$) at the peak of the cell input conductance during the visual response. Left: Exemplary phase plot of reversal potential vs evoked delta G during visual stimulation. Red arrow marks the maximal change of delta G, green arrow points to cell resting potential (-75mV for this cell example). Middle: Distribution of potential values associated with the peaks of the cell*

*conductance across whole cells population. Right: Distribution of the difference between cell potential at the peak conductance change and resting potential (voltage value indicated by red-green arrow) across cell population.*

E/I ratio:

The interplay between excitation and inhibition might influence the synaptic output. However, the relation between the two components during the visually evoked response is highly variable between different cells, and thus difficult to describe in terms of canonical nmodel. The relation between excitatory and inhibitory maximal response to visual stimuli is presented at Figure 56. The inhibitory peaks were always higher than the excitatory one, which is visible only positive rations of I/E ratios (peaks) and range from 0.49 to 13.5 (Figure 56, left inset histogram). On average inhibition peak was $3.3 \pm 2.49$-fold higher in amplitude (mean and SD) than excitatory maximal peak during the response. It is worth to stress that the two peaks of excitation and inhibition were usually not occurring in the same time point during the response.

If we look at the I/E statistics more globally and compare the averaged component response during the whole stimuli duration the I/E ratio range between 0.16-22.25 with mean of $3.06 \pm 3.81$ (mean and SD) (Figure 56, right inset). However, the distribution of ratios is more focused around the median (1.80) and majority of cell averaged over response I/E ratio is below 5.
The scatterplots of inhibitory and excitatory ratios (expressed as amplitude or average value) visualize the variability of I/E ratios within our dataset. There is no clear relationship between the peaks of excitation and inhibition within a cell (correlation coefficient 0.4) nor the averaged values (correlation coefficient 0.2).

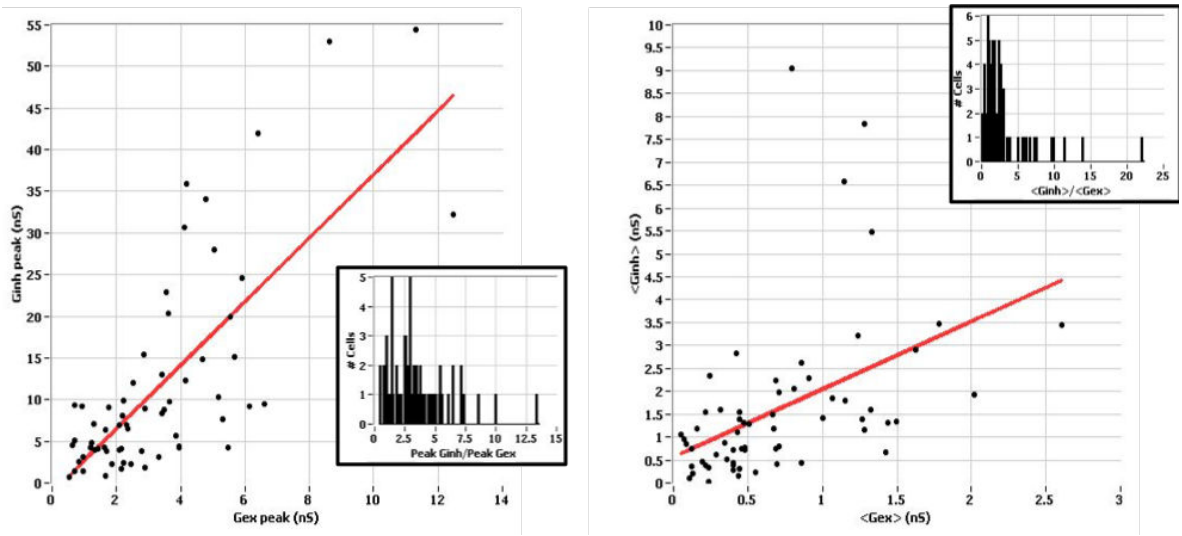


*Figure 56 Excitatory an inhibitory component peak values (left) and averaged over the time of stimuli values (right). The insets present distribution of E/I ratios based on the amplitude of the peak and averaged values (left and right respectively). The differences between the average values of the distributions, and between the peak values of the evoked $G_{inh}$ and $G_{exc}$, are both statistically significant ($p <= 0.001$). No clear relationship between excitatory and inhibitory synaptic component is seen at the cell population level.*

E/I tight balance description:

During recordings it was noted that the excitatory and inhibitory component waveforms have different dynamics. Therefore, it was decided to investigate this topic further in the context of tight balance between synaptic components (Viltart et al. 2018). First, the cross-correlation of the excitatory and inhibitory waveforms was performed, showing a wide distribution of correlations coefficients (Figure 57) and peak lag for the data set (Figure 58). The average correlation coefficient was 0.61 $\pm$ 0.16 (SD) and ranges from 0.18 to 0.88 pointing to variability of relationships between synaptic input components. Additionally, there were no situation when the two components would be following each other or completely out of phase, which would be described by correlation coefficients of 1 and 0 respectively.

The average lag between the peaks was 25 $\pm$23 ms and was not statistically significant. Moreover, the extremely wide distribution of time lag between excitatory and inhibitory component stress the dynamical variability of the components.

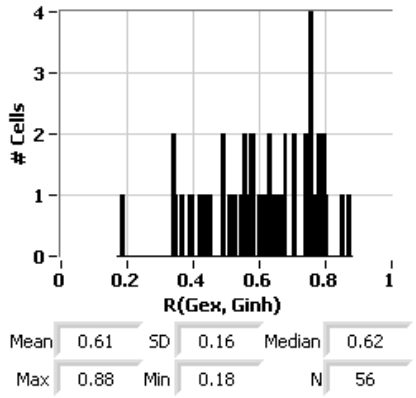


*Figure 57 $G_{exc}$ - $G_{inh}$ Cross Correlation distribution stressing variability of dynamics of both components during visually – evoked response.*

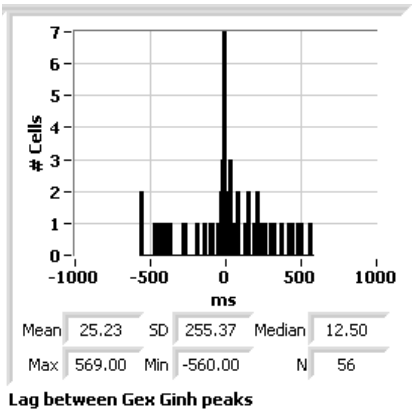


*Figure 58 The average lag between Gex and Ginh peaks (ms), about 25 milliseconds, is not statistically significant. Note the wide distribution of lags in the population.*

Next, the power spectra of the both components were analyzed. Normalized Fourier transform output was compared by finding the center of mass (COM) of each component. The distribution of center of mass for excitatory and inhibitory components is displayed at the Figure 59 (top row). The mean center of mass for inhibitory is equal to 8.42 ±6.12 Hz, whereas for excitatory component 5.47 ± 4.33 Hz. Comparison of the means suggest that the inhibition waveform is characterized by higher frequencies than the excitatory one. This difference was validated by calculating the difference of the COM of the components for each cell. The wide distribution shows various relations between components. Both positive and negative, as well as equal to 0, values are present in the data set. However, on average the difference was -2.95 ±4.47 Hz (statistically significant difference, p<=0.001), thus that inhibition had higher frequencies than excitation.

Additionally, to be able to assess the relative change, the difference of the two centers of mass with the average was compared. The resulting ratio center of mass difference/average distribution is presented at fig. shows ratios ranging from -1.26 to 1, although similarly to the absolute differences distribution, majority of cells show negative values (indicating higher frequency components for inhibition characteristics). The mean and SD is equal to -0.37 ± 0.54. The construction of the ratio indicates low, close to 0 values for small differences between the components and for maximal differences (when one of the components is close to 0) and it would be around 0.5 if one component is about 2/3 of the other (taking into consideration possible values in between 0 -20 which is approximately the ranges of center of mass for excitation and inhibition in our data set). Similarly, the ratio of about 0.3 would indicate that one component is bigger of about ¼ from the other.

The frequency analog of I/E ratio, showing relation of frequencies present in inhibitory component in relation to those describing excitatory one shows that inhibition frequencies were almost twice higher (mean and SD: 1.76 ±0.94). However, as displayed at the scatter plot the cross-correlation coefficient of inhibitory to excitatory center of mass was low – 0.47. Figure 59 presents the revised distributions.

A similar analysis of the cumulative distribution function (CDF) was performed. Both the CDFs of both components were normalized at the frequencies corresponding to the 0.75 level compared.

The distributions of frequencies for inhibitory and excitatory component is characterized by the mean and SD of 12.41 ± 13.82 and 5.8 ±7.88 Hz respectively (Figure 59 bottom row). The distribution of differences and difference to average ratio show similar trend as shown in the analysis of two components center of mass. In majority of cells inhibitory component was characterized by higher frequencies (negative difference of frequencies at 0.75 level) and the mean and SD for difference to average ratio is -0.65 ± 0.77. The ratio around 0.6 indicates that one component was twice as big as the other. The frequency I/E ratio was on average 3.75 ±4.29 favoring inhibition over excitation.

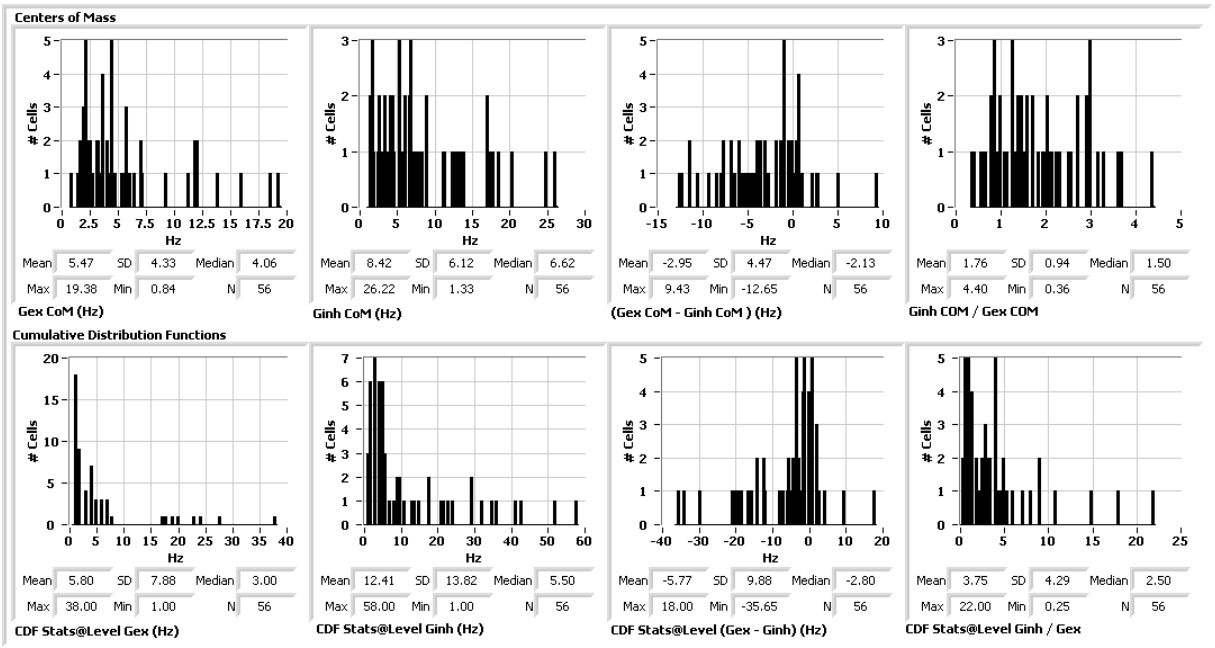


*Figure 59 Statistics of center of mass (COM, top) and cumulative distribution function (CDF, bottom) of $G_{exc}$ and $G_{inh}$ Spectra. On average, both the COM and the 75% level of the CDF for inhibition is at a higher frequency than for excitation (average difference 2.95Hz and 5.77Hz, respectively, p <= 0.001), with a ratio between inhibition relative to excitation of the two measures strongly favoring inhibition (1.76 and 3.75, respectively).*

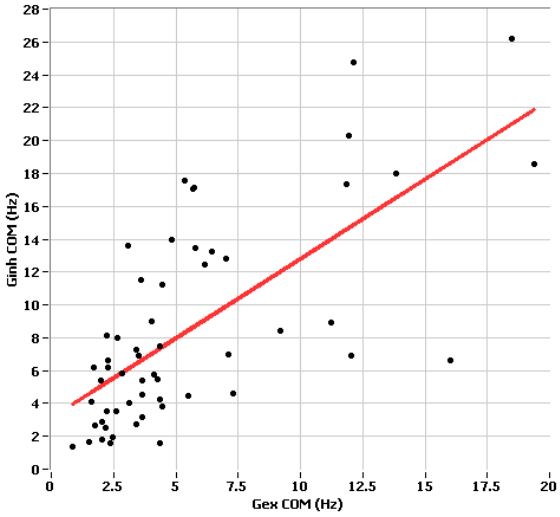


*Figure 60 Relation between $G_{inh}$ COM vs. $G_{exc}$ COM. Higher frequency of inhibitory component is visible.*

Figure 60 displays the I/E frequency ratio for all the data population. Similarly to the amplitude and average I/E ratios there is no clear relation on a cell to cell basis between the frequency. However, in the majority of cases the inhibitory component operates at higher frequencies for each cell.

To provide more insight into the changes of excitatory and inhibitory waveforms I present a few examples coming from our data set (Figure 61). Table 6 contain values of the descriptive parameters for presented cells conductance components.

The visual inspection of these examples illustrates points described previously with respect to the distributions of visually evoked synaptic inputs characterized in our data set. Prevalence of inhibitory content, operating at higher frequency is visible. The variability of dynamics between two components are shown. Maximal peaks amplitude occurs in various moments during evoked response.

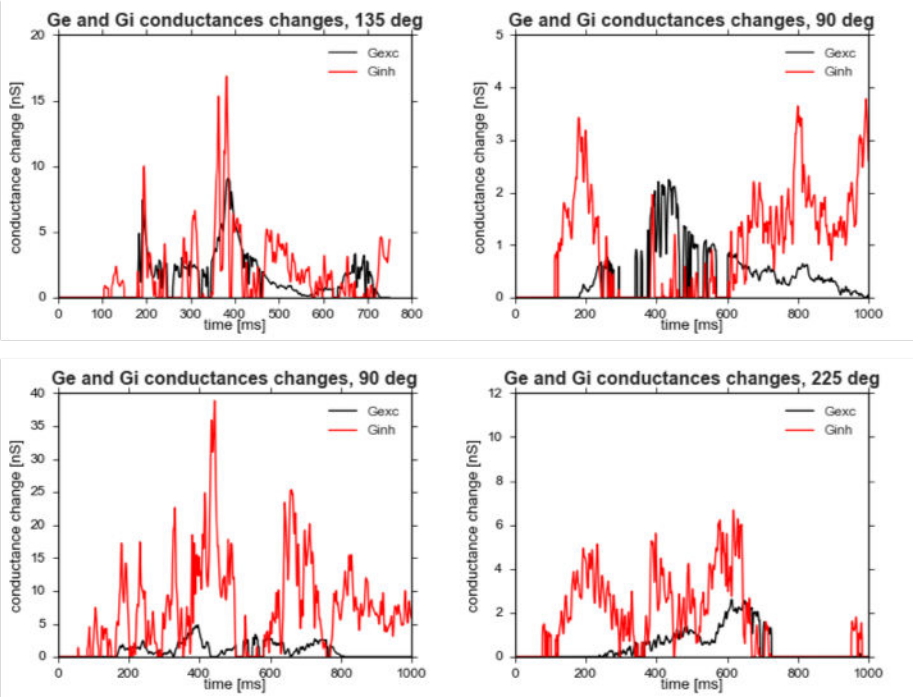


*Figure 61 . Examples of excitatory(black) and inhibitory(red) synaptic input traces to RS cells, measured at the cell soma during 0.5 s grating stimulation. Each example comes from different cell but stimulating conditions were the same. The middle panel shows excitatory and inhibitory waveforms alternating (out of phase) which was not common across all recordings.*

*Table 6 Descriptive parameters of the power spectrum of excitatory and inhibitory conductance. COM-center of mass, CNPS-Cumulative Normalized Power Spectrum*

| | COM diff | COM diff/ mean | CNPS diff | CNPS diff/mean |
|---|---|---|---|---|
| **cell A** | -9,20 | -0,98 | -12,00 | -1,40 |
| **cell B** | -0,32 | -0,14 | -1,00 | 0,67 |
| **cell C** | 0,64 | 0,21 | 1,00 | 0,22 |
| **cell D** | -0,92 | -0,30 | -1,00 | 0,40 |

The difference in the frequency spectrum of excitatory and inhibitory waveforms couldn't be explained by the correlation coefficient between waveforms. For both types of spectrum analysis (COM and at 0.75 level of CDF) were weak (0.16 and 0.06 respectively) (Figure 62 Figure 63). The two types of frequency analysis of the components do not show a strong correlation for COM vs CDF I/E ratio (correlation coefficient of 0.41) (Figure 64).

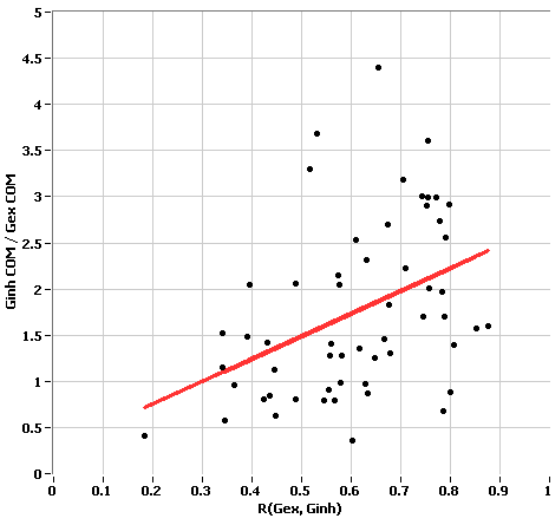


*Figure 62 $G_{inh}$ COM / $G_{exc}$ COM vs. R(Gexc, Ginh)(cross- correlation coefficient of both components). No significant relationship.*

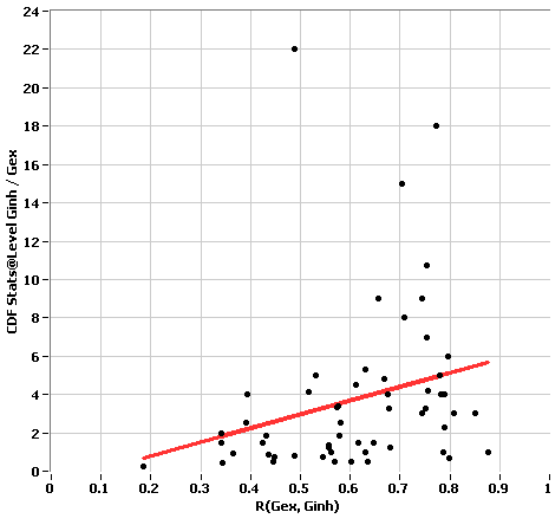


*Figure 63 CDF Stats@Level Ginh / Gex vs. R(Gex, Ginh) (cross- correlation coefficient of both components). No significant relationship.*

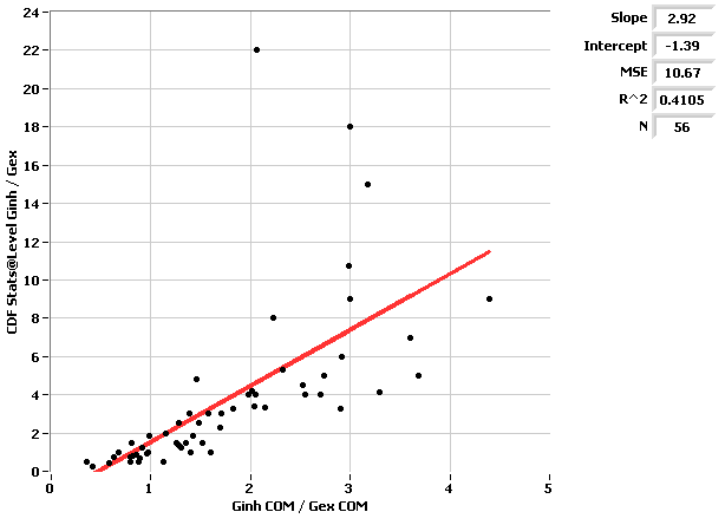


*Figure 64 CDF Stats@Level Ginh / Gex vs. Ginh COM / Gex COM.*

In summary, conductance measurements of visually evoked responses in mouse V1 show a large variability of the synaptic input. High relative amplitudes for both excitation and inhibition were measured, similar to those measured in cats (J S Anderson et al. 2001; Jeffrey S. Anderson, Carandini, and Ferster 2000; Cyril Monier et al. 2003; Borg-graham, Monier, and Fre 1998; Priebe and Ferster 2005). The characteristic of evoked inputs points to the prevalence of inhibitory conductance expressed in higher than 1 I/E ratio seen consequently at different measurements. More fluctuations are present in the inhibitory component, confirmed quantitatively by higher frequencies in the inhibitory response in comparison to the excitatory one. Overall, we do not observe any clear relation between excitatory and inhibitory waveforms and further data analysis in needed.

Figure 65 - Figure 67 provide more perspective to the results. Three cells examples showing described parameters. Additionally, Figure 67 displays the cell conductance which was smoothed with 10 Hz filter. By this operation some part of fluctuations is removed from the synaptic input. The change of cross-correlation between the two components is visible as well as in the frequency spectrum analysis of the components.

In comparison to previously described conductance results, in our work we present data coming from the light anesthesia state. This might be one reason for the larger changes emerging from our data set. Visually-evoked response in the high anesthesia state is characterized by much higher trial to trial variability and, in some preparations, the presence of up and down states, both of which contribute to underestimations of the synaptic conductances. Additionally, the details of the visual stimulation might influence the results. Specifically, a short 100ms flash stimulation and a long 1.5 second grating stimulation might indeed evoke different synaptic amplitudes or averages. On the other hand, it is also likely that different technical details might influence the amplitude of the findings (e.g. high access resistance of recordings).

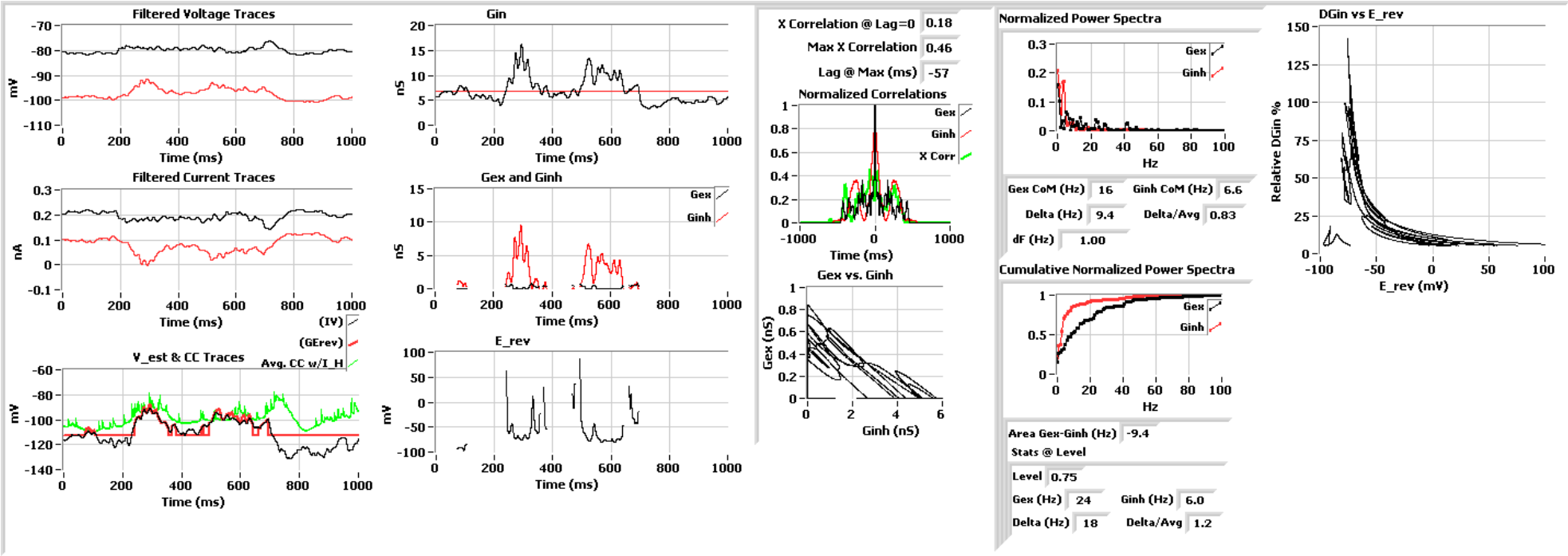


*Figure 65 Conductance analysis of cell with highly uncorrelated $G_{exc}$ and $G_{inh}$. The phase plots of $G_{exc}$ vs. $G_{inh}$, and Delta$G_{in}$ vs $E_{rev}$ reflect this relationship. In the former, the trajectories tend to be orthogonal to that expected for a strong coherence between excitation and inhibition; in the latter, the trajectories trace the "Eiffel tower" form, as seen in Borg-Graham et. al 1998.*

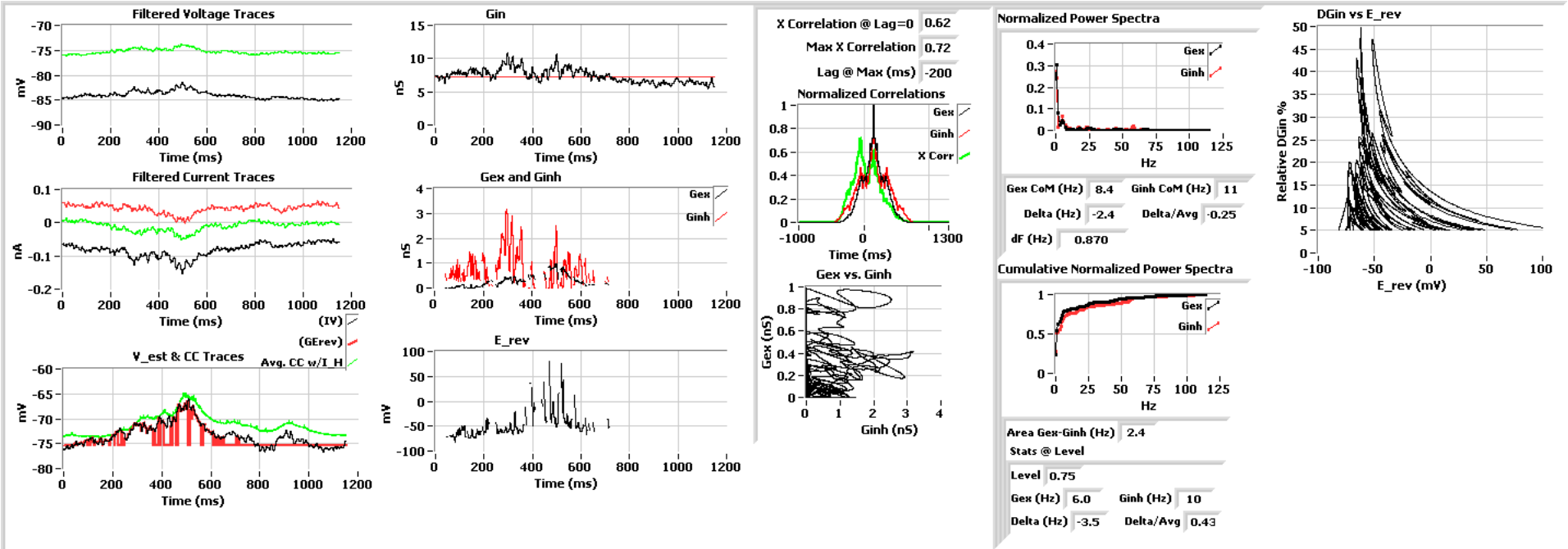


*Figure 66 Conductance analysis of cell with typical correlation between $G_{exc}$ and $G_{inh}$. The phase plot of $G_{exc}$ vs. $G_{inh}$ show a "chaotic" relationship, and Delta$G_{in}$ vs $E_{rev}$ plot shows the "Eiffel tower" form, as seen in Borg-Graham et. al 1998.*

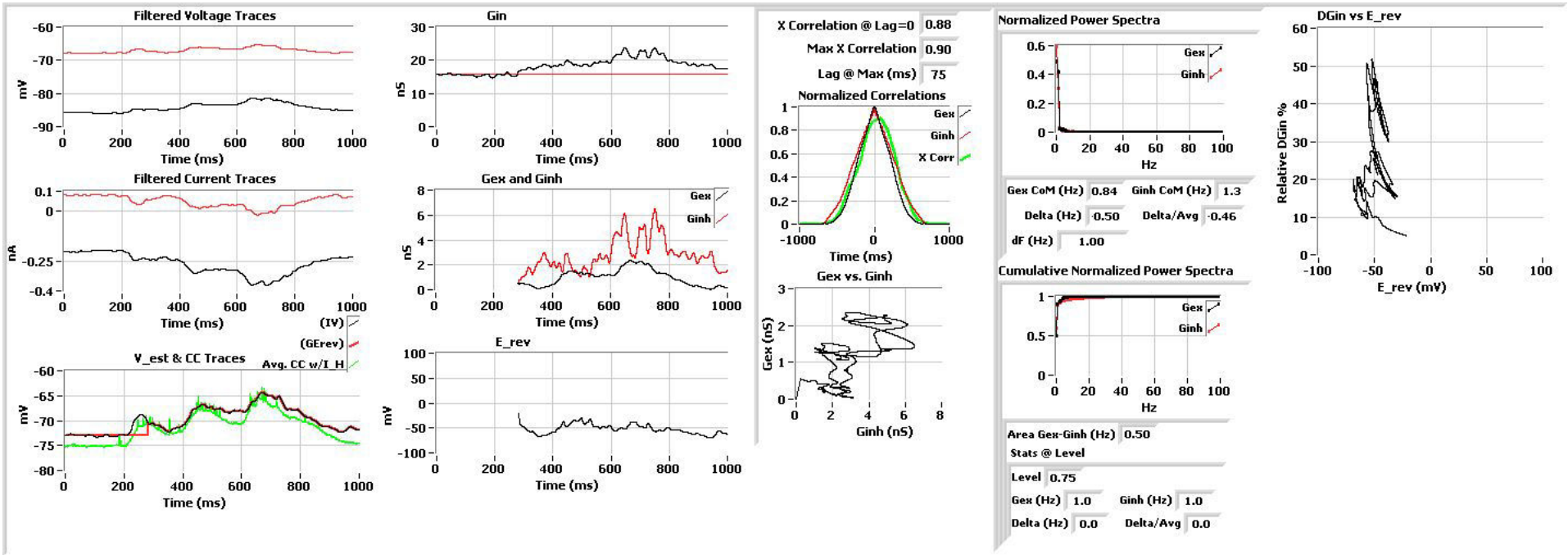


*Figure 67 Conductance analysis of cell with high correlation between $G_{exc}$ and $G_{inh}$. This is evident in the phase plots of $G_{exc}$ vs. $G_{inh}$, where there is a less "chaotic" trajectory as compared to the other examples, and in the Delta$G_{in}$ vs $E_{rev}$ plot, where the domain of $_{Erev}$ is relatively constrained. Note that all the traces displayed comes from filtered (10 Hz Low pass filter) current and voltage traces which results in conductance estimation lacking part of high frequency component. Such traces were introduced back to the cell and the spiking response was assessed (data still under analysis, not presented in the thesis). However, the influence of filtering might be seen in the change of the cross-correlation and frequency powers spectrum analysis.*

# 5. Probing the transfer function of a neuron in vivo

To better understand how neurons integrate its conductance inputs discussed in the previous chapter, we must also consider the cell's response to those same inputs.
This chapter will present the experimental protocol developed for probing the I/O transfer function in vivo and the results of these experiments.

The results from this chapter will be published as two manuscripts (in preparation). Note that the rat and cat data cited in the first manuscript was collected by the laboratory prior to the present thesis work.

> Inhibitory Modulation of the Conductance-Spike Transfer Function of Cortical Neurons of the Cat, Rat and Mouse In vivo
> Marta Gajowa, Adrien Schramm, Daniele Marinazo, Thomas Gener, Lyle Graham
>
> Using whole-cell patch recordings, we examine the conductance-based input-output transfer function of regular-adapting, fast-spiking, bursting and chattering neurons in vivo in the visual cortex of the cat, rat and mouse. We find that the spiking response to steps of simulated synaptic excitation is significantly modulated by inhibition, depending on the physiological firing type. Overall, shunting inhibition increases the excitation threshold, and reduces both the gain and the saturation response. Shunting inhibition also reduces the range of spike voltage thresholds and shortens response latency. Taken together, these results suggest that levels of synaptic inhibition consistent with visually-evoked input may cause diverse and functionally relevant linear and non-linear changes in the transfer function of a single neuron.
>
> The Functional Synaptic Transfer Function of Neurons in Mouse Visual Cortex In vivo
> Marta Gajowa, Lyle Graham
>
> We describe the functional synaptic-spike relationship in neurons of mouse primary visual cortex in vivo, with parameterized excitatory and inhibitory input based on direct measurements of visually-evoked synaptic conductances. Using whole-cell blind patch recordings, we established the functional spiking response under current clamp, followed by estimation of the visually-evoked synaptic excitation and inhibition under voltage clamp. As a final step, we characterized the conductance-spike transfer function of the same cell, based on re-injection of variations of the visually-evoked conductances under dynamic clamp. Consistent with the diverse dynamical relationships between visually-evoked excitation and inhibition, we find a diversity of linear and non-linear effects of visually-evoked inhibition on the spiking response to visually-evoked excitation. Comparison of the original visual spiking responses to those in response to re-injection of band-limited visually-evoked inputs suggest

quantitative constraints on the relevant time-scale for the underlying neuronal code, in particular when considering rate-based versus spike time- based descriptions.

## 5.1. Neuronal code and possible mechanisms of implementation

### 5.1.1. Terminology and scientific context

Characterizing neuron function as a mathematical operation on synaptic input is directly related to the fundamentals of the neuronal code. Historically, two general paradigms for neural codes have been proposed, a rate - based code and one based on spike timing. A rate code assumes that most of the information is encoded in the spiking rate (frequency) considered over some period of time (or, alternatively, over inputs coming from several pre-synaptic cells). This model was first proposed by (D Adrian and Zotterman 1926), who observed that the firing rate of a stimuli evoked response increased in an intensity dependent manner. Supporting evidence was found in other studies examining sensory modalities in cortex e.g. feature selectivity in visual cortex. Several attributes of visual stimuli, such as contrast or orientation, evoke stronger or weaker spiking responses in a stimulus dependent manner (C. M. Niell and Stryker 2008; Gao, DeAngelis, and Burkhalter 2010; Cyril Monier et al. 2003).

In contrast, a spike timing code (sometimes called a correlation code) considers the precise time of the incoming spikes. From first principles, then, this model thus, provides higher information than a rate code (Koch 1999). However, to date the experimental evidence is less evident, with few examples of a spike timing-based code. Detection of the sound localization is based on the coincidence of spikes coming from left and right ear circuits (Grothe, Pecka, and Mcalpine 2010). Additionally, an indirect evidence in favor of an alternative to a rate code comes from the short time scale on which animals can discriminate stimuli and then take a decision (Theunissen and Miller 1995).

A clear distinction between the codes is somewhat ambiguous in the sense that as the time window for calculating rate decreases, the result converges to considering individual spike times (Koch 1999; Brette 2015). In fact, it is likely that both rate and spike timing are important for coding (Brette 2015). Additionally, it is possible that neuron can operate on several time scales (Ratté et al. 2013) and thus, that the difference in codes would depend on the cell's operation mode used to infer information from a particular input stream.

Two operation modes were defined based on how neurons process the input at the biophysical level (Abeles 1982). If neuron summates its inputs, it would be described as an integrator and thus mainly

sensitive to spike rate. In contrast, if neuron responds to coincidentally arriving from synaptic inputs, it would be described as a coincidence detector, thus mainly sensitive to spike timing. (Ratte2013).

Thus, the neuronal code must be considered in terms of the operational mode of the neuron, which would describe where the relevant information is encoded both from the perspective of the cellular properties (integrator vs coincidence detectors) (Ratté et al. 2013), but also in terms of characteristics of the input stream (Rudolph and Destexhe 2003) (Figure 68). Neuronal input can be characterized as synchronous or asynchronous. Stimulus driven synchrony emerging from anatomical connectivity (Singer 1999) could give rise to a range of possible input synchrony arriving at a given post-synaptic target, e.g. a cell receiving several synapses from the same source will obtain a more synchronous input. The highly variable synaptic input that is seen in vivo fulfills requirements of a high conductance state (A Destexhe et al. 2001), which has been shown to shift the operational mode of neurons towards coincidence detection ( Rudolph and Destexhe 2003). In any event it is important to stress that there is likely to be a continuum of operational modes presented by a given cell. For example, a pyramidal neuron is said to operate in between the two modes (Ratté et al. 2013), with result that in a sense both the rate and synchrony-based codes coexist within the same cell (Figure 68).

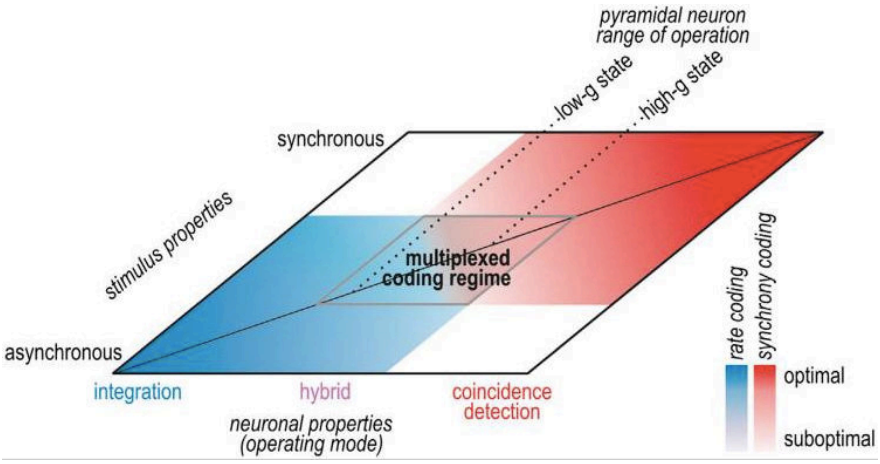


*Figure 68 Proposed by Ratte et al.2013 Interaction between stimuli and cell properties characteristic influencing code used by neuron. Neuronal operating mode presented on horizontal axis, stimulus properties on vertical axis. Area in the middle describes pyramidal neuron operating area modified after Ratte et al.2013).*

Therefore, predictions about neuronal processing of a given neuron requires knowledge about the characteristics of both the input and the output. In this context, a description of the I/O transfer function, that is the transformation between the synaptic inputs and the spiking output, provides important clues concerning the mechanisms used by neurons to fulfill their role as integrator/ coincidence detector, as well as about the relevant code or codes.

In our experiments we construct the I/O transfer function taking into account the level of excitation and inhibition coming from the entire pre-synaptic circuit. Since the method we use for conductance

estimation necessarily averages over several responses (typically 10 trials at two or three holding potentials), we consider the subsequent injected input during dynamic clamp as a rate-based extrapolation on any underlying time-based information stream.

It is important to stress that the binary distinction either between operational modes or the code used by the circuit is a convention. Several theoretical and experimental results have described a range of possible operating modes and inputs characteristics in a controlled condition. On the other hand, our experimental results are coming from in vivo experiments based on physiological visually evoked circuit input to one cell. As such they will be discussed in the context of current theoretical modeling studies.

Both linear and non-linear operations on the synaptic inputs enables a neuron to transform signals in order to discriminate spatial and temporal correlations in the inputs (Silver 2010). At the level of the I/O transfer function describing the total response as a function of the total excitatory input, linear interactions with increasing concomitant inhibition result in a rightward shift of the I/O function, whereas the simplest a non-linear interaction, division, results in reduction of the slope of the function with increased inhibition.

To name a few, the influence of synaptic noise, short term synaptic depression(STD) or shunting inhibition are the possible mechanisms used by neuron. Synaptic noise, defined as input fluctuations causing membrane potential fluctuations, influences the I/O in both linear and divisive manner (Azouz 2005; Wolfart et al. 2005; Shu et al. 2003). In the presence of fluctuating voltage lower excitatory input enables to cross spiking threshold, which shifts the threshold for spiking leftward and lower neuronal gain. On the other hand, noise was also shown to have influence only on the neuronal gain in studies using point conductance model (A Destexhe et al. 2001). In this simulation excitatory and inhibitory input was varying within the same range of values. Studies in cerebral granule cells (CGCs) showed that short term synaptic depression (STD) in excitatory inputs can substantially decrease the influence of inhibition on neuronal gain. The same synaptic depression paradigm simulated in an L5 cortical neuron showed that STD of inhibitory inputs cause a linear shift of the transfer function, whereas STD on the excitatory input had a multiplicative impact on I/O (Rothman et al. 2009). These authors postulated that a functional consequence of STD was that the neuron could combine spatially separated inputs. Further, as synaptic depression or potentiation would influence the gain in an opposite manner, this enables a neuron to adapt its function, for example during learning or context dependent behaviors.

### 5.1.2. Shunting inhibitory conductance

As described previously, shunting inhibition arises from synaptic GABAa conductances whose channels have a reversal potential that is close to the resting cell potential. When activated in isolation this conductance, even if high, will not provide a large current input as the driving force will

be small or zero. The change of conductance however will influence the cell's response to a simultaneous excitatory input, e.g. by reduction of the EPSP amplitude (Koch 1999, chapter 1).

As shown in previous chapter, shunting inhibition constitutes a substantial part of the stimuli evoked conductance change during neuronal activity. Although well studied since at least 30 years (Poggio and Torre 1978), the result of this input on the processing of the cell is not completely understood. Activation of any membrane channel, including synapses, will result in a membrane current according to the difference between the membrane potential and the channel's reversal potential, but will also increase the cell's input conductance, thus both attenuating the voltage change induced by other channels but also reducing the cell time constant. As noted, and in contrast to excitatory and GABAb inhibitory synapses, the reversal potential of GABAa shunting inhibition is near the resting potential, therefore normally close to the operating point of the neuron, and thus the impact of this input on the cell is dominated by its conductance contribution.

The functional impact of shunting inhibition has elicited diverse theories. For example,
(Carandini and Heeger 1994) proposed that in V1 shunting inhibition provides a divisive effect on the gain of the neuronal circuit, and similar influences have been postulated in other cortical areas (Heeger, Simoncelli, Movshon 1996). In contrast, other theoretical studies postulated linear influence of shunting inhibition to the spiking neuron (Holt and Koch 1997). In between the two opposing scenarios, the study (Vu and Krasne 1992) analyzed the shunting inhibition using a two compartment model, where one compartment simulated the soma and its proximity, and the second the distal dendritic arborization. The influence shunting inhibition on the EPSP depended on the post-synaptic location of inhibition (co-localized with excitation). Thus, proximal shunting inhibition had a divisive influence, whereas distal shunting inhibition had a mainly additive (linear) influence on the EPSP.

The impact of shunting inhibition has also been examined experimentally in vitro and in vivo, using the dynamic clamp protocol to simulate synaptic conductances on recorded neurons. *In vitro* studies exploring the change in the I/O transfer function upon applied shunting inhibition described the divisive effect (Kreiner and Jaeger 2004), as well as, postulate linear interaction (Ulrich 2003; Brizzi et al. 2004). Another group of studies confirmed a divisive influence, but only when the synaptic input was fluctuating (Chance and Abbott 2002; Mitchell and Silver 2003), or if a fluctuating dendritic input was considered (Prescott and De Koninck 2006)

The *in vivo* work of (Brizzi et al. 2004) in cat spinal lumbar motor neurons reported a linear effect of shunting inhibition on neuronal gain. In contrast, (Graham and Schramm 2009b) reported that in visual cortex in vivo shunting inhibition resulted in a divisive effect on the spiking rate output in response to simulated steps of excitatory synaptic input. This input not only reduced the spiking response to visual stimulation, but also tightened the temporal span of the PSTH was tighter in comparison to the control PSTH with no shunting inhibition. The study of (B.-H. Liu et al. 2011) postulated a similar divisive influence of shunting inhibition. However, these authors proposed that this influence would vary for the same cell depending on the tuning dependent level of inhibition.

This study applied similar idea to that described in this thesis, using dynamic-clamp in vivo to introduce inhibitory conductances based on measured response or based on a model. However, the number of cells (n=5) probed in this study is low, and only one condition was checked, thus with or without a specified level of inhibition.

In the context of the neuronal code, the relationship between possible operational modes of the cell and shunting inhibition and the influence on the I/O transfer function remains unclear. Thus, the main motivation of this study was to measure and describe the interaction between shunting inhibition and excitation in the mouse V1 in the context of functional processing. Moreover, probing the cell with different E/I ratios will enable the comparison of the resulting I/O transfer function with theoretical predictions of circuit dynamics, including that of balanced vs unbalanced conductance input. Similarly, the influence of conductance fluctuations to the spiking output will be discussed in the light of current theoretical predictions.

## 5.2. Yes, it is possible!

The most important methodological result of the present work is the validation that all the manipulations are feasible in vivo, between measuring the "natural" visual response, estimating the underlying synaptic excitatory and inhibitory input, and finally stimulating the same neuron with parameterized versions of these inputs with dynamic clamp. All previous studies, both using traditional and new optogenetic and /or calcium imaging methods, are only able to deliver a partial perspective (Mariño et al. 2005; Atallah et al. 2012; Xue, Atallah, and Scanziani 2014; A. Y. Y. Tan et al. 2011; B. Liu et al. 2010) thus, reporting the particular neuronal response to a particular situation. In contrast, the application of dynamic clamp in our approach enabled precise control of the synaptic input, thus allowing us to mimic various data-based scenarios to measure the cell response.

### 5.2.1. Dynamic Clamp method

Dynamic clamp (DC) is an intracellular recording technique that allows the introduction of conductances to a cell. As shown in Table 7, DC is used in a wide range of applications in neurophysiology but also in other excitable cells, including investigations of single channel currents, to mimicking synaptic input to a cell.

Starting from the computer side, the computer calculates the current equation of the desired conductance which is imposed by the amplifier command input (in current clamp mode) to the cell. On the cell site, the membrane potential is constantly monitored, and the potential value is used in real time to calculate the applied current according to the model of conductance of interest. The model of conductance is transformed into command current according to the equation:
$I(t) = g(t)(V_m(t) - E_{rev})$, where g and $E_{rev}$ is delivered by the model and Vm (t) is measured in each time point. Such feedback loop ensures that the only effective conductance 'seen' by the cell is the one provided by the equation. Thus, dynamic clamp enables precise control over the cell dynamics by insertion of a desired conductance waveform in to the neuron (Piwkowska et al. 2008).

Application of DC enables both addition and canceling (by reversing the sign before the current equation) of chosen input (Vervaeke et al. 2006).This is an advantage during studies of influence of specific currents. Additionally, DC enables modifications of the conductance input in example - scaling thus, checking several conditions in the same cell.

For these reasons DC was used to investigate the role of both intrinsic (voltage and current dependent channels) (Vervaeke et al. 2006) and extrinsic (synaptic excitatory and inhibitory inputs)(Graham and Schramm 2009a) conductance, as well as network activity influence on the cell (Haider et al. 2006) and network processing (Sohal et al. 2009). Existing theoretical models predicting specific channel contribution can be verified by DC application restoring the current influence on a blocked or genetically modified cell.

In vivo application of dynamic clamp though rarely accomplished to date, has the additional advantage of interacting with the cell (or local circuit) within the whole intact network for example investigating the sensory cell processing with a changed conductance input (Haider et al. 2006; Graham and Schramm 2008; B. Liu et al. 2010).

DC is relatively new experimental approach. It was first demonstrated and used in the '90 both in cardiac cell studies (R. C. Tan and Joyner 1990) and in neurophysiology (Sharp et al. 1993; Robinson and Kawai 1993). Today the processing power limitations present in the '90 do not constitute a problem and DC can be implemented on each electrophysiology rig independently from traditional current/voltage clamp with low cost (100$!) (Desai, Gray, and Johnston 2017). Additionally, a few open source software's are available to facilitate communication between the conductance model and amplifier and model creation as well as programming skills more frequent among scientists than before. Thus, more technical limitations and implementation inconveniences of DC are disappearing.

Two limitations of the DC are still present today. First, by injecting the conductance we induce only electrical effect of a given conductance. If the channel or synaptic input in real conditions undergoes conformational changes or activate a specific cellular pathway it cannot be recreated by DC. A second limitation is that normally the phenomenological conductance can only be considered at the location of the electrode, although methods are in development to apply hybrid conductance plus current models that mimic channels that are electrotonically distant from the recording site.

In summary, DC is a useful tool for dissecting the role of specific membrane currents or synaptic inputs. Providing control over the neuronal dynamic DC enable understanding of biophysical mechanisms underlying neuronal processing.

| reference | reson to use DC | application approach | main findings | in vivo/in vitro |
|---|---|---|---|---|
| Sharp A, O'Niel M.B, Abbott L.F.,Marder E, 1993 | presentation of DC method in neurophysiology | recording of STG crab neuron response to GABA or GABA simulated conductance; -while recording from crab AB neuron addition of picrotoxin and response to simulated picrotoxin conductane was shown; -examples of interactions beetween two neurons: once by inducing spiking at the pre synaps and showing infulencein the post synapse, second by coupling two not conected neurons | demonstration of technique possibilities | in vitro - AB crab neuron, STG crab neuron |
| Chance F.S.,Abbott, L.F., Reyes A. 2002 | showing how background synaptic input influences pyramidal neurons gain modulation | investigation the firing rate (gain modulation changes) of a cell during various level of balanced e/i ratio showed that shunting inhibition is responsible by the linear shift of the transfer function whereas the noise level by the change in the slope | investigation the firing rate (gain modulation changes) of a cell during various level of balanced e/i ratio showed that shunting inhibition is responsible by the linear shift of the transfer function whereas the noise level by the change in the slope | in vitro slices - rat somatosensory cortex |
| Prinz A.A.,Abbott L.F.,Marder E, 2004 | review | paper show various applications of DC and comments on details of the technique | | |
| Brizzi L., Meunier C.,Zytnicki D.,Donnet M., hansel D., Lamotte d'Incamps B., van Vreeswijk C, 2004 | DC used to increase input conductance in the motoneurons to study influence of shunting inhibition for I-f curve | the incresed conductance was mimicked by injecting constant conductance | purely linear shift was observed proportional in the shift to amount of conductance injected | in vivo cat, lumbar motoneurons |
| Vervaeke K., Hu h., Graham L.J., Storm J.F., 2006 | showing how a Na+ channel influences the spiking output of a cell by cancelling the channel influence (no blockers couldbe applied for such investigation) | cancelling the current evoked by INaP | Na+ current (INaP) influences the frequency of spiking and the spiking precision in time by increasing AHP and reducing rheobase; removing of the INaP resulted in broader ISI distribution and changed (increased) in the F/I curve gain | in vitro slices - CA1 hippocampal pyramidal cells |
| Manuel M., Meunier C., Donnet M.,Zytnicki D., 2007 | DC used to mimick AHP current in the motoneurons by that and the linear dependence of AHP amplitude and current conductance could be estimated | AHP current of increasing amplitude injected | AHP conductance estimated in the population of lumbar motoneurons, no dependence on the tau of AHP by the amplitude was found | in vivo cat, lumbar motoneurons |
| Graham L.J., Schramm A.,2009 | Describing how shunting inhibition and potassium IBk current influences the I/O transfer function of cortical neurons | conductance step injections, cancelation of IBK current by injection of reversed polarity current | Shunting inhibition shows divisive effect for the gain of I/O transfer function; IBk current faciliates spiking and thus increase the gain of I/O transfer function as weel as during visualy evoked responses | in vivo - rat and cat; during visual response |
| Destexhe A., 2009 | presentation ho dynamic clamp can be used to study synaptic noice influence on cellular properties and processing | conductance based synaptic noise mimicked | demonstration how to recreate in vivo state in in vitro preparation, showing the noise role in gain modulation and enhanced responsiveness including also recreation of up and down states activity, showing the multiplicative influence of noise (fluctuations) for the I/O function and additive of amplitude of conductance | in vitro rat slices |
| Haider B., Duque A., Hasenstaub A.R., Yu Y., McCormick D.A.,2007 | Describing the up and down states differences in the spiking output of visual stimuli | conductance injections mimicking EPSP of increasing amplitude | During the up stated the injected EPSP like conductances resulted with the higer spiking output caused by depolarization associated with up state | in vivo -cat; during visual stimulation |
| Sohal V.S., Zhang F., Yizhar O. Deisseroth K, 2009 | dissecting PV neurons role in shaping the rythmic activity of PY cells and theinfluence of gamma vs theta rythms on the spiking output | dynamic clamp used to inject EPSP like conductances to PY to induce rythmic activity while inhibiting PV neurons by optogenetics | Confirm the role of PV neurons in influencing rythmic activity. In vivo supression of PV neurons supress rythmic activity. In vitro PV neurons increase the gamma activity. Gamma oscillations apmplify signals and reduce nois in pyramidal cells | in vitro - mouse |
| Nagtegaal A.P., Borst J.G.G., 2010 | study of Ih current influence on cell signal processing | dynamic clamp use to mimic Ih current in the pharmacologically blocked cells | presence of Ih current changes basic cell properties - depolarize membrane potential and decrease membrane resistance | in vivo - mouse; sound stimulation |
| Ravagli E., Bucchi A., Bartolucci C., Paina M., Baruscotti M., DiFrancesco D., Severi S., 2015 | verifying role of If current | dynamic clam used to mimic If current based on two types of models | Severi-DiFrancesco model reproduces effects of If current on rabbit sinoatrial cell, half of the autonomic ratemodulation is caused by the If current | in vitro rabbit sinoatrial cells |
| Takkala P., Prescott S.A., 2017 | investigation of the mechanisms associated with spike initiation dynamics in patchological states and its modulators | dynamic clamp used to inject incresing steps of sodium conductance | neurons can be converted to pathological repetitive spiking by adding virtual conductance, small cells more susceptible, many pathological factors faciliate repetitive spiking but cumulative effect is needed to switch to repetitive spiking mode | in vitro -cellular culture |

### 5.2.2. Step by step protocol description

We have developed a protocol to study functional I/O transfer function using blind whole-cell patch clamp recordings in mouse V1 in vivo, under current clamp (CC), voltage clamp (VC) and dynamic clamp (DC).
This protocol allows to describe how specific patterns of excitatory and inhibitory synaptic input influence the spiking response during visual processing, and includes the following steps for each neuron:

1. CC measurement of firing and membrane potential vs. input current, to establish basic I/O properties.

This first step is crucial for assessing the electrophysiological type of the cell and provide first estimation of the patch quality and stability. By monitoring of the membrane potential response for injected current steps of increasing amplitude we can infer information about cell spiking characteristics including the presence of adaptation and spike shape. These parameters are used during analysis off-line to establish electrophysiological type of the neuron. We record membrane potential changes for repeated current steps of the same amplitude to monitor cell parameters like input resistance, input conductance, cell capacitance, membrane time constant, mean resting potential and the patch quality - assessing the access resistance and bridge error. As explained in chapter 4 the the sum of access resistance and bridge error was monitored closely and conductance measurements were corrected. Additionally, the ratio between total bridge error and input resistance of the cell was important for taking decision about next recordings or braking the patch. The current step protocol is repeated several times during the whole protocol to monitor changes of cell or patch parameters.

2. CC measurement of sub-threshold and spiking visual response, typically to the preferred stimulus (Figure 69)

Once initial cell characterization was performed, we would provide mouse with grating stimuli of 8 different directions. The direction (usually one or two) which resulted with the higher number of spikes was further investigated in detail. All next visually-evoked spiking responses would be performed only with stimulation to this direction to be able to compare visually-spiking response with those obtained by conductance waveform injection. This protocol was repeated few times in before and after conductance estimation as well as on between DC protocols serving cell probing.

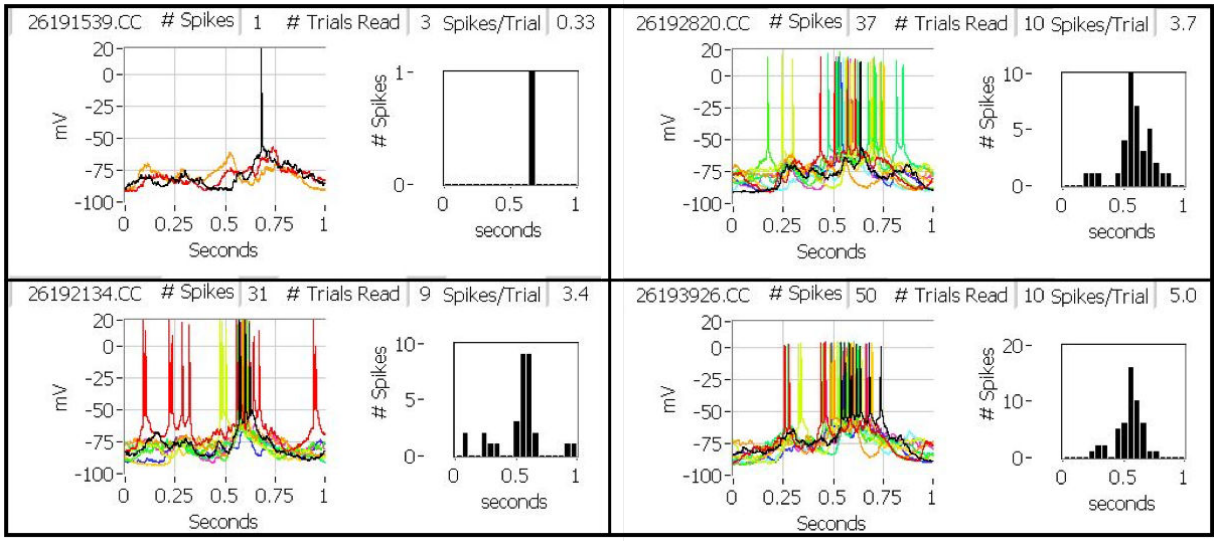


*Figure 69 Exemplary visually evoked spiking and associated PSTH plots for the same direction stimuli recorded at various time points during whole protocol duration.*

3. VC measurement of visually-evoked excitatory and inhibitory synaptic conductance inputs corresponding to the CC response (Figure 70)

This step required change of the clamp mode, which needed to be done in a designed sequence by removing the capacitance and bridge balance compensation first. After the mode would be changed on amplifier and the voltage gain would be increased from 0 to max value on the amplifier. Finally, the voltage step injection (~10 mV) was applied to compensate the cell capacitance and bridge balance up to 50-70 % of initial value form CC mode. The value of the bridge compensation was logged in the experimental notes.

After changing the mode successfully without initializing oscillation in the cell, the visual-evoked currents were recorded at two holding potentials: -65mV and -90mV. Those traces are further used for on-line estimation the visually evoked conductance changes and further, to split them into two waveforms constituting excitatory and inhibitory synaptic input. After the VC recordings, the change of mode back to CC was done. Careful assessment of access resistance and bridge error is done.

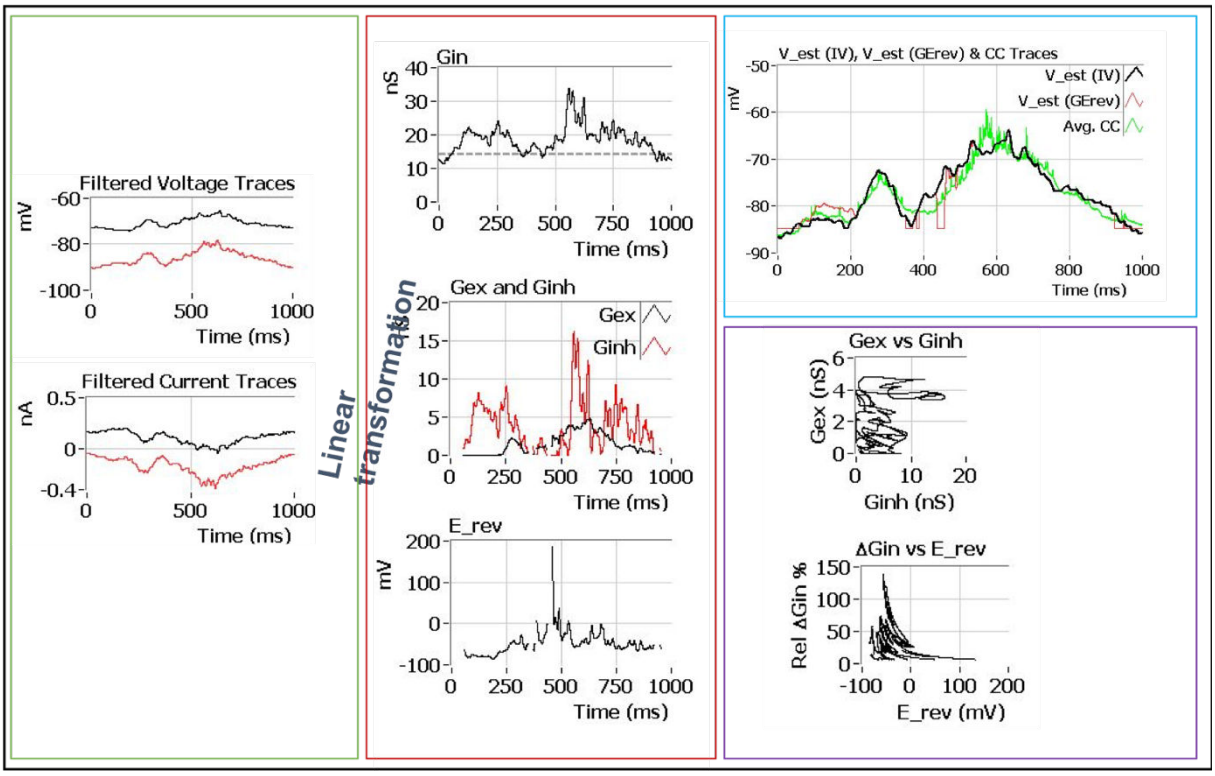


*Figure 70 Conductance estimation step (description in the text). Bridge error used: 38 MΩ. Conductance estimation step occurs. Left, green panel displays average voltage (top) and current (bottom) waveforms obtained during VC recordings (10 trials, same stimuli). Middle, red panel shows the resulting conductance trace (Gin, top), synaptic input components ($G_{exc}$ and $G_{inh}$, middle) and changing in time reversal potential of a cell ($E_{rev}$, bottom). Right, blue panel presents superimposed membrane potential waveforms as a check of conductance estimation and stability of the cell check. Green waveform comes from averaging visually-evoked response presented in previous figure. Black and red waveform potential traces are estimated based on the IV line and synaptic components respectively Note that the red waveform is not continuous during the total response recorded. The gap around 400 ms is a result of changes lower than the 5% threshold and is also visible in the two components plot and $E_{rev}$ plot. Right, purple panel displays additional information about the conductance change – two phase plots. Top: the absolute values of synaptic components in each time point. Note that this phase plot shows relationship between excitation and inhibition for a given direction and eventual linear would be immediately seen. Bottom: change of evoked conductance in comparison to momentary reversal potential in each time point of recording. Note that this phase plot enables to see approximately the reversal potential when the changes of conductance were maximal, which provide insight into the conductance which was dominating.*

4. DC re-injection of parametrized synaptic input based on the visually-evoked conductance, to dissect essential synaptic interactions underlying spike output.

Once conductance traces would be estimated, the sequential protocol calculating changes in the amplitude and temporal characteristic would be used (Figure 71).

Amplitude changes (in the form of current trace applied as command DC current input) are calculated by changing the coefficient A and B scaling the excitatory and inhibitory part in independent way

(equation below). This step result in previously defined grid of E/I ratios which would be iteratively imposed to each cell, enabling future comparison between cells.

$$I(t) = Ag_{Exc}(V_m(t) - E_{Exc}) + Bg_{Inh}(V_m(t) - E_{Inh}),$$

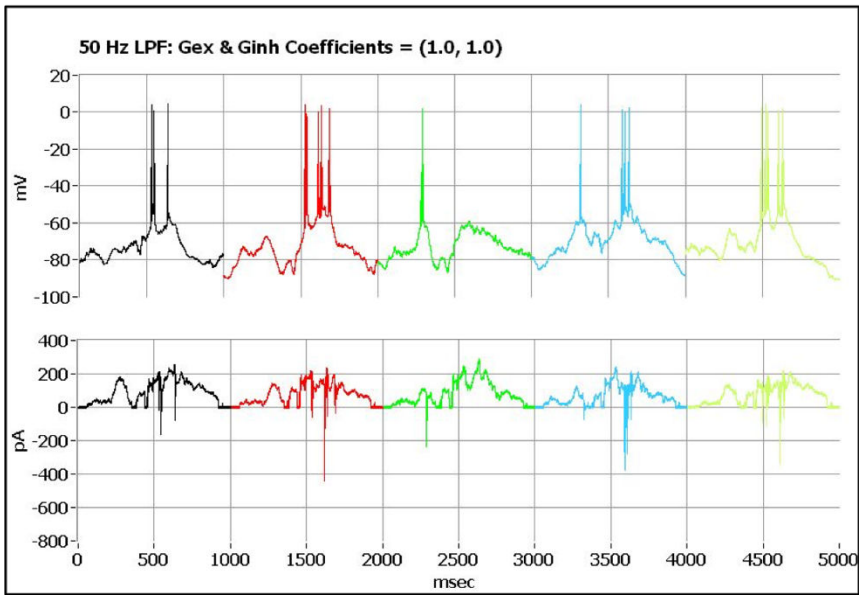


*Figure 71. Dynamic Clamp exemplary recording. Membrane potential (top) recorded in response to command current input (bottom) calculated based on the synaptic conductance input. This particular example presents introduction of the measured synaptic input without any transformation ("souté"/ exactly as measured').*

The temporal characteristic was implemented by application of a low pass filter to measured currents in VC mode. This step removes part of fast fluctuations but also provide an averaged version of the conductance waveform. It would be interpreted as extension of the integration time window for the cell.

The conductance waveforms after the temporal transformation would be introduced to a cell with the same coefficients of E/I ratio as in previous step. This step gives us the possibility to compare cell response at various inhibition levels at two (sometimes more tries was possible) different temporal scales. We chose to compare 10 and 50 Hz filters, but some of the recordings were done with 20 and 50 Hz filters or even 100 and 200Hz. We have chosen to continue with 10 and 50 Hz filters as we noticed some changes in the cell spiking output, which were interesting for us to explore. Additionally, as studies of this kind were never done before experimentally we didn't have any prediction about the filters we should use. Because of restricted time of recording probing of more than two cases was rare.

In between DC protocols the cell stability and parameters would be assessed. Especially the Access resistance and bridge error. Cell visually evoked spiking response would be also recorded to ensure

that the cell didn't changes the spiking response substantially. The DC measurements were repeated until the patch quality allowed.

5. DC measurement of firing vs. injected "synaptic" conductance steps, to establish the conductance-based variant of the f/I curve

Conductance steps injection constitute the most extreme version of a rate code with absolute fixed E/I ratio with no fluctuations (Figure 72). On the other hand, the first, initial part provides extremely sharp onset. This protocol serves for two purposes:

- to describe cell output for injected conductance steps in a population of cells (so far we do not show that)
- to be able to compare the response of the cell to conductance steps vs visually-evoked like conductance waveforms

Depending on what was the recording priority this step was performed at the beginning of the recording or at the end after probing the cell with various E/I pair waveforms.

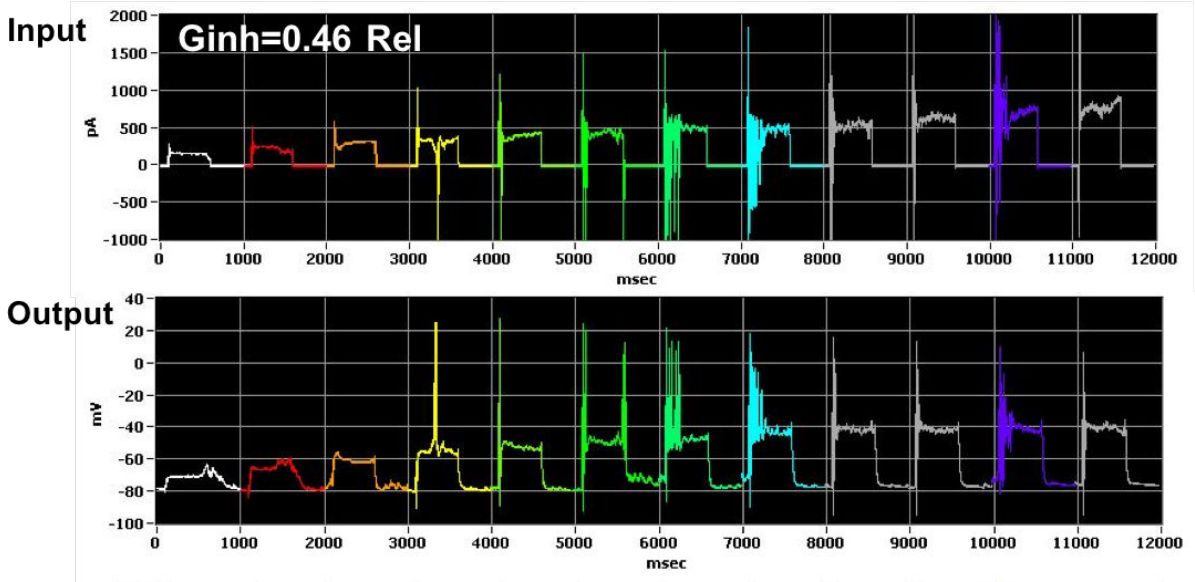


*Figure 72 Exemplary traces illustrating the Input (top) command current during the conductance step DC protocol and the evoked response (bottom) of the cell. Each consecutive step amplitude is increased for excitation value, whereas inhibition stays at the same level during entire recording. Several recordings at different relative inhibition levels serves to construct I/O transfer function.*

Final for each cell result – the I/O transfer function comes from juxtaposition of averaged DC-evoked spiking with scaled excitatory and inhibitory ratio (Figure 73). Such 3D plane describes spiking which would be fired by the cell given the synaptic input conditions.
Investigation of the I/O transfer function allows to see the divisive effect of shunting inhibition. Additionally, in some recordings a small linear shift is also present (to see it look at the spiking threshold change at various inhibition levels).

In summary, the protocol allows for describing changes in spike number and timing in response to DC injections of estimated excitatory and inhibitory synaptic conductance waveforms variations. In particular, the response to DC injected variations of waveforms is being compared to the originally measured visual responses. This allows describing integrative properties of V1 neurons depending on their electrophysiological type (RS vs. FS) and investigate the role fluctuations in the waveform to the spiking cell output (comparison of conductance step injection vs. visually evoked response treated with low pass filters).

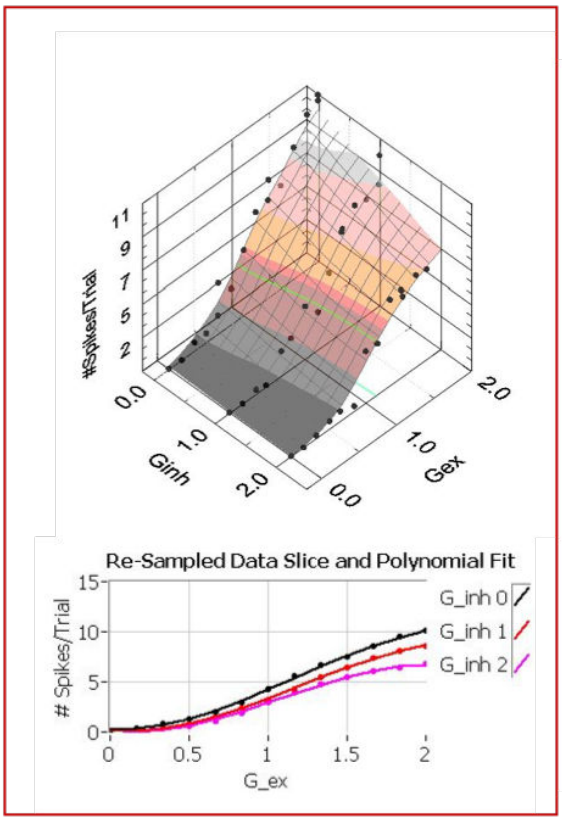


*Figure 73 Final I/O transfer function - 3D (top) and 2D(bottom). Black dots indicate real measurements – the number of spikes evoked in response to visually evoked conductance traces. The space in between is constructed by extrapolation.*

## 5.2.3. Closed loop experiment controls and quality assessment

### *5.2.3.1. Fine tuning of experimental protocol*

Conductance estimation constitute the heart of our protocol. To achieve proper conductance estimation (characterized in chapter 4) and record the data of a good quantitative and qualitative characteristic the initial experimental protocol needed to be fine-tuned. A few challenges needed to be accounted:

1. Low visually-evoked activity

At the beginning, recordings of visually evoked spiking responses were characterized by low number of spikes. In this initial period of experiments visually evoked response was often noticeable only in the changes of membrane potential and no spikes would be elicited. The trial to trial variability in between following responses to the same visual stimuli were also high. The consequences of such activity were following:

a. lack of reference point for the I/O transfer function (low or none spiking)
b. low and non - continuous conductance waveform in a few cells where it was measured (discontinuity of the waveform was partially caused by 5% threshold set for conductance estimation as well as momentary drops of the conductance below the initial conductance)

This led us to rethink our anesthesia protocol. In particular, a high level of isoflurane was reported to significantly influence brain activity. During spontaneous activity, synaptic transmission decreases with an increase of isoflurane concentration (Ferron et al. 2009). During evoked activity, more action potential was elicited in response to moving grating and the response offset was delayed in comparison to awake animals (Bennett, Arroyo, and Hestrin 2013; Haider, Häusser, and Carandini 2013). Both authors agree that inhibition is suppressed during exposure to anesthesia.
In this context we decided to use chlorprothixene hydrochloride (Marshel et al. 2011) as an additional sedative agent, which allowed us to work in a low anesthesia regime. Injection of chlorprothixene resulted in an increase in the heart rate to at the level of 520-600 BPM, within few minutes, which stayed extremely stable for on the order of 6 hours.

On average, cells patched at higher levels of isoflurane (before adding chlorprothixene into protocol) were more hyper-polarized (-80,9 ± 8,95 mV, n=17), than the group of cells patched at a low anesthesia level (-76, 3 ±10, 6 mV, n=19, no statistical significance), (in agreement with Ferron et al). Additionally, at high isoflurane levels (1%) changes in neuronal selectivity were noticed, similarly as described in (Goltstein, Montijn, and Pennartz 2015). We also noted that under high anesthesia, the preferred direction was occasionally changing between two directions of the preferred orientation.

2. Relatively short time of recording

Performing all the protocols and constant monitoring of the cellular parameters required not only constant focus from the experimenter side but also relatively long time taking into account the average duration of an in vivo patch. Additionally, tissue movement were contributing to sudden patch breaking.

To shorten the recording time and increase the chance to perform whole protocol set the majority of the protocol steps were automatized, which enabled us to minimize the time needed for performing an entire protocol to 20-40 minutes. Additionally, access resistance measurement was

automated, providing frequent feedback on the difference between the amplifier bridge balance and the actual value. This provides essential quality monitoring of the recording as well as the necessary correction factors to reliably estimate evoked conductance. This improvement increases the chance for successful recording greatly and provides better control over cell parameters.

Injecting the animal subcutaneously with a 1mL saline based solution every 1-2 h helped to prevent hypo-tension and associated with it brain tissue collapsing which increased the movement. Some of the side effects of isoflurane anesthesia are: arrhythmia and hypertension during induction (Meyler and Aronson 2009). Indeed, both sides effects were visible in the population of animals used to experiment. Moreover, one of the hypertension effect was appearance of a “foggy eye” – a white spot inside the eye. In such condition the visual responses were impaired.

3. High access resistance and not good enough patch quality

Conductance measurements requires low access resistance patch to avoid current filtering by the electrode. In our recordings the first condition to continue with Voltage Clamp measurements was to obtain Access resistance lower than the cell input resistance, with associated low (0-5MOhms) bridge error. The best results though we obtained when the access resistance was lower than 40 MΩ or when the total bridge/Rin ratio was around 0.5 (lower than 0.7).

To increase the chance of obtaining low access resistance patch characteristics we applied a few steps:

- all the electrodes were checked under the microscope before patch attempt to eliminate those containing small bubbles of the internal solution in the tip or other possible dirt residues
- patch pipette solution was modified by adding 1 mM of EGTA chelator, which stabilizes access resistance and duration of recording (Sakmann and Neher 1983) we used Touch and Zap method for seal formation and patching (touch and zap paper)
- after the whole access configuration would be formed and a small positive pressure would be applied (~3-15 mmHg) the electrode would be back up gently by a few microns (2-10)
- the wire in the holder would be chloride frequently every time when the inspected under the loop wire wouldn’t be covered with a smooth layer of $AgCl_2$. Such situation was usually associated with increasing difficulties in obtaining low access resistance patch, developing a seal quickly or in the most extreme cases with characteristic artifact in the signal.

#### *5.2.3.2. Check points*

The delicate nature of in vivo patch recordings and the time needed to collect a complete data set required careful development the experimental procedure. During our closed loop protocol, we deal with an estimated signal and not directly measured one. In the next steps, this signal is imposed to a

cell which output for various signal changes constitute our result. In such a context, we need to validate some assumptions associated with the consecutive protocol steps.

A. Conductance estimation controls

Proposed by us closed loop approach is based on an assumption that the conductance change we measure during visually evoked response is 1. true 2. the same/similar to the one which we observed during CC measurements monitoring spiking output. Therefore, it was necessary to show that estimated by us conductance have a real physiological meaning (ad. 1) and that the response they cause can be compared with the visually evoked one (ad. 2).

To fulfill the two conditions, we compare the averaged cell membrane potential during visually-evoked response with:

- Estimated membrane potential calculated based on the evoked currents and holding potentials during VC step (corrected by the current drop due to the bridge error).

  The good overlap between the two waveforms constitute a proof that the cell response didn't changed between collection of visually-evoked spiking output and assessment of visually-evoked currents. Thus, that we can claim that estimated synaptic input measured during VC mode on average results in the recorded spiking output recorded during CC mode at the beginning of recording and /or after the VC measurements.

- Estimated membrane potential calculated based on the estimated conductance changes

  The overlap between the two waveforms enable assessment of how much the estimated conductance contribute to the cell membrane potential and resulting from it spiking output. This check is especially important in the light of arguments raising space clamp problem as an obstacle in reliable conductance estimation and presence of other than synaptic conductance present during VC measurements. The overlap between the two membrane potentials - coming from recording and calculated based on the estimated conductance, is varying in between the recorded cells.

$$V_m = \frac{E_{exc}g_{exc} + E_{inh}g_{inh} + E_{rest}g_{leak}}{g_{exc} + g_{inh} + g_{leak}}$$

  In our experience, the main reasons of the low overlap between the two waveforms in some experiments are:

  i) to high access resistance summed with bridge error during the VC measurements, which contribute to the space clamp problem

ii) high trial to trial variability in the response to the same visual stimuli. The variable circuit response results in underestimation of evoked conductance, as it is estimated based on the current average of all the trials. In such situation the 5% threshold might not be reached, and the conductance waveforms would have gaps, which results with no overlap between waveforms in our control. The high trial to trial variability was associated with high anesthesia causing up and down states and/or low synaptic activity.

- averaged membrane potential obtained by DC injection of unitary coefficients conductance ratio (exc=1, inh=1)

  Overlap between the visually evoked averaged response and the averaged response coming from DC conductance injection (exactly those which were measured with no modification) provides a final check of stability of cell recording and cellular response. Being able to recreate original membrane potential dynamics by injecting synaptic input as it was measured enables to claim that provided by us I/O transfer function resemble true, physiological neuronal response and gives a statement about quality of the whole recording.

  Additionally, we are checking the overlap between the averaged membrane potential obtained by DC injection of unitary coefficients conductance ratio and the estimated membrane potential calculated based on the evoked conductance changes. Both of the waveforms have their source in the same conductance waveform estimated based on VC measurements. First, we calculate the membrane potential based on that waveform taking into account the momentary reversal potential, second, we introduce it to a cell using Dynamic Clamp method. The mismatch between them would indicate problems in the calculation method or with dynamic clamp software part (Figure 74).

  Similarly, the spikes distribution in time comparison between visually evoked and DC evoked conditions (all) provides additional validation.

We assessed all the recordings during the experiments based on on-line analysis computed by the software, which speeds up the experimental proceedings and help to take the decision about eventual abandoning of recording.

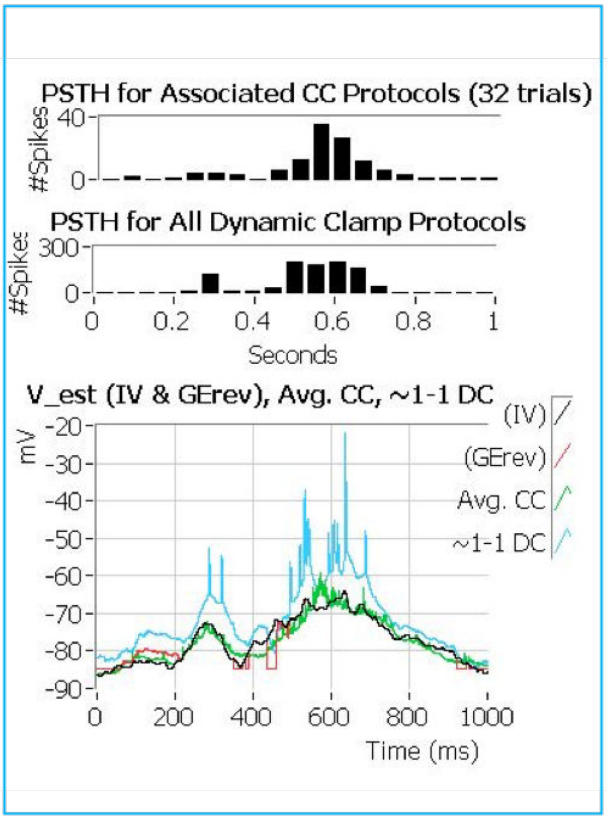


*Figure 74 Results validation of exemplary cell results described in section 'step by step protocol description'. Top: PSTH presenting distribution of spikes in time in response to visually evoked stimulation (CC protocols) and DC-evoked one (DC protocols). Bottom: comparison of estimated (IV and $GE_{rev}$) and evoked (visually – Avg.CC, DC - ~1-1DC) membrane potential changes. Good overlap validates recording.*

B. Verification of the current injected during Dynamic Clamp

The conductance is introduced to the cell during sequential Dynamic Clamp protocol. The current trace is calculated according to the equation

$$I(t) = Ag_{Exc}(V_m(t) - E_{Exc}) + Bg_{Inh}(V_m(t) - E_{Inh}),$$

which is scaled according to the desired E/I ratio in each sequence. To ensure correct data interpretation we have implemented in the software a control calculation enabling inference of the applied scale factors A and B in a particular current trace injected to the neuron.

Knowing the current trace injected and the conductance waveforms estimated, it was possible to infer for each recording the A and B coefficients. This operation provides an additional check for experimental conditions applied. Thus, the data interpretation are not depending on any systematic mistake which could occur in the software.

## 5.3. Playing with input amplitude - I/O dependence on E/I balance

In this section I will describe results concerning the joined influence of shunting inhibition and excitatory input on cell spiking output. Results described are derived from the same data set presented in the Chapter 4.

Conductance waveform DC protocols:

The overall quality of recordings assessed by the overlap between the DC- evoked membrane potential and visually - evoked one was calculated using cross correlation between two voltage waveforms (Figure 75). Both waveforms were low-pass filtered with a cut-off frequency of 20 Hz prior to cross-correlation. On average the fit was $0.67 \pm 0.2$ and was varying in between 0.21 to 0.97 range. The wide range of coefficients indicates that among the recordings both really good fits and weak ones are present. The weak fits are coming from the cells where conductance estimation was not continuous. However, the periods during which conductance was estimated well were still useful for examination of I/O function. Some recordings provided particularly good overlap and would be further analyzed. The high mean of the correlation coefficient points to overall good agreement between the membrane potentials coming from visually- evoked and DC-evoked recordings and finally validates the whole closed loop protocol.

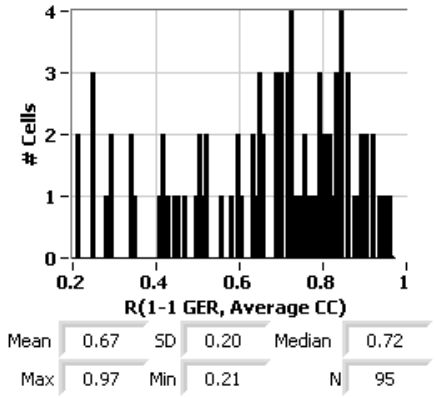


*Figure 75 DC evoked, and visually - evoked voltages fit statistics. The fit is given by cross-correlation between the voltage waveforms relative to the rest, after low-pass filtering (cut off frequency: 20 Hz).*

To provide a more insights into variability of the data base and associated parameters Figure 76 present more examples estimated conductance together with overlap of membrane potential check, as well as Figure 77 different examples of I/O transfer functions.

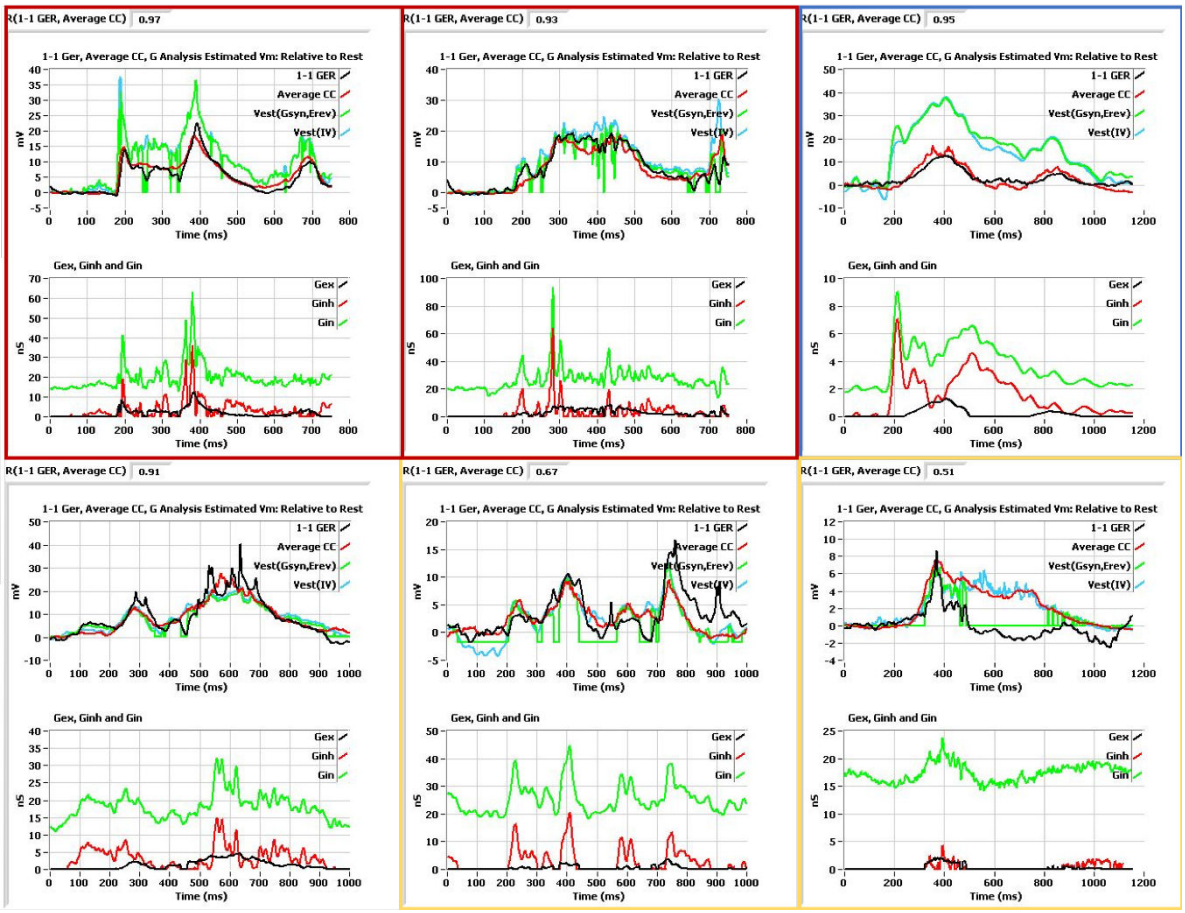


*Figure 76 Protocol examples with varying degrees of correspondence between the 1-1 GER protocol membrane potential and the visually-evoked current clamp membrane potential. These waveforms are compared with the direct estimates of the membrane potential derived from the conductance estimation procedure based on voltage clamp recordings, including that taken from the IV characteristic over time($V_{est}$(IV)), and the reconstructed potential from the estimated reversal potential and total evoked synaptic conductance ($V_{est}$($G_{syn}$, $E_{rev}$). In the bottom plots of each panel are the corresponding estimated evoked excitatory ($G_{exc}$), inhibitory ($G_{inh}$) and total input ($G_{in}$) conductances. Note that the first and second examples are responses to opposing directions from the same cell (mouse\2017.11.18\cell 2).*

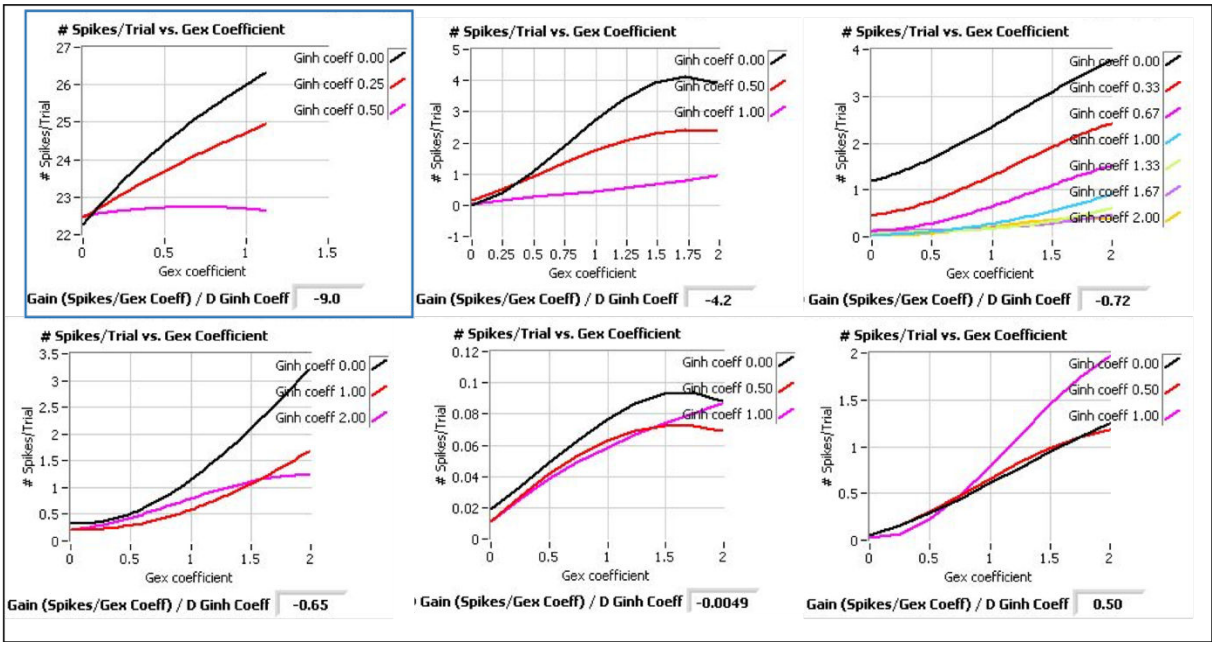


*Figure 77 Examples of impact of inhibition on firing gain. Firing curves are third-order polynomial fits of the re-sampled transfer function surface (spikes/trial vs. $G_{exc}$ and $Gi_{nh}$ coefficients), along slices at constant values of the $G_{inh}$ coefficient. Gain is defined as the maximum slope of the fitted slices. Cell marked in blue presents example of the FS cell.*

Conductance step protocols:

Additionally, for a subset of 19 cells besides the I/O transfer functions based on physiological synaptic input, the conductance step protocol was recorded, and I/O transfer functions based on the conductance step injection were constructed. More I/O transfer functions based on conductance step introduction were done separately in additional population of cells.
Data presented below comes from one cell example, where completed DC protocols for conductance waveforms and conductance steps were performed (Figure 78).
Visually-evoked response provided spiking only in some trials. Increasing of the excitatory part and scaling inhibition to zero (removing inhibition) increases spiking. Shown in the next traces from increased excitation accompanied by inhibition (B coefficient for inhibitory input=1) visibly decrease spiking response.

In F-G traces shown cell starts evoking spiking at 3$^{rd}$ step (Figure 79). Figure 80 presents calculated in absolute values injected steps to that cell show similar absolute value at the 3$^{rd}$ step as the peaks amplitude for excitation in the visually evoked conductance plot. Such coherence in the data enables comparison of the I/O transfer functions obtained from the same cell by application of a bit different stimuli characteristic.

The two I/O functions presented for two input stimuli conditions show similarities and differences (Figure 81). In particular, the divisive influence of inhibition is present in both cases. However, the

GER (conductance waveform based) function shows only initial part of the function (no saturation is seen for the used set of stimulus conductance coefficients). Likewise, the linear rightward shift is more apparent for the F-G (conductance step) based transfer function.

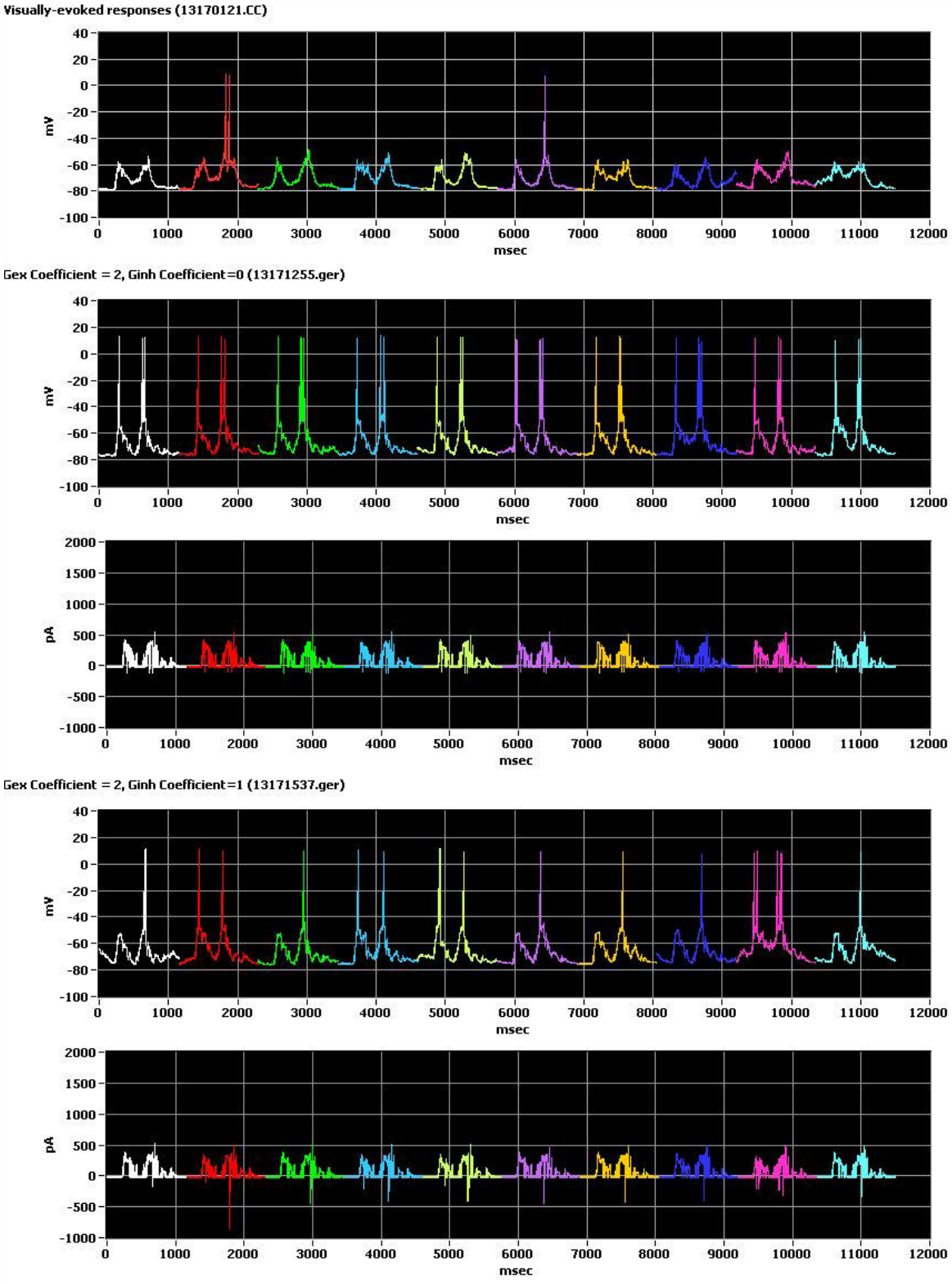


*Figure 78 Visually - evoked responses under current clamp (top) and GER protocols with the $G_{exc}$ coefficient = 2, and the $G_{inh}$ coefficient = 0 (middle) and 1 (bottom).*

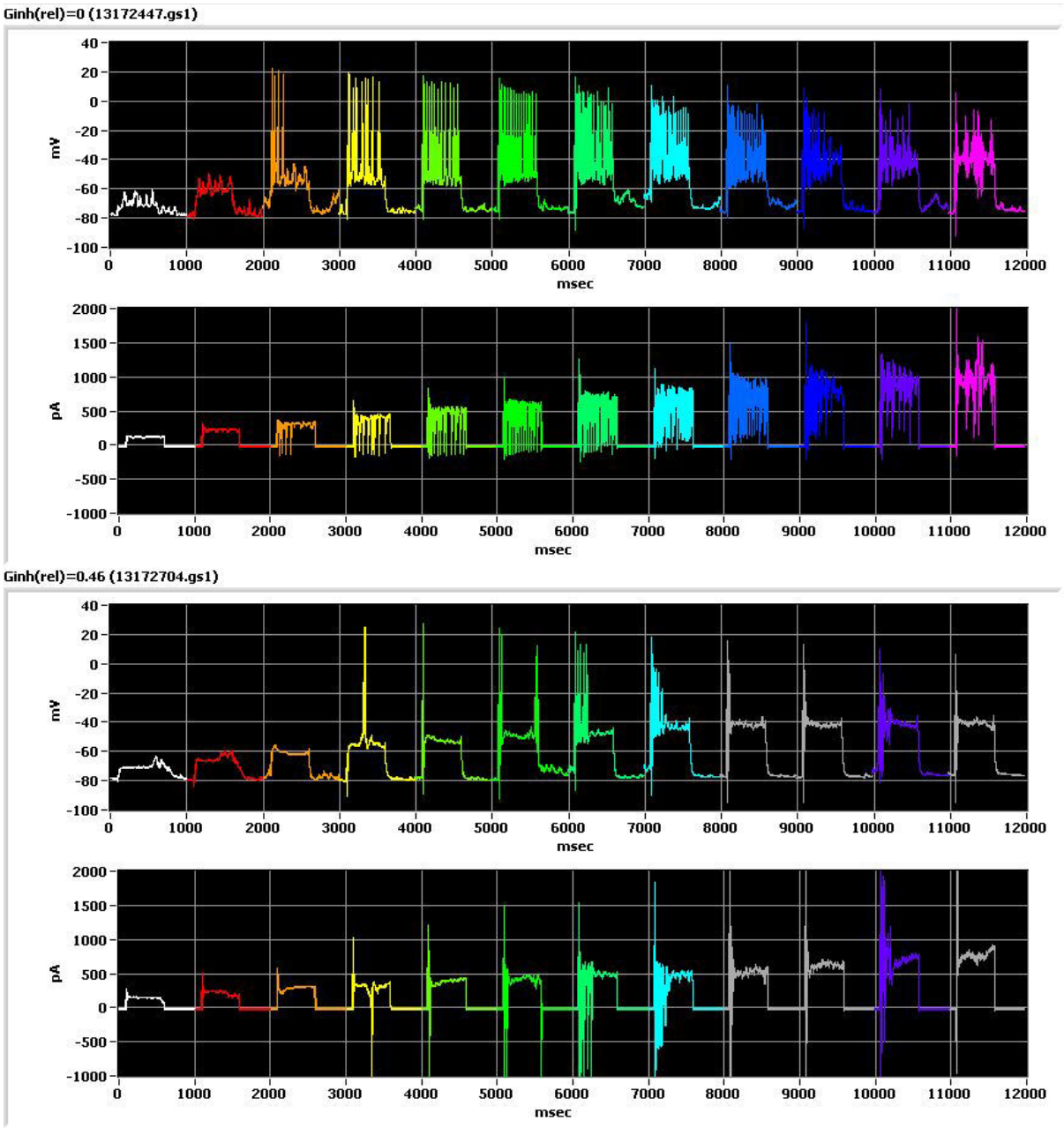


*Figure 79 F-G protocols with $G_{exc}$(rel) stepping from 0.11 to 1.3, with constant $G_{inh}$(rel) = 0 (top) and 0.46 (bottom).*

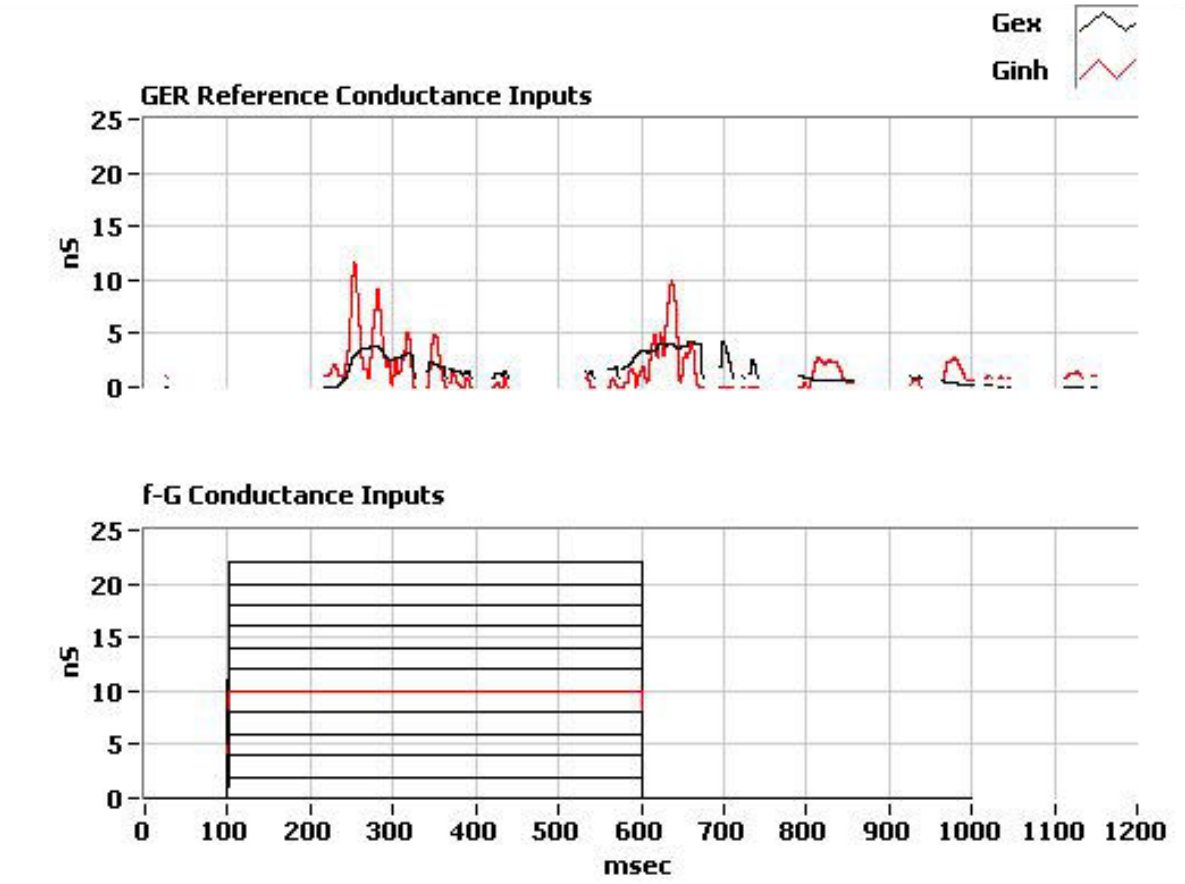


*Figure 80 Conductance inputs for the GER and F-G protocols. The reference inputs for the GER protocols(top) are those estimated from the visually-evoked response, with the GER-based transfer function constructed by applying scaling coefficients to the excitatory and inhibitory components. The inputs for the F-G protocols(bottom) – conductance steps. The resting input conductance for this cell, $G_{rest}$, was 20.1 nS.*

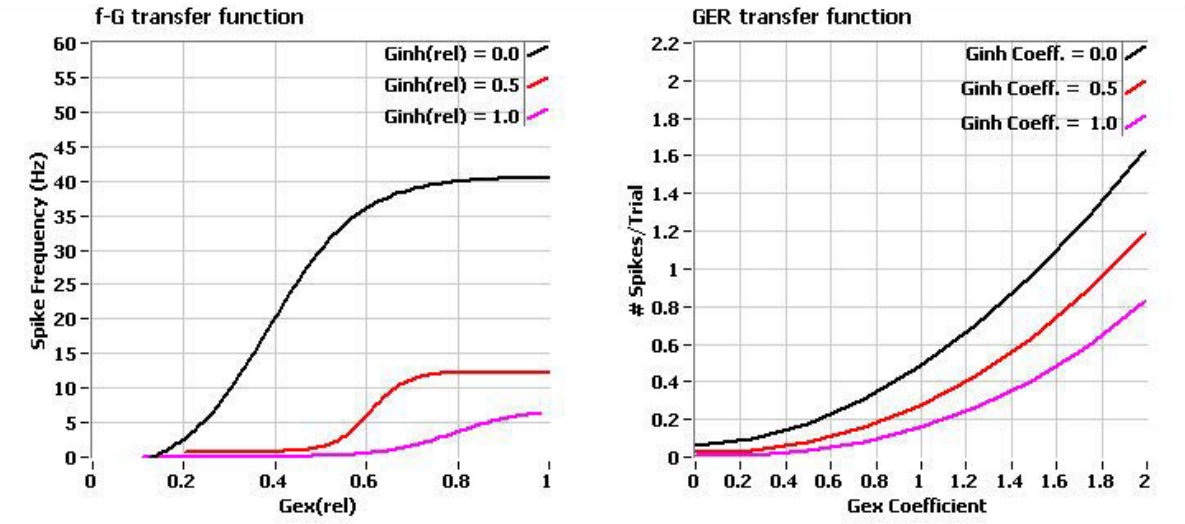


*Figure 81 F-G and GER derived transfer functions, fitted with sigmoid and 3rd order polynomial, respectively (2017.12.13\cell 6).*

The influence of relative bridge error and relative peak of conductance was checked to influence the fit between DC and visually evoked potentials (Figure 82). No clear relation was found.

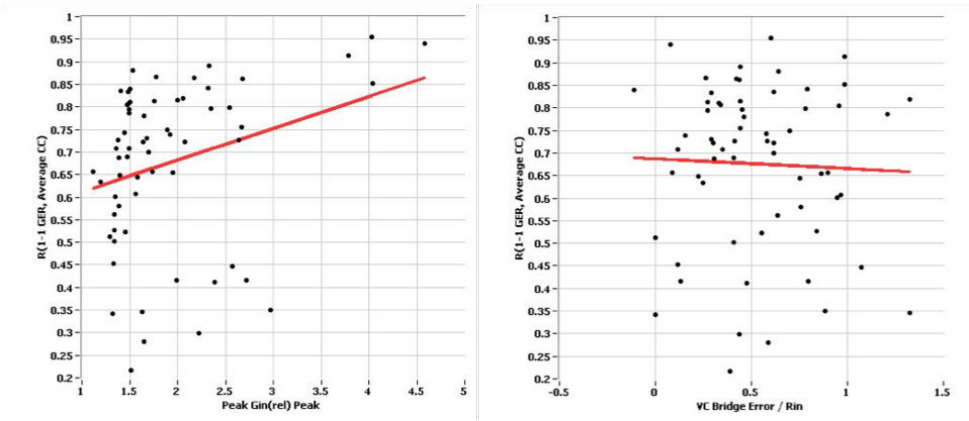


*Figure 82 Gin change and Bridge value do not influence the fit between DC-evoked (for unitary coefficients) and visually evoked membrane potentials.*

To further validate the effect of the shunting inhibition and excitation on spiking output the entire population of cells was analyzed. The change of gain was calculated for each cell as number of spikes divided by excitatory coefficient. This change was further divided by change in inhibitory coefficient. Distribution of shunting inhibition impact is shown on the Figure 83. On average the gain decreased by $0.28 \pm 0.35$ times. The mean effect of the inhibition on the gain is statistically significantly different from 0 ($p<=0.001$, T test). Similarly, the gain change induced by conductance steps injection (FG curves) was calculated. The number of evoked spikes was divided by the relative excitation, divided by change of relative inhibition (relative to $G_{rest}$). The mean gain change for conductance step injected was equal $-0.39 \pm 0.23$. Both gain changes are significantly different from 0 ($p<=0.001$) (Figure 83).

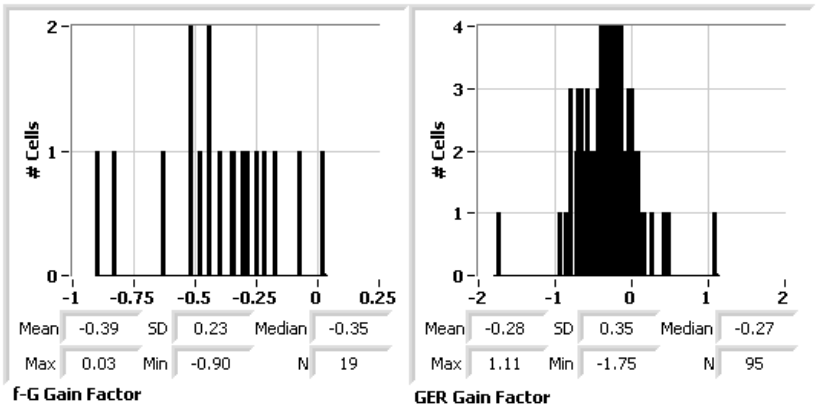


*Figure 83 Impact of inhibition on firing gain. Left: Result from f-G protocols, measured as the relative change in gain (spikes/$G_{exc}$(rel), normalized by the gain with zero inhibition), divided by the change in $G_{inh}$(rel). Right: Result from GER protocols, measured as the relative change in gain (spikes/$G_{exc}$ Coefficient, normalized by the gain with zero inhibition), divided by the change in the $Gi_{nh}$ coefficient. In both cases, the mean effect of inhibition on gain, -0.39 and -0.28, respectively, is statistically significantly different from 0 ($p<= 0.001$).*

The correlation of impact of inhibition with several synaptic changes parameters was checked. A preliminary analysis shows low correlation coefficients (Rxy < 0.2)between the change in the firing gain and:

1. Averaged global I/E ratio
2. Peak I/E ratio
3. Peak of relative G Inh
4. Peak of relative G Exc
5. Grest
6. Resting potential
7. I/E Frequency ratio (based on Cumulative Normalized Power Spectrum analysis at level 0.75)
8. Cross-correlation of excitatory and inhibitory peaks
9. Cross-correlation time lag between two synaptic components

Moreover, there was a low correlation between the FG gain factor and the GER gain factor. This could suggest that different nature of the input not only provides a bit different transfer function, but also that there is variability of this difference over the population level.

In summary, this chapter describes the validation of the protocol used to probe cell output in various input conditions. The good overlap between membrane potentials during 'natural' and 'artificial' synaptic input proofs feasibility of the protocol. The divisive effect of shunting inhibition to the spiking cell output was confirmed in mouse V1 by physiological synaptic input injections and conductance step protocol. Moreover, the linear shift presence in the conductance step injections protocol suggest the potential role of fluctuations present in the synaptic input.

Further analysis needs to be done to fully explore recorded data, in particular, to assess the influence of cell layer or type to the I/O transfer function changes. Additionally, a verification of minimal effective gain change would be useful to judge what changes in the transfer function are physiologically relevant to the neural code.

# 6.Discussion

## 6.1. Alternative methods of conductance estimation:

In principle conductance changes based on current-voltage relationships can be estimated from either VC and CC recordings, with the instantaneous conductance derived from linear (e.g. ohmic) or non-linear (e.g. polynomial, for voltage-dependent conductances) fits. As (C. Monier, Fournier, and Frégnac 2008) showed, the different fitting methods do not produce significant output differences between assessment of excitatory and inhibitory part, which would matter for physiological interpretation of results. On the other hand, depending on the method, the reported delta G might be different. Thus, comparison of G peaks value (if) needs to be done in the context of the conductance estimation technique (C. Monier, Fournier, and Frégnac 2008) and the absolute numbers of comparison should not be the main focus on the interpretation. The same authors show that the peaks of the estimated synaptic conductances, and overall the inhibitory component may be influenced by the recording mode. Thus, measurements in CC mode in vitro provided a lower estimation of the peak conductance than in VC mode. Interestingly, in i*n vivo* conditions authors did not report such a change (C. Monier, Fournier, and Frégnac 2008).

The argument that is most often raised against conductance measurements performed in CC mode is the possibility of AP presence in the recordings. In this case, the conductance of intrinsic channels that are involved in firing will be mixed with the synaptic conductance, thus compromising the precise estimation of the latter (Guillamon, Mclaughlin, and Rinzel 2006).

Space clamp problem

A commonly raised argument against conductance measurements done in VC mode is the space clamp problem, thus that the electrotonic structure of the neuron causes a degradation of the control of the membrane potential with increasing distance from the electrode. However, in the context of the present study, we are not claiming to estimate the synaptic input in terms of the actual conductance values integrated over the entire neuronal membrane, but rather the somatic signature of the input. On the other hand, it remains that the equivalent circuit for a synapse converges to a current source as the distance from the soma increases, and the estimated conductances cannot account for this component. The degree to which the effective current source component of the distal inputs are not accounted for in our measurements was assessed by comparing the cell's response to the DC injected synaptic input to the original visually evoked responses recorded under current clamp, quantified by the cross-correlation of the waveforms. We found that in most cases the membrane potential dynamics of the two conditions overlapped well, with a mean cross-correlation of $0.68 \pm 0.18$ (median 0.72). Some of the lower fits can be explained by a discontinuous conductance waveform, arising from the 5% threshold criteria for accepting a conductance value. In fact, a simple explanation for these periods, in particular when there is a clear response in the

membrane voltage, is that the somatic signature is dominated by current from distal synapses. A more indirect, but in fact more functional, validation of the fidelity of the conductance estimates lies in comparing the PSTHs of the GER protocols with the original visually-evoked response. We find that in general there is a good correspondence between these spike measures, usually peaking at the same times, demonstrating that the response can be recreated artificially.

All above arguments authenticate our results. Although small changes of driving force due to the space clamp problem and electrotonic attenuation can be present in our recording they are not big enough to disrupt the effect of synaptic input to the spiking cell output. The fact that mouse cells in L2/3 are relatively compact, and that majority of synaptic inputs is close to the soma (~150 μm) (Adesnik 2017) works in favor to obtain reliable conductance estimation.

## 6.2. Influence of conductance estimation procedure to results interpretation

The precise technical procedures to estimate conductance, especially the excitatory and inhibitory component, might be influenced depending on the order of averaging and inferring the conductance. As presented in chapter 4, estimating the conductance of each pair and averaging as a second procedure might influence the estimation of excitatory and inhibitory component. Although the absolute numerical differences are not big between the estimated waveforms it put in question analysis done on the base of the peak amplitude.

The second important technical point is the estimation of bridge error. In this work we estimated the bridge value carefully, taking into account not only the uncompensated bridge during VC mode, but also changes in the access resistance over the entire recording. Indeed, as previous work on cats show, incorrect correction of the bridge can result in incorrect qualitative conclusions about evoked synaptic conductances (Carandini and Ferster 1997)vs. (Jeffrey S. Anderson, Carandini, and Ferster 2000). As explained in chapter 4, within limits, the size of the imposed bridge error on the recordings for the conductance estimation mainly scales the output, but it does not strongly influence the dynamics, nor the overlap between the estimated and visually evoked averaged membrane potential (done as an approximate check on the measurement). This qualification is important here since the primary goal for the conductance measurements was in the context of how the excitatory and inhibitory dynamics and the E/I ratio can provide insights into functional circuit processing mechanisms. Since the dynamics are relatively robust to bridge error, this increases the confidence for the results reported here with respect to excitatory and inhibitory spectra and coherence. With respect to scaling, as described in chapter 4, it is important to note that the scaling factor due to incorrect bridge estimation is stronger for the inhibitory component. Thus, in principle there is less confidence in the reported absolute and relative values of the synaptic components, with the most likely error being an underestimation of both parts of the conductance, as well as an overestimation of the E/I ratio.

As shown in (Haider, Häusser, and Carandini 2013), in practice the number of holding potentials used for conductance estimations do not have a strong influence on the estimation, and our experimental results confirm that analysis. In the majority of cases the conductance estimations reported here are based on two holding potentials: typically, at -65mV and either -90 mV or -95mV. The addition of another holding potential did not significantly influence the quality of estimation (judged based on overlap between estimated end evoked membrane potentials). On the contrary, by adding an additional holding potential, the time of the VC recording is longer, and thus the probability of changing conditions higher.

## 6.3. Comparison of experimental findings:

Understanding how synaptic inputs shapes neuronal response is a key question of neuroscience. The circuit architecture differences between higher mammals and rodents allow to assume different synaptic components activity. Indeed, substantial differences were found in the temporal dynamics of orientation tuned excitatory and inhibitory component in mice and cats (A. Y. Y. Tan et al. 2011; Jeffrey S. Anderson, Carandini, and Ferster 2000; Borg-Graham, Monier, and Frégnac 1998). However, reported for mice synaptic conductance input was substantially lower than for cat (Liu et al. 2010; A. Y. Y. Tan et al. 2011) even in awake conditions (Bennett, Arroyo, and Hestrin 2013; Haider, Häusser, and Carandini 2013). Additionally, authors were presenting contradictory results for estimated excitatory and inhibitory component. Some of them were reporting prevalence of inhibition (Liu et al. 2010; A. Y. Y. Tan et al. 2011) whereas data shown by the other suggest balance with a small prevalence of excitation. Conductance estimation presented in this thesis is substantially higher (relative peak conductance change average of ~80% with the increase between 12-358%). Similar amplitudes were measured previously for cats (Borg-Graham, Monier, and Frégnac 1998; Jeffrey S. Anderson, Carandini, and Ferster 2000). The absolute peak amplitude recorded ranged between 6-72 nS which is higher than reported so far ~10 nS amplitudes (Liu et al. 2011; A. Y. Y. Tan et al. 2011) and ~20% (Haider, Häusser, and Carandini 2013). Possible reasons of different measurement might lay in the recording quality and stability and conductance estimation technical details, as well as different anesthesia protocol and different visual stimulation. However, it is hard to claim if all these reasons are enough to fully explain the scale of changes in the recordings among all the authors. Not all the works provide detailed description of the methods and recording conditions. The support of the findings present in this thesis comes from similar conductance changes estimated in cats as well as the closed loop protocol validation, which shown that injection of the estimated by us conductance is able to recreate the visually evoked membrane potential dynamics reliably.

Our analysis of the relation between the evoked relative conductance change and the momentary effective reversal potential agrees with the results from cat V1 (Borg-Graham, Monier, and Frégnac 1998). Similar characteristic shapes of the phase plots were found (‘Eiffel tower shape’), indicating that the peak amplitude of the conductance change was in proximity to the cell resting potential,

pointing to prevalence of shunting inhibition over excitation. The difference between the potential at the peak change and cell resting potential was almost always slightly depolarized in relation to given cell resting potential. The $E_{rev}$ describes also I/E ratio during the ongoing stimuli, assuming that the conductance estimation reflects well synaptic input to the soma.

A more direct comparison of the I/E ratios with those reported in the literature (comparison of ratios of either the peak conductance or those averaged over the entire response duration), do not show any consistent relation between excitatory and inhibitory waveforms. I/E ratios between 0.5 – 4 with a mean about 2 reported in (Liu et al. 2011), in comparison to the work of (A. Y. Y. Tan et al. 2011) (ratio of ~1) and our results show substantially different relations between excitation and inhibition. First, these authors postulate that excitation and inhibition are almost synchronous, whereas we observe typically asynchronous responses, with a range of waveform shapes and temporal alignments. Secondly, (A. Y. Y. Tan et al. 2011) show similar amplitude of excitatory and inhibitory conductance. For either point, it may be speculated that the higher anesthesia used in this study, as well as higher values of access resistance, could be the source of differences.

As shown in the chapter 4 and commented in the beginning of the discussion, the values of the peak can vary depending on technical details of the estimation and recording quality. Changes of around 1 nS or higher can be caused by space clamp problem (Wehr and Zador 2003; Adesnik 2017), high access resistance of recording or lack of compensated bridge error (Borg-Graham, Monier, and Frégnac 1998; Anderson, Carandini, and Ferster 2000), or a different function used to estimate conductance (Monier, Fournier, and Frégnac 2008). Additionally, the distribution of cross-correlation lags of the excitatory and inhibitory components stress the presence of various peaks for conductance estimation within the same response. The wide distribution of the lag between peak excitation and inhibition, up to 0.5s, which is the stimulus duration, suggests that this measure is not informative, taking into account a similarly wide distribution of cross-correlation coefficients emerging from our data base.
For these reasons it is important to avoid operating with peaks statistics, as their maximal values might be influenced by several factors (in this thesis they are used in order to refer to other authors findings). Additionally, the changes of conductance in relation to the cell's resting conductance seems to be more informative than the absolute values. The same amplitude of conductance will probably have different impact depending on a cell initial $G_{rest}$. The peaks relative to $G_{rest}$ amplitude might deliver some insight into tight I/E balance.

Presented results show substantial variability between possible interplay of synaptic components, which pose a challenge to find parameter well describing the various patterns. However, one quite stable among all the result feature is the higher frequency of inhibition in comparison to excitation. Analysis of power spectrum (center of mass analysis and cumulative normalized power spectrum at fixed level analysis) pointed out that indeed frequency of inhibitory waveform contains more higher frequencies than excitatory one. In or data set, inhibition was characterized by ‘faster’ and more variable waveforms in comparison to excitation. Possible reason for different dynamics of excitatory

and inhibitory input could lay in position and kinetics of channels. GABAa channels, which are the source of shunting inhibition in our protocol conditions are characterized by fast kinetics (1 ms of rise time) and synapses in the somatic part of the neuron (Koch 1999). In contrast, the excitatory input is mainly due to AMPA (fast kinetics) and NMDA (slow kinetics) receptors interaction (Koch 1999).

Comparison of technical detail and the quality of data presented suggest high variability of evoked conductance waveforms. Our work fills the gaps in the description of visually evoked changes in mouse V1, additionally providing basis to the further theoretical studies focusing of the influence of synaptic input features to the neuronal processing.

## 6.4. I/O transfer function

The protocol described in this thesis which combines conductance measurements with DC closed loop probing constitutes an important tool for hypothesis verification concerning the role of shunting inhibition, the I/E ratio, and the functional role of fluctuations in the excitatory and inhibitory inputs.

To date several investigators have shown that functionally evoked synaptic responses are typically dominated by components consistent with GABAA inhibition (visual cortex: Borg-Graham et al., 1998; Monier et al., 2003; Anderson et al., 2000; 2001; Hirsch et al., 1998; Marino et al., 2005; Priebe and Ferster, 2005, 2006; auditory cortex: Tan et al., 2004; Wehr and Zador, 2003, 2005; Zhang et al., 2003; barrel cortex: Higley and Contreras, 2006; Wilent and Contreras, 2004, 2005; prefrontal cortex: Haider et al., 2006).

The data presented in this thesis confirm that shunting inhibition provides strong conductance input to neurons in mouse visual cortex. Furthermore, our reinjection of the measured excitatory and inhibitory inputs to the same neuron confirm that levels of shunting inhibition consistent with functional responses have both a significant divisive and linear influence on the I/O transfer function. Although data show variability and different gain change was observed in the cell population, the average gain change ratio suggest about 29% decrease in gain for increase of inhibitory input equal 1. A bit higher value of gain decrease is observed for I/O transfer function constructed by conductance steps injection (FG based I/O transfer function). This difference might suggest the importance of fluctuations for spiking output. The conductance steps, constitute a simplified version of synaptic input, characterized only by the relative to the cell $G_{rest}$ amplitude of the step and therefore stable I/E ratio. In contrast, the synaptic evoked conductance waveforms represent a highly variable data set. Both the tight and global I/E ratio changes across cells and no significant relation was found. Despite the population changes, the influence of shunting inhibition was clearly visible. However, the linear, rightward shift is not as evident as in case of FG based functions. This finding would be in agreement with theoretical studies predicting divisive effect of conductance fluctuations to the cell gain (Destexhe et al. 2001).

## 6.5. E/I balance definition and consequences:

Several paper describes the E/I balance. However, depending on the time scale considered tight and global I/E balance definition was proposed (Denève and Machens 2016; Viltart et al. 2018; Piwkowska et al. 2008; Pospischil et al. 2009; Bal and Destexhe 2009). General (global) balance describes the relative contribution of excitatory and inhibitory synaptic current from the network to a neuron across the range of spatio-temporal conditions. On slow time scale, the E/I balance is approximately constant (Viltart et al. 2018).

Tight temporal balance describes the relative amplitude of excitatory and inhibitory currents in the short temporal scale (1ms). Shu et all 2013 show almost perfect E/I balanced conductance in vitro. (Okun and Lampl 2008) show that synaptic excitatory inputs of one cell and inhibitory input on another cell are receiving balanced input. (Xue, Atallah, and Scanziani 2014) shown that uIPSC and uEPSC are balanced at single cell level (the more inhibition the more excitatory current received), even if the ratio varies in between the cells.

However, in context of these studies the conclusion about balance would be drawn based on the peak value of unitary evoked currents. Such a fine circuity could explain postulated by (Renart et al. 2010) E/I balance emergence from high correlation between E and I on fine temporal scale. On the other, hand proposed model by (van Vreeswijk and Sompolinsky 1996) and describing network using E/I balance assume sparse connectivity, defined as number of synaptic contact substantially lower than the number of cells in the network. In light of dense synaptic connectivity (e.g. almost all neighboring to PY cell SOM and PV cells were connected with it (Xue, Atallah, and Scanziani 2014) in local circuits it is hard to imagine scenario in which the sparse connectivity could took place. And yet, we still obtain balance in some experiments, which points to the strength of synaptic input as important condition for keeping the ‘sparse synaptic input condition’ (as if only few synaptic inputs are strong enough to induce a spike on the postsynaptic cell).

(Boerlin, Machens, and Denève 2013) provided analysis more focused on the E/I balance from neuronal code perspective and demonstrated that tight balance with correlated inputs results in uncorrelated output. Such conditions constitute efficient code and low energy cost. Further, (Sengupta, Laughlin, and Niven 2013) show that tight balance result in low number of spikes (also in agreement with low energy cost theory). Additionally, in the brain at different locations we can have several balances and the wave like behavior of propagation of balance is presented.

In favor of various E/I balance theory findings of (Adesnik 2017) could be recalled, who experimentally presented how E/I balance changes during contrast and stimuli size tuning. However, it is worth to stress that a global E/I ratio was used to describe the findings of this work. The author was averaging over the evoked currents during stimulus time and then in between the cells. Similarly, it was also shown that anesthesia and brain state influences the brain dynamics and as shown by

(Bennett, Arroyo, and Hestrin 2013; Haider, Häusser, and Carandini 2013) the change or the E/I ratio is involved.

The conductance fluctuating synaptic input (A Destexhe et al. 2001) as well as short time depression (Rothman et al. 2009) was shown to influence the neuronal gain. Both of them, as well as described also in this work shunting inhibition changes concern characteristic of the synaptic input (temporal dynamics and E/I ratio). It would be reasonable to assume that some feature of synaptic input might cause observed experimentally change of the neuronal gain. However, the first round of data analysis did not allow to point to any relations of the neuronal gain change to any from the measurements described in this thesis. Therefore, based on the results of the work described in this thesis some verification of proposed scientific hypothesis can be done. Our data set contains characterized on fine and more global temporal scale changes. Additionally, we shown results evidencing the influence of shunting inhibition to the neuronal gain. We hope to understand in the future what synaptic input feature account for observed gain change. Our data provide the numerical description of conductance changes, their frequency content and E/I ratio in time, enabling more realistic modeling studies including network dynamics studies.

# 7. Methods:

## 7.1.in vivo electrophysiology for neuronal code studies:

### 7.1.1. Animal model

#### *7.1.1.1. Well –being of animals before and during experiment*

C57Bl male mice (Janvier, France) between 5- 12 weeks were used in this study. After delivery animals were kept in local animal house in 12:12 dark-light cycle with free access to the food and water in room temperature till the day of experiment. An hour before the start of experiment animals were weighted and moved to cage next to experimental set up in which they were anaesthetized at the beginning of surgery. Behavior of animals were observed (grooming, exploring the cage or freezing), and any signs of stress were reported to the animal house manager.

All the procedures were described and presented to the local ethical committee, approved in the document: N° 2015092118054726, project: N° 14-055 30/09/2015.

#### *7.1.1.2. Surgery procedures*

Surgery procedures started with anaesthetizing animal with an exposure to 3% isoflurane mixed with pure oxygen (1L/min) for 2-3 minutes delivered by isoflurane anesthesia unit (Harvard Apparatus). After the first induction dose isoflurane level was lowered till 2% and animal was placed at the experimental rig on a thermal blanket, where it remained till the end of experiment. The nose of the animal was placed in the inhouse made isoflurane mask which delivered the anesthetic and utilized the residual gases through the scavenger. Pedal reflex was checked several times during the surgery to check anesthesia depth.
Both eyes were protected with the ophthalmological gel(Bauch+Lomb) and a thermal probe (Harvard Apparatus) was inserted to the anus for maintenance of body temperature (37 °C). Sub-cutaneous injection of drugs was performed: Local anesthetic – Xylovet (0.1ml, Ceva) in the area between the ears, and Dexamethasone (10mg/kg, Virbac) and Glycopyrolate (0.25mg/kg, Vetoquinol) at the back. After 2 minutes the skin with a right ear were cut out to expose right part of the scalp. Next, isoflurane level was lowered till 1,5% and additional sedative agent - chlorprothixene hydrochloride (2.5-5 mg/kg, Sigma) was injected subcutaneously (C. M. Niell and Stryker 2008; Haider, Häusser, and Carandini 2013). The scalp was cleaned, and muscles attached to the parietal bone were detached. The bone was rinsed with hemostatic agent (Hemospad, Dentsply) to provide dry bone surface and stop eventual bleeding. Stereotaxic measurements were taken and V1 cortex center was marked on top of the scalp. A thin layer of Vetbond (3M) was provided around the marked place as a base to dental cement used to fix the metal head plate to the scalp. After few minutes animal was mounted in the rig by mounting the headplate in the rig firmly providing mechanically stable preparation for further experiment. Two needles were inserted on both sides of the body as ECG sensors connected

to ECG unit (CT-1000 Cardiotachometer, CWE.INC) for monitoring heart rate during entire experiment. Next, a small plastic ring was attached to the head-plate with diluted dental cement to create a basin for ACSF and melted Agarose (used in next steps).
The prepared scalp was cooled down with frozen ACSF (in mM: 125 NaCl, 2.5 KCl, 26 NaHCO3, 1.25 Na2H2PO4, 25 Glucose, 0.5 Ascorbic Acid, 1.5 CaCl2 and 1 MgCl2 pH=7.45) which melted down slowly at the exposed mouse sculp and 1 mm diameter circular craniotomy was performed. After exposing and cleaning the cortex from bone residuals with cold ACSF, tissue was secured with 2% agarose and left for about 1h. The reference electrode was placed between the skin and the left side of the scalp and secured with agar.

At the end of surgery, the level of isoflurane was slowly lowered till 0,25% while monitoring ECG and animal breath. Animal was hydrated every 1-2h with 1 ml of saline based solution. It was important to perform all procedures quickly (~45min for all procedures) and precisely to obtain stable and repeatable preparation. The typical duration of experiment was 7-9 hours. At the end of experiment high level isoflurane was applied (5% for few minutes) and cervical dislocation was performed. Only 6 mice out of 228 used animals died during the surgery or shortly after.

## 7.1.2. Data acquisition and protocols:

### *7.1.2.1. Visual stimulation*

Black and white grating bars moving in eight directions were used to evoke visual response. Stimulus was displayed on a screen (Dell) with 100% contrast, at 2Hz temporal frequency and 0.04 Hz spatial frequency and random order within a trial. The screen was positioned around 30cm from the mouse eye. The size of the stimulus was modified. For some recordings receptive field was mapped on the screen with 5-10-degree precision. Further two kinds of stimuli were used: small field stimuli – a 20°diameter circular stimuli and full field stimuli - 200°, which covered the whole monitor.
Using TCP communication between Surf Vision software written in LabView programming environment (National Instruments) and visual stimulation computer enabled control of the presence and timing of the stimuli. The VisionEgg (Straw 2008) Python library was used to code the stimulation attributes on the visual stimulation computer.

### *7.1.2.2. Electrophysiology*

Blind patch clamp technique was used in this study using Touch and Zap method in Current Clamp configuration (Schramm et al. 2014). In brief, ~1nA step current pulse is used to monitor resistance increase during tissue penetration, which enabled fast and gentle seal formation and cell opening after releasing the positive pressure after 'touching' the cell with the electrode.
Thin wall borosilicate filaments (WPI) pulled on a horizontal puller (Sutter Instruments P-97) to obtain 4-10 MOhm resistance electrodes of tip diameter around 2 $\mu$m. K-gluconate based Internal solution (in mM:110 K-gluconate, 10 HEPES, 1 EGTA, 20 KCl, 2 MgCl2, 2 Na2ATP, 0.25 Na3GTP,10

Phosphocreatine, 295 Osm, pH=7.45) was used containing EGTA to ensure better access resistance (Sakmann and Neher 1983).

In-house recording system was developed in order to perform Dynamic Clamp protocols with the help of LabView software (National Instruments) and G-clamp software (Kullmann, P.H.M. and Horn J.P. 2004). Degan Instruments BVC-700 intracellular amplifier was connected to two acquisition boards, one – serving as communication with a Real Time computer providing command input during dynamic clamp protocols and second, serving communication during traditional CC and VC recordings. Neuronal signal was low pass filtered at 10 kHz and acquired at either 20kHz or 40kHz.

#### *7.1.2.2.1 Patch-clamp recording of visually evoked response*

Initial cell characterization

After establishing the whole cell configuration both cell capacitance and access resistance was compensated at the amplifier while injecting subthreshold current steps. Next, cell parameters were measured by current-step protocol. Ten hyperpolarizing, or - in case of low resting potential- depolarizing currents steps were injected to assess cell: input resistance (Rin), input conductance (Gin), access resistance error (Ra error), cell capacitance (Cm), time constant (tau), resting potential (Vrest). During entire recording cellular parameters were frequently checked and recorded in between protocols, to ensure the knowledge about eventual changes in Rin and Gin, Ra and Ra error. Next, IV curve protocol was applied – 10-15 current steps of increasing amplitude to evoke spiking. Based on spikes evoked electrophysiological type of cell was assessed.

Visually-evoked response measurements

After initial characterization of cell electrophysiological type and properties, visually evoked cell response was recorded.

First, the cell response to 8 directions of moving grating stimuli was recorded to characterize initial visually evoked response (3-15 trials). Usually, one or two directions have been chosen to continue further recordings, based on number of spikes elicited during presentation of each direction stimuli and trial to trial variability of the response. Visually evoked response for stimulation of chosen direction was repeated few times during the whole recording duration.

Next, the visual stimulus of chosen direction was presented (10-20 repetitions) under the Voltage Clamp configuration and evoked currents were recorded at minimum two different holding potentials (usually -65mV and -90mV). During Voltage Clamp configuration the access resistance was compensated in between 0 and 50% of initial value. Each time the access resistance compensation applied on amplifier was logged. Measurements of Rin, Ra and Ra error performed before and after VC measurements allowed for holding current correction (Vh=Vh+I(t)*error) allowing for more precise conductance estimation.

Based on measured evoked currents and corrected holding potentials linear regression was performed to asses visual evoked conductance, which constituted synaptic input to a cell. Further,

estimated Gin changes were split into excitatory and inhibitory part based on the momentary reversal potential of the cell.

### *Dynamic-Clamp protocols simulating synaptic input*

Initial steps

After switching recording mode back to Current Clamp configuration, a current step protocol was repeated to measure cell properties. Visually-evoked response to the chosen direction was repeated and eventual change in Vrest was logged.

Synaptic input injection

Estimated conductance waveforms constitute the input to the cell in our protocol. To explore wide range of possible inputs two kind of protocols were performed with the use of dynamic clamp protocols:

F-G protocol - conductance step injections:

A step - conductance function of changing amplitude was introduced to the cell. The amplitude of the conductance step was calculated based on the cell resting conductance. The basic protocol started from injecting excitatory conductance step equal to the cell input conductance which would be iteratively (8-15 times) increased by 0.05-0.1 factor (5-10% of Gin). In next repetitions, inhibitory conductance was added, resulting in scaling the conductance step amplitude down to mimic inhibition levels corresponding to the factor of 0.5, 1, 1.5 and sometimes 2 times the Gin of the cell. Each recording condition was repeated 3-5 times. The number of spikes and membrane potential as well as injected current was recorded.

-GER protocol-visually-evoked conductance waveforms injections:

Analogically to the conductance step injection the cell was probed by introducing estimated conductance waveforms low pass filtered at 50Hz ($2^{nd}$ order Butterworth low pass filter). To explore various levels of excitation and inhibition introduced to the cell the excitatory and inhibitory conductance waveforms were scaled according to the originally measured synaptic input. Around 16 scaling factors for excitation and 4-5 for inhibition were usually applied (between 0 and 2) resulting in conductance grid of about 64 conditions. Each recording condition was repeated 5 or 10 times. The iterative algorithm was designed to collect data as efficiently as possible. Therefore, first scaling factors applied to the dynamic clamp current equation were providing main skeleton for a $16^{th}$ elements basic grid. Further, in next iterations the grid was filled with data coming from coefficients laying in between the basic skeleton, providing more dance grid of probed conditions. This enabled using data containing different number of tested parameters. Additionally, for some cells the grid was repeated in random order to exclude possible influence of order of the coefficients applied to synaptic input.

Moreover, in part of the cells, the same conductance grid was repeated with the conductance waveforms estimated based on current and voltage traces low pass filtered by $2^{nd}$ order Butterworth 10 Hz filter. Therefore, for a subset of cells the same grid of E/I coefficients was applied to 10Hz and 50Hz low pass filtered conductance waveform.

## 7.1.3. Data analysis

### *7.1.3.1. Neuronal type classification*

Taking into account the variability and number of possible neuronal classifications (Beierlein, 2003; Markram et al., 2004; McCormick, Connors, Lighthall, & Prince, 1985), especially for interneurons (Ascoli et al. 2008) the basic classification adopted by us differentiate cells into two groups: Regular Spiking and Fast Spiking cells (approximately excitatory pyramidal neurons and inhibitory interneurons).

Few parameters were inferred from spiking evoked during current step injection protocol. For all cells we have measured: first spike and mean for all spikes inter-spike value (ISI), first spike and all spikes mean width, first spike and all spikes mean 5ms fast after-hyperpolarization voltage value (fAHP), median post-hyperpolarization (PHP), spiking threshold. Additionally, presence of adaptation and bursts were noted. Based on that the parameters and overall shape of the action potential cell were assigned to two groups. Presence of bursts in the spiking response indicated bursting type, which in our classification, taking into account spike width and inter-spike periods shape, is a subgroup of RS cells.

To classify cells into group following criteria were used:

- adaptation presence, defined as the difference of mean and first ISI (the stronger adaptation the more positive number)
    - If yes: RS, no: FS
- mean and first spike width
    - ~1ms: RS ~0.5 FS
- presence of fAHP: present, if 5sec window fAHP voltage value is close to the median PHP voltage value
    - if yes: FS, no: RS
- presence of bursts - log ISI distribution and by eye inspection
    - yes: bursting no: other

### *7.1.3.2. Validation of Dynamic Clamp Protocols:*

Validation of the F-G dynamic clamp protocols was established by examining phase plots of the recorded voltage versus the recorded current (Figure 84). In this case, constant values of injected conductances are expected to give linear trajectories on the IV plane, as observed in the phase plots. For the GER protocols, the injected current was compared with a posteriori reconstructions of the expected current, calculated directly from the recorded voltage and the referenced conductance

waveforms (Figure 85). Thus, as a first step, a least-square fit was performed between the recorded and reconstructed currents in order to verify and, if necessary adjust, the scaling coefficients of the visually-evoked conductance waveforms used for a given protocol. As a second step, the two current waveforms were plotted against each other, and the close one-to-one correspondence confirmed that the sampling rate was sufficient to capture the cellular voltage dynamics.

The entire visual response – conductance estimation – conductance injection sequence was validated by comparing the original current clamp visually-evoked response recordings with the GER protocols associated with the unscaled measured Gex and Ginh waveforms (ref. Chapter 4).

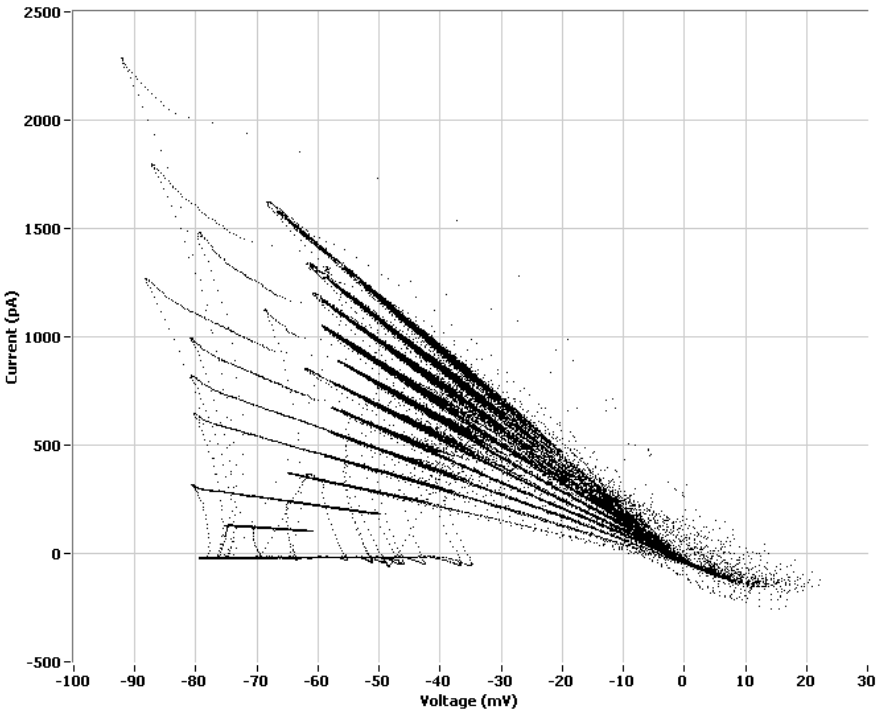


*Figure 84 Plot of current vs voltage for F-G protocol (2017.12.13 cell 6, 13172447.gs1). The responses to steps of constant dynamic clamp conductance are validated by the family of essentially linear characteristics on the IV plane, in particular confirming that the sampling rate is sufficient for the dynamic clamp current to track the voltage dynamics even during action potentials. For this particular protocol the injected conductance has a reversal potential of 0mV, corresponding to pure excitation, which is confirmed by the intercept of the linear trajectories being at the origin.*

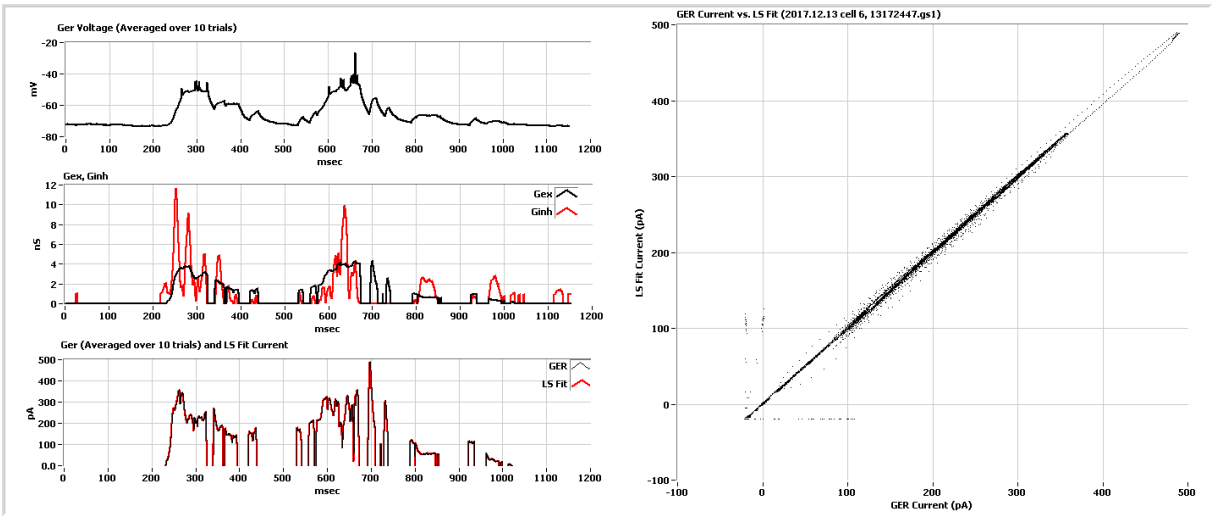


*Figure 85 GER protocol voltage and current responses averaged over 10 trials (2017.12.13 cell 6, 13171537.ger). The current provided by the dynamic clamp is compared a posteriori with a validation based on the recorded voltage and the referenced synaptic conductance waveforms by a least-squared fit procedure. The close one-to-one match between the recorded and estimated current confirms the fidelity of the dynamic clamp with respect to the injected current faithfully following the recorded voltage.*

## 7.2. In vitro electrophysiology for opsin characterization

### 7.2.1. Expressing an opsin in the biological preparation

#### *7.2.1.1. Viral injections*

All opsins used in this project were expressed in a similar way – by AAV injection as a vector in V1 area. All procedures were in agreement to institutional guidelines of the care and use of laboratory animals (Council directive 86/609 EEC).

Swiss male mice (Janvier, France) between 4th and 5th post - natal week were anaesthetized with a mixture of Ketamine (80mg/kg, Ketamine 1000, Virbac France) and Xylasine (10mg/kg, Xylazine Rompun 2%, Bayer Healthcare) by intraperitoneal injection. After obtaining a deep level of anesthesia the animal was placed in a stereotaxic rig and the surgery was started. During the whole procedure the level of anesthesia was monitored by checking the reaction to pinching one of the limbs or the tail, corneal reflex, and observing whisker movement and the breathing pattern. The eyes were protected with lubricant to prevent dehydration (Dexpanthenol; Chauvin Ankerpharm GmbH Berlin). Incision points were locally anaesthetized by subcutaneous injection of 0,05mL of Lidocaine (Xylovet 21.33 mg/mL; CEVA). The skin was incised to uncover the skull and stabilized on each side with bent needles to allow for cleaning the skull with saline and further manipulation. A small craniotomy (1 -2 mm diameter) was performed above V1 (from the bregma: AP= -3 - -4,5; LM=2-3) and the dura mater was pierced. A 36-gauge stainless steel beveled needle (Coopers Needleworks Ltd) or Hamilton needle (Hamilton) was inserted at a depth of 200 µm from brain surface, thus targeting for L2/3. Virus was injected at a rate of either 100nL / min (Coopers Needleworks needle), or 40- 60 nL / min (Hamilton needle). After the injection the skin was closed with cyanoacrylate glue (Super Glue Loctite; Henkel). At the end of the procedure, the animal received an intraperitoneal injection of Antisedan (0.2 mg/kg; Janssen) for faster recovery, and 0,2 mL of 9% saline subcutaneously to avoid dehydration. The animal was then returned to its cage and warmed under a lamp until full recovery (0,5 – 2h).

AAV constructs used (titer, vg/ml; organized in group of viruses used together in each approach):

Multiple opsin expression project (results described in section 3.2.3):

- CatCh
    - o AAV2.7m8-CAG-CatCh (2.9x10e12)
    - o AAV2.7m8-CMV-Gcamp6s (5,9x10e13) o AAV2.7m8-CAG -tdTomato (9,2x10 e13)
- Chronos-1
    - o AAV2.7m8-CAG-Chronos (1x10e12)
    - o AAV2.7m8-CAG-tdTomato (1,27x10 e13)
- Chronos-2
    - o AAV.2.7m8-CAG-Chronos (6,68x10e12)

    - o AAV.2.7m8-CAG-tdTomato (2,81x10e14)
- Chronos-3
    - o AAV9.2YF-CAG-tdTomato (2,26 x10e13)
    - o AAV9.2YF-CAG-Chronos (4x10e13)

Single opsin expression projects:

- ReaChR (results in section 3.2.2.3)
    - o AAV1 Ef1α-ReaChR-p2A-tdTomato (1.1 x10e12)

- ChR86 (CoChR)(results in section 3.2.1.2.)
    - o AAV8 hSyn-ChR86-mCardinal (1.9x10e12)

#### *7.2.1.2. Cultured cells*

The initial screening of some opsin constructs for multiple viral injection project as well as for the biophysical properties investigation of the opsins were done with the use of Chinese Hamster Ovary (CHO) cell culture.

The unthawed portions of the cell cultures were kept in an incubator at 37 °C and 5% CO2 in a D-MEM/F12 GlutaMAX medium (Life Technologies) with the addition of 1 mM glutamine, 1% streptomycin and 10% fetal bovine serum. Bi-weekly passages permitted keeping the culture in good health for multiple transfections, up to 24 passages. Cells were seeded on plastic coverslips (Thermanox, Thermo Scientific) in 24- well plate, 24 hours before transfection (50 – 100 000 cells/well). Plated cells were then transfected with DNA using either Ex-Gen 500(Biomol GmbH) or Jet-PRIME (Polyplus transfection) reagent. Data was collected 24 – 72 hours after transfection.

Plasmid sequences used (concentration in µg/µl):

Multiple viral injection project (initial screening done by plasmid expression in CHO cells)(results in section 3.2.3):

- AAV-CAG-tdtomato-2A-Chronos (1,1803)
- AAV-CAG-tdTomato-2A-CoChR, (1,0529)

Biophysical properties investigations and modeling studies (results in section 3.3):

- AAV-ReaChR-p2A-EYFP (2)
- FCK-Gene90-GFP (4,34)
- FCK-Gene86-GFP
-

## 7.2.2. Electrophysiology

### *7.2.2.1. Brain slices*

#### *Preparation*

300 mm thick cortical slices were prepared 4 – 12 weeks after viral injection. Mice were anaesthetized with isoflurane and decapitated. The brain was extracted in sucrose solution and sliced with a Leica VT1200S slicer. Sucrose solution was saturated with carbogen and contained (in millimoles of compound used to make a liter of solution): 25 glucose, 85 NaCl, 65 sucrose, 0.5 CaCl2, 4 MgCl2, 2.5 KCl, 1.25 NaH2 PO4 and 26 NaHCO3.

Each slice was checked under a magnifying glass with a fluorescent lamp to qualitatively evaluate the level of expression. Slices with visible expression were transferred to an incubator chamber and left for 0,5 – 1 hours at 33°C. Slice preparation and incubation were made under low-light conditions, and the slicer lamp was covered with a red filter to avoid activation of opsin.

#### *Recording*

Slices after incubation were transferred to a recording chamber on a microscope stage. All recordings were performed at room temperature, perfused constantly with Carbogen saturated extracellular solution composed of: 125 mM NaCl, 2.5 mM KCl, 26 mM NaHCO3, 1.25 mM Na2H2PO4, 25 mM Glucose, 0.5 mM Ascorbic Acid, 1.5 mM CaCl2 and 1 mM MgCl2. During some of the recordings the following synaptic blockers were added to the bath solution: NBQX, Strychnine, Biccuculine (1-5 µM). Patch pipettes were pulled (Sutter Instruments) from borosilicate glass filaments (ID 0,86mm, OD 1,5mm) to obtain 5-10 MΩ resistance, and filled with an intracellular solution containing: 130 mM K-gluconate, 7 mM KCl, 2 mM MgCl2, 4 mM 80 Mg ATP, 0.3 mM Na GTP, 10 mM na-phosphocreatine and10 mM HEPES, with pH adjusted to 7.3and osmolarity to 280 mOsm.

### *7.2.2.2. CHO cells*

The cover slip with cultured cells was transferred from the incubation medium to a recording chamber on the microscope stage. All recordings were performed at room temperature with an extracellular solution composed of: 140 mM NaCl, 5 mM KCl, 2 mM CaCl2, 1 mM MgCl2, 20 mM HEPES, 25 mM Glucose, pH adjusted to 7.5. Patch pipettes were pulled (Sutter Instruments) from borosilicate glass filaments (ID 0,86mm, OD 1,5mm) to obtain 3 – 7 MΩ resistance and filled with an intracellular solution containing: KCl 140 mM, MgCl2 2 mM, Mg ATP 2 mM, Na GTP 0.4 mM, Hepes 10 mM, BAPTA 20 mM. PH was adjusted to 7.3; osmolarity 330. Cells were maintained at -40 mV throughout recordings.

### 7.2.3. Data acquisition and protocols

The majority of the electrophysiological measurements were recorded using a Multiclamp 700B patch – clamp amplifier and Digidata 1322A system, using pClamp software. Data analysis was done with the help of Clampex software (Axon Instruments). Some of the experiments were recorded using a Multiclamp 700B amplifier and digitalized using a National Instrument data acquisition board (NI USB-6259). Data was recorded and analysed with the help of NeuroMatic and IgorPro software (Wavemetrics).

#### *7.2.3.1. Patch–clamp recordings from cortical slices*

Opsin positive cells were identified with the help of fluorescence illumination and then patched under IR illumination. After establishing a stable whole - cell patch configuration in voltage clamp mode the access resistance and cell capacitance were measured and compensated automatically by the software. Cell parameters were monitored during the entire recording. After whole-cell access, a current step injection protocol was applied in the current-clamp configuration to elicit a spike train in order to classify the physiological firing type of the recorded neuron. Next, brief light pulses with increasing intensity (duration varied for different opsins, and 1P or 2P illumination was used depending on the set up) were applied in order to record either photo-evoked currents (under voltage clamp) or cell membrane potential responses (under current clamp). For the current clamp recordings, once the light intensity sufficient to elicit an action potential was found ("spike threshold power") the following two approaches were used: a) recording the cell firing pattern during photostimulation with a pulse train of a fixed frequency and duty cycle, with increasing intensity, b) recording the cell membrane potential while moving the phase mask away from the soma.

#### *7.2.3.2. Voltage-clamp measurements of biophysical properties of opsin using CHO cells*

Opsin - positive cells in the CHO culture preparations were identified with the help of a fluorescent lamp, and then patched under IR illumination. After establishing a stable whole – cell patch configuration in voltage clamp mode, the access resistance and cell capacitance were measured and compensated. Cell parameters were monitored during the entire recording, and cells whose access resistance increased by more than 20% were excluded from analysis. Three different types of photostimulation were used for this study:

- A) long lasting (up to 4s) photostimulation with increasing intensity of laser pulse,
- B) pulse trains with increasing frequency (10-100 Hz),
- C) long lasting stimulation repeated while changing the interval between stimulations

## 7.2.3. Imaging and photostimulation

All experiments were done with the use of three set – ups. In each of them, a holographic illumination, either in one or in two photon, was implemented and followed analogous construction allowing for holographic photostimultion. A laser beam was firstly expanded in order to fully illuminate the screen of spatial light modulator (SLM). By the use of homemade software developed in the Neurophotonics Laboratory ("Wavefront"), the user could define any arbitrary illumination pattern and calculate the corresponding phase modulation addressed to the SLM. Such phase modulation imprinted by the SLM on the laser beam was then projected on the back aperture of the microscope objective resulting in the desired illumination pattern on the sample (Fig. XX). All the set ups enabled also electrophysiological recordings and included an infrared light DIC imaging.
In the following paragraphs I will briefly introduce the main characteristic and capabilities of each setup, related to the illumination sources and the imaging they provided.

### *7.2.3.1. 1–Photon imaging and 1-photon stimulation set up*

The first set up was mainly used for initial screening and first testing of opsin expression. It was based completely on 1P illumination.

It consisted of a Zeiss Examiner upright fluorescent microscope combined with a "Phasor", a compact and commercial version of holographic stimulation from "3i Imaging system ", allowing patterned illumination of a 405 nm laser source. The imaging was controlled by the Slidebook software (3i).

Recordings done on this set up allowed for:

- Pre-screening of the opsin expression via epifluorescence detection (brightness, spread, sparseness of opsin fluorescence),
- Targeted patch of opsin expressing cell and assessment of cellular type and electrophysiological parameters
- Photostimulation with 1–photon holographic shape and first estimation of elicited photocurrent and spiking

### *7.2.3.2. 1-Photon imaging and 2- photon stimulation set up*

This set up was the most frequently as it allowed for further assessment of opsin expression level and biophysical properties under 2-photon patterned excitation.

Imaging part:

The system was built on the basis of an upright microscope (Olympus BX51WI) providing wide field fluorescence imaging with an Arc Lamp (OptoSource Illuminator, Cairn Research) coupled with a

monochromator (Optoscan Monochromator, Cairn Research). The fluorescence was collected by a CCD camera (Orca Flash 4.0 Hamamatsu) driven by MicroManager open source software.

Photoactivation part:

The 2P photostimulation source consisted of a conventional pulsed Ti:Sapphire laser (pulse width: 100fs, repetition rate: 80MHz, model: Mai-Tai, Spectra Physics) with a tunable emission wavelength (from 700 to 1030 nm) and output power around 2W (at 900 nm). The patterned illumination was focused on the sample by a 40x objective (40x NA 0.8, LUM PLANFI/IR, Olympus) and the control of intensity and length of the photostimulation pulses was obtained by the use of a Pokel cell, allowing the generation of very short photostimulations pulses (< 1 ms).

Recordings done on this set up allowed for:

- Assessment of the expression under wide field fluorescent illumination,
- Targeted patch of opsin expressing cell and assessment of cellular type and electrophysiological parameters
- Photostimulation with a 1–photon wide-field illumination and fast assessment of cell responsiveness
- Photostimuation with a 2-photon holographic shapes within a range of powers for assessing elicited photocurrents and spike triggering (single pulses and trains)
- Recordings on CHO cells (investigation on kinetics parameters, prescreening of opsin plasmids)

#### *7.2.3.3. 2 - Photon imaging and 2-photon stimulation set up*

The third setup enables full characterization of opsin under 2-photon illumination condition both in vivo and in vitro. Implementation of 2-photon imaging allows for precise assessment of opsin expression and cell morphology, thus very good spatial resolution for targeting desired cell. Additionally, 2-photon activation allows axially confinement patterned stimulation in depth in the tissue.

Imaging part:

In this system, together, with 1P epifluorescence and IR transmitted light imaging, also 2P scanning fluorescence imaging was available.

The system was homemade and build around commercial upright microscope (SliceScope, Scientifica). The photostimulation source for 2P scanning consisted of a mode-locked Ti:Sapphire laser (Coherent Chameleon Vision II, pulse width 140fs, tuning range: 680-1080 nm), scanned through the sample by a couple of galvanometric mirrors (3mm aperture, Cambridge Technology)

imaged at the back aperture of the microscope objective (40x W APO NIR, Nicon). Red and green fluorescence was detected by 2 GaAsP based PMTs.

Photoactivation part:

The laser for patterned holographic photostimulation consisted of illuminated by a regenerative amplifier laser system (Satsuma HP, Amplitude Systems) at fixed wavelength 1030 nm. The main characteristics of the source consist on: high output power (10 W) and low repetition rate (500 kHz). In contrast to more commonly used Ti:Sapphire light source (as set up 2), amplified laser system produces laser pulses of high peak power, allowing very efficient 2-photon opsin stimulation with low average illumination power. Thus, the system is ideal for multiple cell simultaneous photoactivation deep in the tissue.

Recordings done on this set up allowed for:

- 2-photon imaging of opsin expression (*in vivo* and *in vitro*),
- Targeted patch of opsin expressing cell and assessment of cellular type and electrophysiological parameters, as well as cell morphology
- Photostimulation with a 1–photon wide-field illumination and fast assessment of cell responsiveness (such illumination provided support during experiments enabling fast orientation in the tissue)
- Photostimuation with 2-photon holographic shapes within a range of powers for assessing elicited photocurrents and spike triggering (single pulses and trains).
- Recording calcium signal from OGB preparation (both *in vivo* and *in vitro*)
- Recordings on CHO cells (investigation on kinetics parameters, prescreening of opsin plasmids)

## 7.2.4. Data analysis

### *7.2.4.1. Neuronal type classification*

Based on their action potential shape and firing pattern, as well as the shape and amplitude of the after hyperpolarization, cells were classified in either two (pyramidal/ interneuron) or three (Regular Spiking / Fast Spiking / Low Threshold Spiking) groups (Beierlein, 2003; Markram et al., 2004; McCormick, Connors, Lighthall, & Prince, 1985).

### *7.2.4.2. Opsin performance assessment*

Photocurrents (under voltage clamp) or membrane potential changes (under current clamp) were recorded for a series of photostimulations, starting from low power (~ 0,05 mW/µm2 for Ti:Sapphire laser, 0,01 mW/µm2 for amplified pulse laser) and increasing gradually. The current clamp recordings allowed for finding the power at which an action potential could be reliably elicited, defined as an

action potential being present for three consecutive repetitions. Additionally, during consecutive recordings with the use of higher power elicited in each condition photocurrent magnitude was obtained. The current amplitude was further normalized taking as the reference for 100% the current obtained with the highest power applied. Normalized current in relation to applied power allowed for estimation of saturation power (the minimal power which further increase doesn't cause increase of elicited current). Cells in which action potentials were triggered successfully were counted and presented as a percentage of all patched cells. The assessment of the temporal precision of spike occurance in response to light pulse trains was made using the power needed to elicit reliable single spikes (power at AP threshold). Pulse duration was varied depending on cell response, in order to find the minimal time for eliciting a train of action potentials. For the ReaChR experiments to assess the artifact due to non-somatic stimulation, the phase mask was moved away from the soma and focused onto different locations on the cell processes. An automatic protocol written in MATLAB (by Dimitrii Tanese) allowed for specifying a sequence of photostimulation patterns, which were started simultaneously with the electrophysiological recording and photostimulation signal. Additionally, a data sheet containing the centre of the spot position parameters was created, enabling recreation of the exact sequence during subsequent analysis.

Data were analyzed with the help of Clampex, Neuromatic and Excel software. Figures were prepared using Origin, Fiji and Power Point Software. Recreating the spot sequence and inferring the data on the distance from the soma were done with the use of a MATLAB script.

# 8. Appendices:

## 8.1. Appendix 1: Two-photon holographic stimulation of ReaChR

frontiers in Cellular Neuroscience

ORIGINAL RESEARCH
published: 18 October 2016
doi: 10.3389/fncel.2016.00234

# Two-Photon Holographic Stimulation of ReaChR

*Emmanuelle Chaigneau[1†], Emiliano Ronzitti[1], Marta A. Gajowa[1], Gilberto J. Soler-Llavina[2], Dimitrii Tanese[1], Anthony Y. B. Brureau[1], Eirini Papagiakoumou[1,3], Hongkui Zeng[2] and Valentina Emiliani[1*]*

[1] Wavefront-Engineering Microscopy Group, Neurophotonics Laboratory, Centre National de la Recherche Scientifique UMR8250, Paris Descartes University, Paris, France, [2] Allen Institute for Brain Science, Seattle, WA, USA, [3] Institut National de la Santé et de la Recherche Médicale (INSERM), Paris, France

Optogenetics provides a unique approach to remotely manipulate brain activity with light. Reaching the degree of spatiotemporal control necessary to dissect the role of individual cells in neuronal networks, some of which reside deep in the brain, requires joint progress in opsin engineering and light sculpting methods. Here we investigate for the first time two-photon stimulation of the red-shifted opsin ReaChR. We use two-photon (2P) holographic illumination to control the activation of individually chosen neurons expressing ReaChR in acute brain slices. We demonstrated reliable action potential generation in ReaChR-expressing neurons and studied holographic 2P-evoked spiking performances depending on illumination power and pulse width using an amplified laser and a standard femtosecond Ti:Sapphire oscillator laser. These findings provide detailed knowledge of ReaChR's behavior under 2P illumination paving the way for achieving in depth remote control of multiple cells with high spatiotemporal resolution deep within scattering tissue.

**Keywords: optogenetics, 2-photon excitation, computer generated holography, opsin, action-potential generation, neuroscience, cortex**

OPEN ACCESS

***Edited by:***
*Jonathan Mapelli, University of Modena and Reggio Emilia, Italy*

***Reviewed by:***
*Leonardo Sacconi, University of Florence, Italy*
*Matthias Prigge, Weizmann Institute of Science, Israel*

***Correspondence:**
*Valentina Emiliani*
*valentina.emiliani@parisdescartes.fr*

***Present Address:**
*Emmanuelle Chaigneau, Neurophysiology & New Microscopies Laboratory, Institut National de la Santé et de la Recherche Médicale U1128, Paris Descartes University, Paris, France*

***Received:** 08 July 2016*
***Accepted:** 26 September 2016*
***Published:** 18 October 2016*

***Citation:***
*Chaigneau E, Ronzitti E, Gajowa MA, Soler-Llavina GJ, Tanese D, Brureau AYB, Papagiakoumou E, Zeng H and Emiliani V (2016) Two-Photon Holographic Stimulation of ReaChR. Front. Cell. Neurosci. 10:234. doi: 10.3389/fncel.2016.00234*

## INTRODUCTION

Optogenetics has revolutionized neuroscience by enabling remote activation or inhibition of specific populations of neurons in intact brain preparations through genetically-targeted, light-sensitive channels and pumps (Nagel et al., 2003; Boyden et al., 2005; Adamantidis et al., 2015). Despite great advances in opsin engineering and photoactivation methods achieved over the last decade, studying the role of individual neurons within neuronal circuits is still a challenge as it requires photo-stimulation of one or several individually chosen cells within scattering tissues (Peron and Svoboda, 2011; Emiliani et al., 2015), with millisecond time precision and micrometer spatial resolution. Recent developments of *ad hoc* opsins (Mattis et al., 2012; Klapoetke et al., 2014) and innovative illumination approaches (reviewed in Papagiakoumou, 2013; Bovetti and Fellin, 2015) offer the possibility of tackling these challenges.

Red-shifted variants of channelrhodopsin, such as C1V1 (Yizhar et al., 2011), ReaChR (Lin et al., 2013; Hooks et al., 2015) or Chrimson (Klapoetke et al., 2014), with spectral peaks near and above 600 nm, enable deeper brain stimulation relative to blue-green shifted opsins. For instance, red-orange light illumination of ReaChR, has permitted *in vivo* trans cranial optogenetics in deep brain structures (Lin et al., 2013). However, in depth neuronal stimulation using visible light does not enable cellular resolution.

In depth optogenetics at the single cell level requires the use of two-photon (2P) stimulation. However, the small conductance [∼40 fS for ChR2 (Feldbauer et al., 2009)], of most existing

optogenetic actuators and the limited number of channels contained in the micro-sized illumination volume renders 2P-optogenetics challenging. This has prompted the design of new 2P-illumination approaches for optimized photocurrent integration, each with its advantages and limitations. Two-photon scanning approaches optimize current integration by quickly scanning a micrometer-diameter spot across the cell body faster than the channel's closing time (Rickgauer and Tank, 2009; Andrasfalvy et al., 2010; Packer et al., 2012; Prakash et al., 2012). On the contrary, 2P-parallel approaches enable synchronous current integration from all illuminated channels by delivering light simultaneously on axially confined, user-defined regions (Papagiakoumou et al., 2010, 2013; Bègue et al., 2013). Intermediate solutions, using scanning of a low numerical aperture beam (Rickgauer et al., 2014) or multiplexed holographic beams (Packer et al., 2015), have also been developed.

Either approach, combined with red-shifted opsins could enable optimal deep-brain photo-stimulation with cellular resolution. Parallel approaches illuminate all targets simultaneously and provide a higher temporal resolution than scanning methods: action potential (AP) generation is achieved with millisecond temporal resolution (1–10 ms) with a parallel approach (Bègue et al., 2013) whereas it requires 5–70 ms with scanning (Rickgauer and Tank, 2009; Andrasfalvy et al., 2010; Packer et al., 2012; Prakash et al., 2012). However, parallel approaches divide the available laser power among all targets. As a consequence, the maximum area photo-excited within a single illumination pattern, and therefore the maximum number of target cells, is limited by the available laser power and the cross-section of the opsin. Consequently simultaneous, multiple cell targeting requires using high cross-section opsins and efficient illumination methods.

To date, 2P activation of red-shifted opsins has only been demonstrated for C1V1 (Packer et al., 2012, 2015; Prakash et al., 2012; Bègue et al., 2013; Rickgauer et al., 2014). ReaChR offers improved membrane trafficking, as well as higher photocurrent for 1P stimulation (Lin et al., 2013). Therefore, ReaChR has the potential to be highly sensitive for 2P stimulation.

Here, we characterized the 2P absorption spectrum and kinetics parameters of ReaChR in cultured cells and in acute brain slices. We demonstrated that using computer generated holography with an amplified laser combined with ReaChR enables 2P generation of photo-currents in the range of one nanoampere. Moreover, we demonstrated reliable action potential generation with millisecond temporal resolution and sub-millisecond temporal precision (jitter). These results open new possibilities for in depth, simultaneous 2P stimulation of multiple targets.

# MATERIALS AND METHODS

## ReaChr Expression in Biological Samples

### Cultured Cells

ReaChR was first expressed in cells in culture. We used Chinese Hamster Ovary (CHO) cells as they have few gap junctions which would interfere with measurements of currents for single cell photo-stimulation, lowering their amplitude and slowing kinetics (Conti et al., 2016). CHO cells were cultured in an incubator at 37°C and 5% $CO_2$ in a D-MEM/F12 GlutaMAX medium (Life Technologies) with the addition of 1 mM glutamine, 1% streptomycin and 10% fetal bovine serum. Cells were plated on Thermanox plastic coverslips (Thermo Scientific) 24 h prior to transfection. The DNA was transfected using the EX-Gen 500 transfection reagent and cells were recorded 24–48 h after transfection. The plasmid used had a p2A sequence (Prakash et al., 2012) which allowed for the simultaneous expression of the photochannel and the YFP marker but independent targeting (pAAV-ReaChR-p2A-eYFP) (provided by the Allen Institute). CHO cells were transfected with pAAV-ReaChR-p2A-EYFP, and examined 2–3 days after transfection.

### Brain Slices

#### *Virus injections*

ReaChR was expressed in mouse brain tissue using AAVs as vectors. All experimental procedures were approved by the Paris Descartes Ethics Committee for Animal Research (registered number CEEA34.EV.118.12) and institutional guidelines of the care and use of laboratory animals (Council directive 86/609 EEC). Swiss male mice (Janvier, France) were injected 25–35 days post-natal with AAV1 CamKII-ReaChR-p2A-YFP or AAV1 Ef1α-ReaChR-p2A-dTomato ($n = 94$ mice). The dimer of Tomato (dTomato) (Shaner et al., 2004) was used in the latter construct to meet AAV genome size constraints. Mice were anesthetized with a mixture of ketamine (80 mg/kg body weight; Ketamine 1000, Virbac France) and xylazine (10 mg/kg body weight; Xylazine Rompun 2%, Bayer Healthcare) via intraperitoneal injection. They were placed in a stereotactic frame and the head was stabilized with ear bars and a mouth holder. Eyes were covered with lubricant (Dexpanthenol; Chauvin Ankerpharm GmbH Berlin) to prevent dehydration. The scalp was locally anesthetized with 0.03 mL lidocaine (Xylovet 21.33 mg/mL; CEVA). The skull was exposed by an incision of ∼0.5 cm length on the anterior-posterior axis of the scalp above the visual cortex. The injection site was located 3.5 mm posterior of bregma and 2 mm lateral. A craniotomy of ∼1 $mm^2$ was performed and the dura mater was cut through. A 36-gauge stainless steel beveled needle (Coopers Needleworks Ltd) was placed at a depth of 200 μm from the brain surface and a volume of 1.5 μL AAV (total genome copies: 1.5 $10^{12}$ to 1.5 $10^{14}$) was injected at a rate of 100 nL per minute. After injection, the scalp was closed with cyanoacrylate (super glue Loctite; Henkel). Finally, a peritoneal injection of Antisedan (0.2 mg/kg; Janssen) and a subcutaneous injection with 0.2 mL of 9% saline solution were performed to allow for quick recovery from anesthesia.

To check for expression, 2 mice were fixed with PFA. They were deeply anesthetized with Pentobarbital 0.2 mg/g mouse. After clearing the blood with PBS though transcardiac perfusion, 4% PFA was used to fixate the animal. The fixed brain was removed, post-fixed in PFA for 1 h, and then washed with PBS. The fixed brains were sliced into 50 μm thick sagittal sections and mounted on glass cover slips for confocal imaging.

*Acute brain slice preparation*

Three hundred micrometer thick parasagittal slices, were prepared 4–10 weeks after viral injection, in accordance with European guidelines. Mice were decapitated. Slices were prepared using a Leica VT1200S slicer. The sucrose slicing solution contained (in millimoles of compound used to make a liter of solution): 25 glucose, 85 NaCl, 65 sucrose, 0.5 $CaCl_2$, 4 $MgCl_2$, 2.5 KCl, 1.25 $NaH_2PO_4$ and 26 $NaHCO_3$. It was saturated with 95% $O_2$/5% $CO_2$. Slices were then incubated at 32–33°C for 30 min in a sucrose recovery solution containing (in millimoles of compound used to make a liter of solution): 25 glucose, 115 sucrose, 1 $CaCl_2$, 2.5 $MgCl_2$, 105 NaCl, 2.5 KCl, 1.25 $NaH_2PO_4$ and 26 $NaHCO_3$ saturated with 95% $O_2$/5% $CO_2$.

## Imaging

### Widefield IR and Fluorescence System

For screening cells morphology and checking cell localization in acute brain slices we used a widefield infrared illumination system. This consisted of an IR-LED source (M780L2, Thorlabs) installed at the rear port of a SliceScope Scientifica microscope, an orientable blocking element to create oblique illumination and a condenser focusing the light on the sample. IR light transmitted through the sample was collected with an IR antireflection coated water-immersion objective (Nikon NIR MRD07420 N40X/0.80W) and sent to an IR CCD (IR-1000, DAGE-MIT).

For a first control of ReaChR expression, we performed widefield fluorescence imaging with a system comprising 2 interchangeable LED sources (Thorlabs M470L2, for YFP and M565L3 for dTomato) filtered by 2 interchangeable bandwidth excitation filters (Semrock FF01-452/45 for YFP and F01-545/55-25 for dTomato) and coupled to a diffuser (DG10-1500, Thorlabs) and an achromatic lens ($f$ = 30 mm, #LA1805 Thorlabs). Fluorescence was collected through a tube lens ($f$ = 200 mm), separated from excitation light using a dichroic mirror (Semrock FF510-Di02 for YFP and FF580-FDi01 for dTomato) and detected by a CCD camera (Orca-05G, Hamamatsu) after passing through a visible bandwidth filter (Semrock FF01-609/181 for YFP and FF01-665/150-25 for dTomato).

### Two-Photon Scanning Imaging System

For high-resolution fluorescence imaging we used a 2P raster scanning microscope consisting of a femtosecond tunable Laser (Coherent Chameleon Vision II, pulse width 140 fs, tuning range 680–1080 nm), relayed on a custom-made galvanometer-based scanhead (3 mm aperture, 6215H series, Cambridge Technology), imaged at the back aperture of an IR antireflection coated water-immersion objective (Nikon NIR MRD07420 N40X/0.80W) through an afocal telescope (scan lens: $f$ = 100 mm, Thorlabs #AC508-100-B; tube lens: $f$ = 300 mm, Thorlabs #AC508-300-B). For imaging of dTomato the Chameleon laser was tuned at 930 nm. Galvanometric mirrors were driven by two servo drivers (MicroMax series 671, Cambridge Technology) controlled by a Digital/Analog converter board (PCI-6110, National Instrument).

Epi-fluorescence signals were collected during imaging. Fluorescence photons were separated from excitation photons using a dichroic mirror (Semrock FF705-Di0) and a band-pass filter (Semrock FF01-750/SP) and then separated according to their wavelength using a second dichroic mirror (Semrock FF555-Di03). Red fluorescence was further isolated using a band-pass emission filter (Semrock FF02-617/73) and detected using a multi-alkali photomultiplier (Hamamatsu R9110). Green fluorescence light was further isolated using a blocking edge short-pass emission filter (Semrock FF01-750/SP) as well as a band-pass emission filter (Semrock FF01-510/84), and detected using a multi-alkali photomultiplier (Hamamatsu R3896).

Images were acquired with ScanImage software. The laser intensity was controlled using a combination of an electrically-controlled liquid crystal variable phase retarder (LRC-200-IR1, Meadowlark Optics) and a polarizer beamsplitter (BB-050-IR1, Meadowlark Optics). A 4 μs dwell time was used when imaging. Anatomical images were averages of 2 consecutive images.

### Confocal System

A confocal Microscope Zeiss LSM 510 was used to examine fixed slices. YFP was excited with the 488 nm beam from an Argon/2 laser though a dichroic HFT488 and a Zeiss Plan Neofluar 20x/0.50 Objective. Epi-fluorescence was filtered through the dichroic HFT488 and a long pass filter LP505.

## Photo-Stimulation

### Two-Photon Holographic Stimulation with Amplified Laser System

The 2P computer-generated holographic (CGH) system (**Figure 1A**) has been already described in (Ronzitti et al., 2016). Briefly, the system is based on an LCoS-SLM (Hamamatsu X10468-07) illuminated by an Ytterbium-doped photonic crystal fiber amplifier laser system (Satsuma HP, Amplitude Systems; pulse width 250 fs, tunable repetition rate 500–2000 kHz, gated from single shot to 2000 kHz with an external modulator, maximum pulse energy 20 μJ, maximum average power 10 W, $\lambda$ = 1030 nm) operated at 500 kHz. The output of the amplifier was relayed and expanded to cover the SLM surface. Zero-order excitation was suppressed by a cylindrical lens (Hernandez et al., 2014). Then the SLM was imaged through an afocal telescope ($f_1$ = 500 mm and $f_2$ = 300 mm) at the back focal plane of an IR antireflection coated water-immersion objective (Nikon CFI APO 40X WI NIR NA 0.80) mounted on an upright microscope (Scientifica). Total power at the exit of the objective was 2 W.

We used an amplified pulsed laser (500 kHz, 20 μJ) instead of a conventional femtosecond oscillator, to maximize the peak power and minimize the average power necessary to photo-stimulate a single cell. This solution has previously been implemented to maximize the efficiency of excitation in conventional 2P microscopy imaging (Theer and Denk, 2006).

The SLM was controlled by a custom-designed software (Lutz et al., 2008) based on a Gerchberg and Saxton iterative algorithm, which converts an arbitrary intensity pattern on the sample plane to a specific phase profile to be addressed at the SLM plane. Photo-stimulation light power densities (LPDs) given in the text correspond to values after the objective, at the surface of samples.

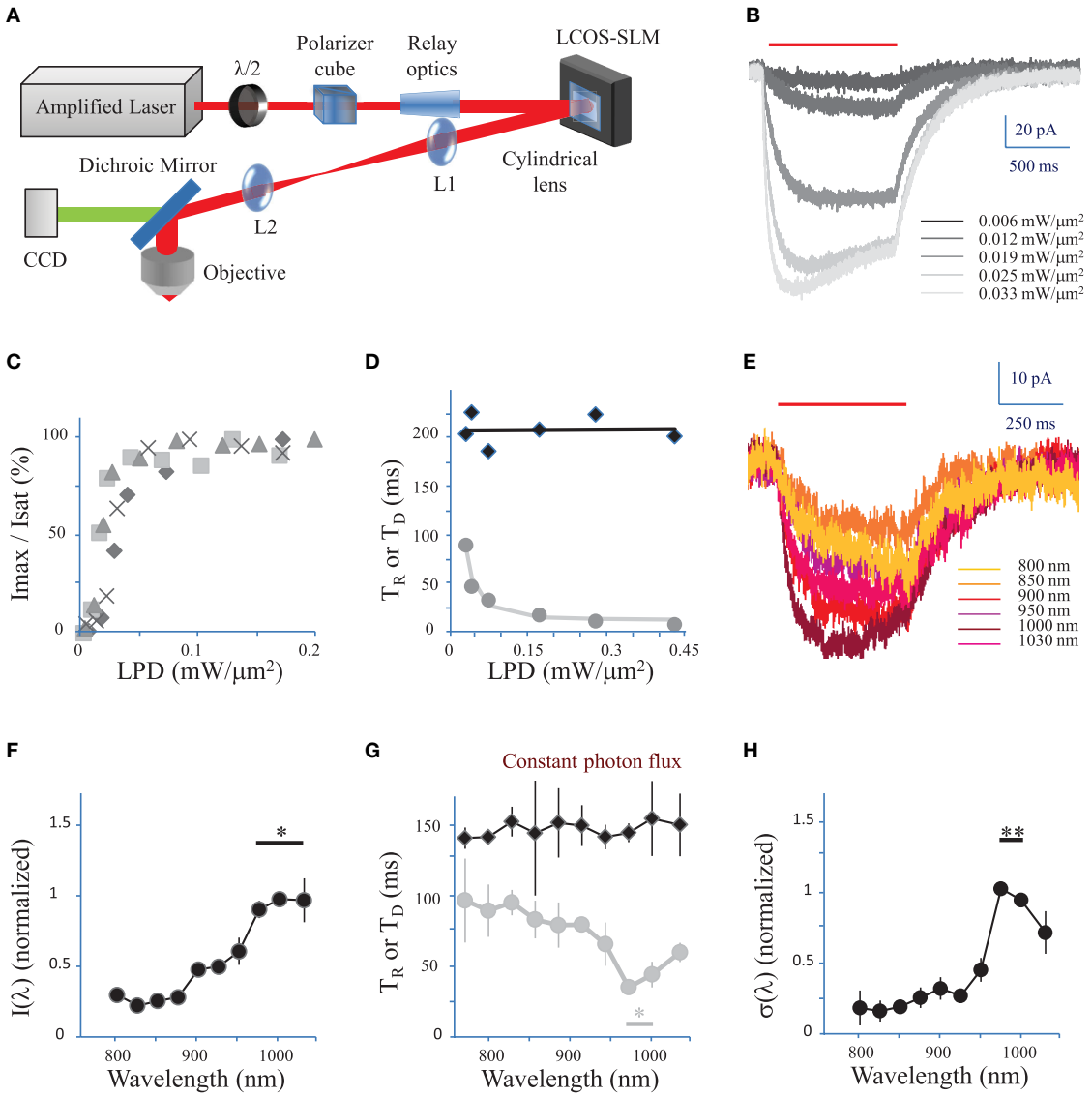


**FIGURE 1 | Characterization of currents evoked by 2P holographic stimulation and two-photon excitation spectrum. (A)** Simplified scheme of the 2P holographic stimulation microscope. The output beam from an Ytterbium-doped photonic crystal fiber amplifier Laser System was attenuated by rotating a half-waveplate combined to a polarizer cube. The beam was relayed and expanded to cover the surface of an LCoS-SLM (Hamamatsu X10468-07). Zero-order excitation was suppressed by aberrating it with a cylindrical lens. Then the SLM was imaged through a telescope (L1, L2 lenses) at the back focal plane of an IR antireflection coated water-immersion objective (Nikon CFI APO 40X WI NIR NA 0.80) mounted on an upright microscope (Scientifica). **(B)** CHO cells were voltage clamped at −40 mV and the current response to 2P holographic stimulation (1000 ms, red bar, $\lambda = 1030$ nm) with patterns matching the cell shape was recorded. Evoked response for increasing Laser Power Densities (LPDs) in a single cell. Average of $n = 3$ repetitions. **(C)** The maximum current ($I_{max}$) reached by 2P holographic stimulation at 1030 nm of 4 CHO cells was normalized to the saturation current ($I_{sat}$) and plotted vs. LPD. Average of $n = 3$ repetitions for each cell and LPD. Data recorded above a LPD of 0.2 mW/μm$^2$ was not shown as all cells had reached the saturation current. **(D)** Rise time ($T_R$, gray dots) and decay time ($T_D$, black diamonds) for 2P holographic stimulation of a single CHO cell. Average of $n = 3$ repetitions. $T_D$ and $T_R$ were fit, respectively, by a linear function (black line) and following Equation 4 (in Methods see Section Currents evoked by photo-stimulation of opsins) (gray line). **(E)** CHO cells were voltage clamped at −40 mV and the current response to 2P Generalized Phase Contrast (GPC) stimulation (400 ms, red bar) was recorded at a wavelength range from 720 to 1030 nm, while keeping the photon flux constant (2.7 × 10$^{26}$ photons/s/m$^2$). Average of $n = 3$ repetitions for each wavelength. **(F)** The maximum current reached by 2P GPC stimulation was normalized to the current generated with stimulation at 1000 nm and plotted vs. excitation wavelengths. A constant photon flux of 2.7 × 10$^{26}$ photons/s/m$^2$ was used. The current generated between 975 and 1030 nm (*) was significantly larger than currents generated at other wavelengths ($p = 0.05$, Wilcoxon paired $T$-test; $n = 6$ cells). **(G)** Decay time ($T_D$, black diamonds) and rise time ($T_R$, gray dots) for a constant photon flux of 2.7 × 10$^{26}$ photons/s/m$^2$ for 2P holographic stimulation of CHO cells. Average of $n = 6$ cells. $T_R$ between 975 nm and 1000 nm (*) was significantly larger than currents generated at other wavelengths ($p = 0.05$, Wilcoxon paired $T$-test; $n = 6$ cells). **(H)** The 2P cross-section, normalized to its value for excitation at 1000 nm, was plotted vs. excitation wavelengths. The 2P cross-section at 975 and 1000 nm (**) was very significantly larger than the cross-section at other wavelengths ($p = 0.01$, Wilcoxon paired $T$-test; $n = 11$ cells).

### Two-Photon Holographic Stimulation with Standard Femtosecond Oscillator

To assess the impact of using an amplified pulsed laser we also tested AP generation using ReaChR 2P holographic stimulation with a standard femtosecond oscillator. To do that we used a system similar to the previous one but with a 80 MHz Ti:Sapphire Laser (Mai Tai Deepsee, Newport-Spectra Physics) delivering 100 fs impulsions as a light source.

### Two-Photon GPC Stimulation for Measurement of Spectra

Spectra were obtained via a Generalized Phase Contrast (GPC) shaped illumination (Gluckstad, 1996) through a tunable wavelength Ti:Sapphire laser. GPC, with respect to CGH, provides homogeneous intensity patterns and therefore the same excitation intensity to light-gated channels distributed all over the membrane (Papagiakoumou et al., 2010; Bañas et al., 2014). The optical system is similar to the one described in (Papagiakoumou et al., 2010) with the difference that the grating for temporal focusing was replaced by a mirror. Briefly, the expanded (4x) beam of a Ti:Sapphire Laser (Mai Tai Deepsee, Newport-Spectra Physics) was phase modulated by a Liquid Crystal on Silicon Spatial Light Modulator (LCOS-SLM) (Hamamatsu Photonics X10468-02) placed at the entrance of a GPC common path interferometer and controlled by a custom-designed software. The interferometer is based on a $4f$ ($f$: focal length) imaging path ($f_1 = 300$ mm, $f_2 = 400$ mm) with a half-wave phase shifting contrast filter (PCF) at the confocal plane between the lenses. The output pattern of the interferometer is demagnified at the sample plane by a telescope made of a $f = 500$ mm lens and an Olympus LUMPLF 40x W/IR, NA 0.8 objective. The PCF is a patterned glass-based phase mask containing circular pits (the size of the pit used corresponds to 70 μm in diameter). It is designed to provide a π-phase shift for 900 nm wavelength. The robustness of GPC light patterning under a broad wavelength range (Palima and Glückstad, 2008), allowed us the spectra acquisition. The femtosecond laser was tuned from 800 to 1030 nm. During experiments, the wavelength was varied non-monotonically in order to avoid any bias in the spectra.

## Electrophysiology

Patch pipettes were pulled from borosilicate glass capillaries (outer diam. 1.5 mm, inner diam. 0.86 mm Harvard apparatus). Voltage and current signals were recorded using a MultiClamp 700B amplifier (Molecular Devices)), in the whole-cell recording configuration, low-pass filtered at 10 kHz, digitized at 20–40 kHz and recorded using Neuromatic (http://www.neuromatic.thinkrandom.com, written in Igor Pro). Data was analyzed using Neuromatic or pClamp (Axon Instruments) and Microsoft Excel. Membrane potentials are given without correction for the liquid junction potential.

### Cultured Cells

Cultured cells were transferred for recording in a chamber mounted on the headstage of an upright microscope (Scientifica or Olympus BX50WI for spectra measurements). Recordings were performed at room temperature (18–22°C). The extracellular medium during electrical recording was of the following composition (in millimoles of compound used to make a liter of solution): 140 NaCl, 5 KCl, 2 $CaCl_2$, 1 $MgCl_2$, 20 HEPES, 25 Glucose. pH adjusted to 7.5. Patch pipettes, filled with an intracellular solution was composed of (in millimoles of compound used to make a liter of solution): 140 KCl, 2 $MgCl_2$, 2 Mg ATP, 0.4 Na GTP, 10 HEPES, 20 BAPTA. PH adjusted to 7.3, and had a resistance that ranged from 4.5 to 10 MΩ. Experiments were performed in the dark to avoid any direct stimulation of cells by ambient light.

### Brain Slices

Brain slices were transferred for recording in a chamber mounted on the headstage of an upright microscope (Scientifica). Cortical layer 2/3 was localized using infrared illumination and custom-made contrast. Slices were then washed for 15 min with external solution saturated with 95% $O_2$/5% $CO_2$ containing (in millimoles of compound used to make a liter of solution): 125 NaCl, 2.5 KCl, 26 $NaHCO_3$, 1.25 $Na_2H_2PO_4$, 25 Glucose, 0.5 Ascorbic Acid, 1.5 $CaCl_2$ and 1 $MgCl_2$. For recordings, slices were continuously perfused with the same external solution at room temperature (18–22°C). Patch pipettes, filled with an intracellular solution of the following composition (in millimoles of compound used to make a liter of solution): 130 K-Gluconate, 7 KCl, 10 HEPES, 4 Mg ATP, 0.3 Na GTP, 10 Na phosphocreatine, pH adjusted to 7.35, and had a resistance that ranged from 5 to 10 MΩ. The slices were used for 1–5 h. Recorded cells were stable for at least 1 h. Experiments were performed in the dark to avoid any direct stimulation of cells by ambient light.

Cells were characterized based on their location and classified based on their firing pattern in response to steps of somatic current injection (Beierlein et al., 2003; Xu et al., 2006). We assessed the presence / absence of a fast and a slow after-hyperpolarization (AHP) based on the AHP rise time. Cells were considered as having a fast AHP when their AHP had a component with a rise time shorter than 10 ms and a slow AHP when their AHP had a component with a rise time larger than 10 ms. Cells were classified as pyramidal cells when they did not have fast AHP but had a slow AHP. Cells were classified as fast-spiking interneurons when they had a fast AHP and when they did not have a slow AHP. Their fast AHP amplitude was $18 \pm 4$ mV ($n = 12$). Cells were classified as low threshold spiking interneurons when they had a fast and a slow AHP. Their fast AHP amplitude was $10 \pm 5$ mV ($n = 4$). Many LTS cells evoked rebound spikes in response to hyperpolarizing current.

### Currents Evoked by Photo-Stimulation of Opsins

Following the models previously suggested for ChR2 (Rickgauer and Tank, 2009) for short illumination time, temporal photocurrent traces can be modeled by assuming a 2-state open (O) and closed (C), model: C ↔ O. With such a model the time-dependence of evoked currents will be determined by single exponentials.

Based on these assumptions, the change in the open channel density *[O]* at time *t*, is given by the difference between the rate at which channels open and the rate at which they close. The rate at which channels open can be expressed as the product

of the rate at which ReaChR absorbs excitation photons: $\sigma_m(\lambda)$ $LPD^2$ *[C]* (Xu and Webb, 1996), where LPD is the Laser Power Density, *[C]* is the closed channel density at time $t$, $\sigma_m(\lambda)$ is the wavelength dependent excitation cross-section of ReaChR, by $\alpha(\lambda)$ the wavelength dependent quantum yield. The product $\alpha\sigma_m(\lambda)$ is called the "action cross-section", $\sigma(\lambda)$ and depends on the excitation wavelength, $\lambda$ used for illumination (Zipfel et al., 2003). The rate at which the channels close is given by the product of the off-rate coefficient $k_{off}$ by *[O]* (Rickgauer and Tank, 2009).

Therefore:

$$d[\mathcal{O}] / dt = \sigma(\lambda)\, LPD^2\, [C] - k_{off}\, [O]. \quad (1)$$

As $[C] + [\mathcal{O}] = c$, with c = total density of opsins:

$$d[\mathcal{O}] / dt = \sigma(\lambda)\, LPD^2\, c - (\sigma(\lambda)\, LPD^2 + k_{off})\, [O]. \quad (2)$$

Solving Equation (2) gives for any time $t$ before the end of the excitation pulse:

$$[O] = O_{max}\,(1 - e^{-t/T_R}), \quad (3)$$

where

$$T_R = 1 / (\sigma(\lambda)\, LPD^2 + k_{off}) \quad (4)$$

is the expression for the rise time and

$$O_{max} = c\,\sigma(\lambda)\, LPD^2 / (\sigma(\lambda)\, LPD^2 + k_{off}) \quad (5)$$

describes the maximum number of channels opened at saturation.

As the current induced by photo-stimulation is the product of the single channel conductance and the density of opened channels,

$$I = I_{max}(\lambda)(1 - e^{-t/TR}) \quad (6)$$

with

$$I_{max}(\lambda) = I_{sat}\,\sigma(\lambda)\, LPD^2 / (\sigma(\lambda)\, LPD^2 + k_{off}) \quad (7a)$$

and $I_{sat}$ is the saturation current.

For $LPD << (k_{off} / \sigma(\lambda))^{1/2}$, i.e., for LPDs inducing currents far below $I_{sat}$,

$$I_{max}(\lambda) \approx I_{sat}\,\sigma(\lambda)\, LPD^2 / k_{off} \quad (7b)$$

and the plot of $I_{max}(\lambda)$ as a function of $\lambda$ enables to obtain the corresponding dependence of the excitation cross-section, $\sigma(\lambda)$. Normalizing to the peak (reached at $\lambda = 1000$ nm) we have:

$$\sigma(\lambda) / \sigma(1000) \approx I_{max}(\lambda)/I_{max}(1000). \quad (8)$$

Alternatively, by setting

$$T_D = 1 / k_{off},$$

where $T_D$ is the decay time constant, Equation (4) becomes:

$$1/T_R - 1/T_D = \sigma(\lambda)\, LPD^2 \quad (9)$$

and assuming $\alpha$ independent of $\lambda$, we can derive a dependence of the excitation cross-section on the excitation wavelength valid also for high LPD values:

$$\sigma(\lambda) / \sigma(1000) = (1/T_R - 1/T_D)_\lambda / (1/T_R - 1/T_D)_{1000}. \quad (10)$$

Furthermore, the LPD is linked to the photon flux $\Phi$ by the equation:

$$LPD = hc_0\, \Phi / \lambda \quad (11)$$

where $h$ is the Planck constant and $c_0$ the speed of light.

Using a constant photon flux Equations (8) and (10) become respectively:

$$\sigma(\lambda) / \sigma(1000) \approx (\lambda/1000)^2 I_{max}(\lambda) / I_{max}(1000), \quad (12)$$

and

$$\sigma(\lambda) / \sigma(1000) = (\lambda/1000)^2\, (1/T_R - 1/T_D)_\lambda / (1/T_R - 1/T_D)_{1000}. \quad (13)$$

### Voltage Clamp Measurements of Currents Evoked by Photo-Stimulation of Opsins

CHO cells were voltage-clamped at −40 mV. Cortical cells were voltage-clamped at −70 mV. We adjusted the length of the photo-activation pulse (300 to 1000 ms) depending on the LPD such as the maximum current was reached but inactivation is minimized. Each trial was repeated 3 times and the average of the 3 repetitions was used for further analysis.

The photo-stimulation evoked currents were filtered 100 times with a binomial filter and $I_{max}(\lambda)$ was determined as their maximal absolute value. The rise time constant $T_R$ and the decay time constant $T_D$ were determined by fitting the rising phase and the decaying phase of the trace with single exponentials and extracting the 1/e time constants, $T_R$ and $T_D$.

$I_{sat}$ was determined by fitting $I_{max}(\lambda)$ vs. LPD according to (Equation 7). The distribution of $I_{sat}$ over the population of cells tested was calculated, as well as its cumulative distribution. The LPD at current saturation was defined as the LPD used to reach a current equal to 95% of $I_{sat}$.

### Voltage Response to Photo-Stimulation of Opsins

Each trial was repeated 3 times. APs were detected for each trial and their average frequency calculated. Conditions for which at least 2 trials out of the 3 induced APs or trains of APs were considered as positive. The average frequency of the 3 repetitions was used for further analysis.

Data through the manuscript is expressed as mean ± s.d.

## RESULTS

### Two-Photon Current Generation and Two-Photon Action Spectra in Cell Culture

We first tested 2P stimulation of ReaChR in cell culture under 2P holographic illumination provided by an amplified laser source

(**Figure 1A**). Patterns of increasing LPDs and matching the cell shape ($65 \pm 13\,\mu m^2$, $n = 4$ cells) evoked currents of increasing amplitude (**Figure 1B**) that saturated [**Figure 1C**, in Methods see Section Voltage clamp measurements of currents evoked by photo-stimulation of opsins and Equation (7)] at $113 \pm 54$ pA ($n = 4$ cells) for a LPD of $0.10 \pm 0.03$ mW/$\mu m^2$ ($n = 4$ cells) after the objective. These results demonstrate that ReaChR is sensitive to 2P stimulation even at low LPDs.

The Rise time ($T_R$) (defined in Methods see Section Voltage clamp measurements of currents evoked by photo-stimulation of opsins) varied from $8 \pm 2$ ms for a LPD of $0.3 \pm 0.1$ mW/$\mu m^2$, to $145 \pm 39$ ms for a LPD of $0.008 \pm 0.002$ mW/$\mu m^2$ ($n = 4$ cells) (**Figure 1D**). Decay time ($T_D$) (defined in Methods see Section Voltage response to photo-stimulation of opsins) was independent on LPD and equal to $212 \pm 24$ ms ($n = 4$ cells) (**Figure 1D**). These values are consistent with the slow kinetics of ReaChR found under 1P illumination (at current saturation: $T_R = 20 \pm 0.6$ ms; $T_D = 137 \pm 7.1$ ms Lin et al., 2013).

We then investigated the dependence of 2P-photocurrent on the excitation wavelength for a range of wavelengths from 720 to 1030 nm (**Figure 1E**). This was achieved by illuminating the cells with a circular shape generated using the GPC method coupled to a tunable Ti-Sapphire laser (see Section Methods) and a constant photon flux of $2.7 \times 10^{26}$ photons/s/$m^2$ after the objective, corresponding to an LPD of 0.04 mW/$\mu m^2$ at 1030 nm. The maximum photocurrent was reached at wavelengths between 975 and 1030 nm ($n = 6$ cells) (**Figure 1F**; $p = 0.05$, Wilcoxon paired $T$-test). The Rise time ($T_R$) reached a minimum of $41 \pm 9$ ms between 975 and 1000 nm ($n = 6$ cells) (**Figure 1G**, $p = 0.05$, Wilcoxon paired $T$-test). Decay time ($T_D$) was independent on wavelength (**Figure 1G**).

In order to keep a good signal to noise ratio for photocurrents registered at the tail of the action spectra ($\lambda < 850$ nm), we also used relative high photon flux ($7.5 \times 10^{26}$ photons $m^{-2}$ $s^{-1}$ after the objective) which was close to the saturation power for excitation wavelength within the absorption peak. To derive the exact wavelength dependence of the 2P-cross-section, $\sigma(\lambda)$, we calculated its expression as a function of the rise and decay times (see Section Methods, Equations 9, 10). The resulting plot revealed a peak at 975–1000 nm ($n = 11$ cells) (**Figure 1H**; $p = 0.01$, Wilcoxon paired $T$-test).

These results demonstrate that at the wavelength of the employed amplified laser (1030 nm), currents close to 70% of the maximum achievable current ($\lambda = 975$ nm) can be evoked.

## Two-Photon Holographic Activation of ReaChr-Expressing Neurons in Brain Slices

ReaChR was expressed in the visual cortex of mice using AAV1 CamKII-ReaChR-p2A-YFP or AAV1 Ef1α-ReaChR-p2A-dTomato (see Section Methods). Constructs with the p2A sequence between ReaChR and the fluorescent reporter facilitate the identification of opsin-expressing cells (Castelló et al., 2011; Prakash et al., 2012) as they allow for the reporter to be freely-diffusing in the intracellular medium, while the opsin is targeted to the membrane. Therefore, opsin-expressing cells are filled with the fluorescent reporter and can be easily identified under 1P or 2P imaging. Five or six weeks after injection of AAV1 CamKII-ReaChR-p2A-YFP and 6–8 weeks after injection of AAV1 Ef1-ReaChR-p2A-dTomato, cortical layer 2/3 was relatively sparsely labeled (**Figures 2A,B**). In agreement with previous findings (Lin et al., 2013), cells expressing ReaChR had normal morphology and physiological membrane properties, suggesting minimal toxic effects of expression. Indeed their resting potential was $-70 \pm 7$ mV ($n = 35$) for pyramidal cells, $-64 \pm 7$ mV ($n = 11$) for fast spiking (FS) cells and $-66 \pm 10$ mV ($n = 4$) for low threshold spiking (LTS) cells.

Fifteen micrometer diameter 2P holographic spots were targeted at the somas of L2/3 cortical cells expressing ReaChR in acute brain slices for 0.1–1 s. Evoked currents saturated on average at $740 \pm 210$ pA ($n = 12$ pyramidal cells) (**Figure 2C**) for a LPD of $0.04 \pm 0.02$ mW/$\mu m^2$) (see Section Methods). $T_R$ varied from $28 \pm 15$ ms for a LPD of 0.06 mW/$\mu m^2$ ($n = 5$ cells), to $55 \pm 29$ ms for a LPD of 0.02 mW/$\mu m^2$ ($n = 10$ cells).

These results demonstrated that 2P illumination of ReaChR enables generation of currents in the nanoampere scale, in neurons, at LPDs below 0.1 mW/$\mu m^2$ using 1 to 10 ms long 2P stimulation pulses.

## Characterization of Light Power Density Necessary to Reach the AP Threshold Using Amplified Laser or Ti:Sapphire Oscillator

Next we investigated the 2P stimulation conditions to evoke an AP in cortical layer 2/3 cells following infection with either of the ReaChR-carrying viruses. 15-μm diameter 2P-holographic spots were applied for 10 ms to depolarize the cells and the laser power was increased until an AP was evoked (**Figure 2D**). The AP threshold was reached for LPDs of $0.03 \pm 0.02$ mW/$\mu m^2$ ($n = 26$) in pyramidal cells, $0.02 \pm 0.02$ mW/$\mu m^2$ ($n = 8$) in FS cells and $0.02 \pm 0.02$ mW/$\mu m^2$ ($n = 7$) in LTS cells. This is about half the LPD needed to reach current saturation.

For comparison, we also investigated ReaChR excitability using a standard femtosecond Ti:Sapphire oscillator (MaiTai-DeepSee, Spectra-Physics, in Methods see Section Two-photon holographic stimulation with standard femtosecond oscillator). We found that an average LPD of $0.2 \pm 0.04$ mW/$\mu m^2$ ($n = 5$ cells) was necessary to reach the AP threshold with at 950 nm and an excitation spot of 15 μm in diameter for 10 ms illumination pulses (**Figures 3A,B**).

Interestingly, at the LPD used at AP threshold, only 2P stimulation on the cell body resulted in an action potential. However, 2P holographic stimulation of the processes using the same spot resulted in a $3.72 \pm 2.29$ mV depolarization ($n = 3$ cells, average of 3 to 8 spots at distances of 15 to 100 μm from the soma) (**Figures 3A,C,D**).

These results demonstrated that the combination of an amplified laser with ReaChR enables reproducible ($n \geq 3$) AP generation in 97% of ReaChR expressing-cells in which it was tested, using an average LPD of $0.025 \pm 0.022$ mW/$\mu m^2$ for an average depth of $48 \pm 19$ μm ($n = 43$ cells). This corresponds to less than 6 mW of total power per cell.

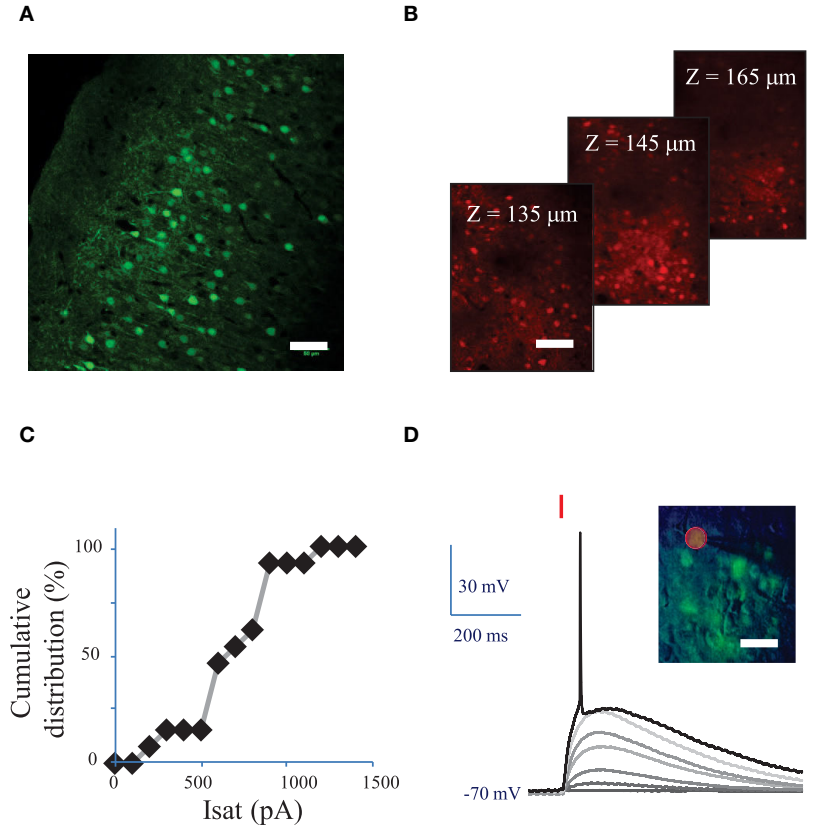


**FIGURE 2 | Conditions to evoke an action potential in neurons of mouse visual cortex Layer 2/3 with a fiber amplified Laser System at 1030 nm. (A)** Maximum intensity projection of a z-stack of confocal images of a fixed sagittal brain slice from mouse injected with AAV1 CamKII-ReaChR-p2A-YFP, 2 weeks after injection. Scale bar: 50 µm. **(B)** 2P microscopy images of visual cortex layer 2/3 from an anesthetized mouse (1% isoflurane) injected with AAV1 Ef1α-ReaChR-p2A-dTomato, 7 weeks after injection. Scale bar: 50 µm. Selected images from a stack of 101 images (100 to 200 µm under the surface of the brain). **(C)** Cumulative distribution of the saturation current (in Methods see Section Voltage clamp measurements of currents evoked by photo-stimulation of opsins) generated by 2P holographic stimulation in L2/3 cells when cells were voltage-clamped at −70 mV. **(D)** Voltage response of a L2/3 pyramidal cell to a series of 10-ms long 2P holographic spots (15 µm diameter, over the cell soma) of constant Laser Power Density (LPD) (red bar). Steady state current injection was used to keep the cell voltage at −70 mV in resting conditions. The LPD was increased from 0 to 0.014 mW/µm$^2$ within the series until an action potential (AP) was evoked. Inset: overlay of infrared (IR) slice image (grayscale), fluorescence (green) and 2P stimulation mask (red circled area) of V1 layer 2/3 in an acute sagittal brain slice from mouse injected with AAV1 CamKII-ReaChR-p2A-YFP, 5 weeks after injection. Scale bar: 30 µm.

## Conditions to Minimize Action Potential Latency and Temporal Jitter

We investigated the effect of the photo-stimulation pulse length (1 to 10 ms) on the spiking performances using cells expressing ReaChR following infection with either of the ReaChR-carrying viruses. At the AP threshold, the LPD was 0.03 ± 0.02 mW/µm$^2$ for 5 ms pulses ($n$ = 16 cells), 0.06 ± 0.06 mW/µm$^2$ for 2 ms pulses ($n$ = 16 cells) and 0.09 ± 0.1 mW/µm$^2$ for 1 ms pulses ($n$ = 14 cells) (**Figure 4A** and Supplementary Figure 2A for pyramidal cells only), thus very significantly larger than for 10 ms pulses, 0.02 ± 0.02 mW/µm$^2$ ($p$ = 0.01, Wilcoxon paired $T$-test; $n$ = 16 cells).

APs were generated with a latency, i.e., delay between the photo-stimulation onset and the peak of the AP, of 28 ± 11 ms ($n$ = 22 cells), with an AP jitter, i.e., standard deviation of the latency, of 2.4 ± 2.2 ms (for 3 repetitions, average of 22 cells) at AP threshold. At AP threshold, both the latency ($p$ > 0.1 Wilcoxon paired $T$-test, $n$ = 16 cells) (**Figure 4B** and Supplementary Figure 2B for pyramidal cells only) and jitter ($p$ > 0.1 Wilcoxon paired $T$-test, $n$ = 16 cells) (**Figure 4C** and Supplementary Figure 2C for pyramidal cells only) were independent of the pulse length.

In pyramidal cells, increasing the LPD above the value used to reach the AP threshold reduced significantly both the AP latency and the AP jitter (**Figures 4D–F**). The latter could be decreased down to 0.3 ± 0.3 ms ($n$ = 7 pyramidal cells, $p$ = 0.01, Wilcoxon paired $T$-test) by increasing the LPD by a factor of 1.5. Therefore, reliable and millisecond-range controlled single AP generation could be achieved by using 10-ms-long illumination with 2P holographic spots at LPDs about 1.5 as large as LPDs needed to reach AP threshold, i.e., 0.032 ± 0.019 mW/µm$^2$ ($n$ = 7 cells), which is still below the saturation LPDs (∼0.04 mW/µm$^2$). In this dataset, all recorded cells had been infected with AAV1 CamKII-ReaChR-p2A-YFP.

Interestingly ReaChR combined with the efficient current integration under parallel photo-stimulation, enables using

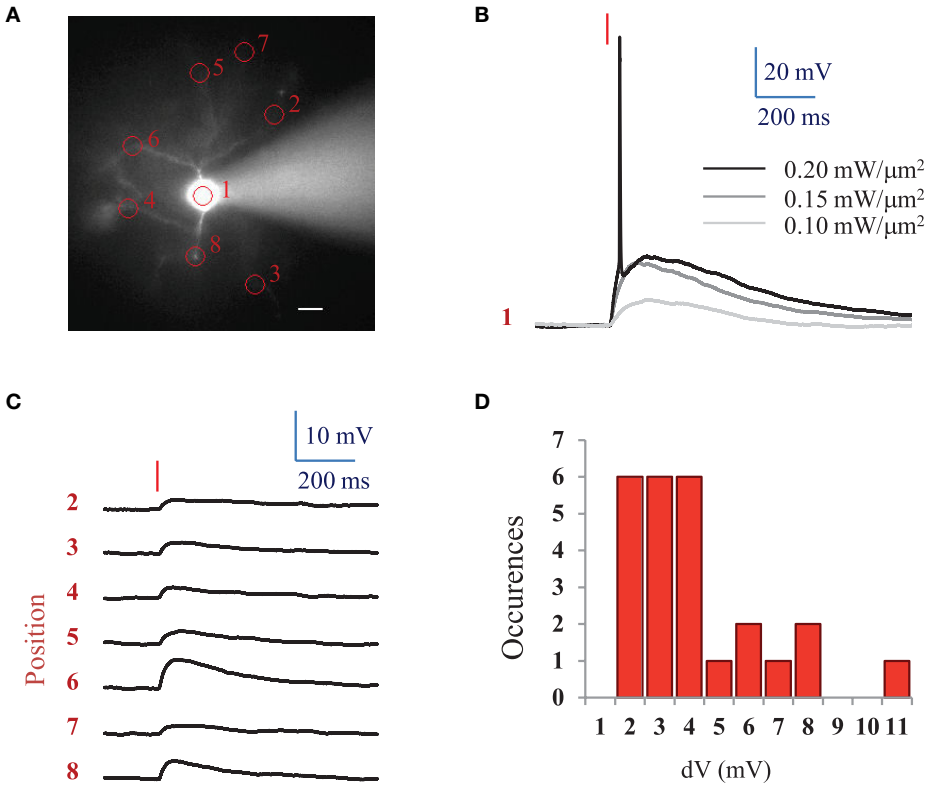


**FIGURE 3 | AP threshold with standard femtosecond Ti:Sapphire oscillator and spatial specificity of 2P holographic stimulation of ReaChR. (A)** Widefield fluorescence image of L2/3 ReaChR-expressing neuron filled with 20 μM Alexa 594. Scale bar: 15 μm. **(B)** Voltage response (single recording) to a 10 ms long (red line) 2P holographic stimulation with a standard femtosecond Ti:Sapphire oscillator at 950 nm using a circular spot on the cell soma (1 in panel A, 15 μm diameter) for increasing LPDs. **(C)** Average voltage response ($n = 3$ repetitions) to a 10 ms long (red line) 2P holographic stimulation with a standard femtosecond Ti:Sapphire oscillator at 950 nm on numbered circular spots (15 μm diameter) in panel A. LPD: 0.2 mW/μm$^2$. **(D)** Distribution of average voltage response ($n = 3$ repetitions, 25 spots, 3 cells) to a 10 ms long (red line) 2P holographic stimulation with a standard femtosecond Ti:Sapphire oscillator at 950 nm on cell processes. Distance from the soma from 15 to 100 μm, as shown in panel A. LPD corresponding to the one used to reach the AP threshold for 2P stimulation on the cell soma for each cell (0.15 to 0.25 mW/μm$^2$).

photo-stimulation pulses much shorter than the channel rise time (see **Table 1**), therefore enabling AP generation with millisecond temporal resolution despite the slow on-kinetics of the channels.

## Conditions to Evoke a Train of Action Potentials

We next assessed the ability of ReaChR to generate AP trains at various frequencies and on different cell types (**Figures 5A,B**) following infection with either of the ReaChR-carrying viruses. Trains of up to 10 APs could be generated, but often the cells failed to evoke APs in response to the last few light pulses. On average, 7 ± 3 APs were evoked ($n = 18$ cells, including pyramidal cells and interneurons) by trains of 10 light pulses (10 ms pulse duration) at 20 Hz. The number of APs evoked was strongly dependent on the cell type and, within the same population of cells, on cell membrane properties and ReaChR expression level, which was estimated from the fluorescence of the reporter: at 20 Hz, in FS cells 11 ± 2 APs ($n = 3$ cells) were evoked, in LTS cells 8 ± 3 APs ($n = 3$ cells) were evoked, whereas in pyramidal cells only 6 ± 2 APs ($n = 11$ cells) were evoked. Although synchronicity between light-pulses and spikes can be altered across the overall stimulation train, the frequency of the evoked AP trains remained as large as the frequency of the photo-stimulation train up to 34 ± 12 Hz for FS cells ($n = 4$ cells), up to 22 ± 6 Hz for LTS cells ($n = 5$ cells), and up to 16 ± 9 Hz for RS cells ($n = 16$ cells) for a stimulation train of 5 pulses (**Figure 5C**) (see Section Methods). This frequency decreased as the number of light pulses increased (**Figure 5D**). As under 1P illumination, the slow kinetics of the opsin between light pulses generated plateau potentials in all cases and occasionally extra spikes for LTS cells or FS cells (**Figure 5B**). Therefore, the combination of ReaChR and 2P holographic stimulation allows the reliable generation of 5 AP trains at up to ∼15 Hz for pyramidal cells, ∼35 Hz for FS cells and ∼20 Hz for LTS cells.

# DISCUSSION

We have found that the red-shifted opsin ReaChR can be activated with 2P amplified laser holographic photostimulation when expressed in both cultured cells and mouse neurons in

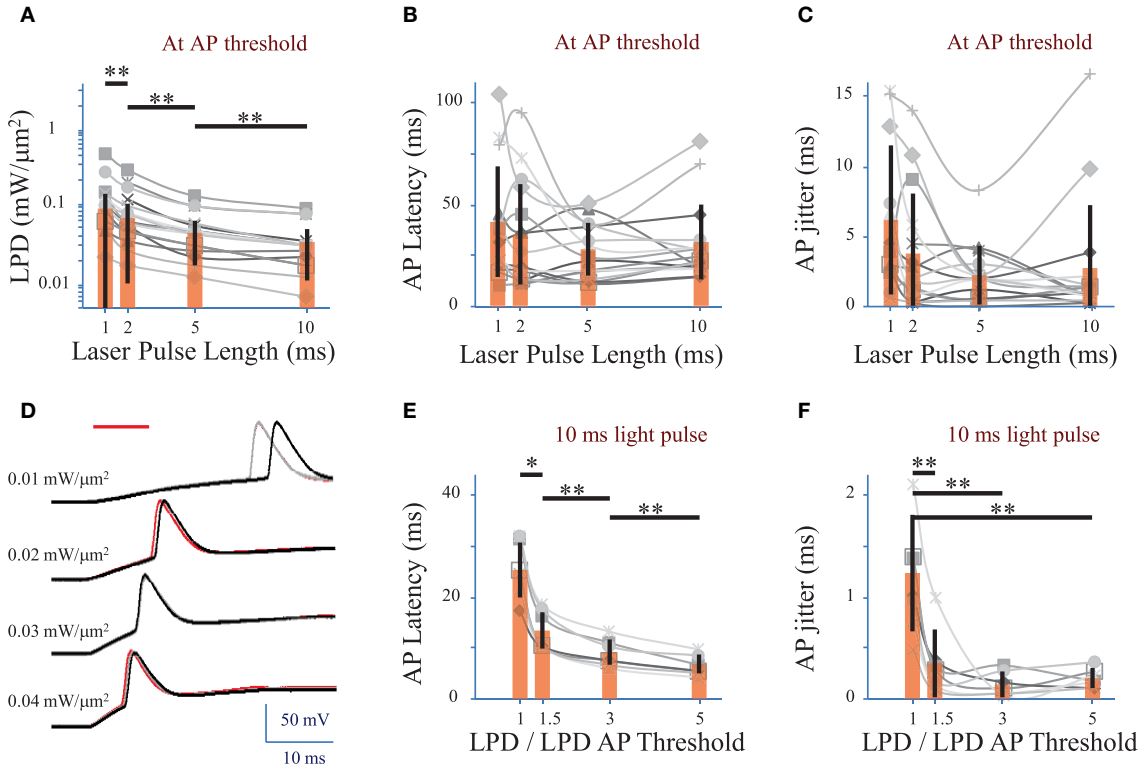


**FIGURE 4 | Optimization of parameters to evoke an action potential in neurons of mouse visual cortex Layer 2/3 with a fiber amplified Laser System at 1030 nm. (A)** Laser power density (LPD) necessary to evoke an AP with 1 to 10 ms long 2P holographic spots (15 μm diameter, over the cell soma) ($n = 16$ cells, average of 3 repetitions for each). Individual cells (gray), average (orange bars) and s.d. (error bars). (**) ($p = 0.01$, Wilcoxon paired $T$-test). **(B)** Latency between the AP evoked by 1 to 10 ms long 2P holographic spots (15 μm diameter, over the cell soma) at the LPD for AP threshold and the onset of the 2P stimulation ($n = 16$ cells, average of 3 repetitions for each). Individual cells (gray), average (orange bars) and s.d. (error bars). The latency did not vary significantly with the pulse length at AP threshold. **(C)** Same as **(B)** with AP jitter. The jitter did not vary significantly with the pulse length at AP threshold. **(D)** Voltage response of a L2/3 pyramidal cell infected with AAV1 CamKII-ReaChR-p2A-YFP to a series of 10-ms long 2P holographic spots (15 μm diameter, over the cell soma) of constant Laser Power Density (LPD) (red bar). Steady state current injection was used to keep the cell voltage at −70 mV in resting conditions. Three repetitions for each LPD. **(E)** Latency between the AP evoked by 10 ms long 2P stimulation and the onset of 2P stimulation ($n = 7$ pyramidal cells, average of 3 repetitions for each), at LPDs varying from the LPD necessary to reach the AP threshold to 5 times this value. Example of recording on panel D. Individual cells (gray), average (orange bars) and s.d. (error bars). The latency significantly (*) ($p = 0.05$, Wilcoxon paired $T$-test) or very significantly (**) ($p = 0.01$, Wilcoxon paired $T$-test) decreased when the LPD was increased. **(F)** Same as **(E)** with AP jitter. The jitter very significantly decreased (**) ($p = 0.01$, Wilcoxon paired $T$-test) when LPD was increased in comparison to the jitter at LPD used to reach the AP threshold.

**TABLE 1 | Properties of ReaChR 2P-holographic activation.**

| Laser Pulse Length (ms) | 1 | 2 | 5 | 10 |
|---|---|---|---|---|
| LPD (mW/μm²) to reach AP threshold | 0.09 ± 0.10 ($n = 15$) | 0.061 ± 0.061 ($n = 17$) | 0.031 ± 0.024 ($n = 19$) | 0.025 ± 0.022 ($n = 43$) |
| $T_R$ (ms) to reach the maximum current in Voltage Clamp at LPD used to reach AP threshold | 30 ± 11 ($n = 2$) | 28 ± 15 ($n = 5$) | 36 ± 22 ($n = 8$) | 55 ± 29 ($n = 10$) |

*Mean ± s.d., all cell types.*

acute brain slices. To our knowledge, this study provides the first demonstration that ReaChR is 2P-sensitive and its activation enables reliable millisecond range control of AP generation with low illumination doses despite its slow activation kinetics.

We have measured the spectrum of ReaChR under 2P excitation. The action cross-section of ReaChR is maximal at 975–1000 nm but it is still 75% of its maximum value at 1030 nm, thus enabling using both a conventional tunable Ti:Sapphire oscillator and a single wavelength amplified laser peaked at 1030 nm. In the first case, LPD necessary to evoke an AP with ReaChR was ∼0.2 mW/μm². Because of the higher peak power, the use of an amplified (low repetition rate) laser enabled to reduce the average power necessary to evoke an AP down to 0.03 mW/μm² which is about ten-fold lower than what was required with the conventional laser. This low LPDs corresponds to only 3.5–6 mW per cell. Considering that the total available laser power (after the objective) is ∼2 W, these results suggest that, at this depth, it might be possible to achieve simultaneous photo-stimulation

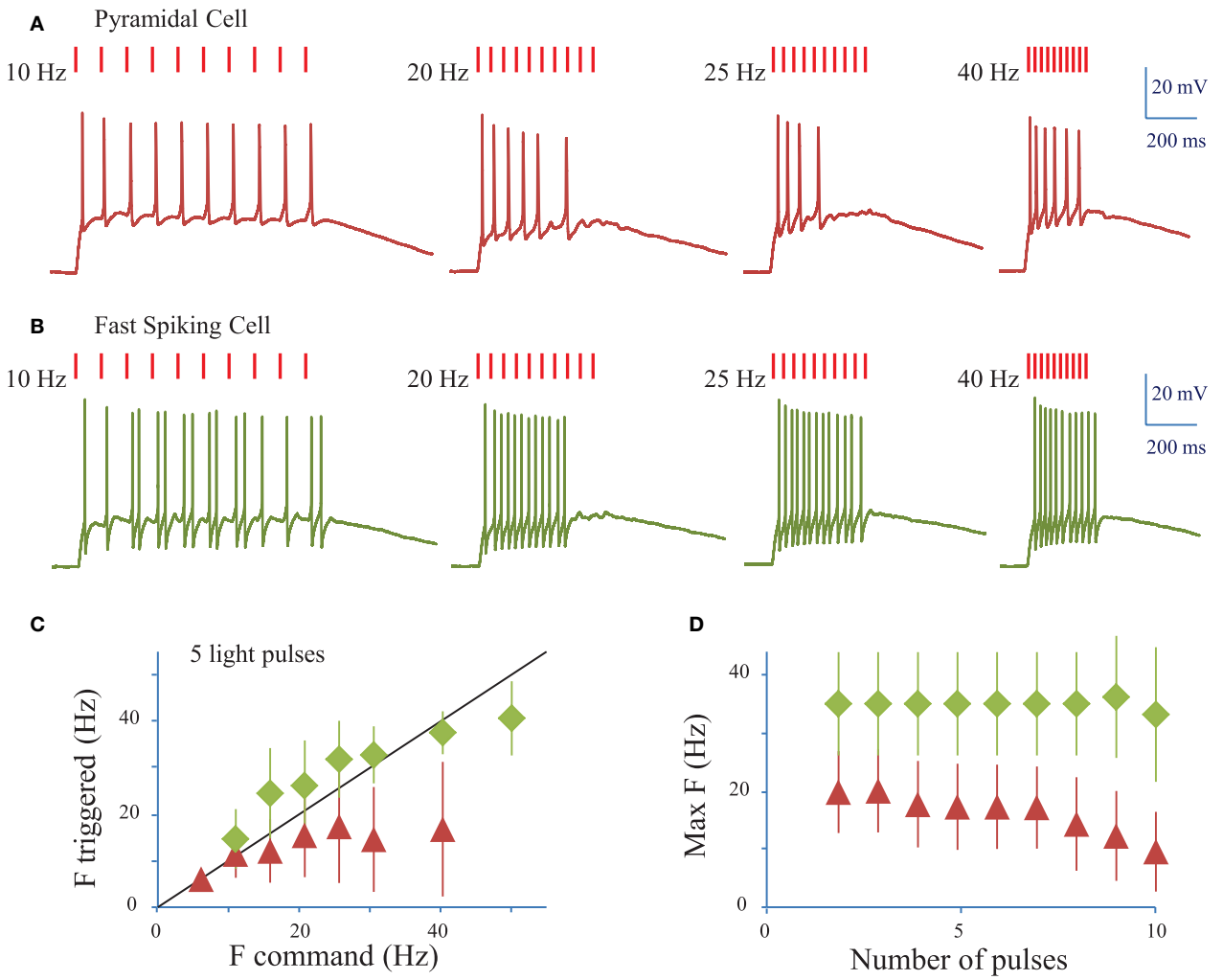


**FIGURE 5 | Conditions to evoke a train of action potentials in neurons of mouse visual cortex Layer 2/3 with a fiber amplified Laser System at 1030 nm. (A)** Trains of 2P holographic stimulation pulses were used to evoke trains of APs in single L2/3 cells: example of a pyramidal cell. Trains of 10 pulses at frequencies ranging from 5 to 40 Hz and LPDs at AP threshold were used. **(B)** Same as **(A)** for a fast spiking cell. **(C)** Plot of the maximum AP frequency vs. the photo-stimulation light pulses frequency, for pyramidal cells and LTS cells (red triangles, average of $n = 19$ cells) and FS cells (green diamonds, average of $n = 4$ cells). Black line corresponds to an AP frequency equal to the light pulse frequency. **(D)** Maximum AP frequency reached for trains of a given number of light pulses for pyramidal cells and LTS cells (red triangles, average of $n = 19$ cells) and FS cells (green diamonds, average of $n = 4$ cells).

of hundreds of cells. For greater depths this number needs to be rescaled to take into account the power losses due to scattering (e.g. at a depth of ~150 μm the effective available power will be reduced by nearly a factor of three; Chaigneau et al., 2011).

Confirming what has been demonstrated using 1P illumination, we found that ReaChR shows slow on- and off-kinetics with 2P stimulation. This could prevent rapid AP generation. However, ReaChR combined with parallel photo-stimulation can surpass the threshold for AP generation with stimulation pulses much shorter than the corresponding rise time. This, similarly to what we demonstrated with C1V1 (Bègue et al., 2013), enabled reducing the effective temporal resolution down to 1 ms. Similar results may be achieved with other slow opsins e.g., CoChR or Chrimson (Klapoetke et al., 2014). We also demonstrated that using pulse durations of 10 ms and light power density ≥1.5-fold of the AP threshold power (~0.02 mW/μm$^2$) enabled AP generation with sub-millisecond temporal jitter, as it was achieved with Chronos, an opsin having ten times faster on- and off-kinetics (Ronzitti et al., 2016). This is of the same order of magnitude as the temporal jitter of mono-synaptic events. As 2P holographic stimulation of ReaChR also provides selective AP generation in targeted cells, it provides sufficient spatiotemporal control to trigger AP in chosen presynaptic cells. Thus, it can enable studies concerning postsynaptic activity in well-chosen anatomical configurations. Furthermore, ReaChR and 2P holographic stimulation allows generating trains of 5 APs at up to ~15 Hz for pyramidal cells and LTS cells, and ~35 Hz for FS cells reliably. Therefore, 2P holographic stimulation of

ReaChR provides a way to generate repetitive activity in chosen cells and study resulting physiological events.

The measured 2P excitation spectra revealed a peak around 970 nm, and a significantly reduced absorption below 900 nm. These findings indicate a potential efficient use of ReaChR for all-optical monitoring of brain activity if 2P-stimulation of ReaChR is combined with 1P or 2P voltage or calcium imaging (e.g., using OGB bulk loading). Conversely, we expect that the slow off-kinetics and absorption peak at 970 nm will make it difficult to combine ReaChR with GCaMP (Akerboom et al., 2012) or RCaMP (Dana et al., 2016) imaging without evoking spurious photo-stimulation during imaging.

In brain slices, we tested two viral constructs (AAV1 CamKII-ReaChR-p2A-YFP or AAV1 Ef1α-ReaChR-p2A-dTomato) and found in both cases conditions for efficient expression, that didn't alter normal morphological appearances and healthy physiological properties (Supplementary Figure 1) The construct using dTomato as fluorescent reporter could be particularly interesting for in depth cell targeting, or for combination with green calcium indicators. Also it could be used for dual color optogenetics if combined with blue-shifted opsins (e.g., ChR2) conjugated to green fluorescent indicators.

To conclude, 2P holographic stimulation of ReaChR using an amplified laser is very powerful for flexible light patterning using very low average power. These results open the route for high temporal resolution, multiple-cell optogenetic stimulation *in vitro* and *in vivo*.

## AUTHOR CONTRIBUTIONS

EC performed photo-stimulation experiments and data analysis. ER and EP designed and built the microscope for CGH and 2P scanning imaging. EC, ER, and VE designed experiments. MG performed and analyzed photo-stimulation experiments using the mode locked Ti:Sapphire laser. GS and HZ designed and provided constructs and viruses. AB contributed to viral injections and together with ER acquired 2P *in vivo* images. DT and EP built the GPC illumination system and participated in the experiments for the measurements of the absorption spectrum. EC and VE wrote the paper with the contribution of HZ and GS. All authors read and approved the manuscript. VE conceived and supervised the project.

## ACKNOWLEDGMENTS

We thank Rossella Conti and Cecile Jouffret for taking care of CHO cell cultures and transfections, Nidal Bouzekri for his help with figures preparation, Amanda Foust for contributing in the design and the construction of the 2P scanning imaging system and Lyle Graham for proof-reading the manuscript. VE acknowledges the Agence Nationale de la Recherche (grants ANR-12-BSV5-0011-01, ANR-12-BSV5-0011, ANR-14-CE13-0016), the National Institutes of Health (NIH 1-U01-NS090501-01), the Medical Research foundation FRM (DVS20131228920) the FRC and the Rotary Club through the program "Espoir en Tête 2012". HZ and GS thank the Allen Institute founders, Paul G. Allen and Jody Allen, for their vision, encouragement, and support.

## SUPPLEMENTARY MATERIAL

The Supplementary Material for this article can be found online at: http://journal.frontiersin.org/article/10.3389/fncel.2016.00234

## REFERENCES

Adamantidis, A., Arber, S., Bains, J. S., Bamberg, E., Bonci, A., Buzsáki, G., et al. (2015). Optogenetics: 10 years after ChR2 in neurons-views from the community. *Nat. Neurosci.* 18, 1202–1212. doi: 10.1038/nn.4106

Akerboom, J., Chen, T.-W., Wardill, T. J., Tian, L., Marvin, J. S., Mutlu, S., et al. (2012). Optimization of a GCaMP Calcium Indicator for Neural Activity Imaging. *J. Neurosci.* 32, 13819–13840. doi: 10.1523/JNEUROSCI.2601-12.2012

Andrasfalvy, B. K., Zemelman, B. V., Tang, J., and Vaziri, A. (2010). Two-photon single-cell optogenetic control of neuronal activity by sculpted light. *Proc. Natl. Acad. Sci. U.S.A.* 107, 11981–11986. doi: 10.1073/pnas.1006620107

Bañas, A., Palima, D., Villangca, M., Aabo, T., and Glückstad, J. (2014). GPC light shaper for speckle-free one-and two-photon contiguous pattern excitation. *Opt. Express* 22, 5299–5310. doi: 10.1364/Oe.22.005299

Bègue, A., Papagiakoumou, E., Leshem, B., Conti, R., Enke, L., Oron, D., et al. (2013). Two-photon excitation in scattering media by spatiotemporally shaped beams and their application in optogenetic stimulation. *Biomed. Opt. Express* 4, 2869–2879. doi: 10.1364/Boe.4.002869

Beierlein, M., Gibson, J. R., and Connors, B. W. (2003). Two dynamically distinct inhibitory networks in layer 4 of the neocortex. *J. Neurophysiol.* 90, 2987–3000. doi: 10.1152/jn.00283.2003

Bovetti, S., and Fellin, T. (2015). Optical dissection of brain circuits with patterned illumination through the phase modulation of light. *J. Neurosci. Methods* 241, 66–77. doi: 10.1016/j.jneumeth.2014.12.002

Boyden, E. S., Zhang, F., Bamberg, E., Nagel, G., and Deisseroth, K. (2005). Millisecond-timescale, genetically targeted optical control of neural activity. *Nat. Neurosci.* 8, 1263–1268. doi: 10.1038/nn1525

Castelló, A., Álvarez, E., and Carrasco, L. (2011). The multifaceted poliovirus 2A protease: regulation of gene expression by picornavirus proteases. *J. Biomed. Biotechnol.* 2011:369648. doi: 10.1155/2011/369648

Chaigneau, E., Wright, A. J., Poland, S. P., Girkin, J. M., and Silver, R. A. (2011). Impact of wavefront distortion and scattering on 2-photon microscopy in mammalian brain tissue. *Opt. Express* 19, 6540–6552. doi: 10.1364/OE.19.022755

Conti, R., Assayag, O., de Sars, V., Guillon, M., and Emiliani, V. (2016). Computer generated holography with intensity-graded patterns. *Front. Cell. Neurosci.* 10:236. doi: 10.3389/fncel.2016.00236

Dana, H., Mohar, B., Sun, Y., Narayan, S., Gordus, A., Hasseman, J. P., et al. (2016). Sensitive red protein calcium indicators for imaging neural activity. *Elife* 5:e12727. doi: 10.7554/eLife.12727

Emiliani, V., Cohen, A. E., Deisseroth, K., and Häusser, M. (2015). All-optical interrogation of neural circuits. *J. Neurosci.* 35, 13917–13926. doi: 10.1523/JNEUROSCI.2916-15.2015

Feldbauer, K., Zimmermann, D., Pintschovius, V., Spitz, J., Bamann, C., and Bamberg, E. (2009). Channelrhodopsin-2 is a leaky proton pump. *Proc. Natl. Acad. Sci. U.S.A.* 106, 12317–12322. doi: 10.1073/pnas.0905852106

Gluckstad, J. (1996). Phase contrast image synthesis. *Opt. Commun.* 130, 225–230. doi: 10.1016/0030-4018(96)00339-2

Hernandez, O., Guillon, M., Papagiakoumou, E., and Emiliani, V. (2014). Zero-order suppression for two-photon holographic excitation. *Opt. Lett.* 39, 5953–5956. doi: 10.1364/OL.39.005953

Hooks, B. M., Lin, J. Y., Guo, C., and Svoboda, K. (2015). Dual-channel circuit mapping reveals sensorimotor convergence in the primary motor cortex. *J. Neurosci.* 35, 4418–4426. doi: 10.1523/JNEUROSCI.3741-14.2015

Klapoetke, N. C., Murata, Y., Kim, S. S., Pulver, S. R., Birdsey-Benson, A., Cho, Y. K., et al. (2014). Independent optical excitation of distinct neural populations. *Nat. Methods* 11, 338–346. doi: 10.1038/nmeth.2836

Lin, J. Y., Knutsen, P. M., Muller, A., Kleinfeld, D., and Tsien, R. Y. (2013). ReaChR: a red-shifted variant of channelrhodopsin enables deep transcranial optogenetic excitation. *Nat. Neurosci.* 16, 1499–1508. doi: 10.1038/nn.3502

Lutz, C., Otis, T. S., DeSars, V., Charpak, S., DiGregorio, D. A., and Emiliani, V. (2008). Holographic photolysis of caged neurotransmitters. *Nat. Methods* 5, 821–827. doi: 10.1038/nmeth.1241

Mattis, J., Tye, K. M., Ferenczi, E. A., Ramakrishnan, C., O'Shea, D. J., Prakash, R., et al. (2012). Principles for applying optogenetic tools derived from direct comparative analysis of microbial opsins. *Nat. Methods* 9, 159–172. doi: 10.1038/nmeth.1808

Nagel, G., Szellas, T., Huhn, W., Kateriya, S., Adeishvili, N., Berthold, P., et al. (2003). Channelrhodopsin-2, a directly light-gated cation-selective membrane channel. *Proc. Natl. Acad. Sci. U.S.A.* 100, 13940–13945. doi: 10.1073/pnas.1936192100

Packer, A. M., Peterka, D. S., Hirtz, J. J., Prakash, R., Deisseroth, K., and Yuste, R. (2012). Two-photon optogenetics of dendritic spines and neural circuits. *Nat. Methods* 9, 1202–1205. doi: 10.1038/nmeth.2249

Packer, A. M., Russell, L. E., Dalgleish, H. W. P., and Häusser, M. (2015). Simultaneous all-optical manipulation and recording of neural circuit activity with cellular resolution *in vivo*. *Nat. Methods* 12, 140–146. doi: 10.1038/nmeth.3217

Palima, D., and Glückstad, J. (2008). Multi-wavelength spatial light shaping using generalized phase contrast. *Opt. Express* 16, 1331–1342. doi: 10.1364/OE.16.001331

Papagiakoumou, E. (2013). Optical developments for optogenetics. *Biol. Cell* 105, 443–464. doi: 10.1111/boc.201200087

Papagiakoumou, E., Anselmi, F., Bègue, A., de Sars, V., Glückstad, J., Isacoff, E. Y., et al. (2010). Scanless two-photon excitation of channelrhodopsin-2. *Nat. Methods* 7, 848–854. doi: 10.1038/nmeth.1505

Papagiakoumou, E., Begue, A., Leshem, B., Schwartz, O., Stell, B. M., Bradley, J., et al. (2013). Functional patterned multiphoton excitation deep inside scattering tissue. *Nat. Phot.* 7, 274–278. doi: 10.1038/nphoton.2013.9

Peron, S., and Svoboda, K. (2011). From cudgel to scalpel: toward precise neural control with optogenetics. *Nat. Methods* 8, 30–34. doi: 10.1038/nmeth.f.325

Prakash, R., Yizhar, O., Grewe, B., Ramakrishnan, C., Wang, N., Goshen, I., et al. (2012). Two-photon optogenetic toolbox for fast inhibition, excitation and bistable modulation. *Nat. Methods* 9, 1171–1179. doi: 10.1038/nmeth.2215

Rickgauer, J. P., Deisseroth, K., and Tank, D. W. (2014). Simultaneous cellular-resolution optical perturbation and imaging of place cell firing fields. *Nat. Neurosci.* 17, 1816–1824. doi: 10.1038/nn.3866

Rickgauer, J. P., and Tank, D. W. (2009). Two-photon excitation of channelrhodopsin-2 at saturation. *Proc. Natl. Acad. Sci. U.S.A.* 106, 15025–15030. doi: 10.1073/pnas.0907084106

Ronzitti, E., Conti, R., Papagiakoumou, E., Tanese, D., Zampini, V., Chaigneau, E., et al. (2016). Sub-millisecond optogenetic control of neuronal firing with two-photon holographic photoactivation of Chronos. *BioRxiv* 1, 1–22. doi: 10.1101/062182

Shaner, N. C., Campbell, R. E., Steinbach, P. A., Giepmans, B. N. G., Palmer, A. E., and Tsien, R. Y. (2004). Improved monomeric red, orange and yellow fluorescent proteins derived from Discosoma sp. red fluorescent protein. *Nat. Biotechnol.* 22, 1567–1572. doi: 10.1038/nbt1037

Theer, P., and Denk, W. (2006). On the fundamental imaging-depth limit in two-photon microscopy. *J. Opt. Soc. Am. A Opt. Image Sci. Vis.* 23, 3139–3149. doi: 10.1364/JOSAA.23.003139

Xu, C., and Webb, W. W. (1996). Measurement of two-photon excitation cross sections of molecular fluorophores with data from 690 to 1050 nm. *J. Opt. Soc. Am. B.* 13, 481–491. doi: 10.1364/Josab.13.000481

Xu, X., Roby, K. D., and Callaway, E. M. (2006). Mouse cortical inhibitory neuron type that coexpresses somatostatin and calretinin. *J. Comp. Neurol.* 499, 144–160. doi: 10.1002/cne.21101

Yizhar, O., Fenno, L. E., Prigge, M., Schneider, F., Davidson, T. J., O'Shea, D. J., et al. (2011). Neocortical excitation / inhibition balance in information processing and social dysfunction. *Nature* 477, 171–178. doi: 10.1038/nature10360

Zipfel, W. R., Williams, R. M., and Webb, W. W. (2003). Nonlinear magic: multiphoton microscopy in the biosciences. *Nat. Biotechnol.* 21, 1369–1377. doi: 10.1038/nbt899

**Conflict of Interest Statement:** The authors declare that the research was conducted in the absence of any commercial or financial relationships that could be construed as a potential conflict of interest.

## 8.2. Appendix 2: Two-photon optogenetics by computer-generated holography

# Chapter 10

# Two-Photon Optogenetics by Computer-Generated Holography

**Eirini Papagiakoumou, Emiliano Ronzitti, I-Wen Chen, Marta Gajowa, Alexis Picot, and Valentina Emiliani**

## Abstract

Light patterning through spatial light modulators, whether they modulate amplitude or phase, is gaining an important place within optical methods used in neuroscience, especially for manipulating neuronal activity with optogenetics. The ability to selectively direct light in specific neurons expressing an optogenetic actuator, rather than in a large neuronal population within the microscope field of view, is now becoming attractive for studies that require high spatiotemporal precision for perturbing neuronal activity in a microcircuit. Computer-generated holography is a phase-modulation light patterning method providing significant advantages in terms of spatial and temporal resolution of photostimulation. It provides flexible three-dimensional light illumination schemes, easily reconfigurable, able to address a significant excitation field simultaneously, and applicable to both visible or infrared light excitation. Its implementation complexity depends on the level of accuracy that a certain application demands: Computer-generated holography can stand alone or be combined with temporal focusing in two-photon excitation schemes, producing depth-resolved excitation patterns robust to scattering. In this chapter, we present an overview of computer-generated holography properties regarding spatiotemporal resolution and penetration depth, and particularly focusing on its applications in optogenetics.

**Key words** Light patterning, Phase modulation, Spatial light modulator, Temporal focusing, Optogenetics, Opsin kinetics

## 1 Introduction

The coordinated activation of neuronal microcircuits is proposed to regulate brain functioning in health and disease. A common approach to investigate the mechanisms that reduce network complexity is to outline microcircuits and infer their functional role by selectively modulating them. Combined with suitable illumination approaches, optogenetics offers today the possibility to achieve such selective control with its ever-growing toolbox of reporters and actuators.

Albrecht Stroh (ed.), *Optogenetics: A Roadmap*, Neuromethods, vol. 133,
DOI 10.1007/978-1-4939-7417-7_10, 

Wide-field single-photon (1P) illumination was the first method employed to activate optogenetic actuators [1–8], and continues to be widely used for neural circuit dissection [9, 10] (*see* also Chap. 9). Using genetic tools, including viruses, Cre-dependent systems, and transgenic lines to target optogenetic actuators to neurons of interest (*see* Chaps. 1 and 2), investigators have used wide-field illumination to dissect correlation and causal interactions in neuronal subpopulations both in vitro [11–15] and in vivo [13, 16–18]. With this approach, population specificity is achieved through genetic targeting, and temporal resolution and precision are only limited by the channels' temporal kinetics and cell properties (e.g., opsin expression level and membrane potential). Suitable combinations of opsins have also enabled independent optical excitation of distinct cell populations [19]. The primary drawback of wide-field illumination is that all opsin-expressing neurons are stimulated simultaneously, and thus wide-field schemes lack the temporal flexibility and spatial precision necessary to mimic the spatiotemporal distribution of naturally occurring microcircuits activity.

Replacing 1P visible light excitation with two-photon (2P) near infrared light illumination enables improved axial resolution and penetration depth [20]. However, the small single-channel conductance of actuators such as ChR2 (40–80 fS; [21]), in combination with the low number of channels excitable within a femtoliter-two-photon focal volume, makes it difficult to generate photocurrents strong enough to bring a neuron to firing threshold. This challenge has prompted the development of 2P-stimulation approaches that increase the excitation volume.

2P-stimulation approaches for optogenetics can be grouped in two main categories: scanning and parallel excitation techniques. 2P laser scanning methods use galvanometric mirrors to quickly scan a laser beam across several positions covering a single or multiple cells [22–25] (*see* also Chap. 9). Parallel approaches enable to simultaneously cover the surface of a single cell using a low-numerical aperture (NA) beam [26], or multiple cells using computer-generated holography [27–31] and generalized phase contrast [32]. In this chapter, we will specifically focus on the description of computer-generated holography and its application to optogenetic neuronal control. A broader overview on the different approaches for 2P optogenetics can be found in Refs. [33–36] and Chap. 9.

## 2 Computer-Generated Holography

Originally proposed for generating multiple-trap optical tweezers [37], the experimental scheme for computer-generated holography (CGH) (Fig. 1a) consists in computing with a Fourier transform-

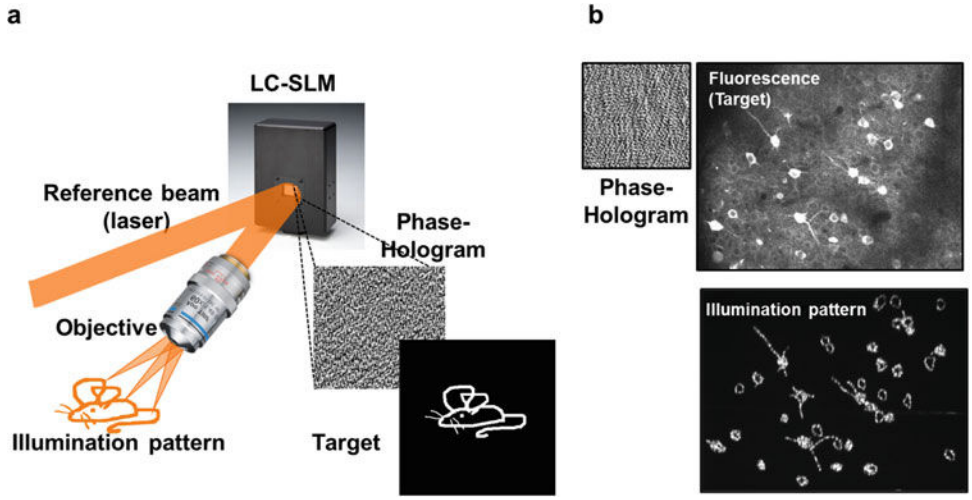


**Fig. 1** Computer-generated holography. (**a**) In CGH an arbitrary light distribution (*target*) is used as the input source to a Fourier transform-based iterative algorithm to calculate the interference pattern or phase hologram, that after interfering with the reference beam (*laser*) at the diffraction plane would reproduce the target at the imaging plane. The calculated phase hologram is addressed to a liquid-crystal spatial light modulator (LC-SLM). The reference beam plane, after diffraction through the LC-SLM, will generate at the objective focal plane a light distribution (*illumination pattern*) reproducing the original target shape. (**b**) For precise light stimulation, the whole fluorescence image or a defined region of interest can be used to select the excitation targets that will be sent to the iterative algorithm for producing the corresponding phase hologram

based iterative algorithm [38] the interference pattern or phase-hologram that back-propagating light from a defined target (input image) will form with a reference beam, on a defined "diffractive" plane. The computer-generated phase-hologram is converted into a grey-scale image and then addressed to a liquid-crystal matrix spatial light modulator (LC-SLM), placed at the diffractive plane. In this way, each pixel of the phase-hologram controls, proportionally to the analogous grey-scale-level, the voltage applied across the corresponding pixel of the LC matrix such as the refractive index and thus the phase of each pixel can be precisely modulated. As a result, the calculated phase-hologram is converted into a pixelated refractive screen and illumination of the screen with the laser beam (or reference beam) will generate at the objective focal plane a light pattern reproducing the desired template. This template can be any kind of light distribution in two (2D) or three dimensions (3D), ranging from diffraction-limited spots or spots of bigger sizes (bigger surface) to arbitrary extended light patterns.

Precise manipulation of neuronal activity via holographic light patterns requires an accurate control of the spatial colocalization between the generated light pattern and the target. To do so, a few years ago we proposed to generate the template for the calculation of phase-holograms on the base of the fluorescence image [39].

Briefly, a fluorescence image of the preparation is recorded and used to draw the excitation pattern. In this way it is possible to generate a holographic laser pattern reproducing the fluorescence image or a user defined region of interest (Fig. 1b) [33, 40].

In CGH, the pixel size and number of pixels of the LC-SLM define the lateral and axial field of excitation (FOE). The maximum lateral FOE, $FOE_{xy}$, is given by [41–43]:

$$FOE_{xy} = \Delta X \times \Delta Y = \left(2 \cdot \frac{\lambda f_{eq}}{2dn}\right) \times \left(2 \cdot \frac{\lambda f_{eq}}{2dn}\right), \quad (1)$$

where $\lambda$ is the excitation wavelength, $d$ the LC-SLM pixel size, $n$ is the medium refractive index, and $f_{eq}$ is the equivalent focal lens including all the lenses located between the LC-SLM and the sample plane (*see* **Note 1**).

Within this region, the diffraction efficiency, $\delta(x, y)$, defined as the intensity ratio of the incoming to the diffracted beam, depends on the lateral spot position coordinates, $x$, $y$:

$$\delta(x, y) = b\left(\sin c^2\left(\frac{\pi d}{\lambda f_{eq}} x\right) \sin c^2\left(\frac{\pi d}{\lambda f_{eq}} y\right)\right), \quad (2)$$

with $b$ being a proportionality factor considering the frontal window LC-SLM reflectivity. Consequently, $\delta(x, y)$ reaches its maximum value at the center of the $FOE_{xy}$ and the minimum one at the borders of the $FOE_{xy}$. Existing LC-SLM devices permit nowadays to reach diffraction efficiency values of ~95% at the center and ~38% at the border, which are the values close to the limit imposed by theory. The remaining light is distributed among the higher diffraction orders and an un-diffracted component, so-called zero-order, resulting in a tightly focused spot at the center of the FOE. Depending on the applied phase profile, the intensity of the zero-order spot can reach 25% of the input light. This value can be reduced down to 2–5%, regardless of the projected hologram, by performing ad hoc pre-compensation of the LC-SLM phase pixel values [44]. The focused zero-order spot can be removed from the FOE by adding a block or diaphragm at a plane conjugated to the sample plane [45, 46]. Nevertheless, this limits the accessible FOE. Alternatively, the intensity of the zero-order component can be strongly reduced by using a cylindrical lens placed in front of the LC-SLM, which stretches the zero order into a line [47]. A phase hologram compensating the cylindrical lens effect is then addressed onto the LC-SLM in addition to the original phase hologram generating the target spot, so that the holographic-pattern-shape is restored (Fig. 2) (*see* **Note 2**). Importantly, the use of cylindrical lenses enables suppressing excitation from the zero-order component in the $FOE_{xy}$ without using intermediate blocks, thus having access to the entire FOE.

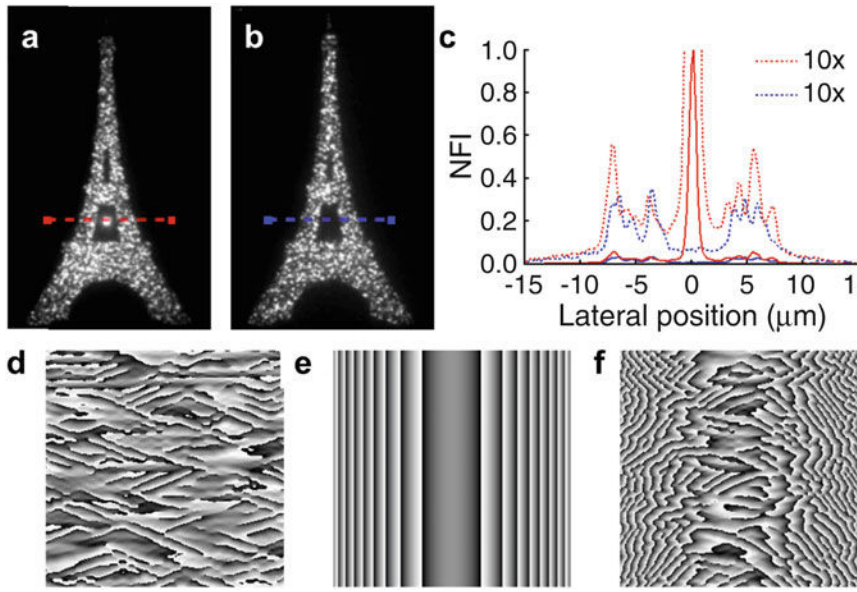


**Fig. 2** Zero order removal by using cylindrical lenses. Comparison between a computer-generated holographic image of the Eiffel Tower (**a**) without and (**b**) with a single 1-m cylindrical lens, aberrating the zero order in the optical path. (**c**) 2P normalized fluorescence intensity (NFI) profiles along the lines drawn in (**a**), *red*, and (**b**), *blue*. *Dotted lines* represent the signal of solid lines multiplied by 10 for better view. (**d**) Phase mask reproducing the image of the Eiffel Tower at the focal plane of the objective, calculated with a Gerchberg-Saxton-type algorithm. (**e**) Conjugated cylindrical Fresnel lens hologram added to the one of (**d**) for aberration compensation. (**f**) Final corrected phase mask addressed to the SLM. Reproduced from Ref. [47]

Intensity inhomogeneities due to diffraction efficiency are a limiting factor for applications requiring lateral displacing of a single spot or multiple spots within the FOE. Therefore, we have proposed approaches that compensate those inhomogeneities for keeping the spot intensity constant independently on the lateral position. In the case of single spot generation, a homogenization of light distribution can be achieved by projecting one or multiple spots outside the $FOE_{xy}$ and tuning their brightness or size to compensate the intensity loss due to the diffraction efficiency curve. Thus, a constant intensity value in the excitation spot is maintained for each position of the $FOE_{xy}$. The extra spots can be blocked by adding an external diaphragm placed at an intermediate imaging plane of the optical system, conjugated to the sample plane [43]. For multispot excitation, one can use graded input images in order to generate brighter spots into regions in the border of the FOE, where the diffraction efficiency is lower, and dimmer spots into the central part of the FOE, where diffraction efficiency is higher [43, 48, 49] (Fig. 3). Graded input patterns can also be used to compensate for sample inhomogeneity. For example they can be applied to equalize photocurrents from cells with different expression levels [48].

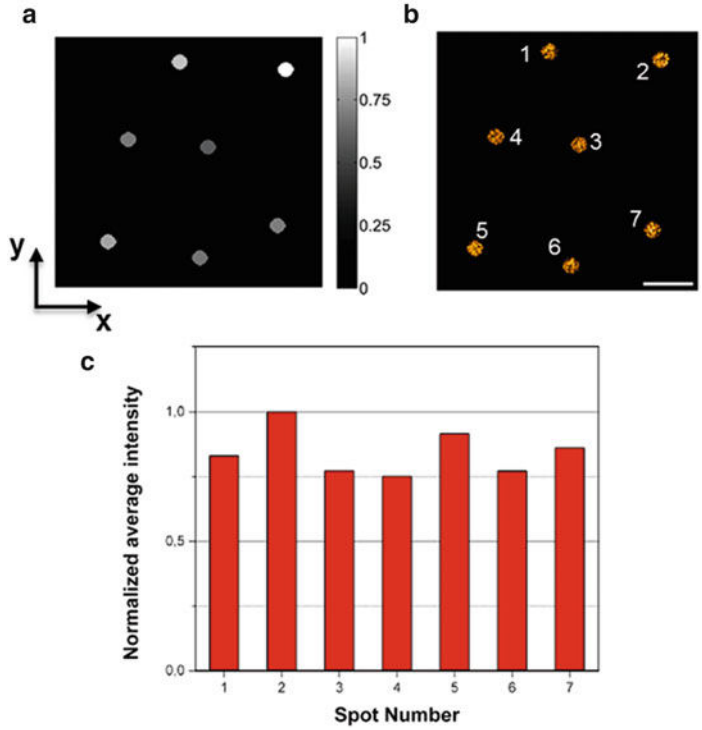


**Fig. 3** Diffraction efficiency compensation. (**a**) A graded input image to the iterative algorithm is used to equalize the light distribution across multiple spots (10 μm in diameter) generated on regions of different diffraction efficiency. (**b**) The corresponding light distribution is visualized by illuminating a uniform rhodamine fluorescent layer and by collecting the fluorescence on a CCD camera. Scale bar 30 μm. (**c**) Histogram of the normalized average intensity on the spots shown in (**b**). Intensity is averaged over the area of the spots. Intensity variations among the spots are of the order of 9%

CGH pattern generation also suffers from "speckle", i.e., undesired intensity variations of high spatial frequency, within the same spot. This is an intrinsic limitation of CGH and it is due to phase discontinuities at the sample plane inherent to the Gerchberg-Saxton algorithm [38], the most commonly used Fourier transform-based iterative algorithm. Speckle fluctuations reach 20% in 1P and 50% in 2P CGH implementations. Different approaches have been proposed to reduce or eliminate speckles, each with its advantages and limitations. Temporally averaging of speckle-patterns can be achieved by mechanical rotating a diffuser [50] or by generating multiple shifted versions of a single hologram [51]. Also smoother intensity profiles can be created by ad hoc

algorithms that remove phase vortices in the holographic phase mask [52]. Alternatively, the interferometric method, generalized phase contrast (GPC) (*see* **Note 3**) [53], generates speckle-free 2D extended shapes with adequate precision, e.g., to precisely reproduce the shape of a thin dendritic process [32]. Recently, researchers showed that GPC can be also extended to 3D by combining it with CGH, an approach called Holo-GPC [54]. In that case, a holographic phase mask is used to multiplex a GPC pattern in different lateral or axial positions.

### 2.1 Spatial Resolution

In general, the lateral spatial resolution of an optical microscope is defined on the basis of the maximum spatial frequency that can be transferred through the focusing objective. That is related to the maximum angle of convergence of the illumination rays, i.e., to the objective angular aperture. Consequently, in CGH the smallest obtainable illumination pattern is a diffraction-limited Gaussian spot whose full width at half maximum (FWHM) is equal to $\Delta x \approx \lambda/NA_{eff}$, where $NA_{eff}$ is the effective numerical aperture (with $NA_{eff} < NA$ for an under-filled pupil). Conjointly with the concept of resolution, it is useful to introduce the notion of spatial localization accuracy, i.e. the precision to target a certain position at the sample plane [55]. This is ultimately related to the minimum displacement, $\Delta\delta_{min}$, of the illumination spot that is possible to achieve by spatially modulating the phase of the incoming light beam. In particular, an illumination spot can be laterally shifted by a certain step $\Delta\delta$ by applying at the objective back aperture a prism-like phase modulation of slope $\alpha \approx \Delta\delta/f_{obj}$, where $f_{obj}$ is the objective focal length. The spatial localization accuracy therefore depends on the SLM capability to approximate a prism-like phase shift [55]. This ultimately is limited by the number of pixels, $N$, and grey levels, $g$, of the SLM. More precisely the theoretical upper limit for the minimum step $\Delta\delta_{min}$ is inversely proportional to $N \cdot g$ [55, 56].

In CGH, axial resolution scales linearly with the lateral spot size and inversely with the objective numerical aperture ($NA$). Precisely, defining as $s$ the holographic spot radius and $\sigma \approx \lambda/\left(\mathrm{NA}\sqrt{8\cdot\ln(2)}\right)$ the speckle size, the 1P and 2P axial resolution is twice the axial distance, $\Delta z$, at which the 2P intensity drops at 50% (FWHM), where $\Delta z$ is given by:

$$\Delta z(s)_{1P} = \frac{2\sqrt{3}z_R\sigma}{\sqrt{s^2+\sigma^2}}; \Delta z(s)_{2P} = \frac{2z_R\sigma}{\sqrt{s^2+\sigma^2}}, \tag{3}$$

with $z_R = \pi\cdot s^2/2\lambda$. This means that a spot size of, e.g., 10 μm in diameter will correspond to an axial resolution of 14 μm using a $NA = 0.9$ objective and 2P illumination at 900 nm [57]. The corresponding illumination volume has roughly the size of a cell soma (yellow circle, Fig. 4a), thus enabling in principle optical photostimulation with single-cell precision (Fig. 4a).

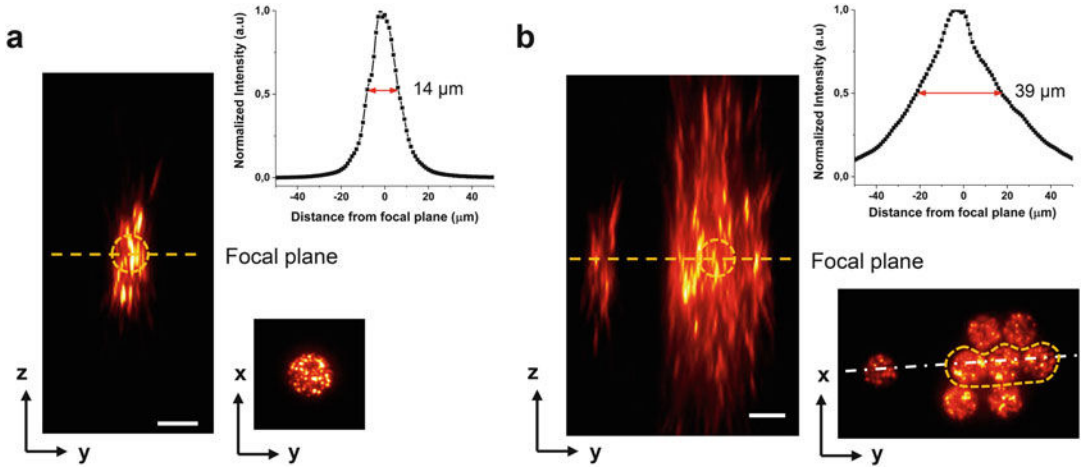


**Fig. 4** Axial propagation of holographic beams. Experimental *y-z* and *x-y* intensity cross-sections for holographic beams generated to produce at the objective focal plane (**a**) a circular spot, or (**b**) multiple spots of 10-µm diameter. *y-z* cross-section in (**b**) is shown along the *white dash-dotted line*. The *yellow circle* in both panels approximates the size of a cell soma. Integrated intensity profiles of *y-z* cross-sections around the circular spot (**a**) and in an area covering three spots (*dashed yellow*) of the multispot light configuration (**b**) are shown on the top of the panels. For comparison, the full width at half maximum of the axial integrated intensity profile of the single 10-µm spot is around 14 µm. Scale bars: 10 µm

Optical stimulation with near cellular resolution was indeed achieved in freely moving mice using 1P holographic stimulation [58]. Briefly, holographic light patterning coupled to a fiber bundle with a micro-objective at the end, was used to photostimulate and monitor functional responses in cerebellar molecular layer interneurons coexpressing a calcium indicator (GCaMP5-G) and an opsin (ChR2-tdTomato) in freely behaving mice (Fig. 5). These experiments proved optical photostimulation with near cellular resolution using sparse staining and sparse distribution of excitation spots. However, a similar approach would not reach the same precision if applied for multisite photostimulation of a densely labeled neuronal population as in this case the axial resolution would quickly deteriorate both using 1P and 2P excitation (Fig. 4b).

A few years ago, we demonstrated that micrometer-size optical sectioning independent of the lateral spot dimension [50] can be achieved by combining CGH and GPC with temporal focusing. Briefly, the technique of temporal focusing (TF), originally demonstrated to perform wide-field 2P microscopy [59, 60], uses a dispersive grating to diffract the different frequencies comprising the ultra-short excitation pulse toward different directions. The various frequencies thus propagate toward the objective focal plane at different angles, such that the pulse is temporally smeared above and below the focal plane, which remains the only region irradiated at peak powers efficient for 2P excitation.

The combination of TF with CGH is achieved by adding to the conventional TF optical path a LC-SLM and a focusing lens (L1) so

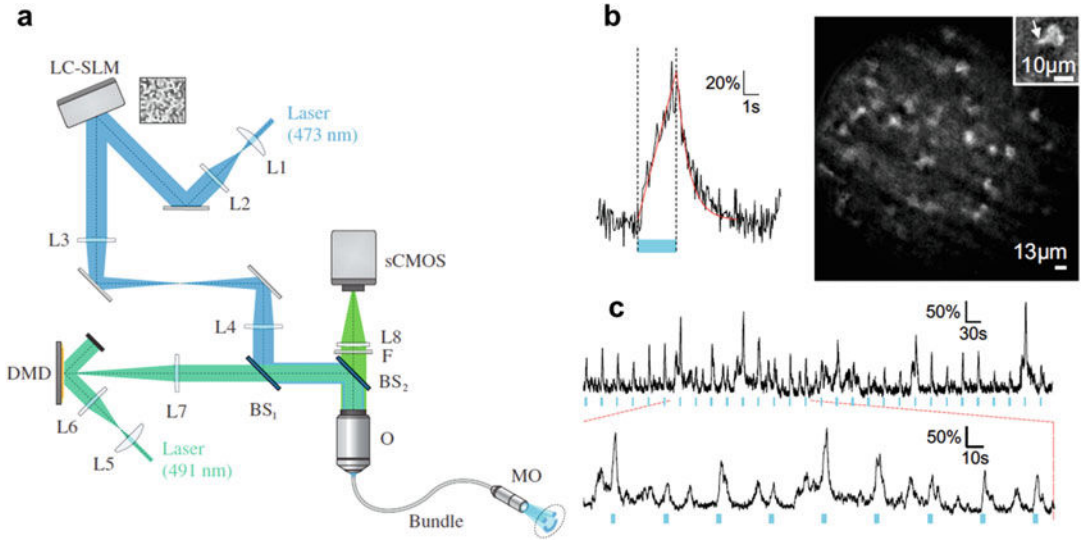


**Fig. 5** Holographic photostimulation and functional imaging in freely behaving mice. (**a**) Schematic of the holographic fiberscope composed of two illumination paths: one for photoactivation with CGH including a LC-SLM, and a second for fluorescence imaging including a digital micromirror device (DMD). Backward fluorescence was detected on a scientific complementary metal oxide semiconductor (sCMOS) camera. Both paths were coupled to the sample using a fiber bundle attached to a micro-objective (MO). *L* Lens, *BS* beam splitter, *O* microscope objective. (**b**) *Left*, Calcium signal triggered by photoactivation (*blue line*; $p = 50$ mW/mm$^2$) with a 5-µm diameter holographic spot placed on the soma of a ChR2-expressing cell recorded in a freely behaving mouse coexpressing GCaMP5-G and ChR2 in cerebellar molecular layer interneurons (MLIs). *Right*, Structure illumination image recorded in a freely behaving mouse and showing MLI somata and a portion of a dendrite (insert). Scale bar: 10 µm. (**c**) *Top*, The same photoactivation protocol as in (**a**) was repeated every 30 s for 15 min (photostimulation power, 50 mW/mm$^2$; imaging power, 0.28 mW/mm$^2$). *Bottom*, Expansion of the top trace showing that spontaneous activity frequently occurs between evoked transients. Adapted from Ref. [58]

that the TF grating lies at the focal plane of L1 and is illuminated by the holographic pattern. A second telescope, made by a second lens (L2) and the objective, conjugates the TF plane with the sample plane, thus enabling the generation of spatiotemporally focused patterns (Fig. 6a). Notably, TF enables decoupling lateral and axial resolution so that the same axial resolution is achieved independently on the lateral extension of the excitation spot (Fig. 6b, c) [50]. TF combined with low-*NA* Gaussian beams, GPC and CGH has enabled efficient 2P optogenetic excitation with micrometer axial resolution and millisecond temporal resolution both in vitro and in vivo [23, 26, 27, 32].

Although wavefront shaping and TF enable precise sculpting of the excitation volume, the ultimate spatial precision achievable for 2P optogenetics depends also on the opsin distribution within the expressing neurons: opsins are efficiently trafficked to the membrane of cell soma, as well as to dendrites and axons. Consequently, illumination with a theoretically micrometer-sized focal volume

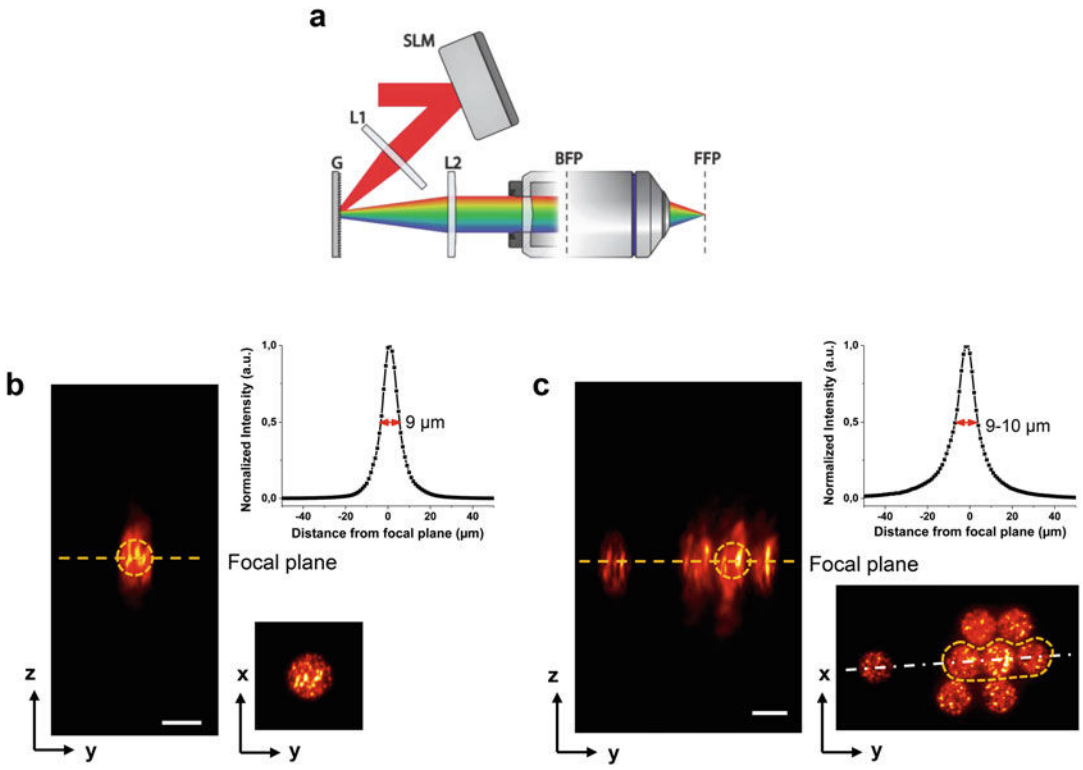


**Fig. 6** Computer-generated holography and temporal focusing. (**a**) Schematic representation of an experimental setup combining CGH with TF. *G* grating, *L1 and L2* lenses, *BFP* Back focal plane, *FFP* Front focal plane. (**b**–**c**) Experimental *y-z* and *x-y* intensity cross-sections for temporally focused holographic beams generated to produce at the objective focal plane a circular spot (**b**), or multiple spots of 10-μm diameter (**c**). *y-z* cross-section in (**c**) is shown along the *white dash-dotted line*. *Yellow circles* approximate the size of a cell soma. Integrated intensity profiles of *y-z* cross-sections around the circular spot (**b**) and in an area covering three spots (*dashed yellow*) of the multispot light configuration (**c**) are shown on the top of the panels. For comparison, the full width at half maximum of the axial integrated intensity profile of the single 10-μm spot is around 9 μm. The axial confinement thanks to temporal focusing is well preserved, even when multiple spots are projected close together. Scale bars: 10 μm

could depolarize all cells whose processes (dendrites and axons) cross the target excitation volume, even if their somata are located micrometers away from the illumination spot (Fig. 7). This activation cross talk needs to be carefully considered, for example when performing connectivity experiments, as it could prevent distinguishing if a postsynaptic response, recorded while photostimulating a presynaptic cell, originates from a true connection between the two cells rather from direct stimulation of postsynaptic dendrites or axons crossing the photostimulation volume. Reaching a true cellular resolution for exciting densely labeled samples requires combining optical focusing with molecular strategies enabling confined opsin expression in restricted cell areas (soma or axonal hillock) [49, 61].

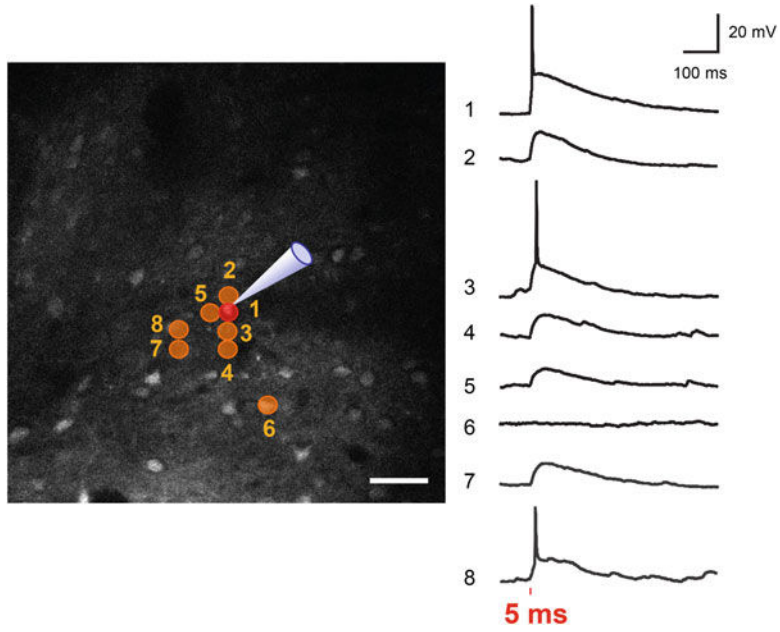


**Fig. 7** Two-photon holographic photostimulation of ReaChR-expressing cells in vivo. The opsin ReaChR was expressed in neurons at layer 2/3 of mouse visual cortex via injection of the viral vector rAAV1-Ef1α-ReaChR-P2A-tdTomato. Positive neurons expressing ReaChR (fluorescent cells in the 2P fluorescence image of the left panel) in isoflurane-anesthetized mouse were photostimulated with a 12-μm diameter excitation spot and 5-ms illumination duration at 0.15 mW/μm$^2$ and $\lambda = 1030$ nm (*red shaded area in the right panel*). Action potentials were induced by holographic excitation of one positive cell soma (spot 1), whose membrane potential was measured using 2P-guided whole-cell recording (trace 1). Sub-threshold or supra-threshold activation was induced in the patched cell (trace 2–8) upon holographic excitation of spots targeting around its soma (respective radial distance from spot 1 for spots 2–8: 12 μm, 12 μm, 24 μm, 12 μm, 67.6 μm, 40.4 μm, 35 μm), caused by exciting opsin-channels distributed into axon, proximal, and distal dendrites of the patched neuron. Scale bar: 40 μm

### 2.2 Temporal Resolution

Parallel light illumination enables simultaneous excitation of all selected targets. The temporal resolution is therefore only limited by the illumination time needed to evoke, e.g., an action potential (AP), a detectable $Ca^{2+}$ response or a defined behavioral change [33, 34]. This ultimately depends on opsin conductance, virus promoter, serotype, titer, kinetics parameters and excitation power (*see* Chaps. 1–3). In the following we will specifically focus on reviewing how the opsin kinetics parameters determine temporal resolution, temporal precision (temporal jitter) and AP spiking rate.

Light illumination of an opsin-expressing cell with a hundred-millisecond illumination pulse generates a characteristic photocurrent trace (Fig. 8a) where one can distinguish an activation, inactivation and deactivation part, characterized by a temporal decay, $\tau_{on}$, $\tau_{inact}$ and $\tau_{off}$, respectively. The overall kinetics of the current, as well as the peak-to-plateau ratio of current can be qualitatively well

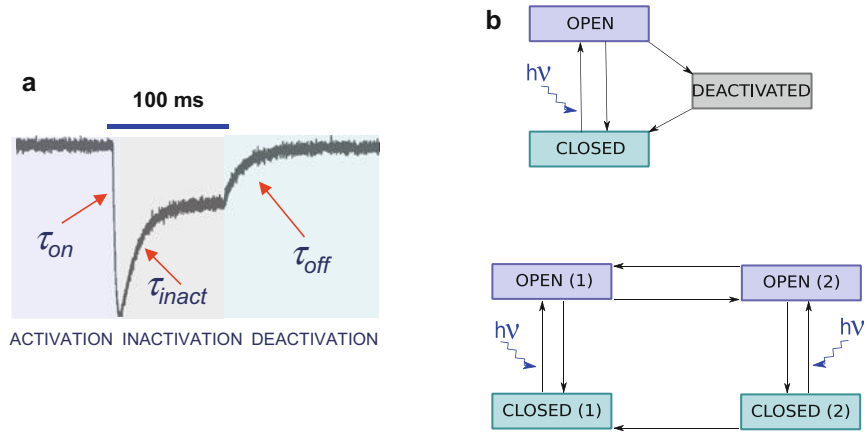


**Fig. 8** ChR2 photocurrent and photocycle. (**a**) Typical photocurrent trace of a CHO cell expressing ChR2 under visible light illumination (1P excitation) for 100 ms. (**b**) *Top*, schematic of the three-state model with a closed/ground state, an open state and a closed/desensitized state. *Bottom*, schematic of the four-state model with two closed, and two open states. For a detailed description of the models see Ref. [66]

**Table 1**
**Kinetics parameters for different opsins**

| | Chronos | CoChR | ReaChR |
|---|---|---|---|
| $\tau_{on}$ (ms) | 0.73 | 2.4 | 8 |
| $\tau_{inact}$ (ms) | 9.3 | 200 | 443 |
| $\tau_{off}$ (ms) | 4.2 | 31 | 94 |

Chronos, CoChR, and ReaChR were expressed in Chinese Hamster Ovary (CHO) cells following the protocol described in Refs. [27, 28]. Electrophysiological data were recorded 24—60 h after transfection using 2P ($\lambda = 950$ nm, pulse duration 4 s for ReaChR and CoChR and 1 s for Chronos; three trials at 1-min intervals holographic illumination at variable power (from 0.05 to 1.1 mW/μm$^2$). The current curves at saturation (defined as the power at which the peak current reaches 90% of its maximum) where fitted using a mono-exponential decay for the three transitions: activation, inactivation, and deactivation. The corresponding decay times, $\tau_{on}$ (ms), $\tau_{off}$ (ms), $\tau_{inact}$ (ms), are reported in the table and correspond to power close to saturation (0.86 mW/μm$^2$, 0.54 mW/μm$^2$, and 0.28 mW/μm$^2$ for Chronos, CoChR, and ReaChR, respectively (Emiliani Laboratory, unpublished data).

reproduced by using a 3- or 4-state model [62–66] (Fig. 8b), the latter being more accurate to reproduce the bi-exponential decay of the light-off current and the photocurrent voltage dependence [63]. A qualitative value for the characteristic temporal decay, $\tau_{on}$, $\tau_{inact}$ and $\tau_{off}$, can be directly extracted by assuming a mono-exponential process for the three transitions. In Table 1 we report the values of $\tau_{on}$ (at saturation), $\tau_{inact}$ and $\tau_{off}$ measured under 2P holographic illumination of CHO (Chinese Hamster Ovary) cells

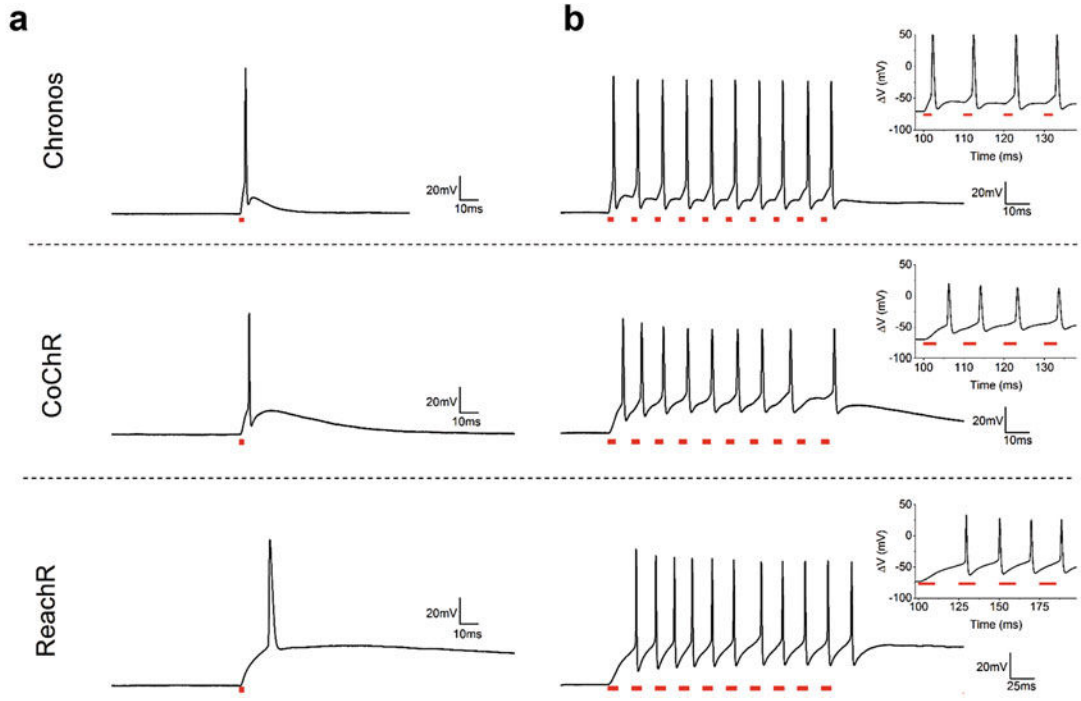


**Fig. 9** Temporal resolution and spiking rate. (**a**) Light-elicited single-spike by 2P holographic illumination (spot diameter: 15 μm; $\lambda = 1030$ nm) with short light illumination pulses ($t = 2$ ms) of Chronos ($P = 0.09$ mW/μm$^2$), CoChR ($P = 0.1$ mW/μm$^2$; Emiliani Laboratory, unpublished data) and ReaChR ($P = 0.07$ mW/μm$^2$) expressing interneurons from layer 2/3 of the mouse visual cortex. (**b**) Light-driven firing fidelity in opsin-positive interneurons by illuminating with a train of 10 light pulses, Chronos ($t = 2$ ms; $f = 100$ Hz; $P = 0.12$ mW/μm$^2$), CoChR ($t = 3$ ms; $f = 100$ Hz; $P = 0.1$ mW/μm$^2$) and ReaChR ($t = 10$ ms; $f = 40$ Hz; $P = 0.04$ mW/μm$^2$). The first 4 pulses are zoomed in, in the insets. Chronos data are adapted from Ref. [29] and ReaChR data are adapted from Ref. [28]

expressing a fast (Chronos) [19], an intermediate (CoChR) [19] and a slow (ReaChR) [67] opsin.

In practice, the efficient current integration obtained under parallel photostimulation enables using photostimulation pulses much shorter than the channel rise time therefore enabling in vitro AP generation with millisecond temporal resolution and sub-millisecond temporal jitter, independently on $\tau_{on}$ [28, 29, 49] (Fig. 9a). Conversely, the value of $\tau_{off}$ has a key role in limiting the achievable spiking rate, as shown in Fig. 9b, where the in vitro spike generation under 2P holographic illumination of interneurons (layer 2/3 of visual cortex) expressing different opsins (Chronos, ReaChR, CoChR) is reported. Fast opsins, such as Chronos, enabled generation of light-evoked AP trains up to 100 Hz spiking rate [29], while for ReaChR, with a ~50 times slower $\tau_{off}$, the light-evoked firing rate was limited at ~35 Hz (~15 Hz for pyramidal cells) [28]. Photostimulation of interneurons expressing CoChR, which has an intermediate value of $\tau_{off}$ (~30 ms), could still generate

light-evoked trains at 100 Hz but the temporal precision and fidelity were progressively lost across the train.

Interestingly the efficient current integration achievable with parallel holographic illumination enables reliable AP generation with millisecond temporal resolution and sub-millisecond precision using, at depths of ~100 μm, excitation densities less than 1 mW/μm$^2$ or 100 μW/μm$^2$, with a conventional mode-locked high-repetition rate (80 MHz) laser oscillator or a low-repetition rate (500 kHz) amplifier, respectively [28, 29, 49].

### 2.3 Penetration Depth

As previously described, temporal focusing coupled with CGH or GPC enables micrometer-range axial confinement. A further advantage of this approach is that it also enables robust light propagation through scattering media [27, 43, 68]. Scattering deviates the original photon trajectory, thus deforming the excitation spot shape at the focal plane. For light illumination with diffraction-limited spots, this mainly translates into occurrence of aberrations and loss of axial and lateral resolution. Moreover, scattered photons do not contribute to signal arising from the focal volume, which translates in loss of light intensity [69].

For large illumination areas, the presence of scattering also generates speckle in the excitation spot due to the random interference between ballistic and scattered photons (Fig. 10). A few years ago, we demonstrated that TF combined with both CGH [27] and GPC [68] enables to reduce this effect as scattered photons have less probability to interfere with the ballistic ones (Fig. 11). Light propagation of patterns generated using CGH [27] and GPC [68] through cortical brain slices or zebrafish larvae [43] have revealed robust conservation of lateral shape and axial resolution up to depths twice the scattering length (Fig. 10), enabling in-depth optogenetic stimulation [68] (*see* also Chap. 13).

### 2.4 Multiplane Light Activation

One important feature of CGH is the ability to generate spots in different axial planes, a feature used to generate multi-diffraction-limited traps for optical tweezers [37, 70], 3D glutamate uncaging [42, 71–73], and, combined with spiral scanning, to achieve multi-plane 2P optogenetic stimulation [74].

Adding lens-phase modulations to 2D-phase holograms also enables remote axial displacement and 3D positioning of laterally shaped targets [75]. This configuration, combined with optogenetics, enables simultaneous control of neurons and substructures in different planes, as well as provides a flexible means to stimulate locations lying above or below the imaging plane [30]. Conventional 3D-CGH optical designs are not, however, compatible with TF because axially shifted excitation planes cannot be simultaneously imaged onto the TF grating. To overcome this limitation, we have recently developed a new optical system including two LC-SLMs that enable simultaneous TF at multiple planes (Fig. 12a)

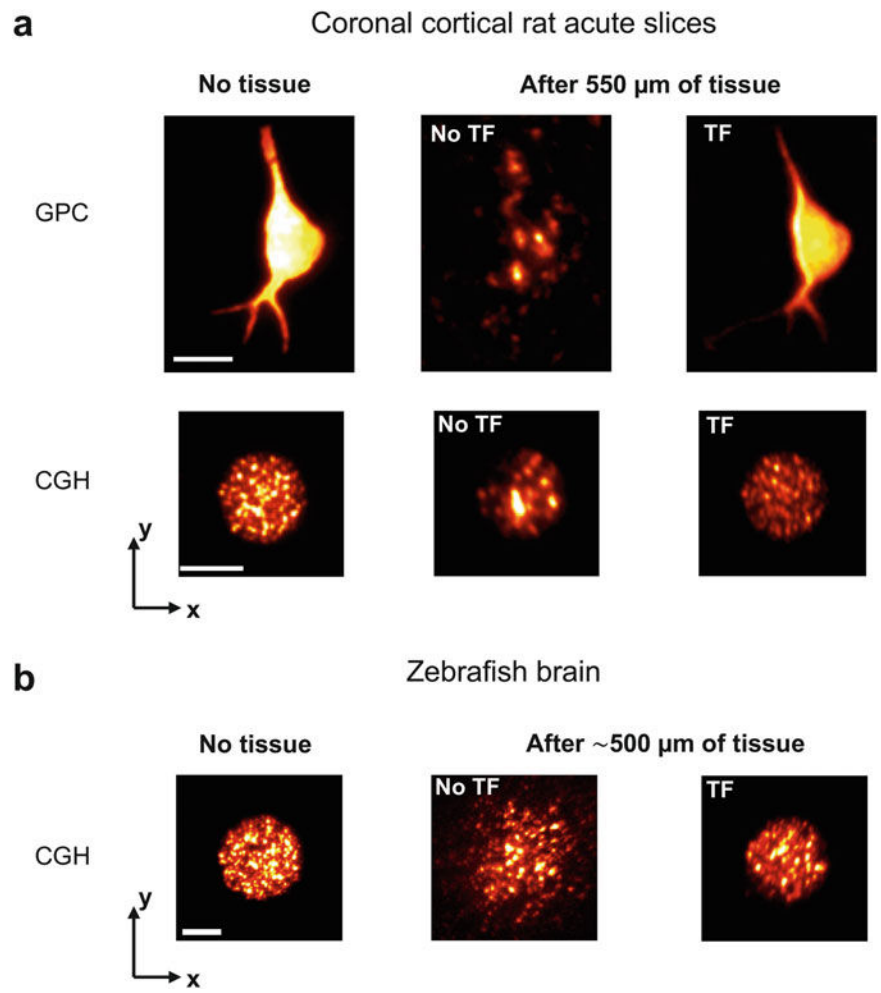


**Fig. 10** Temporal focusing and penetration depth. (**a**) 2P fluorescence *x*–*y* cross-sections of GPC-generated excitation patterns mimicking a neuron with small processes (*top*) and a 15-µm-diameter CGH spot (*bottom*) after propagation through 550 µm of acute coronal cortical brain slices without (*middle panel*) and with (*right panel*) temporal focusing ($\lambda = 950$ nm). Non-temporally focused beams are transformed to speckled patterns after traveling through the tissue. (**b**) 2P fluorescence *x*–*y* cross-sections of a 20-µm-diameter CGH spot after propagation through the whole brain of a zebrafish larva (~500 µm thick) without (*middle panel*) and with (*right panel*) temporal focusing ($\lambda = 920$ nm). Left panels in all cases are obtained from unscattered beams. Scale bars: 10 µm. Adapted from Refs [27, 43, 68]

[43]. The system achieves remote axial displacement of temporally focused holographic beams, as well as multiple temporally focused planes, by shaping the incoming wave-front in two steps, using two LC-SLMs. The first LC-SLM (SLM1 in Fig. 12a), laterally shapes the target light distribution that is focused onto the TF grating, which disperses the spectral components of the illumination pattern onto the second LC-SLM (SLM2 in Fig. 12a). SLM2, conjugated to the objective back focal plane, is addressed with a single or

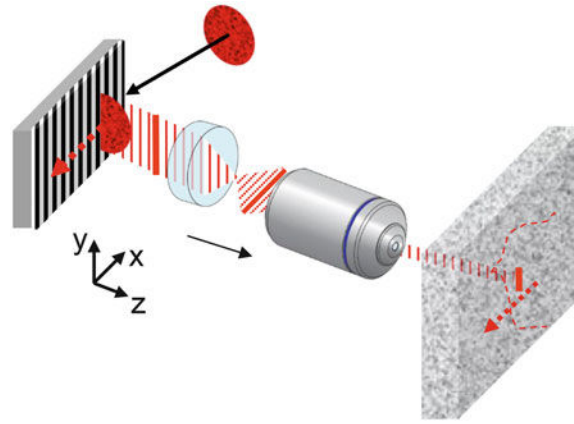


**Fig. 11** Temporal focusing in the temporal domain. The propagation of a large beam (a holographic spot in this case) diffracted by the grating produces an ultrafast line scanning of the sample. Scattering events off the scanning line at a single moment in time cannot interfere with the ballistic photons in the line. Adapted from Ref. [27]

multiple Fresnel-lens phase-profiles to control the target's axial position in the sample volume. In this way, the spatial and temporal focal planes coincide at the grating, and are jointly translated by SLM2 across the sample axial extent (Fig. 12b).

Similarly, to what has been discussed for the generation of 2D multiple spots, the pixel size, $d$, and pixels number of the LC-SLM limit the axial FOE, FOEz, to:

$$\mathrm{FOE_z} = \Delta Z = \left( \frac{\lambda f_{\mathrm{eq}} \sqrt{n^2 - NA^2}}{2dNA} \right), \tag{4}$$

where $NA$ is the objective numerical aperture, and $n$ is the refractive index of the immersion medium, giving rise to an axial-position-dependent diffraction efficiency [43] (Fig. 12c). Similarly to the 2D case, homogeneous light distribution can be obtained by using graded input images (Fig. 12d).

## 3 Notes

1. When CGH is used for microscopy, in principle it is sufficient to address the proper phase modulation at the back focal plane of the objective for having the desired illumination pattern at the sample plane. However, practically it is difficult to place a spatial light modulator there. The common practice is to image the back focal plane of the objective at another conjugated plane where the LC-SLM is placed, through a telescope of lenses. Typically, this includes a first lens (L1 of focal length

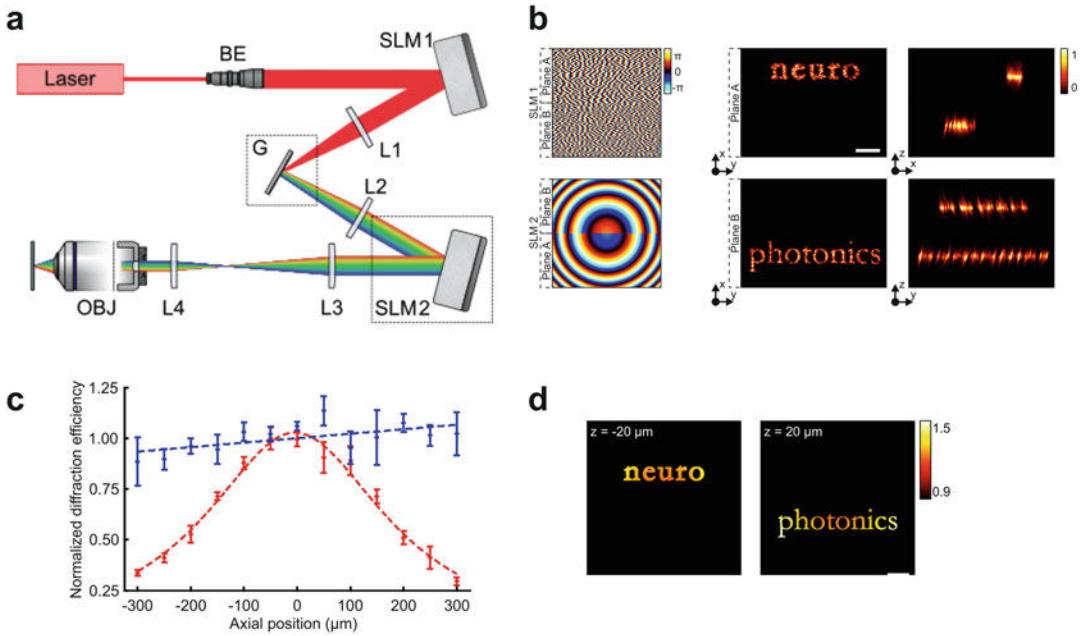


**Fig. 12** Multiplane generation of spatiotemporal focused holographic patterns. (**a**) Schematic of the experimental setup for 3D-CGH-TF. *BE* Beam expander, *G* diffraction grating, *L1, L2, L3, L4* Lenses, *OBJ1* Microscope objective. (**b**) *Left panel*, *top*, tiled phase profiles addressed to SLM1 for encoding the words "neuro" (plane A) and "photonics" (plane B). *Bottom*, Fresnel lens-phase profiles addressed to SLM2 to axially displace each holographic pattern generated by SLM1 on separated planes at +20 μm (plane A) and −20 μm (plane B). Middle panel, *x–y* 2P fluorescence intensity cross-sections at planes A and B generated by phase-holograms in the *left*. *Right panel*, orthogonal maximum 2P intensity projection along *x* (*top*) and *y* (*bottom*). (**c**) Axial diffraction efficiency curve, where the intensity of each holographic spot projected at each axial plane is normalized to the one of a spot projected at the center of the nominal focal plane. Experimental data (*red points*) represent the average of four realizations and follow a Lorentzian distribution (*red dashed line*) with $\Delta z_{FWHM} = 360$ μm. Weighting the axially displaced holographic spot intensity according to the calculated diffraction efficiency enables intensity equalization between holographic patterns in separated axial positions (*blue points* and *dashed line* represent the corrected intensity ratio and fitting, respectively). Vertical error bars show the standard deviation for the different realizations. (**d**) Input patterns to the Gerchberg-Saxton algorithm used to calculate the holograms that generate the holographic patterns shown in (**b**): low-diffraction efficiency regions appear brighter over those closer to the center of the excitation field. To improve the observation of differences between conditions, the amplitude scale of the images was chosen from 0.9 to 1.5. Adapted from Ref. [43]

$f_1$), placed at a distance equal to $f_1$ after the LC-SLM, which generates a first holographic intensity pattern at its focal plane, and a second lens (L2 of focal length $f_2$), placed at a distance $f_1 + f_2$ from L1 and $f_2 + f_{obj}$ from the objective (focal length $f_{obj}$), which conjugates the LC-SLM plane to the objective back focal plane. In this case $f_{eq} = (f_1 \cdot f_{obj})/f_2$. The focal lengths $f_1$ and $f_2$ are chosen to match the LC-SLM short axis to the objective back aperture size (usually 6–8 mm), in order to achieve the best possible axial resolution for the holographic

patterns. As a numerical example, considering a standard commercial LC-SLM array of 12 mm, with a pixel size of 20 μm, and a typical water-immersion 40× objective ($f_{obj} = 4.5$ mm) often used in neurophysiology experiments, the ratio $f_1/f_2$ is chosen to be ~2, which would give a $FOE_{xy} \sim 230 \times 230\ \mu m^2$ or $\sim 420 \times 420\ \mu m^2$ according to Eq. (1), using $\lambda = 520$ nm or $\lambda = 950$ nm, respectively.

2. In particular, for 2P–CGH combined with temporal focusing (see Sect. 2.1), two cylindrical lenses with opposite focal lengths, orthogonally oriented, with preference at 45° relatively to the direction of the axes of the LC-SLM array, enable generating two axially displaced zero-order lines. Then, thanks to the out-of-focus pulse dispersion of temporal focusing, the zero order contribution to the 2P signal can be reduced by 4–6 orders of magnitude [47]. The choice of 45° direction is related to the orientation of the grating grooves that is used for temporal focusing and the dispersion direction of spectral frequencies. Usually, the diffraction grating is placed with its grooves perpendicularly oriented in respect to the plane of incidence (i.e., the plane which contains the grating's surface normal and the propagation vector of the incoming radiation), or simply in respect to the lab's floor. This means that dispersion occurs parallel to the incidence plane. If the cylindrical lenses are oriented with their focusing axes one perpendicular and one parallel to the grating's grooves, then at the focal plane only fluorescence that originates from the line that lies along the direction of temporal focusing, i.e. the direction where the spectral frequencies are dispersed, will be efficiently suppressed. Fluorescence from the other line will be reduced, but still present at another plane. If the cylindrical lenses are oriented with their focusing axes at 45° in respect to the grating's grooves then both zero-order lines at the sample volume undergo temporal focusing and thus out-of-focus fluorescence suppression.
3. The generalized phase contrast method (GPC) is an alternative approach to CGH for generating speckle-free arbitrarily shaped illumination patterns. It is a common-path interferometry visualization technique, i.e., the output image is obtained by the interference between a signal and a reference wave travelling along the same optical axis, based in Zernike's phase contrast [76]. The basic principle of GPC involves separating a light beam into its Fourier components by using a lens. The on-axis, low spatial frequency components are shifted in phase (usually by $\pi$ or $\lambda/2$) using a small wave retarder or phase contrast filter (PCF). A second lens then recombines the high and low spatial frequencies. The introduced phase shift by the PCF causes the two different components to interfere and produces an

intensity distribution according to the phase information carried by the higher spatial frequencies [77]. By controlling the value of the input phase function at the LC-SLM plane and by choosing appropriate phase retardation at the PCF, a pure phase to intensity imaging is accomplished. A simple binary phase modulation is sufficient in this case (e.g., addressing with 0 phase dark areas and π phase bright areas of the desired pattern, when a π phase retardation is introduced by the PCF). This means that a phase modulation is finally turned to an intensity modulation, without using any iterative algorithm that provides approximate solutions for the phase hologram, resulting to speckle patterns, like in CGH. The rapid phase variations of the holographic phase profile do not longer exist when GPC is used and patterns generated are speckle-free. The phase wavefront of the output beam is smooth, similar to the one of a Gaussian beam. This results in a long axial propagation, revealing the interferometric character of the beam [32], meaning that GPC patterns lack of axial confinement. For 2P excitation, the remedy to this issue is combination of GPC with temporal focusing. Temporally focused 2P-GPC patterns result with an axial resolution similar to that obtained by 2P line-scan microscopy [32].

## 4 Outlook

Computer-generated holography combined with 2P excitation enables in depth optical stimulation with millisecond temporal resolution and sub-millisecond temporal precision. The combination of CGH with temporal focusing enables generation of excitation volumes with micrometer axial resolution and robust propagation through scattering media. For neuronal activation the efficient current integration achievable with parallel holographic illumination combined with laser amplifiers at low-repetition rate (500 kHz) and laser pulses of moderate excitation intensities (100 $\mu W/\mu m^2$) enables reliable AP generation with millisecond temporal resolution and sub-millisecond precision. These findings, together with high average power available nowadays in commercially available laser systems (more than 10 W at laser output), indicate that laser power is not the limiting factor for the maximum achievable number of targets using CGH. More likely, this will be limited by other factors, such as sample heating and deterioration of the photostimulation spatial resolution. Indeed, for multiple-cell stimulation, photostimulating neurites crossing the illumination volume affects cellular resolution, thus limiting the maximum number of targets that can be stimulated with single-cell precision. Recent progresses in engineering of somatic opsins should enable to solve these limitations in the close future [61].

## Acknowledgments

We thank Marco Pascucci and Benoît C. Forget for helpful discussions on the fitting procedure to extract opsins kinetics parameters; Valeria Zampini for recording data on CoChR-expressing neurons (Fig. 9); Dimitrii Tanese and Nicolò Accanto for help with preparation of Figs. 3, 4 and 6. We thank the National Institutes of Health (NIH 1-U01-NS090501-01), the "Agence Nationale de la Recherche" (grants ANR-10-INBS-04-01; France-BioImaging Infrastructure network, ANR-14-CE13-0016; HOLOHUB, ANR-15-CE19-0001-01; 3DHoloPAc) and the Human Frontiers Science Program (Grant RGP0015/2016) for financial support.

### References

1. Boyden ES, Zhang F, Bamberg E et al (2005) Millisecond-timescale, genetically targeted optical control of neural activity. Nat Neurosci 8:1263–1268
2. Nagel G, Brauner M, Liewald JF et al (2005) Light activation of Channelrhodopsin-2 in excitable cells of caenorhabditis elegans triggers rapid behavioral responses. Curr Biol 15:2279–2284. doi:10.1016/j.cub.2005.11.032
3. Zhang F, Wang LP, Brauner M et al (2007) Multimodal fast optical interrogation of neural circuitry. Nature 446:633–639
4. Adamantidis AR, Zhang F, Aravanis AM et al (2007) Neural substrates of awakening probed with optogenetic control of hypocretin neurons. Nature 450:420–424. doi:10.1038/nature06310
5. Gradinaru V, Thompson KR, Zhang F et al (2007) Targeting and readout strategies for fast optical neural control in vitro and in vivo. J Neurosci 27:14231–14238
6. Aravanis AM, Wang LP, Zhang F et al (2007) An optical neural interface: in vivo control of rodent motor cortex with integrated fiberoptic and optogenetic technology. J Neural Eng 4: S143–S156
7. Huber D, Petreanu L, Ghitani N et al (2008) Sparse optical microstimulation in barrel cortex drives learned behaviour in freely moving mice. Nature 451:61–64
8. Anikeeva P, Andalman AS, Witten I et al (2012) Optetrode: a multichannel readout for optogenetic control in freely moving mice. Nat Neurosci 15:163–170. doi:10.1038/nn.2992
9. Weible AP, Piscopo DM, Rothbart MK et al (2017) Rhythmic brain stimulation reduces anxiety-related behavior in a mouse model based on meditation training. Proc Natl Acad Sci U S A 114(10):2532–2537. doi:10.1073/pnas.1700756114
10. Makinson CD, Tanaka BS, Sorokin JM et al (2017) Regulation of thalamic and cortical network synchrony by Scn8a. Neuron 93:1–15. doi:10.1016/j.neuron.2017.01.031
11. Petreanu L, Huber D, Sobczyk A, Svoboda K (2007) Channelrhodopsin-2-assisted circuit mapping of long-range callosal projections. Nat Neurosci 10:663–668. doi:10.1038/nn1891. nn1891 [pii]
12. Petreanu L, Mao T, Sternson SM, Svoboda K (2009) The subcellular organization of neocortical excitatory connections. Nature 457:1142–1145. doi:10.1038/nature07709
13. Tovote P, Esposito MS, Botta P et al (2016) Midbrain circuits for defensive behaviour. Nature 534:206–212. doi:10.1038/nature17996
14. Joshi A, Kalappa BI, Anderson CT, Tzounopoulos T (2016) Cell-specific cholinergic modulation of excitability of layer 5B principal neurons in mouse auditory cortex. J Neurosci 36:8487–8499. doi:10.1523/JNEUROSCI.0780-16.2016
15. Morgenstern NA, Bourg J, Petreanu L (2016) Multilaminar networks of cortical neurons integrate common inputs from sensory thalamus. Nat Neurosci 19:1034–1040. doi:10.1038/nn.4339
16. Lee S-H, Kwan AC, Zhang S et al (2012) Activation of specific interneurons improves V1 feature selectivity and visual perception. Nature 488:379–383. doi:10.1038/nature11312
17. Adesnik H, Bruns W, Taniguchi H et al (2012) A neural circuit for spatial summation in visual cortex. Nature 490:226–231. doi:10.1038/nature11526

18. Atallah BV, Bruns W, Carandini M, Scanziani M (2012) Parvalbumin-expressing interneurons linearly transform cortical responses to visual stimuli. Neuron 73:159–170. doi:10.1016/j.neuron.2011.12.013
19. Klapoetke NC, Murata Y, Kim SS et al (2014) Independent optical excitation of distinct neural populations. Nat Methods 11:338–346. doi:10.1038/nmeth.2836
20. Denk W, Strickler JH, Webb WW (1990) Two-photon laser scanning fluorescence microscopy. Science 248:73–76
21. Feldbauer K, Zimmermann D, Pintschovius V et al (2009) Channelrhodopsin-2 is a leaky proton pump. Proc Natl Acad Sci U S A 106:12317–12322
22. Rickgauer JP, Tank DW (2009) Two-photon excitation of channelrhodopsin-2 at saturation. Proc Natl Acad Sci U S A 106:15025–15030. doi:10.1073/pnas.0907084106
23. Andrasfalvy BK, Zemelman BV, Tang J, Vaziri A (2010) Two-photon single-cell optogenetic control of neuronal activity by sculpted light. Proc Natl Acad Sci U S A 107:11981–11986
24. Prakash R, Yizhar O, Grewe B et al (2012) Two-photon optogenetic toolbox for fast inhibition, excitation and bistable modulation. Nat Methods 9:1171–1179. doi:10.1038/nmeth.2215
25. Packer AM, Peterka DS, Hirtz JJ et al (2012) Two-photon optogenetics of dendritic spines and neural circuits. Nat Methods 9:1171–1179. doi:10.1038/nmeth.2249
26. Rickgauer JP, Deisseroth K, Tank DW (2014) Simultaneous cellular-resolution optical perturbation and imaging of place cell firing fields. Nat Neurosci 17:1816–1824. doi:10.1038/nn.3866
27. Bègue A, Papagiakoumou E, Leshem B et al (2013) Two-photon excitation in scattering media by spatiotemporally shaped beams and their application in optogenetic stimulation. Biomed Opt Express 4:2869–2879
28. Chaigneau E, Ronzitti E, Gajowa AM et al (2016) Two-photon holographic stimulation of ReaChR. Front Cell Neurosci 10:234
29. Ronzitti E, Conti R, Zampini V et al (2017) Sub-millisecond optogenetic control of neuronal firing with two-photon holographic photoactivation of Chronos. J Neurosci:1246–1217. https://doi.org/10.1523/JNEUROSCI.1246-17.2017
30. dal Maschio M, Donovan JC, Helmbrecht TO, Baier H (2017) Linking neurons to network function and behavior by two-photon holographic optogenetics and volumetric imaging. Neuron 94:774–789.e5. doi:10.1016/j.neuron.2017.04.034
31. Förster D, Maschio MD, Laurell E, Baier H (2017) An optogenetic toolbox for unbiased discovery of functionally connected cells in neural circuits. Nat Commun 8(1):116
32. Papagiakoumou E, Anselmi F, Bègue A et al (2010) Scanless two-photon excitation of channelrhodopsin-2. Nat Methods 7:848–854. doi:10.1038/nmeth.1505
33. Oron D, Papagiakoumou E, Anselmi F, Emiliani V (2012) Two-photon optogenetics. Prog Brain Res 196:119–143. doi:10.1016/B978-0-444-59426-6.00007-0
34. Vaziri A, Emiliani V (2012) Reshaping the optical dimension in optogenetics. Curr Opin Neurobiol 22:128–137. doi:10.1016/j.conb.2011.11.011
35. Bovetti S, Fellin T (2015) Optical dissection of brain circuits with patterned illumination through the phase modulation of light. J Neurosci Methods 241:66–77. doi:10.1016/j.jneumeth.2014.12.002
36. Packer AM, Roska B, Häusser M (2013) Targeting neurons and photons for optogenetics. Nat Neurosci 16:805–815. doi:10.1038/nn.3427
37. Curtis JE, Koss BA, Grier DG (2002) Dynamic holographic optical tweezers. Opt Commun 207:169–175
38. Gerchberg RW, Saxton WO (1972) A pratical algorithm for the determination of the phase from image and diffraction pictures. Optik (Stuttg) 35:237–246
39. Lutz C, Otis TS, DeSars V et al (2008) Holographic photolysis of caged neurotransmitters. Nat Methods 5:821–827. doi:10.1038/nmeth.1241
40. Papagiakoumou E (2013) Optical developments for optogenetics. Biol Cell 105:443–464. doi:10.1111/boc.201200087
41. Golan L, Reutsky I, Farah N, Shoham S (2009) Design and characteristics of holographic neural photo-stimulation systems. J Neural Eng 6:66004
42. Yang S, Papagiakoumou E, Guillon M et al (2011) Three-dimensional holographic photostimulation of the dendritic arbor. J Neural Eng 8:46002. doi:10.1088/1741-2560/8/4/046002. S1741-2560(11)87640-8 [pii]
43. Hernandez O, Papagiakoumou E, Tanesee D et al (2016) Three-dimensional spatiotemporal focusing of holographic patterns. Nat Commun 7:11928. doi:10.1038/ncomms11928
44. Ronzitti E, Guillon M, de Sars V, Emiliani V (2012) LCoS nematic SLM characterization and modeling for diffraction efficiency optimization, zero and ghost orders suppression. Opt Express 20:17843–17855

45. Polin M, Ladavac K, Lee S-H et al (2005) Optimized holographic optical traps. Opt Express 13:5831–5845
46. Zahid M, Velez-Fort M, Papagiakoumou E et al (2010) Holographic photolysis for multiple cell stimulation in mouse hippocampal slices. PLoS One 5:e9431
47. Hernandez O, Guillon M, Papagiakoumou E, Emiliani V (2014) Zero-order suppression for two-photon holographic excitation. Opt Lett 39:5953–5956
48. Conti R, Assayag O, De Sars V et al (2016) Computer generated holography with intensity-graded patterns. Front Cell Neurosci 10:236
49. Shemesh OA, Tanese D, Zampini V, Linghu C, Piatkevich K, Ronzitti E, Papagiakoumou E, Boyden ES, Emiliani V (2017) Temporally precise single-cell resolution optogenetics. Nat Neurosci (in press)
50. Papagiakoumou E, de Sars V, Oron D, Emiliani V (2008) Patterned two-photon illumination by spatiotemporal shaping of ultrashort pulses. Opt Express 16:22039–22047
51. Golan L, Shoham S (2009) Speckle elimination using shift-averaging in high-rate holographic projection. Opt Express 17:1330–1339. doi: 176064 [pii]
52. Guillon M, Forget BC, Foust AJ et al (2017) Vortex-free phase profiles for uniform patterning with computer-generated holography. Opt Express 25:12640. doi:10.1364/OE.25.012640
53. Glückstad J (1996) Phase contrast image synthesis. Opt Commun 130:225–230
54. Bañas A, Glückstad J (2017) Holo-GPC: holographic generalized phase contrast. Opt Commun 392:190–195. doi:10.1016/j.optcom.2017.01.036
55. Schmitz CHJ, Spatz JP, Curtis JE (2005) High-precision steering of multiple holographic optical traps. Opt Express 13:8678–8685
56. Engström D, Bengtsson J, Eriksson E, Goksör M (2008) Improved beam steering accuracy of a single beam with a 1D phase-only spatial light modulator. Opt Express 16:18275–18287. doi:10.1364/OE.16.018275
57. Hernandez Cubero OR (2016) Advanced optical methods for fast and three-dimensional control of neural activity. Paris Descartes University, France
58. Szabo V, Ventalon C, De Sars V et al (2014) Spatially selective holographic photoactivation and functional fluorescence imaging in freely behaving mice with a fiberscope. Neuron 84:1157–1169. doi:10.1016/j.neuron.2014.11.005
59. Oron D, Tal E, Silberberg Y (2005) Scanningless depth-resolved microscopy. Opt Express 13:1468–1476
60. Zhu G, van Howe J, Durst M et al (2005) Simultaneous spatial and temporal focusing of femtosecond pulses. Opt Express 13:2153–2159. doi: 83023 [pii]
61. Baker CA, Elyada YM, Parra-Martin A, Bolton M (2016) Cellular resolution circuit mapping in mouse brain with temporal-focused excitation of soma-targeted channelrhodopsin. eLife 5:1–15. doi:10.7554/eLife.14193
62. Nagel G, Szellas T, Huhn W et al (2003) Channelrhodopsin-2, a directly light-gated cation-selective membrane channel. Proc Natl Acad Sci U S A 100:13940–13945
63. Williams JC, Xu J, Lu Z et al (2013) Computational optogenetics: empirically-derived voltage- and light-sensitive channelrhodopsin-2 model. PLoS Comput Biol 9:e1003220. doi:10.1371/journal.pcbi.1003220
64. Hegemann P, Ehlenbeck S, Gradmann D (2005) Multiple photocycles of channelrhodopsin. Biophys J 89:3911–3918. doi:10.1529/biophysj.105.069716
65. Nikolic K, Degenaar P, Toumazou C (2006) Modeling and engineering aspects of ChannelRhodopsin2 system for neural photostimulation. Annu Int Conf IEEE Eng Med Biol Soc 1:1626–1629
66. Nikolic K, Grossman N, Grubb MS et al (2009) Photocycles of Channelrhodopsin-2. Photochem Photobiol 85:400–411. doi:10.1111/j.1751-1097.2008.00460.x
67. Lin JY, Knutsen PM, Muller A et al (2013) ReaChR: a red-shifted variant of channelrhodopsin enables deep transcranial optogenetic excitation. Nat Neurosci 16:1499–1508. doi:10.1038/nn.3502
68. Papagiakoumou E, Bègue A, Leshem B et al (2013) Functional patterned multiphoton excitation deep inside scattering tissue. Nat Photonics 7:274–278
69. Booth MJ, Débarre D, Jesacher A (2012) Adaptive optics for biomedical microscopy. Opt Photonics News 23:22. doi:10.1364/OPN.23.1.000022
70. Leach J, Sinclair G, Jordan P et al (2004) 3D manipulation of particles into crystal structures using holographic optical tweezers. Opt Express 12:220
71. Anselmi F, Ventalon C, Bègue A et al (2011) Three-dimensional imaging and photostimulation by remote-focusing and holographic light patterning. Proc Natl Acad Sci U S A 108:19504–19509. doi:10.1073/pnas.1109111108

72. Daria VR, Stricker C, Bowman R et al (2009) Arbitrary multisite two-photon excitation in four dimensions. Appl Phys Lett 95:93701
73. Yang S, Emiliani V, Tang C-M (2014) The kinetics of multibranch integration on the dendritic arbor of CA1 pyramidal neurons. Front Cell Neurosci 8:127. doi:10.3389/fncel.2014.00127
74. Packer AM, Russell LE, Dalgleish HWP, Häusser M (2014) Simultaneous all-optical manipulation and recording of neural circuit activity with cellular resolution in vivo. Nat Methods 12:140–146. doi:10.1038/nmeth.3217
75. Haist T, Schönleber M, Tiziani H (1997) Computer-generated holograms from 3D-objects written on twisted-nematic liquid crystal displays. Opt Commun 140:299–308. doi:10.1016/S0030-4018(97)00192-2
76. Zernike F (1942) Phase contrast, a new method for the microscopic observation of transparent objects. Physica 9:686–698. doi:10.1016/S0031-8914(42)80035-X
77. Glückstad J, Mogensen PC (2001) Optimal phase contrast in common-path interferometry. Appl Optics 40:268–282

# Bibliography:


Abeles, M. 1982. “Role of the Cortical Neuron: Integrator or Coincidence Detector?” *Israel Journal of Medical Sciences* 18 (1): 83–92. http://www.ncbi.nlm.nih.gov/pubmed/6279540.

Adesnik, Hillel. 2017. “Synaptic Mechanisms of Feature Coding in the Visual Cortex of Awake Mice.” *Neuron* 95 (5). Elsevier Inc.: 1147–1159.e4. doi:10.1016/j.neuron.2017.08.014.

Adesnik, Hillel, William Bruns, Hiroki Taniguchi, Z Josh Huang, and Massimo Scanziani. 2012. “A Neural Circuit for Spatial Summation in Visual Cortex.” *Nature* 490 (7419). Nature Publishing Group: 226–31. doi:10.1038/nature11526.

Adesnik, Hillel, and Massimo Scanziani. 2010. “Lateral Competition for Cortical Space by Layer-Specific Horizontal Circuits.” *Nature* 464 (7292). Nature Publishing Group: 1155–60. doi:10.1038/nature08935.

Akerboom, J., T.-W. Chen, T. J. Wardill, L. Tian, J. S. Marvin, S. Mutlu, N. C. Calderon, et al. 2012. “Optimization of a GCaMP Calcium Indicator for Neural Activity Imaging.” *Journal of Neuroscience* 32 (40): 13819–40. doi:10.1523/JNEUROSCI.2601-12.2012.

Andermann, Mark L, Nathan B Gilfoy, Glenn J Goldey, Robert N S Sachdev, Markus Wölfel, David a McCormick, R Clay Reid, and Michael J Levene. 2013. “Chronic Cellular Imaging of Entire Cortical Columns in Awake Mice Using Microprisms.” *Neuron* 80 (4): 900–913. doi:10.1016/j.neuron.2013.07.052.

Anderson, J S, I Lampl, D C Gillespie, and D Ferster. 2001. “Membrane Potential and Conductance Changes Underlying Length Tuning of Cells in Cat Primary Visual Cortex.” *J Neurosci* 21 (6): 2104–12. http://www.ncbi.nlm.nih.gov/entrez/query.fcgi?cmd=Retrieve&db=pubmed&dopt=Abstract&list_uids=11245694.

Anderson, Jeffrey S., Matteo Carandini, and David Ferster. 2000. “Orientation Tuning of Input Conductance, Excitation, and Inhibition in Cat Primary Visual Cortex.” *Journal of Neurophysiology* 84 (2). American Physiological SocietyBethesda, MD : 909–26. doi:10.1152/jn.2000.84.2.909.

Anderson, Jeffrey S, Matteo Carandini, David Ferster, and S Murray Sherman. 2014. “Orientation Tuning of Input Conductance , Excitation , and Inhibition in Cat Primary Visual Cortex Orientation Tuning of Input Conductance , Excitation , and Inhibition in Cat Primary Visual Cortex,” 909–26.

Aschauer, Dominik F., Sebastian Kreuz, and Simon Rumpel. 2013. “Analysis of Transduction Efficiency, Tropism and Axonal Transport of AAV Serotypes 1, 2, 5, 6, 8 and 9 in the Mouse Brain.” *PLoS ONE* 8 (9): 1–16. doi:10.1371/journal.pone.0076310.

Ascoli, Giorgio A., Lidia Alonso-Nanclares, Stewart A. Anderson, German Barrionuevo, Ruth Benavides-Piccione, Andreas Burkhalter, György Buzsáki, et al. 2008. “Petilla Terminology: Nomenclature of Features of GABAergic Interneurons of the Cerebral Cortex.” *Nature Reviews Neuroscience* 9 (7): 557–68. doi:10.1038/nrn2402.

Atallah, Bassam V., William Bruns, Matteo Carandini, and Massimo Scanziani. 2012. “Parvalbumin-Expressing Interneurons Linearly Transform Cortical Responses to Visual Stimuli.” *Neuron* 73 (1). Elsevier Inc.: 159–70. doi:10.1016/j.neuron.2011.12.013.

Azouz, Rony. 2005. “Dynamic Spatiotemporal Synaptic Integration in Cortical Neurons: Neuronal Gain, Revisited.” doi:10.1152/jn.00542.2005.

Baker, Christopher A, Yishai M Elyada, Andres Parra-Martin, and McLean Bolton. 2016. “Cellular Resolution Circuit Mapping in Mouse Brain with Temporal-Focused Excitation of Soma-Targeted Channelrhodopsin.” *ELife* 5: 1–15. doi:10.7554/eLife.14193.

Bal, Thierry, and Alain Destexhe, eds. 2009. *Dynamic-Clamp*. New York, NY: Springer US. doi:10.1007/978-0-387-89279-5.

Banghart, Matthew, Katharine Borges, Ehud Isacoff, Dirk Trauner, and Richard H Kramer. 2004. "Light-Activated Ion Channels for Remote Control of Neuronal Firing." *Nature Neuroscience* 7 (12): 1381–86. doi:10.1038/nn1356.

Barbour, Boris. 2014. "Electronics for Electrophysiologists," 1–24.

Bathellier, Brice, Lyubov Ushakova, and Simon Rumpel. 2012. "Discrete Neocortical Dynamics Predict Behavioral Categorization of Sounds." *Neuron* 76 (2). Cell Press: 435–49. doi:10.1016/J.NEURON.2012.07.008.

Bennett, Corbett, Sergio Arroyo, and Shaul Hestrin. 2013. "Subthreshold Mechanisms Underlying State-Dependent Modulation of Visual Responses." *Neuron* 80: 350–57. doi:10.1016/j.neuron.2013.08.007.

Berndt, André, Matthias Prigge, Dietrich Gradmann, and Peter Hegemann. 2010. "Two Open States with Progressive Proton Selectivities in the Branched Channelrhodopsin-2 Photocycle." *Biophysical Journal* 98 (5). Biophysical Society: 753–61. doi:10.1016/j.bpj.2009.10.052.

Betley, J Nicholas, and Scott M Sternson. 2011. "Adeno-Associated Viral Vectors for Mapping, Monitoring, and Manipulating Neural Circuits." *Human Gene Therapy* 22 (6): 669–77. doi:10.1089/hum.2010.204.

Bi, Anding, Jinjuan Cui, Yu Ping Ma, Elena Olshevskaya, Mingliang Pu, Alexander M. Dizhoor, and Zhuo Hua Pan. 2006. "Ectopic Expression of a Microbial-Type Rhodopsin Restores Visual Responses in Mice with Photoreceptor Degeneration." *Neuron* 50 (1): 23–33. doi:10.1016/j.neuron.2006.02.026.

Bock, Davi D, Wei-chung Allen Lee, Aaron M Kerlin, Mark L Andermann, Arthur W Wetzel, Sergey Yurgenson, Edward R Soucy, Hyon Suk Kim, and Clay Reid. 2011. "Neurons" 471 (7337): 177–82. doi:10.1038/nature09802.Network.

Boerlin, Martin, Christian K. Machens, and Sophie Denève. 2013. "Predictive Coding of Dynamical Variables in Balanced Spiking Networks." Edited by Olaf Sporns. *PLoS Computational Biology* 9 (11). Public Library of Science: e1003258. doi:10.1371/journal.pcbi.1003258.

Borg-Graham, L J, C Monier, and Y Frégnac. 1998. "Visual Input Evokes Transient and Strong Shunting Inhibition in Visual Cortical Neurons." *Nature* 393 (6683): 369–73. doi:10.1038/30735.

Boyden, E S, F Zhang, E Bamberg, G Nagel, and K Deisseroth. 2005. "Millisecond-Timescale, Genetically Targeted Optical Control of Neural Activity." *Nature Neuroscience* 8 (9): 1263–68. doi:10.1038/nn1525.

Brette, Romain. 2015. "Philosophy of the Spike: Rate-Based vs. Spike-Based Theories of the Brain." *Frontiers in Systems Neuroscience* 9 (151): 1–14. doi:10.3389/fnsys.2015.00151.

Brizzi, L., C. Meunier, D. Zytnicki, M. Donnet, D. Hansel, B. Lamotte D'Incamps, and C. Van Vreeswijk. 2004. "How Shunting Inhibition Affects the Discharge of Lumbar Motoneurones: A Dynamic Clamp Study in Anaesthetized Cats." *The Journal of Physiology* 558 (2): 671–83. doi:10.1113/jphysiol.2003.059964.

Brown, T. H., and D. Johnston. 1983. "Voltage-Clamp Analysis of Mossy Fiber Synaptic Input to Hippocampal Neurons." *Journal of Neurophysiology* 50 (2): 487–507. doi:10.1152/jn.1983.50.2.487.

Burg, John S, Niloufar J Ataie, Amy J Lam, and Paula J Cranfill. 2014. "HHS Public Access" 11 (5): 572–78. doi:10.1038/nmeth.2888.Non-invasive.

Carandini, M, and D Ferster. 1997. "A Tonic Hyperpolarization Underlying Contrast Adaptation in Cat Visual Cortex." *Science (New York, N.Y.)* 276 (5314). American Association for the

Advancement of Science: 949–52. doi:10.1126/SCIENCE.276.5314.949.
Carandini, M, and D J Heeger. 1994. “Summation and Division by Neurons in Primate Visual Cortex.” *Science (New York, N.Y.)* 264 (5163): 1333–36. http://www.ncbi.nlm.nih.gov/pubmed/8191289.
Ch’ng, Yeang H, and R Clay Reid. 2010. “Cellular Imaging of Visual Cortex Reveals the Spatial and Functional Organization of Spontaneous Activity.” *Frontiers in Integrative Neuroscience* 4 (August): 1–9. doi:10.3389/fnint.2010.00020.
Chaigneau, Emmanuelle, Emiliano Ronzitti, Marta Gajowa, G Soler-Llavina, Dimitrii Tanese, Anthony Brureau, Eirini Papagiakoumou, Hongkui Zeng, and Valentina Emiliani. 2016. “2-Photon Holographic Photo-Activation of ReaChR Provides Sub-Millisecond Control of Action Potential Generation.” *In Preparation* 10 (October). doi:10.3389/fncel.2016.00234.
Chance, F S, and L F Abbott. 2002. “Neuron - Gain Modulation from Background Synaptic Input” 35 (4): 773–82. http://www.cell.com/neuron/abstract/S0896-6273(02)00820-6.
Chen, I-Wen, Emiliano Ronzitti, Brian R Lee, Tanya L Daigle, Hongkui Zeng, Eirini Papagiakoumou, and Valentina Emiliani. 2018. “Title Page Classification Neuroscience Title Parallel Holographic Illumination Enables Sub-Millisecond Two-Photon Optogenetic Activation in Mouse Visual Cortex in Vivo.” Accessed October 10. doi:10.1101/250795.
Chen, Tsai-Wen, Trevor J Wardill, Yi Sun, Stefan R Pulver, Sabine L Renninger, Amy Baohan, Eric R Schreiter, et al. 2013. “Ultrasensitive Fluorescent Proteins for Imaging Neuronal Activity.” *Nature* 499 (7458): 295–300. doi:10.1038/nature12354.
Cossell, Lee, Maria Florencia Iacaruso, Dylan R Muir, Rachael Houlton, Elie N Sader, Ho Ko, Sonja B Hofer, and Thomas D Mrsic-flogel. 2015. “Strength in Primary Visual Cortex.” doi:10.1038/nature14182.
D Adrian, BY E, and Yngve Zotterman. 2018. “THE IMPULSES PRODUCED BY SENSORY NERVE ENDINGS. Part 3. Impulses Set up by Touch and Pressure.” Accessed October 28. https://www.ncbi.nlm.nih.gov/pmc/articles/PMC1514868/pdf/jphysiol02525-0003.pdf.
Dalkara, D, L C Byrne, T Lee, N V Hoffmann, D V Schaffer, and J G Flannery. 2012. “Enhanced Gene Delivery to the Neonatal Retina through Systemic Administration of Tyrosine-Mutated AAV9.” *Gene Therapy* 19 (2): 176–81. doi:10.1038/gt.2011.163.
Dana, Hod, Tsai-Wen Chen, Amy Hu, Brenda C Shields, Caiying Guo, Loren L Looger, Douglas S Kim, and Karel Svoboda. 2014. “Thy1-GCaMP6 Transgenic Mice for Neuronal Population Imaging In Vivo.” *PloS One* 9 (9). Public Library of Science: e108697. doi:10.1371/journal.pone.0108697.
Deisseroth, Karl. 2015. “Optogenetics : 10 Years of Microbial Opsins in Neuroscience.” *Nature Neuroscience* 18 (9): 1213–25. doi:10.1038/nn.4091.
Denève, Sophie, and Christian K Machens. 2016. “Efficient Codes and Balanced Networks.” *Nature Neuroscience VOLUME* 19. doi:10.1038/nn.4243.
Desai, Niraj S., Richard Gray, and Daniel Johnston. 2017. “A Dynamic Clamp on Every Rig.” *Eneuro* 4 (5): ENEURO.0250-17.2017. doi:10.1523/ENEURO.0250-17.2017.
Destexhe, A, M Rudolph, J.-M Fellous, and T J Sejnowski. 2001. “FLUCTUATING SYNAPTIC CONDUCTANCES RECREATE IN VIVO-LIKE ACTIVITY IN NEOCORTICAL NEURONS.” https://www.ncbi.nlm.nih.gov/pmc/articles/PMC3320220/pdf/nihms366778.pdf.
Destexhe, Alain, Michael Rudolph, and Denis Paré. 2003. “The High-Conductance State of Neocortical Neurons in Vivo.” *Nature Reviews. Neuroscience* 4 (9): 739–51. doi:10.1038/nrn1289.
Evans, Benjamin D., Sarah Jarvis, Simon R. Schultz, and Konstantin Nikolic. 2016. “PyRhO: A Multiscale Optogenetics Simulation Platform.” *Frontiers in Neuroinformatics* 10 (March). Frontiers: 8. doi:10.3389/fninf.2016.00008.

Feldbauer, Katrin, Dirk Zimmermann, Verena Pintschovius, Julia Spitz, Christian Bamann, and Ernst Bamberg. 2009. “Channelrhodopsin-2 Is a Leaky Proton Pump.” *Proceedings of the National Academy of Sciences of the United States of America* 106 (30): 12317–22. doi:10.1073/pnas.0905852106.

Ferron, J F, D Kroeger, O Chever, and F Amzica. 2009. “Cortical Inhibition during Burst Suppression Induced with Isoflurane Anesthesia.” *J.Neurosci.* 29 (31): 9850–60. doi:29/31/9850 [pii];10.1523/JNEUROSCI.5176-08.2009 [doi].

Fino, Elodie, and Rafael Yuste. 2011. “Dense Inhibitory Connectivity in Neocortex.” *Neuron* 69 (6). Elsevier Inc.: 1188–1203. doi:10.1016/j.neuron.2011.02.025.

Frégnac, Yves, Cyril Monier, Frédéric Chavane, Pierre Baudot, and Lyle Graham. 2003. “Shunting Inhibition, a Silent Step in Visual Cortical Computation.” *Journal of Physiology Paris* 97 (4–6): 441–51. doi:10.1016/j.jphysparis.2004.02.004.

Gamper, Nikita, James D Stockand, and Mark S Shapiro. 2005. “The Use of Chinese Hamster Ovary ( CHO ) Cells in the Study of Ion Channels” 51: 177–85. doi:10.1016/j.vascn.2004.08.008.

Gao, Enquan, Gregory C DeAngelis, and Andreas Burkhalter. 2010. “Parallel Input Channels to Mouse Primary Visual Cortex.” *The Journal of Neuroscience : The Official Journal of the Society for Neuroscience* 30 (17): 5912–26. doi:10.1523/JNEUROSCI.6456-09.2010.

Gilbert, C.D.;, and T.N. Wiesel. 1979. “Morphology and Intracortical Projections of Functionally Characterised Neurons in Cat Visual Cortex.” *Nature* 280 (9): 120–25. doi:10.1017/CBO9781107415324.004.

Goedhart, Joachim, Laura van Weeren, Merel J W Adjobo-Hermans, Ies Elzenaar, Mark A. Hink, and Theodorus W J Gadella. 2011. “Quantitative Co-Expression of Proteins at the Single Cell Level - Application to a Multimeric FRET Sensor.” *PLoS ONE* 6 (11): 1–8. doi:10.1371/journal.pone.0027321.

Goltstein, Pieter M., Jorrit S. Montijn, and Cyriel M. a. Pennartz. 2015. “Effects of Isoflurane Anesthesia on Ensemble Patterns of Ca2+ Activity in Mouse V1: Reduced Direction Selectivity Independent of Increased Correlations in Cellular Activity.” *Plos One* 10 (2): e0118277. doi:10.1371/journal.pone.0118277.

Graham, Lyle J., and Adrien Schramm. 2009. “In Vivo Dynamic-Clamp Manipulation of Extrinsic and Intrinsic Conductances: Functional Roles of Shunting Inhibition and I BK in Rat and Cat Cortex.” In *Dynamic-Clamp*, 141–63. New York, NY: Springer US. doi:10.1007/978-0-387-89279-5_7.

Grothe, Benedikt, Michael Pecka, and David Mcalpine. 2010. “Mechanisms of Sound Localization in Mammals.” doi:10.1152/physrev.00026.2009.-The.

Grubb, Matthew S, and Juan Burrone. 2010. “Channelrhodopsin-2 Localised to the Axon Initial Segment.” *PloS One* 5 (10). Public Library of Science: e13761. doi:10.1371/journal.pone.0013761.

Guillamon, Antoni, David Mclaughlin, and John Rinzel. 2006. “Estimation of Synaptic Conductances.” *J Physiol Paris*. Vol. 100. https://www.ncbi.nlm.nih.gov/pmc/articles/PMC2042540/pdf/nihms15171.pdf.

Gunaydin, Lisa a, Ofer Yizhar, André Berndt, Vikaas S Sohal, Karl Deisseroth, and Peter Hegemann. 2010. “Ultrafast Optogenetic Control.” *Nature Neuroscience* 13 (3): 387–92. doi:10.1038/nn.2495.

Guo, Zengcai V, Anne C Hart, and Sharad Ramanathan. 2009. “Optical Interrogation of Neural Circuits in Caenorhabditis Elegans.” *Nature Methods* 6 (12): 891–96. doi:10.1038/nmeth.1397.

Haider, Bilal, Alvaro Duque, Andrea R Hasenstaub, and David A Mccormick. 2006. “Behavioral/Systems/Cognitive Neocortical Network Activity In Vivo Is Generated through a Dynamic Balance of Excitation and Inhibition.” doi:10.1523/JNEUROSCI.5297-05.2006.

Haider, Bilal, Michael Häusser, and Matteo Carandini. 2013. “Inhibition Dominates Sensory Responses in the Awake Cortex.” *Nature* 493 (7430): 97–100. doi:10.1038/nature11665.

Han, Xue. 2012. “In Vivo Application of Optogenetics for Neural Circuit Analysis.” *ACS Chemical Neuroscience* 3 (8): 577–84. doi:10.1021/cn300065j.

Han, Xue, and Edward S Boyden. 2007. “Multiple-Color Optical Activation, Silencing, and Desynchronization of Neural Activity, with Single-Spike Temporal Resolution.” *PLoS ONE* 2 (3): e299. doi:10.1371/journal.pone.0000299.

Hansel, David, and Carl van Vreeswijk. 2012. “The Mechanism of Orientation Selectivity in Primary Visual Cortex without a Functional Map.” *The Journal of Neuroscience : The Official Journal of the Society for Neuroscience* 32 (12): 4049–64. doi:10.1523/JNEUROSCI.6284-11.2012.

Hegemann, Peter, and Andreas Möglich. 2011. “Channelrhodopsin Engineering and Exploration of New Optogenetic Tools.” *Nature Methods* 8 (1). Nature Publishing Group: 39–42. doi:10.1038/nmeth.f.327.

Higley, Michael J, and Diego Contreras. 2006. “Behavioral/Systems/Cognitive Balanced Excitation and Inhibition Determine Spike Timing during Frequency Adaptation.” doi:10.1523/JNEUROSCI.3506-05.2006.

Hofer, Sonja B, Ho Ko, Bruno Pichler, Joshua Vogelstein, Hana Ros, Hongkui Zeng, Ed Lein, Nicholas A. Lesica, and Thomas D. Mrsic-Flogel. 2011. “Supp: Differential Connectivity and Response Dynamics of Excitatory and Inhibitory Neurons in Visual Cortex.” *Nature Neuroscience* 14 (8): 1045–52. doi:10.1038/nn.2876.

Holt, G R, and C Koch. 1997. “Shunting Inhibition Does Not Have a Divisive Effect on Firing Rates.” *Neural Computation* 9: 1001–13. doi:10.1162/neco.1997.9.5.1001.

Hubel, David H, and Torsten N Wiesel. 1962. “Receptive Fields, Binocular Interaction and Functional Architecture in the Cat’s Visual Cortex.” *Journal of Physiology* 160 (1): 106–154.2. doi:10.1523/JNEUROSCI.1991-09.2009.

Inagaki, Hidehiko K, Yonil Jung, Eric D Hoopfer, Allan M Wong, Neeli Mishra, John Y Lin, Roger Y Tsien, and David J Anderson. 2014. “Optogenetic Control of Drosophila Using a Red-Shifted Channelrhodopsin Reveals Experience-Dependent Influences on Courtship.” *Nature Methods* 11 (3): 325–32. doi:10.1038/nmeth.2765.

Jensen, Ellen C. 2012. “Use of Fluorescent Probes: Their Effect on Cell Biology and Limitations.” *The Anatomical Record* 295 (12): 2031–36. doi:10.1002/ar.22602.

Jia, H., N. L. Rochefort, X. Chen, and A. Konnerth. 2010. “Dendritic Organization of Sensory Input to Cortical Neurons in Vivo.” *Neuroforum* 16 (3): 236–37. doi:10.1038/nature08947.

Judkewitz, Benjamin, Matteo Rizzi, Kazuo Kitamura, and Michael Häusser. 2009. “Targeted Single-Cell Electroporation of Mammalian Neurons in Vivo.” *Nature Protocols* 4 (6): 862–69. doi:10.1038/nprot.2009.56.

Kaschube, Matthias. 2014. “Neural Maps versus Salt-and-Pepper Organization in Visual Cortex.” *Current Opinion in Neurobiology* 24 (February). Elsevier Ltd: 95–102. doi:10.1016/j.conb.2013.08.017.

Kato, Hideaki E, Feng Zhang, Ofer Yizhar, Charu Ramakrishnan, Tomohiro Nishizawa, Kunio Hirata, Jumpei Ito, et al. 2012. “Crystal Structure of the Channelrhodopsin Light-Gated Cation Channel.” *Nature* 482 (7385): 369–74. doi:10.1038/nature10870.

Kerlin, Aaron M, Mark L Andermann, Vladimir K Berezovskii, and R Clay Reid. 2010. “Article Broadly Tuned Response Properties of Diverse Inhibitory Neuron Subtypes in Mouse Visual Cortex.” doi:10.1016/j.neuron.2010.08.002.

Khabou, Hanen, Mélissa Desrosiers, Céline Winckler, Stéphane Fouquet, Gwenaëlle Auregan, Alexis-Pierre Bemelmans, José-Alain Sahel, and Deniz Dalkara. 2016. “Insight into the Mechanisms of

Enhanced Retinal Transduction by the Engineered AAV2 Capsid Variant -7m8." *Biotechnology and Bioengineering* 113 (12). Wiley Online Library: 2712–24. doi:10.1002/bit.26031.

Kim, Jin Hee, Sang Rok Lee, Li Hua Li, Hye Jeong Park, Jeong Hoh Park, Kwang Youl Lee, Myeong Kyu Kim, Boo Ahn Shin, and Seok Yong Choi. 2011. "High Cleavage Efficiency of a 2A Peptide Derived from Porcine Teschovirus-1 in Human Cell Lines, Zebrafish and Mice." *PLoS ONE* 6 (4): 1–8. doi:10.1371/journal.pone.0018556.

Klapoetke, Nathan C. 2014. "Independent Optical Excitation of Distinct Neural Populations." *Nat Methods* 11 (3): 338–46. doi:10.1038/nmeth.2836.Independent.

Kleinlogel, Sonja, Katrin Feldbauer, Robert E Dempski, Heike Fotis, Phillip G Wood, Christian Bamann, and Ernst Bamberg. 2011. "Ultra Light-Sensitive and Fast Neuronal Activation with the Ca2+-Permeable Channelrhodopsin CatCh." *Nature Neuroscience* 14 (4). Nature Publishing Group: 513–18. doi:10.1038/nn.2776.

Ko, Ho, Sonja B Hofer, Bruno Pichler, Katherine a Buchanan, P Jesper Sjöström, and Thomas D Mrsic-Flogel. 2011. "Functional Specificity of Local Synaptic Connections in Neocortical Networks." *Nature* 473 (7345): 87–91. doi:10.1038/nature09880.

Koch, Christof, and Christof. 1999. *Biophysics of Computation : Information Processing in Single Neurons*. Oxford University Press. https://dl.acm.org/citation.cfm?id=1137840.

Kreiner, Lisa, and Dieter Jaeger. 2004. "Synaptic Shunting by a Baseline of Synaptic Conductances Modulates Responses to Inhibitory Input Volleys in Cerebellar Purkinje Cells." doi:10.1080/14734220410031990.

Kwan, Alex C, and Yang Dan. 2012. "Article Dissection of Cortical Microcircuits by Single-Neuron Stimulation In Vivo," 1459–67. doi:10.1016/j.cub.2012.06.007.

Lee, Seung-Hee, Alex C. Kwan, Siyu Zhang, Victoria Phoumthipphavong, John G. Flannery, Sotiris C. Masmanidis, Hiroki Taniguchi, et al. 2012. "Activation of Specific Interneurons Improves V1 Feature Selectivity and Visual Perception." *Nature* 488 (7411). Nature Publishing Group: 379–83. doi:10.1038/nature11312.

Lin, John Y, Per Magne Knutsen, Arnaud Muller, David Kleinfeld, and Roger Y Tsien. 2013. "ReaChR: A Red-Shifted Variant of Channelrhodopsin Enables Deep Transcranial Optogenetic Excitation." *Nat Neurosci* 16 (10). Nature Publishing Group, a division of Macmillan Publishers Limited. All Rights Reserved.: 1499–1508. http://dx.doi.org/10.1038/nn.3502.

Liu, Bao-hua, Pingyang Li, Ya-tang Li, Yujiao J Sun, Yuchio Yanagawa, Kunihiko Obata, Li I Zhang, and Huizhong W Tao. 2009. "Visual Receptive Field Structure of Cortical Inhibitory Neurons Revealed by Two-Photon Imaging Guided Recording." *J Neurosci* 29 (34): 10520–32. doi:10.1523/JNEUROSCI.1915-09.2009.

Liu, Bao-hua, Pingyang Li, Yujiao J Sun, Ya-tang Li, Li I Zhang, and Huizhong Whit Tao. 2010. "Intervening Inhibition Underlies Simple-Cell Receptive Field Structure in Visual Cortex." *Nature Neuroscience* 13 (1). Nature Publishing Group: 89–96. doi:10.1038/nn.2443.

Liu, Bao-Hua, Ya-Tang Li, Wen-Pei Ma, Chen-Jie Pan, Li I Zhang, and Huizhong Whit Tao. 2011. "Broad Inhibition Sharpens Orientation Selectivity by Expanding Input Dynamic Range in Mouse Simple Cells." *Neuron* 71 (3). Zilkha Neurogenetic Institute, University of Southern California, Los Angeles, CA 90033, USA.: Elsevier Ltd: 542–54. http://eutils.ncbi.nlm.nih.gov/entrez/eutils/elink.fcgi?dbfrom=pubmed&id=21835349&retmode=ref&cmd=prlinks.

Lutz, Christoph, Thomas S Otis, Vincent Desars, Serge Charpak, A David, and Valentina Emiliani. 2015. "EFA Steering Committee 26" 5 (May 2014): 2030. doi:10.1038/nmeth.1241.

Mardinly, Alan R, Ian Antón Oldenburg, and Nicolas C Pégard. 2018. "Precise Multimodal Optical Control of Neural Ensemble Activity." doi:10.1038/s41593-018-0139-8.

Mariño, Jorge, James Schummers, David C Lyon, Lars Schwabe, Oliver Beck, Peter Wiesing, Klaus Obermayer, and Mriganka Sur. 2005. “Invariant Computations in Local Cortical Networks with Balanced Excitation and Inhibition.” *Nature Neuroscience* 8 (2): 194–201. doi:10.1038/nn1391.

Markram, Henry, Maria Toledo-Rodriguez, Yun Wang, Anirudh Gupta, Gilad Silberberg, and Caizhi Wu. 2004. “Interneurons of the Neocortical Inhibitory System.” *Nat Rev Neurosci* 5 (10): 793–807. doi:10.1038/nrn1519.

Marshel, James H., Marina E. Garrett, Ian Nauhaus, and Edward M. Callaway. 2011. “Functional Specialization of Seven Mouse Visual Cortical Areas.” *Neuron* 72 (6). Elsevier Inc.: 1040–54. doi:10.1016/j.neuron.2011.12.004.

Mattis, Joanna, K.M. Tye, E.A. Ferenczi, Charu Ramakrishnan, D.J. O’Shea, Rohit Prakash, L.A. Gunaydin, et al. 2011. “Principles for Applying Optogenetic Tools Derived from Direct Comparative Analysis of Microbial Opsins.” *Nature Methods* 9 (2). Nature Publishing Group: 159–172. doi:10.1038/NMeth.1808.

Mattis, Joanna, Kay M Tye, Emily a Ferenczi, Charu Ramakrishnan, Daniel J O’Shea, Rohit Prakash, Lisa a Gunaydin, et al. 2012. “Principles for Applying Optogenetic Tools Derived from Direct Comparative Analysis of Microbial Opsins.” *Nature Methods* 9 (2): 159–72. doi:10.1038/nmeth.1808.

Meyler, L., and J. K. Aronson. 2009. *Meyler’s Side Effects of Drugs Used in Anesthesia*. Elsevier Science. https://books.google.fr/books?id=W2k21o30Eg4C&dq=Meyer+side+effect+of+drugs+used+in+anesthesia&hl=pl&source=gbs_navlinks_s.

Mitchell, Simon J, and R Angus Silver. 2003. “Shunting Inhibition Modulates Neuronal Gain during Synaptic Excitation.” *Neuron* 38 (3): 433–45. doi:10.1016/S0896-6273(03)00200-9.

Monier, C., J. Fournier, and Y. Frégnac. 2008. “In Vitro and in Vivo Measures of Evoked Excitatory and Inhibitory Conductance Dynamics in Sensory Cortices.” *Journal of Neuroscience Methods* 169 (2): 323–65. doi:10.1016/j.jneumeth.2007.11.008.

Monier, Cyril, Pierre Baudot, Lyle J Graham, and Yves Fre. 2003. “Orientation and Direction Selectivity of Synaptic Inputs in Visual Cortical Neurons : A Diversity of Combinations Produces Spike Tuning” 37: 663–80.

Mountcastle, V.B. 1997. “The Columnar Organization of the Cerebral Cortex.” *Brain* 120: 701–22.

Murlidharan, Giridhar, Richard J Samulski, and Aravind Asokan. 2014. “Biology of Adeno-Associated Viral Vectors in the Central Nervous System.” *Frontiers in Molecular Neuroscience* 7 (September): 76. doi:10.3389/fnmol.2014.00076.

Nagel, Georg, Martin Brauner, Jana F. Liewald, Nona Adeishvili, Ernst Bamberg, and Alexander Gottschalk. 2005. “Light Activation of Channelrhodopsin-2 in Excitable Cells of Caenorhabditis Elegans Triggers Rapid Behavioral Responses.” *Current Biology* 15 (24): 2279–84. doi:10.1016/j.cub.2005.11.032.

Nagel, Georg, Tanjef Szellas, Wolfram Huhn, Suneel Kateriya, Nona Adeishvili, Peter Berthold, Doris Ollig, Peter Hegemann, and Ernst Bamberg. 2006. “Cation-Selective Membrane Channel.” *Pnas*. doi:10.1073/pnas.1936192100.

Niell, C. M., and M. P. Stryker. 2008. “Highly Selective Receptive Fields in Mouse Visual Cortex.” *Journal of Neuroscience* 28 (30): 7520–36. doi:10.1523/JNEUROSCI.0623-08.2008.

Niell, Cristopher. 2015. “Cell Types, Circuits, and Receptive Fields in the Mouse Visual Cortex.” *Annual Review of Neuroscience*, no. April: 413–31. doi:10.1146/annurev-neuro-071714-033807.

Niell, Cristopher M, and Michael P Stryker. 2008. “Highly Selective Receptive Fields in Mouse Visual Cortex.” *The Journal of Neuroscience : The Official Journal of the Society for Neuroscience* 28

(30): 7520–36. doi:10.1523/JNEUROSCI.0623-08.2008.
Nikolic, Konstantin, Patrick Degenaar, and Chris Toumazou. 2006. “Modeling and Engineering Aspects of ChannelRhodopsin2 System for Neural Photostimulation.” In *2006 International Conference of the IEEE Engineering in Medicine and Biology Society*, 1626–29. IEEE. doi:10.1109/IEMBS.2006.260766.
Okun, Michael, and Ilan Lampl. 2008. “Instantaneous Correlation of Excitation and Inhibition during Ongoing and Sensory-Evoked Activities B R I E F C O M M U N I C AT I O N S.” *NATURE NEUROSCIENCE VOLUME* 11 (5). doi:10.1038/nn.2105.
Oron, D, E Tal, and Y Silberberg. 2005. “Scanningless Depth-Resolved Microscopy.” *Optics Express* 13 (5): 1468–76. doi:10.1364/OPEX.13.001468.
Packer, Adam M, Darcy S Peterka, Jan J Hirtz, Rohit Prakash, Karl Deisseroth, and Rafael Yuste. 2012. “Two-Photon Optogenetics of Dendritic Spines and Neural Circuits.” *Nature Methods* 9 (12): 1202–5. doi:10.1038/nmeth.2249.
Packer, Adam M, Lloyd E Russell, Henry W P Dalgleish, and Michael Häusser. 2015. “Simultaneous All-Optical Manipulation and Recording of Neural Circuit Activity with Cellular Resolution in Vivo.” *Nature Methods* 12 (2): 140–46. doi:10.1038/nmeth.3217.
Papagiakoumou, E., E. Ronzitti, I.-W. Chen, M. Gajowa, A. Picot, and V. Emiliani. 2018. *Two-Photon Optogenetics by Computer-Generated Holography*. *Neuromethods*. Vol. 133. doi:10.1007/978-1-4939-7417-7_10.
Papagiakoumou, Eirini, Francesca Anselmi, Aurélien Bègue, Vincent de Sars, Jesper Glückstad, Ehud Y Isacoff, and Valentina Emiliani. 2010. “Scanless Two-Photon Excitation of Channelrhodopsin-2.” *Nature Methods* 7 (10): 848–54. doi:10.1038/nmeth.1505.
Piwkowska, Zuzanna, Martin Pospischil, Romain Brette, Julia Sliwa, Michelle Rudolph-Lilith, Thierry Bal, and Alain Destexhe. 2008. “Characterizing Synaptic Conductance Fluctuations in Cortical Neurons and Their Influence on Spike Generation.” *Journal of Neuroscience Methods* 169 (2): 302–22. doi:10.1016/j.jneumeth.2007.11.010.
Poggio, T., and V. Torre. 1978. “A New Approach to Synaptic Interactions.” In , 89–115. Springer, Berlin, Heidelberg. doi:10.1007/978-3-642-93083-6_6.
Pospischil, M., Z. Piwkowska, T. Bal, and A. Destexhe. 2009. “Extracting Synaptic Conductances from Single Membrane Potential Traces.” *Neuroscience* 158 (2): 545–52. doi:10.1016/j.neuroscience.2008.10.033.
Prescott, Steven A, and Yves De Koninck. 2076. “Gain Control of Firing Rate by Shunting Inhibition: Roles of Synaptic Noise and Dendritic Saturation.” Vol. 100. www.pnas.orgcgidoi10.1073pnas.0337591100.
Priebe, Nicholas J., and David Ferster. 2005. “Direction Selectivity of Excitation and Inhibition in Simple Cells of the Cat Primary Visual Cortex.” *Neuron* 45 (1): 133–45. doi:10.1016/j.neuron.2004.12.024.
Ratté, Stéphanie, Sungho Hong, Erik DeSchutter, and Steven A. Prescott. 2013. “Impact of Neuronal Properties on Network Coding: Roles of Spike Initiation Dynamics and Robust Synchrony Transfer.” *Neuron* 78 (5): 758–72. doi:10.1016/j.neuron.2013.05.030.
Renart, Alfonso, Jaime De La Rocha, Peter Bartho, Liad Hollender, Néstor Parga, Alex Reyes, and Kenneth D Harris. 2010. “The Asynchronous State in Cortical Circuits” 327 (5965): 587–90. doi:10.1126/science.1179850.
Rickgauer, John P, Karl Deisseroth, and David W Tank. 2014. “Simultaneous Cellular-Resolution Optical Perturbation and Imaging of Place Cell Firing Fields.” *Nature Neuroscience* 17 (12): 1816–24. doi:10.1038/nn.3866.
Rickgauer, John P, and David W Tank. 2009. “Two-Photon Excitation of Channelrhodopsin-2” 106

(35).
Robinson, H P, and N Kawai. 1993. “Injection of Digitally Synthesized Synaptic Conductance Transients to Measure the Integrative Properties of Neurons.” *Journal of Neuroscience Methods* 49 (3): 157–65. doi:10.1016/0165-0270(93)90119-C.
Ronzitti, Emiliano, Rossella Conti, Valeria Zampini, Dimitrii Tanese, Xamanda J Foust, Nathan Klapoetke, Edward S Boyden, Eirini Papagiakoumou, and Valentina Emiliani. 2017. “Submillisecond Optogenetic Control of Neuronal Firing with Two-Photon Holographic Photoactivation of Chronos.” doi:10.1523/JNEUROSCI.1246-17.2017.
Rothman, Jason S, Laurence Cathala, Volker Steuber, R Angus Silver, and R A Silver. 2009. “Synaptic Depression Enables Neuronal Gain Control Europe PMC Funders Group.” *Nature* 457 (7232): 1015–18. doi:10.1038/nature07604.
Rudolph, Michael, and Alain Destexhe. 2003a. “Tuning Neocortical Pyramidal Neurons between Integrators and Coincidence Detectors.” *Journal of Computational Neuroscience*. Vol. 14. https://link.springer.com/content/pdf/10.1023%2FA%3A1023245625896.pdf.
Rudolph, Michelle, Martin Pospischil, Igor Timofeev, and Alain Destexhe. 2007. “Behavioral/Systems/Cognitive Inhibition Determines Membrane Potential Dynamics and Controls Action Potential Generation in Awake and Sleeping Cat Cortex.” doi:10.1523/JNEUROSCI.4652-06.2007.
Sakmann, Bert, and Erwin Neher. 1983. *Single-Channel Recording*. Plenum Press. https://books.google.fr/books?id=H1PaBwAAQBAJ&dq=Sakmann,+Bert,+and+Erwin+Neher.+“Single-Channel+Recording.”&hl=pl&source=gbs_navlinks_s.
Schneider, Franziska, Dietrich Gradmann, and Peter Hegemann. 2013. “Ion Selectivity and Competition in Channelrhodopsins.” doi:10.1016/j.bpj.2013.05.042.
Schneider, Franziska, Christiane Grimm, and Peter Hegemann. 2015. “Biophysics of Channelrhodopsin.” *Annu. Rev. Biophys* 44: 167–86. doi:10.1146/annurev-biophys-060414-034014.
Schramm, Adrien E., Daniele Marinazzo, Thomas Gener, and Lyle J. Graham. 2014. “The Touch and Zap Method for in Vivo Whole-Cell Patch Recording of Intrinsic and Visual Responses of Cortical Neurons and Glial Cells.” *PLoS ONE* 9 (5). doi:10.1371/journal.pone.0097310.
Sengupta, Biswa, Simon B. Laughlin, and Jeremy E. Niven. 2013. “Balanced Excitatory and Inhibitory Synaptic Currents Promote Efficient Coding and Metabolic Efficiency.” *PLoS Computational Biology* 9 (10). doi:10.1371/journal.pcbi.1003263.
Shadlen, M. N., and W. T. Newsome. 1998. “The Variable Discharge of Cortical Neurons: Implications for Connectivity, Computation, and Information Coding.” *The Journal of Neuroscience : The Official Journal of the Society for Neuroscience* 18 (10): 3870–96. doi:0270-6474/98/183870-27$05.00/0.
Shadlen, Michael N., and William T. Newsome. 1994. “Noise, Neural Codes and Cortical Organization.” *Current Opinion in Neurobiology* 4 (4): 569–79. doi:10.1016/0959-4388(94)90059-0.
Sharp, A. A., M. B. O’Neil, L. F. Abbott, and E. Marder. 1993. “Dynamic Clamp: Computer-Generated Conductances in Real Neurons.” *Journal of Neurophysiology* 69 (3): 992–95. doi:10.1152/jn.1993.69.3.992.
Shemesh, Or A, Dimitrii Tanese, Valeria Zampini, Changyang Linghu, and Nat Neurosci Author. 2017. “Temporally Precise Single-Cell Resolution Optogenetics HHS Public Access Author Manuscript.” *Nat Neurosci* 20 (12): 1796–1806. doi:10.1038/s41593-017-0018-8.
Shu, Yousheng, Andrea Hasenstaub, Mathilde Badoual, Thierry Bal, and David A Mccormick. 2003. “Cellular/Molecular Barrages of Synaptic Activity Control the Gain and Sensitivity of Cortical

Neurons." http://www.jneurosci.org/content/jneuro/23/32/10388.full.pdf.
Silver, R. Angus. 2010. "Neuronal Arithmetic." *Nature Reviews Neuroscience*. doi:10.1038/nrn2864.
Snapp, Erik. 2005. "Design and Use of Fluorescent Fusion Proteins in Cell Biology." *Current Protocols in Cell Biology*, chapter 21:Unit 21.4. doi:10.1002/0471143030.cb2104s27.Design.
Sohal, Vikaas S, Feng Zhang, Ofer Yizhar, and Karl Deisseroth. 2009. "Parvalbumin Neurons and Gamma Rhythms Enhance Cortical Circuit Performance." *Nature* 459 (7247). Macmillan Publishers Limited. All rights reserved: 698–702. doi:10.1038/nature07991.
Sohya, Kazuhiro, Katsuro Kameyama, Yuchio Yanagawa, Kunihiko Obata, and Tadaharu Tsumoto. 2007. "GABAergic Neurons Are Less Selective to Stimulus Orientation than Excitatory Neurons in Layer II/III of Visual Cortex, as Revealed by in Vivo Functional Ca2+ Imaging in Transgenic Mice." *The Journal of Neuroscience : The Official Journal of the Society for Neuroscience* 27 (8): 2145–49. doi:10.1523/JNEUROSCI.4641-06.2007.
Stosiek, Christoph, Olga Garaschuk, Knut Holthoff, and Arthur Konnerth. 2003. "In Vivo Two-Photon Calcium Imaging of Neuronal Networks." *Proceedings of the National Academy of Sciences of the United States of America* 100 (12): 7319–24. doi:10.1073/pnas.1232232100.
Straw, Andrew D. 2008. "Vision Egg: An Open-Source Library for Realtime Visual Stimulus Generation." *Frontiers in Neuroinformatics* 2 (November): 4. doi:10.3389/neuro.11.004.2008.
Szabo, Vivien, Cathie Ventalon, Vincent De Sars, Jonathan Bradley, and Valentina Emiliani. 2014. "NeuroResource Spatially Selective Holographic Photoactivation and Functional Fluorescence Imaging in Freely Behaving Mice with a Fiberscope." *Neuron* 84 (6). Elsevier Inc.: 1157–69. doi:10.1016/j.neuron.2014.11.005.
Tan, a. Y. Y., B. D. Brown, B. Scholl, D. Mohanty, and N. J. Priebe. 2011. "Orientation Selectivity of Synaptic Input to Neurons in Mouse and Cat Primary Visual Cortex." *Journal of Neuroscience* 31 (34): 12339–50. doi:10.1523/JNEUROSCI.2039-11.2011.
Tan, Andrew Y. Y, Brandon D Brown, Benjamin Scholl, Deepankar Mohanty, and Nicholas J Priebe. 2011. "Orientation Selectivity of Synaptic Input to Neurons in Mouse and Cat Primary Visual Cortex." *The Journal of Neuroscience* 31 (34): 12339–50. doi:10.1523/JNEUROSCI.2039-11.2011.
Tan, R C, and R W Joyner. 1990. "Electrotonic Influences on Action Potentials from Isolated Ventricular Cells." *Circulation Research* 67 (5): 1071–81. http://www.ncbi.nlm.nih.gov/pubmed/2225348.
Theunissen, Frédéric, and John P. Miller. 1995. "Temporal Encoding in Nervous Systems: A Rigorous Definition." *Journal of Computational Neuroscience* 2 (2): 149–62. doi:10.1007/BF00961885.
Tsien, Roger Y. 1980. "C. (1969) ~," no. 1966: 2396–2404.
Tye, Kay M, Rohit Prakash, Sung-Yon Kim, Lief E Fenno, Logan Grosenick, Hosniya Zarabi, Kimberly R Thompson, Viviana Gradinaru, Charu Ramakrishnan, and Karl Deisseroth. 2011. "Amygdala Circuitry Mediating Reversible and Bidirectional Control of Anxiety." *Nature* 471 (7338). Nature Publishing Group: 358–62. doi:10.1038/nature09820.
Ulrich, D. 2003. "Differential Arithmetic of Shunting Inhibition for Voltage and Spike Rate in Neocortical Pyramidal Cells." *The European Journal of Neuroscience* 18 (8). Institute of Physiology, University of Bern, Buhlplatz 5, CH-3012 Bern, Switzerland. ulrich@pyl.unibe.ch: 2159–65. http://www.ncbi.nlm.nih.gov/entrez/query.fcgi?cmd=Retrieve&db=PubMed&dopt=Citation&list_uids=14622176.
Vacher, P, and B Dufy. 1994. "Voltage-Dependent Ca2' Channels in Chinese Hamster Ovary (CHO) Cells" 349 (I 994): 289–94.
van Vreeswijk, C, and H Sompolinsky. 1996. "Chaos in Neuronal Networks with Balanced Excitatory

and Inhibitory Activity." *Science (New York, N.Y.)* 274 (5293): 1724–26. doi:10.1126/science.274.5293.1724.

Vervaeke, Koen, Hua Hu, Lyle J Graham, and Johan F Storm. 2006. "Contrasting Effects of the Persistent Na+ Current on Neuronal Excitability and Spike Timing." *Neuron* 49 (2): 257–70. doi:10.1016/j.neuron.2005.12.022.

Viltart, Odile, Danke Zhang, Clare Howarth, Yuguo Yu, and Shanglin Zhou. 2018. "Synaptic E-I Balance Underlies Efficient Neural Coding." *Front. Neurosci* 12: 46. doi:10.3389/fnins.2018.00046.

Vu, E T, and F B Krasne. 1992. "Evidence for a Computational Distinction between Proximal and Distal Neuronal Inhibition." *Science (New York, N.Y.)* 255 (5052). American Association for the Advancement of Science: 1710–12. doi:10.1126/SCIENCE.1553559.

Watakabe, Akiya, Masanari Ohtsuka, Masaharu Kinoshita, Masafumi Takaji, Kaoru Isa, Hiroaki Mizukami, Keiya Ozawa, Tadashi Isa, and Tetsuo Yamamori. 2015. "Comparative Analyses of Adeno-Associated Viral Vector Serotypes 1, 2, 5, 8 and 9 in Marmoset, Mouse and Macaque Cerebral Cortex." *Neuroscience Research* 93. Elsevier Ireland Ltd and Japan Neuroscience Society: 144–57. doi:10.1016/j.neures.2014.09.002.

Wehr, M. S., and a. M. Zador. 2003. "Balanced Inhibition Underlies Tuning and Sharpens Spike Timing in Auditory Cortex." *Nature* 426 (6965): 442–46. doi:10.1038/nature02116.

Wehr, Michael, and Anthony M Zador. 2005. "Synaptic Mechanisms of Forward Suppression in Rat Auditory Cortex." *Neuron* 47: 437–45. doi:10.1016/j.neuron.2005.06.009.

Wertz, Adrian, Stuart Trenholm, Keisuke Yonehara, Daniel Hillier, Zoltan Raics, Marcus Leinweber, Gergely Szalay, et al. 2015. "Network Modules" 349 (6243).

Wilent, W Bryan, and Diego Contreras. 2005. "Dynamics of Excitation and Inhibition Underlying Stimulus Selectivity in Rat Somatosensory Cortex." *Nature Neuroscience* 8 (10). Nature Publishing Group: 1364–70. doi:10.1038/nn1545.

Wilson, Authors Daniel E, David E Whitney, Benjamin Scholl, and David Fitzpatrick. 2016. "Title : Orientation Selectivity and the Functional Clustering of Synaptic Inputs in Primary Visual Cortex" 19 (8). doi:10.1038/nn.4323.

Wolfart, Jakob, Damien Debay, Gwendal Le Masson, Alain Destexhe, and & Thierry Bal. 2005. "Synaptic Background Activity Controls Spike Transfer from Thalamus to Cortex." doi:10.1038/nn1591.

Wu, Guangying K, Robert Arbuckle, Bao-Hua Liu, Huizhong W Tao, and Li I Zhang. 2018. "Article Lateral Sharpening of Cortical Frequency Tuning by Approximately Balanced Inhibition." Accessed October 28. doi:10.1016/j.neuron.2008.01.035.

Xu, Xiangmin, Nicholas D Olivas, Taruna Ikrar, Tao Peng, Todd C Holmes, Qing Nie, and Yulin Shi. 2016. "Primary Visual Cortex Shows Laminar Specific and Balanced Circuit Organization of Excitatory and Inhibitory Synaptic Connectivity." *The Journal of Physiology* 7: 1891–1910. doi:10.1113/JP271891.

Xue, Mingshan, Bassam V Atallah, and Massimo Scanziani. 2014. "Equalizing Excitation-Inhibition Ratios across Visual Cortical Neurons." *Nature* 511 (7511). Nature Publishing Group: 596–600. doi:10.1038/nature13321.

Yoshimura, Yumiko, and Edward M Callaway. 2005. "Fine-Scale Specificity of Cortical Networks Depends on Inhibitory Cell Type and Connectivity." *Nature Neuroscience* 8 (11): 1552–59. doi:10.1038/nn1565.

Zemelman, Boris V, Georgia A Lee, Minna Ng, and Gero Miesenbo. 2002. "Of Genetically ChARGed Neurons." *Cerebral Cortex* 33: 15–22.

Zemelman, Boris V, Nasri Nesnas, Georgia a Lee, and Gero Miesenbock. 2003. "Photochemical

Gating of Heterologous Ion Channels: Remote Control over Genetically Designated Populations of Neurons." *Proceedings of the National Academy of Sciences of the United States of America* 100 (3): 1352–57. doi:10.1073/pnas.242738899.

Zhang, Feng, Li-Ping Wang, Martin Brauner, Jana F Liewald, Kenneth Kay, Natalie Watzke, Phillip G Wood, et al. 2007. "Multimodal Fast Optical Interrogation of Neural Circuitry." *Nature* 446 (7136): 633–39. doi:10.1038/nature05744.